The Hong Kong Polytechnic University

Department of Mechanical Engineering

INVESTIGATION OF THE THERMAL AND EMISSION CHARACTERISTICS OF AN IMPINGING INVERSE DIFFUSION FLAME

Ng Tsz Kwan

A thesis submitted in partial fulfilment of the requirements for the Degree of Master of Philosophy

November 2006

CERTIFICATE OF ORIGINALITY

I here by declare that this thesis is my own work and that, to the best of my knowledge and belief, it reproduces no material previously published or written, nor material that has been accepted for the award of any other degree or diploma, except where due acknowledgement has been made in the text.

Ng Tsz Kwan

ABSTRACT

The main objective of this study is to determine the thermal and emission characteristics of an inverse diffusion LPG/air flame as a single jet impinged vertically upward on a horizontal flat copper plate under different conditions. Experiments were carried out on finding their characteristics and inter relationships under different air-Reynolds number (Re_{air}), overall equivalence ratio (Φ) and the nozzle-to-plate distance (H/d_{IDF}). Similar experiments were also carried out using a premixed flame jet for comparison. Five major tasks were performed successfully by using two main experimental setups to achieve the main objectives of this study.

In the first task, the physical appearance of the IDF as a free jet and also an impinging jet was qualitatively noted. The effects of the Re_{air}, Φ and H/d_{IDF} on the flame shape and length were recorded using a digital camera. Such images were useful in explaining the results obtained in the experiments.

In the second task, the temperature distribution and the pollutant exhaust emissions of the free jet IDF were investigated experimentally. The effect of Re_{air} at Φ=1 on the axial and radial temperature distributions were examined and the IDF was shown to have low pollutant exhaust emissions.

In the third task, the stagnation and radial profiles for the flame temperature and heat flux were measured under impinging experiments, while the radial combustion species concentrations were also measured. The effects of Re_{air}, Φ and H/d_{IDF} on the flame temperature, heat flux and also the combustion species were fully studied. The cool core zone significantly affected heat transfer for the impinging IDF when H/d_{IDF} is low. High temperature and high heat flux, together with high CO_2, CO and NO concentrations and low O_2 concentration were found near the stagnation point. Such effects became more obvious when Re_{air} or Φ was increased. Also, the concentrations of HC and CO showed that there was more incomplete combustion in the IDF in higher values of Φ or when Re_{air} was increased.

In the fourth task, the area-averaged heat flux and the heat transfer efficiency of the impinging IDF were calculated by considering the radial heat flux distribution in the integration area with 50 mm in radius. H/d_{IDF} had slightly effect on the two parameters at $4 \leq H/d_{IDF} \leq 10$. The area-averaged heat flux increased with Re_{air} and Φ, while higher heat transfer efficiency was obtained at Re_{air}=1500 when Φ=0.8 and Re_{air}= 2000 when Φ=1.2.

In the fifth task, similar experimental investigations were performed to study the thermal and emissions characteristics of the round premixed impinging flame jet. Comparison between the results obtained from the impinging IDF and the premixed impinging flame jet provided the evidence that the IDF seems to have the advantage of having higher heat transfer efficiency than the premixed flame over a rather large range of nozzle-to-plate distances with lower pollutant species emissions.

This study provided a fully investigation on the heat performance and also the pollutant emissions of the IDF. The IDF could achieve quite high heat transfer efficiency over a rather large range of nozzle-to-plate distances. Also, less pollutant emissions were produced by the IDF when compare to a premixed flame.

LIST OF PUBLICATIONS

1. Ng T.K., Leung C.W. and Cheung C.S., 2005, “Investigation of the Thermal and Emission Characteristics of an Impinging Inverse Diffusion Flame”, the 4th International Conference on Heat Transfer, Fluid Mechanics and Thermodynamics, Cairo, Egypt, Paper number: NT1.

2. Cheung C.S., Sze L.K., Ng T.K., Leung C.W., 2005, “A Comparison of Two Types of Inverse Diffusion Flames”, ”, the 4th International Conference on Heat Transfer, Fluid Mechanics and Thermodynamics, Cairo, Egypt, Paper number: CC5.

3. Ng T.K., Leung C.W. and Cheung C.S., 2007, “Experimental Investigation on the Heat Transfer of an Impinging Inverse Diffusion Flame”, International Journal of Heat and Mass Transfer, vol.50, pp.3366-3375.

ACKNOWLEDGEMENTS

I would like to give special thanks to Professor C. W. Leung and Dr. C.S. Cheung, my project supervisors, for their support and guidance through my work. They have provided insights into the combustion aspects of my study and patiently helped me in establishing the foundation of my knowledge. They kindly give their encouragement and suggestion on my works.

Besides, I would like to thank the technicians of the Department of Mechanical Engineering in the HKPU for their helps in developing the experimental setups. I also appreciate the help of Dr. Tse, the technician in the Thermodynamics Laboratory, who provided me with tools required in the experiments and gave much valuable opinion to solve the technical problems.

I thank my family for their support, understanding and encouragement. Home is the place to relax and lay your soul when you fall.

I thank all my friends, with whom I have met and learned from life's challenges.

TABLE OF CONTENTS

LIST OF FIGURES

LIST OF TABLES

NOMENCLATURE

Symbol	*Definition*
A	integration area (m^2)
A/F	air-fuel ratio
H	distance between the nozzle and the impingement plate(mm)
H/d	nozzle-to-plate distance
IDF	inverse diffusion flame
LHV	low heating value of gas fuel (kJ/kg)
LPG	liquefied petroleum gas
NDF	normal diffusion flame
Nu	Nusselt number
Pr	Prandtl number
T	temperature (K)
$\dot{Q}$	volumetric flow rate (m^3/s)
R	radius of the integration area (m)
Ra	random errors
Re	Reynolds Number
d	effective diameter (mm)
h	heat transfer coefficient (W/m^2K)
k	thermal conductivity (W/mK)
$\dot{q}$	heat flux density (W/m^2)
$\bar{\dot{q}}$	area-averaged heat flux (W/m^2)
r	radial distance from stagnation point (mm)

rms	root mean square
t	temperature (^oC)
u	velocity (m/s)
z	axial distance from the burner (mm)

Greek Symbols

Φ	overall equivalence ratio
η	heat transfer efficiency
ρ	density (kg/m^3)
μ	dynamic viscosity (kg/ms)
ε	emissivity
σ	Stefan-Boltzmann constant

Subscripts

air	compressed air
bead	thermocouple bead
c	convection
f	fuel
g	gas
mix	mixture of air and fuel
p	premixed flame
stoic	stoichiometric condition
T	thermocouple
W	wall of the impingement plate

Chapter 1 Introduction

1.1 A General Classification of Flames

Combustion process plays an important role in our daily life. We use it for cooking and heating. A flame is usually generated during the combustion process, in which a substance reacts with oxygen to produce heat and radiation. There are numerous ways to classify flames. Some of the common ones are discussed in this section.

The most common classification considers how the fuel and the oxidizer are mixed. A flame can be directly classified as premixed or diffusion if there is an existence or absence of mixing of the fuel and oxidizer before combustion occurs. A premixed flame is often shorter and more intense, compared to a diffusion flame. As a result, a high temperature region is developed in the flame, which leads to non-uniform heat transfer to a load and higher NO emissions. A diffusion flame is typically longer, but does not have a hot region and has a more uniform temperature and heat flux distribution. In practice, a flame may not be totally premixed or diffusion. It may be a partially premixed flame, in which the oxidizer is mixed with a portion of fuel. This is done for stability and safety reasons since the partial premixing helps anchoring the flame and thus decreases the chance for flashback.

A flame can also be classified into laminar or turbulent according to the fluid dynamics of the gas streams. The mixing and transport of a laminar flame is achieved by microscopic molecular processes, while in a turbulent flame, these processes are the result of macroscopic eddy motions. Theoretically, the Reynolds number is used to distinguish laminar and turbulent flames, but in non-premixed flames, the Reynolds number is sometimes difficult to define. This is because the oxidizer and fuel may have different velocities when exiting the burner.

Another classification takes into consideration the boundary of the combustion system; the flames may be open or enclosed. Industrial flames usually occur in a combustion chamber with controlled air and fuel supply. Such flames are called enclosed flames in contrast to open flames which are formed in an unbounded surrounding atmosphere. There is usually more intense radiation heat transfer from the boundaries to a load in an enclosed flame.

A flame can also be classified as normal or inverse, depending on the arrangement of the fuel and oxidizer jets. Basically, a normal flame refers to a flame burns with a central fuel jet surrounded by an oxidizer jet. An inverse flame has a reverse arrangement in which the oxidizer jet is surrounded by the fuel jet. However, this classification applies only to a non-premixed flame.

Although flame phenomena consist of many complicated physical and chemical processes, any flame can be classified properly according to the foregoing classifications. Literature on different types of flame have been widely

published. However, there is little literature on the inverse diffusion flame (IDF). Normally an inverse diffusion flame is generated with a two coaxial tubes with the inner one supplying air and the outer one supplying fuel.

1.2 Flame Impingement

Flame impingement heating has been extensively studied because of its importance in many industrial and also the domestic applications. Direct flame impingement can enhance heat transfer to a surface, improve the heat transfer efficiency, reduce fuel consumption and pollutant emissions. It has been proved that the thermal performance of a flame impingement system is influenced by four factors of the system, namely, burner style, jet properties, impingement surface condition, and configuration between the nozzle and the surface.

As far as impinging flame is concerned, there have been many investigations on impinging premixed flames. However, the flammability range of premixed flame is small and the effective heating area is also relatively small. Premixed burners are rarely used in industry for safety reasons, but are commonly used in domestic applications. On the other hand, impinging diffusion flame burner with high Reynolds number flame jet has long been used in industrial rapid-heat transfer furnaces, but the formation of soot is an associated problem. There is lack of investigations on the application of the IDF for impingement heating. However, the impinging IDF used in industrial and domestic heating may give a cleaner flame than the diffusion flame and provide

a wider range of flammability than the premixed flame and is hence worth investigation.

1.3 Importance of Research

Figure 1.1 shows the figure of historical and projected world energy consumption. The demand for energy is expected to continue to increase rapidly. Most of the energy (86%) is produced by the combustion of fossil fuels like oil, natural gas and coal. According to the U.S. Department of Energy, the demand in the residential and industrial sectors is projected to increase by 1.5% and 2.1% per year from 2002 to 2025 respectively. Associated with the energy utilization is the generation of air pollutants. Therefore, there is a need to protect our threatened environment by improving the heat transfer efficiency and pollutant emissions of the combustion processes.

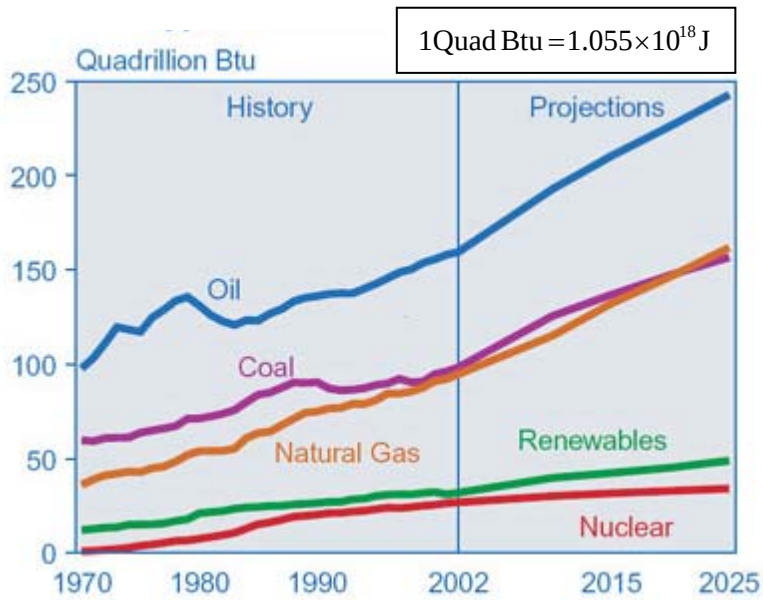

Figure 1.1. Historical and projected world energy consumption. (U.S. Department of Energy, Energy Information Administration) [1]

Gaseous fuel burns in the cleaner way than the solid and the liquid fuels. Most of the flame jet studies are concentrated on methane flames or natural gas flames, and numerous investigations have already been carried out in understanding the characteristics of the flame. However, in Hong Kong, liquefied petroleum gas (LPG) is used both in domestic burners and in cars. Therefore, this study is focused on analyzing the LPG flame. In Hong Kong a fully filled commercial LPG bottle is composed of about 30% of propane and 70% of butane.

The structure of IDF has been studied experimentally and numerically, most of the literature is related to the coaxial type of the IDF. The burner used in this study is newly designed. It has a central air jet with twelve fuel jets surrounding circumferentially. The schematic design of the burner is shown in *Figure 1.2*. This IDF burner was first investigated by Sze et al. [2, 3]. They found that the circumferentially arranged fuel ports enable better air fuel mixing than the coaxial jets. Understanding of the fundamental processes involved in IDF combustion can lead to improved predictive capability and design of more practical combustors, resulting in enhanced efficiency and reduced pollutant emissions. As a result, this study may contribute in the development of new technologies for non-premixed low emission combustion devices for both industrial and domestic applications.

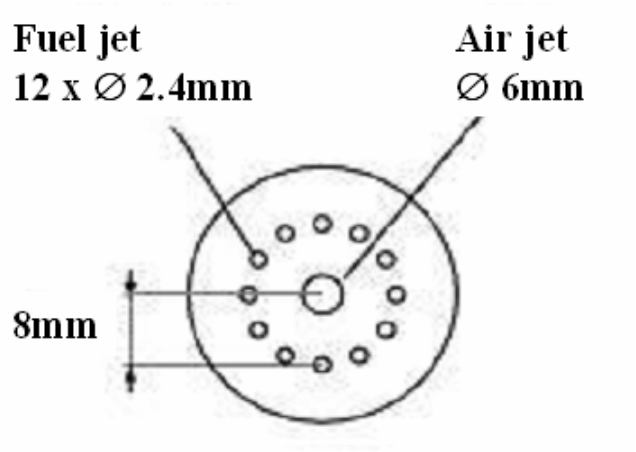

Figure 1.2. The dimensions of the inverse diffusion burner with circumferentially arranged fuel ports designed.

1.4 Thesis Objectives

This study aims to investigate the characteristics of the LPG/air IDF using the circumferentially arranged fuel ports (*Figure 1.2*) as a free jet and also an impinging jet. Finding out how are the heat and emission performances of the IDF and how are the performances for the IDF over a premixed flame. The four main performance characteristics of the flame, which include flame temperature, heat flux, heat transfer efficiency and combustion species concentrations, will be investigated. The combustion species to be measured will include O_2, CO_2, CO, NO and HC. Their characteristics and inter relationships under different air jet Reynolds number, equivalence ratio and the distance between the nozzle to the heating target will be studied experimentally. Similar experiments will also be carried out on a circular premixed impinging flame for briefly comparison.

The detailed objectives of the present study are:

- To qualitatively note the physical appearance of the IDF as a free jet and also an impinging jet under various operating conditions.
- To briefly investigate experimentally the temperature distribution and pollutant emissions of the open IDF jet.
- To investigate experimentally the effects of air jet Reynolds number, equivalence ratio and the distance between the nozzle and the heating target on the thermal performances and emission characteristics of the IDF impinging jet.
- To calculate the heat transfer efficiency of the IDF impinging jet according to the radial heat flux distributions at different nozzle to heating target distances.
- To conduct similar tests with a premixed flame jet. The characteristics between the two different types of flame jet will be compared.

1.5 Organization of Thesis

The thesis contains seven integrated chapters.

A comprehensive review of the relevant literatures is provided in Chapter 2, which includes the flame shape and structure of premixed and non-premixed flame, experimental conditions on impinging heat transfer, heat transfer efficiency, soot formation in inverse diffusion flames, the pollutant emission in flame impingement and different inverse diffusion flame burner designs.

The experimental set-up, experimental procedures and handling of experimental data are described in Chapter 3. Chapter 4 and Chapter 5 present the results of the experiments in free jet and impinging jet, respectively. The important parameters include the flame observations, flame temperature and combustion species in both free jet and impinging jet experiments. The parameters of heat flux, area-averaged heat flux and also the heat transfer efficiency are also discussed.

Chapter 6 describes the experimental results obtained from the round premixed flame jet. Comparisons between the IDF and the premixed flame are also provided in the same chapter.

The overall conclusions of this study are given in Chapter 7.

Chapter 2 Literature Review

Several areas of interest need to be reviewed before starting the experimentation with the inverse diffusion flames. As mentioned in the previous chapter, there are different classification of flames, each of them have different flame shape, thermal and emission characteristics during combustion. However, it is difficult to review exhaustively all the papers and different aspects of the flames. This chapter mainly focuses on the inverse diffusion flames, while premixed flames and normal diffusion flames will be mentioned for comparison.

There are six sub-sections of reviews, first is the flame shape and structure of free jet and impinging jet for both premixed and non-premixed flame. The second provides the review of experimental conditions on impingement heat transfer. Then, the third section is the review concerned with heat transfer efficiency. The soot formation in inverse diffusion flames and the pollutant emission in flame impingement are also reviewed. The last sub-section is the review of different inverse diffusion flame burner designs.

2.1 Flame Shape and Structure

2.1.1 Free Flame Jet

Premixed flames have long being studied because they have the property of highly intense combustion. Hargrave et al. [4] examined the flame structure of the stoichiometric methane/air premixed flame from the laminar to fully turbulent. They stated that a stable inner conical reaction zone was formed as a boundary between the unburnt and burnt gas when the flow was laminar. When the Reynolds number increased, the flame appeared irregular and wrinkled and the reaction zone was extended and became thicker, more diffuse and ill-defined. Maximum temperature was found in the reaction zone, which increased and occurred at greater axial distance with increasing Reynolds number.

As a premixed flame have limited flame length and flammability range, researchers have also investigated the characteristics of non-premixed flames. Normal diffusion flame is a type of non-premixed flame. The term ‘diffusion flame’ was first used by Burke and Schumann [5] in their investigation of the structure of enclosed cylindrical diffusion flames. Two flame shapes were found: a conical flame surface converging towards the tube axis, called an “over-ventilated” flame; and an upside down cone shape, called “under-ventilated” flame. Barr [6] investigated and characterized ten different types of normal diffusion flames according to their appearance. He studied the length of enclosed laminar butane-air flames experimentally. He reported that as the fuel flow rate of the diffusion flame was increased, the flame length increased also.

Moreover, the influences of burner tube diameter and tube thickness, as well as air and fuel flow rate on the variation of the flame length were discussed. Mitchell et al. [7] found that the adiabatic flame temperature was approached in the narrow annular reaction zone of a confined laminar methane/air diffusion flame. Cavaliere and Ragucci [8] gave an overview of gaseous diffusion flames on their simple structures and interaction. According to their review, most active and recent research was partly to enhance mixing, shaping and control in diffusion flame stabilization.

An inverse diffusion flame is another type of non-premixed flame which is the main flame type investigated in this study. The “inverse diffusion flame” was first described as “reciprocal flames” by Friend [9], who was the first person developed the concept of an inverse diffusion flame. Wu [10] conducted a comprehensive study of an inverse diffusion flame and classified the flame into six types, according to the flame appearance and the flame stability. The common features are showed in *Figure 2.1(A)* by Wu and Essenhigh [11]. Zone 1 is a blue emission region while zone 2 is an orange emission region. The measured temperature profiles indicated that the peak temperature was reasonably coincident with the blue zone and symmetrical along the center axis. Later, Bindar and Irawan [12] generated an inverse diffusion flame with flame shape different from Wu and Essenhigh [11], *Figure 2.1(B)*, which consisted of a base and a tower flame. They emphasized that when the air momentum rate was very low, a normal diffusion flame shape was formed in a laminar flow; when it increased, a base-tower shape was developed in a turbulent flow, which

increased the flame temperature due to the intensity of mixing of fuel and air increased.

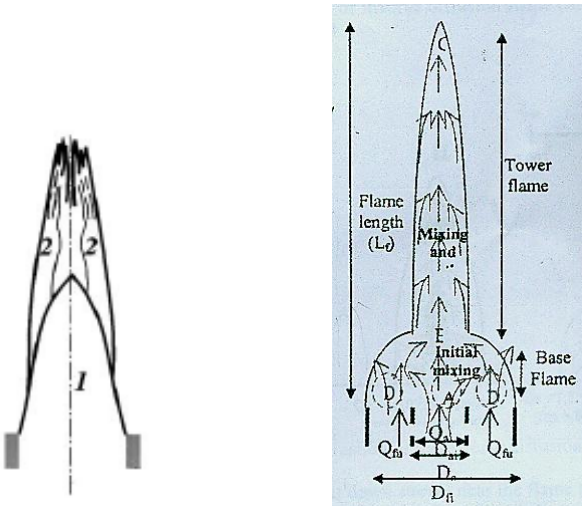

(A) (B)

Figure 2.1. Schematic inverse diffusion flames:
(A) From Wu and Essenhigh [11]. (B) From Bindar et al. [12].

Some researchers have tried to introduce a central air microjet into a diffusion flame in order to control the flame shape and luminosity. The flame so generated can also be considered as an inverse diffusion flame. *Figure 2.2* shows the direct images of six non-premixed flames as described by Sinha et al. [13]. They used a microjet to modify the structure of a diffusion flame. *Figure 2.2(A)* is a normal diffusion flame, which is characterized by buoyance-induced flickering and a large luminosity that is indicative of soot formation, while *Figure 2.2(B)* to *Figure 2.2(F)* are the inverse diffusion flames with velocity increasing in the central air microjet.

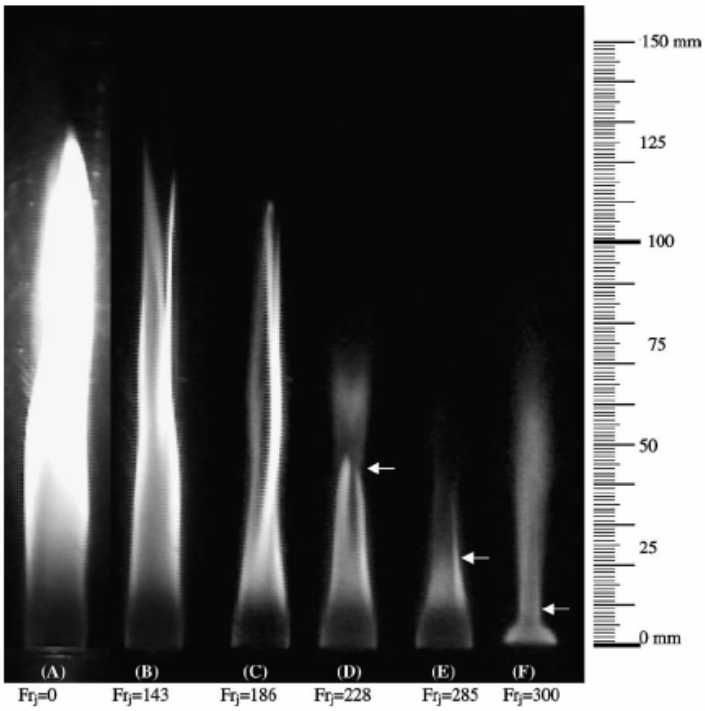

Figure 2.2. Direct image of non-premixed flames: (A) Normal diffusion flame; (B-F) Increasing central air microjet velocity from B to F with constant fuel supplied. [13]

The shapes of the normal and inverse diffusion flame are different from each other. As mentioned by Sinha et al [13], the normal diffusion flame was more luminous and diffusive than the inverse diffusion flame. They also found that when the air microjet velocity increased, the flame length decreased from (B) to (E) because the entrained oxidizer enhanced the reaction rate and limited the diffusion of the flame. When the velocity was further increased, the flame (F) became bright blue and a neck region was formed. Such results are similar to those obtained by other researchers [2-3, 12, 14-17]. They also found that the flame length increased with increasing fuel flow rate at constant air flow rate.

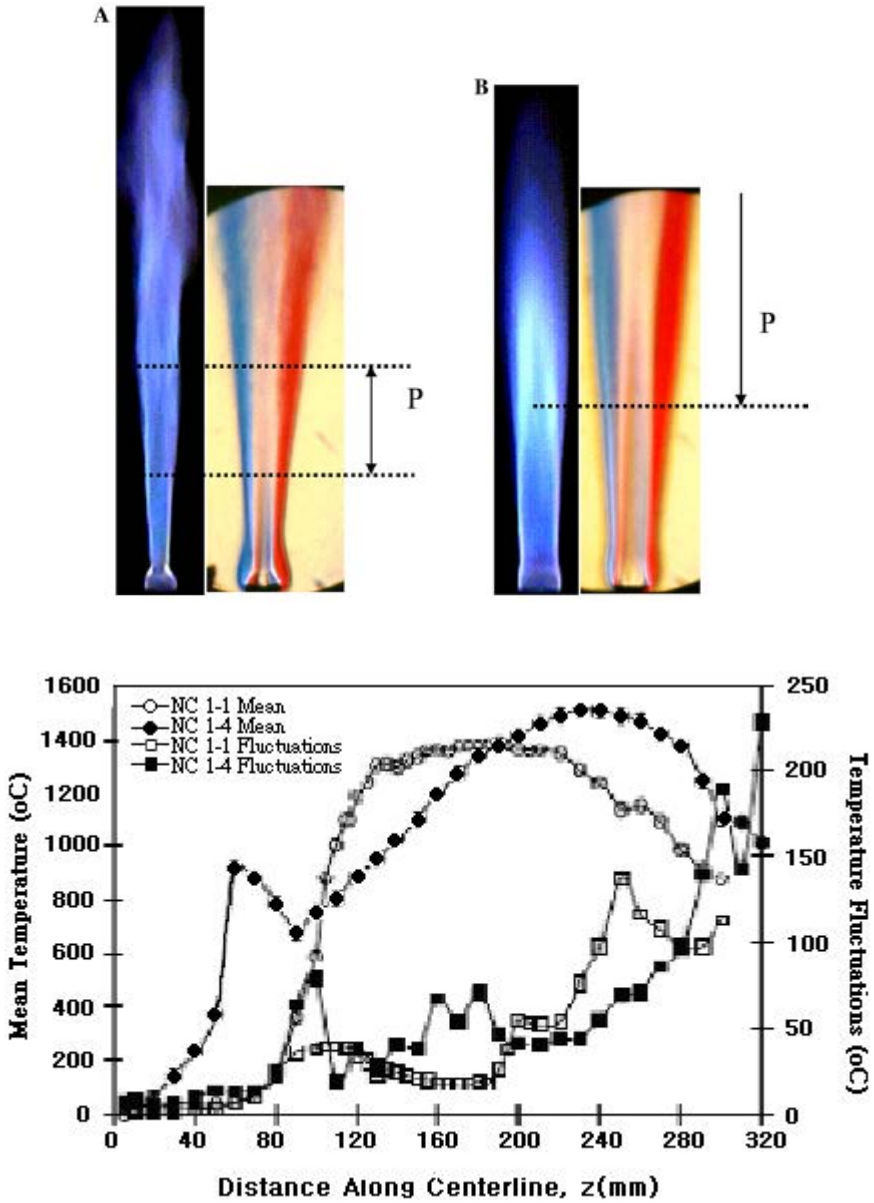

Figure 2.3. Upper: Depicts direct and Schliern images of two coaxial burners with the same outer diameter 14.84 mm. (A) NC 1-4, 3.86 mm inner air jet diameter; and (B) NC 1-1, 10.21 mm inner air jet diameter. Lower: Axial profiles of mean and fluctuating temperatures for the two flames [14].

Besides the air and fuel jet velocities, the nozzle conditions and the air and fuel equivalence ratio will affect the flame length, temperature distributions and stability limits. The coaxial inverse diffusion flames produced from different combinations of air and fuel nozzle diameters have been studied by Sobiesiak

and Wentzell [14]. They stated that the velocity ratio, fuel/air nozzle diameter ratio, and fuel/air jet equivalence ratio could be optimized to produce an extended region of uniform and high temperature. Two of the inverse flames are shown in *Figure 2.3*. In the Schlieren images, a uniform temperature region, marked with P, can be found. This region coincides with the local peak temperature at z=50mm for the NC 1-4 flame and the steep increase in the temperature at z=100 for the NC 1-1 flame together with the radial temperature profiles indicates that a premixed combustion region occurs within the envelope of a diffusion flame.

In addition, the stabilization of the non-premixed flame can be improved by adding a circular disk placed concentrically at the exit of the central jet acting as a bluff-body [18-19], which is shown in *Figure 2.4*. Huang and Lin [18] investigated the characteristics of a circular-disc stabilized normal diffusion flame. Later on, Huang et al. [19] used the same experimental setup to further investigate for the inverse diffusion flame. In normal diffusion flames, increase in the central fuel jet leads to an increase of the flame height and decrease of the flame lift-off height. However, in inverse diffusion flames, when the central air jet velocity increases, a partially premixed flame sits on a diffusion bubble flame. The partially premixed flame blows off for central jet velocity higher than about 55m/s.

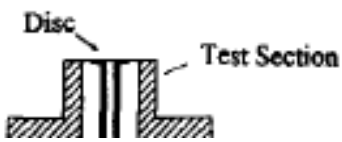

Figure 2.4. Bluff-body stabilized burner [18].

Comparison on the structures between the normal and inverse diffusion flame can be found in [11-14, 20-21]. Sinha et al. [13] also compared the axial centerline temperature profiles, as showed in *Figure 2.5*, of the two flames. The burner exit temperature is lower for the inverse diffusion flame due to the advective cooling caused by the cold central air stream. Also, the temperature rise for the inverse flame is steeper because of the enhancement of the entrained oxidizer [15]. However, the two flames have similar peak flame temperature, which shows that the central air jet does not have effects on the thermal performance when the axial distance is about 10mm far from the burner.

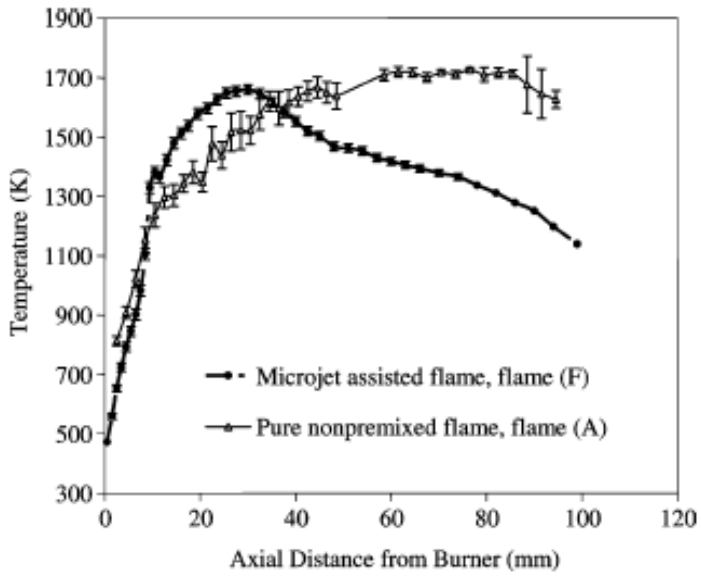

Figure 2.5. Axial centerline temperature profile: (F) Microjet assisted inverse flame; (A) Pure normal diffusion flame [13].

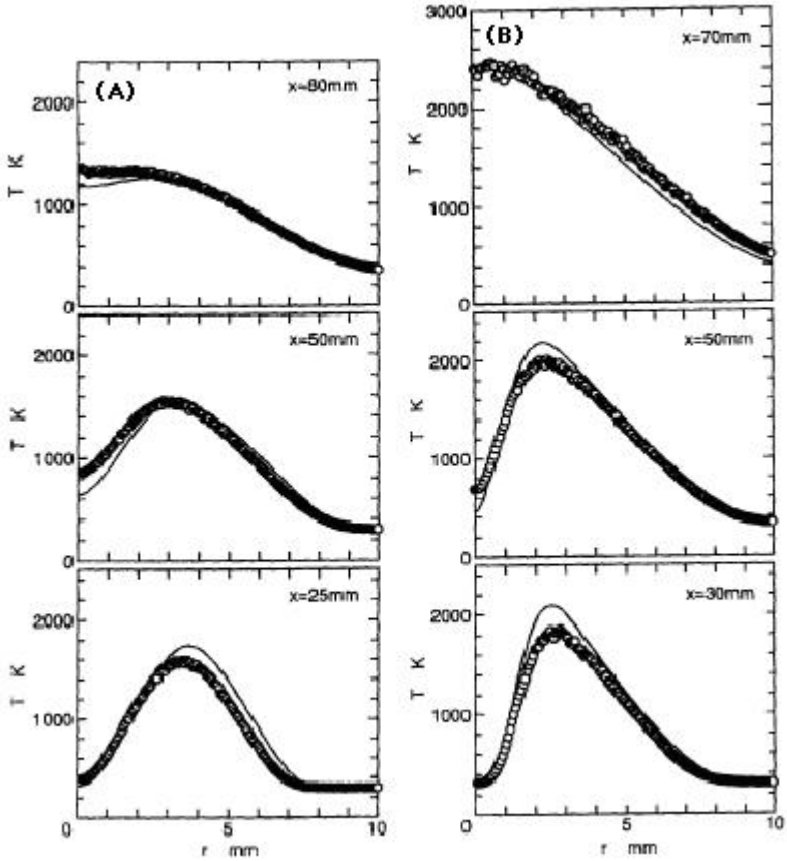

Figure 2.6. Radial temperature profiles.
(A) Normal diffusion flame, (B) Inverse diffusion flame [20].

Figure 2.6 shows the radial temperature profiles of the normal and inverse diffusion flames at different flame heights [20]. The radial maximum temperature is found at lower flame height in normal diffusion flame, while it is found near the flame tip in inverse flame. Moreover, Takagi et al. [20] mentioned that the radial maximum temperature measured from the normal flame was significantly lower than the maximum adiabatic equilibrium temperature, but for the inverse flame, temperature was found closer to the adiabatic equilibrium temperature for the same fuel. It is because IDF has certain level of partial premixing with central air jet, which exhibits the higher flame temperature.

Shaddix et al. [21] studied the flame structure of both the normal and inverse diffusion flames using a slot burner. They observed the direct images and noted that the blue chemiluminescence, which marked the fuel-rich edge of the reaction zone, was clearly seen to lie outside of the yellow-orange soot luminosity for normal diffusion flame and inside of the luminous zone for the inverse diffusion flame.

2.1.2 Impinging Flame Jet

When there is a flat plate placed above a flame, the flame is impinging and the part below the plate, the free jet region, is affected little as shown in *Figure 2.7*. The potential core zone or the reaction zone can be observed if the nozzle to plate distance is larger than the corresponding height. The stagnation zone is the region that the flame reaches the plate before distortion. The part above the plate will be highly distorted and spread horizontally along the plate, forming the wall jet region.

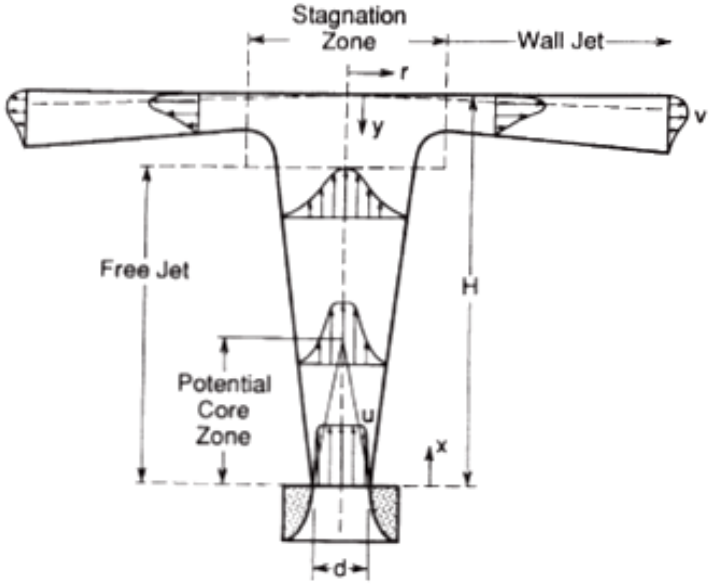

Figure 2.7. Schematic of flow of a jet impinging on a flat plate [22].

In all impinging flame jet systems, Zhang and Bray [23] reported five basic combustion modes, which could be identified experimentally. These five typical impinging flow reacting patterns were conical flame, disc flame, envelope flame, ring flame and cool central core flame. It was concluded that flow conditions affected directly the shape and stability of a flame.

Foat et al. [24] visualized the structures of turbulent premixed impinging flames with a high-speed digital camera and a high shutter speed colour video camera, which were effective tools for the detailed study of flame structures and dynamics, offering unique physical insight into flame structure and dynamics. Eight different flame modes were observed by changing the initial ignition locations. They were a blown ring, ring, disc, detached, conic, envelope, cool central core, and complex flames.

Different zones for the impinging premixed and diffusion flames are shown in *Figure 2.8* schematically. Milson and Chigier [25] found that, both flames had a cool central core of unreacted gas at low H/d=10-16. In the premixed flame, a high turbulence appears in the 'very intense combustion zone' near the target surface leading to good mixing of air/fuel. Rigby and Webb [26] showed that the reaction zone of the diffusion flame was relatively steady and stationary for low Reynolds number at relatively small nozzle to plate distances.

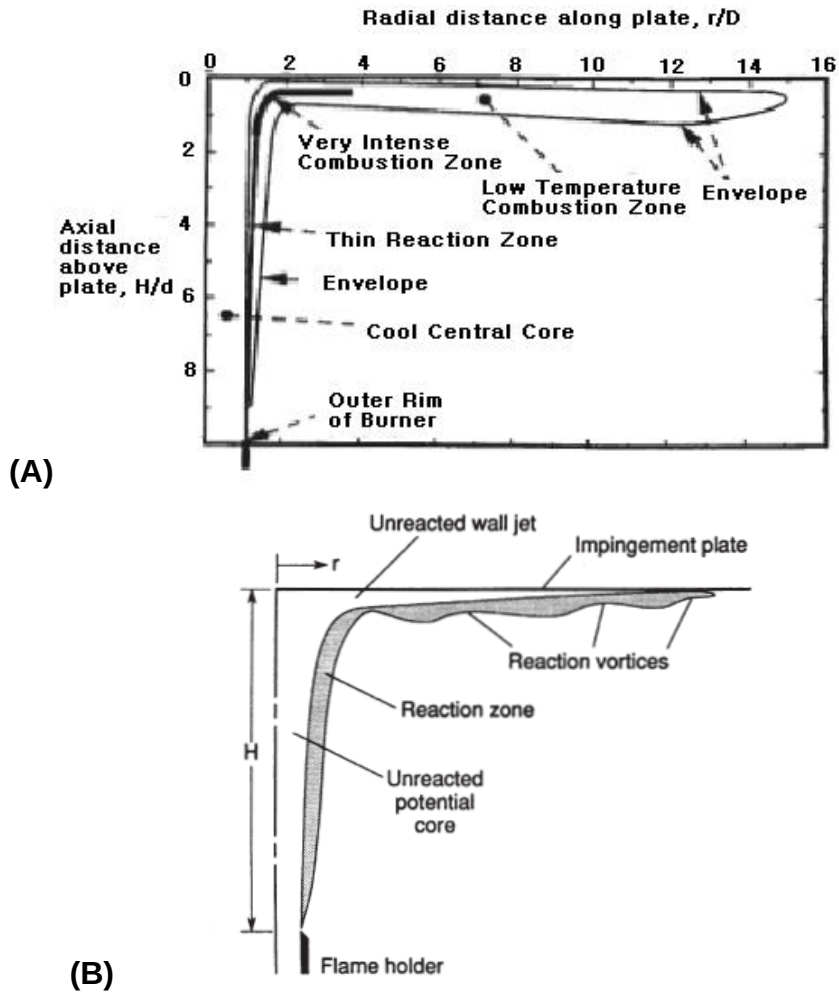

Figure 2.8. Regions in impinging flames on a horizontal surface.
(A) A premixed methane/air flame [25]. (B) A diffusion natural-gas flame [26].

The structure of the impinging diffusion flame emerged from a radial jet reattachment burner was investigated by Wu et al. [27]. The surface pressure measurement indicates the symmetric structure of the flame. Besides, several researchers investigated the reattachment flames [27-31]. Mohr et al. [31] found that the reattachment flame had very low surface pressure coefficients, which could suggest application in processes that require surface heat treating of delicate materials.

Sze et al. [2] investigated the impingement and spread of an inverse diffusion flame emerging from a burner with a central air jet and circumferentially arranged fuel ports. From their results, the stagnation and the wall region of the flame were not obvious at Φ=1.0, but became obvious at Φ=1.4. The visible length of the open flame at Φ=1.0 was measured as 80 mm. Thus, the impingement plate cooled the flame which led to the disappearance of the non-luminous outer flame.

2.2 Experimental Impinging Heat Transfer

Six heat transfer mechanisms have been identified in previous flame impingement studies: convection (forced and natural), conduction (steady-state and transient), radiation (surface, luminous, and nonluminous), thermochemical heat release (equilibrium, catalytic, and mixed), water vapor condensation, and boiling (internal and external) [32]. It has been verified that forced convection is a predominant mechanism. Thermochemical heat release (TCHR) is a large fraction of the total heat flux when the oxidizer is pure oxygen. Natural

convection is only important for very low velocity flames. Surface radiation plays a significant role for experiments where the target is located inside a hot furnace. Nonluminous radiation does not have a very large effect. Luminous radiation is important for very fuel rich flames. Condensation occurs when the temperature of impingement surface is lower than the dew point of the combustion gases. A comprehensive review of flame impingement heat transfer has been given by Chander and Ray [33].

The effect of radiation heat transfer from gaseous flames has been neglected in most of the investigations owing to the very small contribution. Most of the gaseous flames are non-luminous and due to their low opacity, the effect of radiation heat transfer is very small. Wu et al. [27] found that in an array of impinging radial jet reattachment flame nozzles, 90% of the heat is transferred to the surface by forced convection and the effect of radiation (≈10%) is negligible.

In this study, the total heat flux due to convection and radiation is measured by a heat flux transducer, which had been applied satisfactorily in the former studies [2, 34, 35].

2.2.1 Configuration

Dong et al. [34] performed an experimental study to determine the heat transfer characteristics of a premixed butane/air round flame jet of low Reynolds number impinging upwards normally on a flat rectangular plate. Dong et al. [35] also conducted a series of experiments to determine the heat transfer characteristics of a round, premixed butane/air flame jet impinging upwards on an inclined flat plate at different angles of incidence. The inclination angles chosen for investigation were 57 ^{o}, 67 ^{o}, 80 ^{o} and 90°. They found that the maximum heat flux decreased as the inclination angle was reduced. Subhash and Anjan [36] summarized that there were five different types of configuration which had been studied for impinging flames. These are flame impinging normal to a cylinder, flame impinging normal to a hemispherical nosed cylinder, flame impinging normal to plane surfaces, flame striking parallel to plane surfaces and flame striking at some angle to plane surfaces. Of these six configurations, the perpendicular impingement has higher combustion efficiency, but the impinging flame may induce flashback and damage the combustor injector.

For the sake of brevity, this study emphasizes the flame impingement normal to a plane surface.

2.2.2 Operating Conditions

Operating conditions have a strong influence on heat transfer and flame stability during flame impingement heating. These operating conditions include the type of fuel, type of flame, equivalence ratio, nozzle to plane distance, Reynolds number, etc.

Milson and Chigier [37] studied the heat transfer characteristics of methane and methane/air flames, and a comparison was given between diffusion and pre-mixed flames for Re=7000. The maximum temperature at the plate in the premixed flame was higher by 35 K and occurred at the same position as that of the diffusion flame, but the stagnation temperature was almost the same. The maximum heat flux in the case of premixed flames was also higher. So, ultimately, it was concluded that the effect of using the premixed flame as compared to a diffusion flame was to increase the rate of combustion so that the combustion could be completed more quickly.

A wide range of equivalence ratios has been used in different experiments, from fuel lean mixtures to fuel rich mixtures. Baukal and Gebhart [38] used different kinds of burners that could vary the oxygen composition in the oxidizer from Φ= 0.3 to 1.0. Mohr et al. [31] used a radial jet re-attachment combustion nozzle at Re=8855, Φ=1.0 for maximum heat transfer. If Φ was greater than unity, luminous radiation becomes more important. It was because more yellowish flame would be observed at higher values of Φ and more heat would be lost by radiation.

A wide range of Reynolds number has been studied, ranging from very low values to very high values. It is seen that the Reynolds number is not always given, but the flow velocity or whether the flow is laminar or turbulent is mentioned. Dong et al. [39] observed that the effect of Re was quite significant on the heat transfer. The heat transfer rate in both the stagnation region and the wall jet region was enhanced with an increase in Re.

The nozzle to plane distance refers to the dimensionless axial distance between the burner exit and the target surface, which affects the heat transfer and flame stability. In general, shorter distances result in higher flux rates. One reason for this is smaller ambient air entrainment. Another reason is that the flame widens at longer distances. Mizuno et al. [40] observed that as H/d was decreased, the heat flux increased. This was because, for smaller H/d, there was less entrainment of cold air into the flame and the temperature became higher. Schulte [41] used a water-cooled heat flux transducer to determine the heat transfer profiles of small natural gas/oxygen and acetylene/air flames. The results showed that although the heat transfer rate could be varied by adjusting the length of the primary cone, the H/d also must be changed in order to maintain a relatively flat heat flux profile.

The dimensionless radial distance refers to the distance from the burner centerline to the location on the target where the heat flux was measured. In some studies, the average heat flux to the entire target was measured. For those studies, R/d refers to the range over which the heat flux was measured.

2.3 Heat Transfer Efficiency

One important aspect of heat transfer is the efficiency of the heat transfer process, which has been mentioned only in a limited number of literatures. Hou and Ko [42] investigated the effects of heating height on the appearance, temperature field and efficiency of a premixed impinging laminar jet flame jet. They showed that, with increasing heating height, the thermal efficiency first increased to a maximum value and then decreased. They found that the maximum efficiency occurred when the heating height was slightly lower than the tip of the inner rich premixed flame. Mizuno et al. [40] investigated the heat transfer efficiency of an impinging premixed flame, and concluded that the heat transfer increased with increasing heat input but the thermal efficiency decreased at the same time. They reported that the thermal efficiency decreased with the firing rate and the heating height, but increased with the oxidizer purity. Therefore, in application, high firing rates can enhance productivity but reduce the thermal efficiency. Jugjai et al. [43,44] also reported improvement to gas burner efficiency using swirling flame or heat re-circulation.

There is no published literature on the thermal efficiency of an impinging inverse diffusion flame.

2.4 Soot Formation in Inverse Diffusion Flames

Although the present work does not include the soot analysis in inverse diffusion flames, the reviews in this section are for a better understanding about the soot problems in the inverse flames. The primary source of the luminosity observed in a flame is caused by the incandescent soot. Soot also contributes to radiant heat losses from flames. Soot formation proceeds in a four-step sequence:

1. Formation of precursor species.
2. Particle inception
3. Surface growth and particle agglomeration
4. Particle oxidation.

Most of the previous studies emphasize the low soot formation characteristic of the inverse diffusion flames. Kaplan and Kailasanath [45] investigated the effect of the flow-field on soot formation in methane/air inverse diffusion flames. Their research indicated that surface growth rate of inverse diffusion flames was very small along the particle path line, and as a consequence much less soot was produced in inverse diffusion flames than in normal diffusion flames.

Less soot formation was also found in the study by Sidebotham and Glassman [46], who determined that the soot inception of a coflowing inverse diffusion flame was observed only when the local temperature exceeded a critical value in a region sufficiently far from the oxidation zone. Also, they reported that the effect of fuel concentration changes could be more important

than the effect of temperature change when a fuel was diluted in the inverse diffusion flames. According to Lee et al. [47], the fuel dilution resulted in a decrease of temperature and an enhancement of residence time, but the critical dilution mole fraction was found for which temperature did not affect soot growth. Soot inception was also found to be weakly dependent on temperature as influenced by fuel dilution.

2.5 Pollutant Emission in Impinging Flame

The analysis of the combustion gas products has become very important recently and more researchers have contributed to study in the field. Viskanta [48] pointed out that the interaction of a flame jet with a cold surface will affect chemical reactions and may have an adverse effect on the emission of pollutants. According to Mohr [49], flame impingement is expected to enhance the formation of pollution because the cold impingement surface acts to quench the flame, thus reducing the residence time and inhibiting the complete reaction of fuel and oxidizer. Dong et al. [50] conducted an experimental study to determine the characteristics of the combustion species concentration and heat transfer from a premixed slot butane/air flame jet impinging on a cooled flat plate. The high heat fluxes found in the reaction zone coincided with high concentrations of CO, NO and CO_2, and very low concentrations of O_2 and HC occurred around the stagnation point.

Mishra [51] also studied the emission characteristics of premixed flames burning LPG. He stated that the CO level increased with separation distance for all Reynolds number which might be attributed to the excess entrainment of air

leading to the dilution of mixture. The NO level was found to decrease with increase in equivalence ratio due to decrease in flame temperature. The CO_2 level increases with equivalence ratio for all Reynolds number, but decreases with increase in Reynolds number. This result may be attributed to the local quenching effect of the flame.

Sze et al. [3] investigated the NO_X emission of free jet inverse diffusion flames emerging from a coaxial burner and a burner with circumferentially arranged fuel ports (CAP). It was found that the intense combustion process located at around a height of 50 mm in the inverse flame from the CAP burner with CAP, while mixing was limited in the coaxial flame. The $EINO_X$ curves for the two flames were bell-shaped and the maximum $EINO_X$ was 3.2g/kg at Φ=1.2 for the CAP flame and 3.0 g/kg at Φ=2.2 for the coaxial flame. It can be explained that mixing is more intense in the CAP flame and higher temperature can be attained in such flame. Sze et al. [2] also investigated the emission of the impinging inverse diffusion flame. In the intense combustion region, as indicated by the lowest O_2 level, the highest values of NO, CO_2 and CO levels were found.

2.6 Inverse Diffusion Flame Burner Design

Many different types of burner have been used to study the non-premixed flames. Within the literature reviewed in this study, the burners can be classified into four types. First type is the simple concentric coaxial type burner [8-16]. Most of the previous studies used this type of burner with double or multi jets. Different combinations of the air/fuel nozzle diameters and velocities have been studied.

Second type is the bluff-body stabilized burner [18-19]. This type of burner has been used extensively for the industrial combustors. The non-premixed flame emerged has the characteristics between the extreme cases of the premixed flames and the pure diffusion flames. This burner design can avoid preignition and explosion dangers inherent in premixed flames or increase flame luminosity and improve stability in non-premixed flames.

The third type of burner is the radial jet reattachment burner [26-30]. The internal air stream is forced to exit the nozzle in an outward radial direction, then, viscous mixing occurs at the boundary between the moving air and the stagnant air, causing secondary mass entrainment. As a result, the mixing between the gaseous fuel and oxidizer can be improved. It was said to exhibit a stable flame with very little soot formation, and high heat transfer rate under a wide range of air/fuel ratios [29].

The last type of burner is the circumferentially arranged jets burner [2-3]. There are 12 outer fuel jets arranged circumferentially around a central air jet in order to form an inverse diffusion flame. This arrangement could enhance the mixing between the air and fuel, as there was more uniform heating around the stagnation point in impingement heating. In this study, this type of burner was used; however, the distance between the air jet and the surrounding fuel jets were changed to 8 mm, instead of 11.5 mm as used by Sze et al. [2]. The shortening of such distance would further enhance the mixing of the air and fuel.

2.7 Summary

It is seen that the studies related to inverse diffusion flames are concentrated on their flame structure and soot analysis, and they are often compared with normal diffusion flames. Very few studies are cited in the literature in which the impingement heat transfer and emission of inverse diffusion flames are studied. Therefore, it is valuable to investigate such characteristics of the impinging inverse diffusion flames using an improved design of burner, the burner with circumferentially arranged fuel ports. The performance will also be compared with a premixed flame. It is believed that, the inverse diffusion flames investigated in the present work can provide heat flux efficiency as high as the premixed flames but with lower NO_x emissions compared to the coaxial inverse diffusion flames.

Chapter 3 Experimental Work

In this chapter, the design of the test rig is discussed in the first section. The second section discusses the measurement techniques and instruments. The third section describes the handling of the experimental data. The last two sections discuss the experimental procedures and the reliability of the experimental results.

3.1 Design of Test Rig

Two sets of experiments were carried out. The first set was the free jet flame experiment. *Figure 3.1.*1 shows the experimental setup for measuring the flame temperatures of the free jet inverse diffusion flame. In the Figure, two thermocouples of type B were used in order to decrease the time of the measurements. They were separated by 80 mm in the z-direction to reduce the interference between each other.

Figure 3.1.2 displays the schematic of the measurement of the exhaust combustion species of the free jet inverse diffusion flame.

The second was the impinging jet experiment, which is shown in *Figure 3.1.3.* The system composed of two parts: the heat generation system and the heat absorption system. In the set-up, temperature and heat flux were recorded at the same time while combustion species were measured separately.

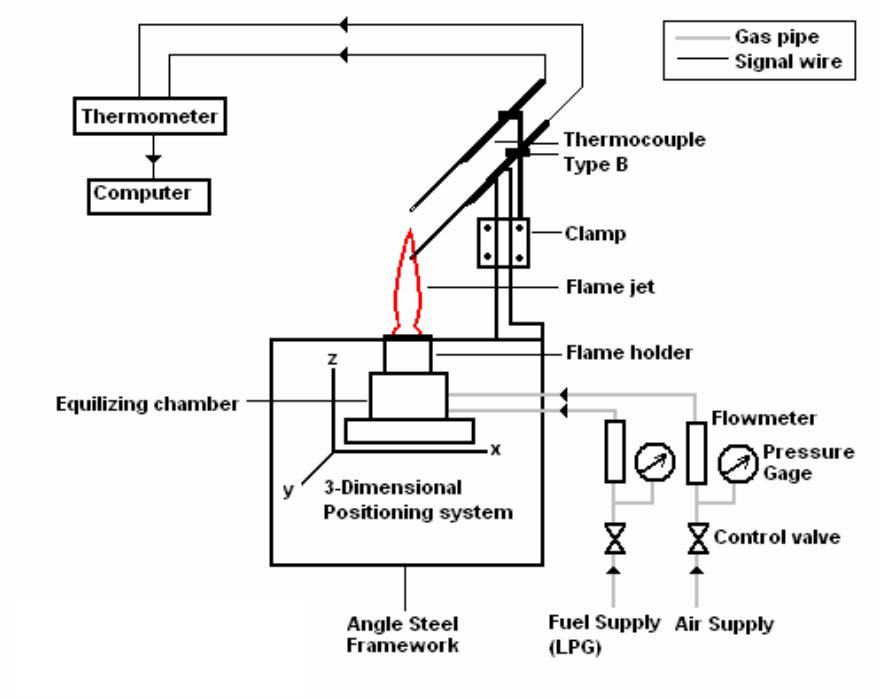

Figure 3.1.1 IDF free jet experimental set-up for measuring flame temperature

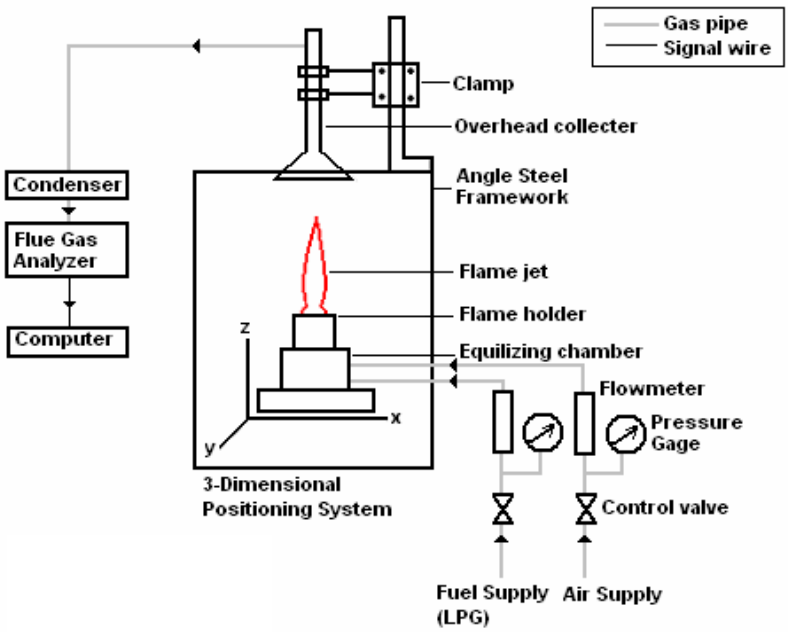

Figure 3.1.2 IDF free jet experimental set-up for measuring exhaust combustion species

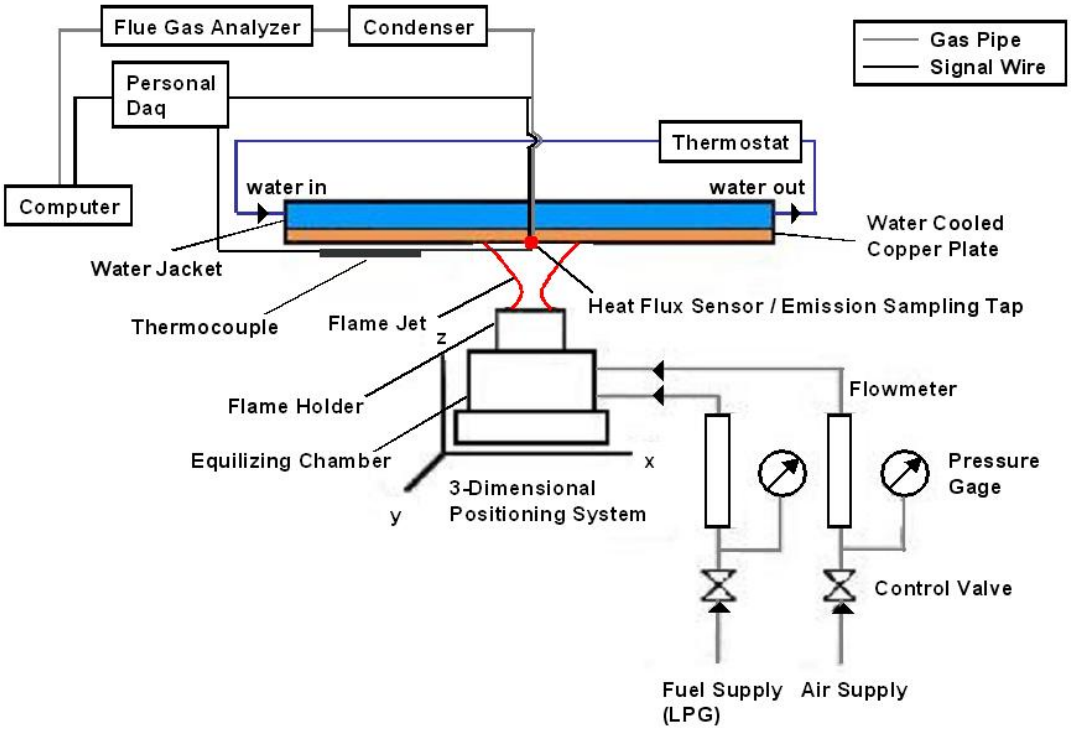

Figure 3.1.3. IDF impinging jet experimental set-up

A flue-gas analyzer (Anapol EU-5000) was used to measure the combustion species concentrations, O_2, CO_2, CO, NO and HC and the data measured were in dry condition.

In the set-up, a heat flux sensor was located at the center of the plate (ie., x=0, y=0, z=0) to measure the heat flux. A type B thermocouple (Pt-30%/Rh as the positive lead and Pt-6%/Rh as the negative lead) was placed 50mm horizontally away from the center of the plate, which was used to measure the flame temperature. A nut was fabricated to replace the heat flux sensor, so that, the sample combustion gas could be collected from the 1.5 mm hole at the center of the nut as shown in *Figure 3.1.4*.

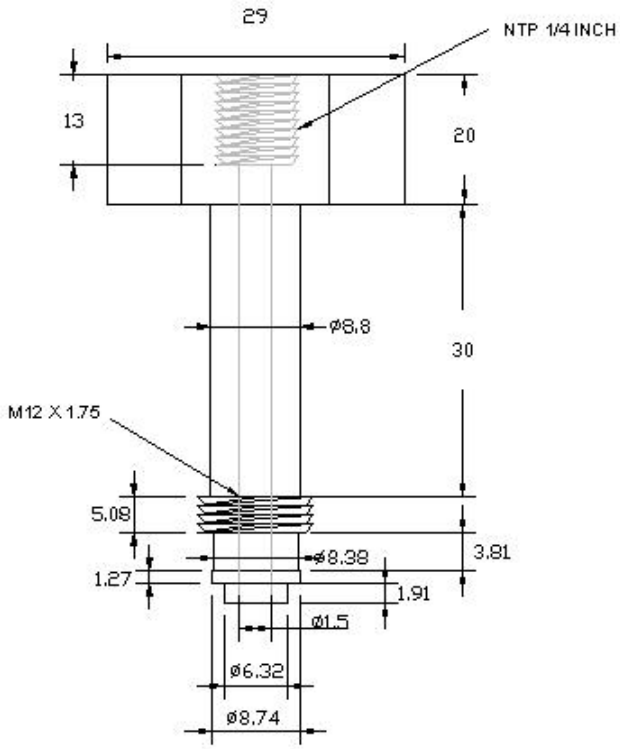

Figure 3.1.4. The nut fabricated to collect the sample combustion products.

3.1.1 Burners

Two burners have been used in the study, a circumferentially arranged IDF burner and a circular premixed burner. The IDF burner was the main burner used and investigated in the experiments.

The IDF burner, made of copper, is shown in *Figure 3.1.5*. There were twelve outer fuel jets, of 2.4 mm diameter each, surrounding a central air jet of 6mm diameter. The center-to-center distance between the air jet and the fuel jets was 8mm. The circular premixed burner, also made of copper, was used in the impinging experiments for comparison, which had a nozzle of 9.3 mm inner diameter. LPG and compressed air were metered by rotameters (Matheson

m603 and m605) and passed through the corresponding jets. The burner was fixed on a positioning system so that the burner could be moved in X, Y and Z directions. The positioning system had the accuracy of ±1mm.

Figure 3.1.5 Photo of the inverse diffusion flame burner

3.1.2 Target Plate

The target plate was a water-cooled copper plate with a surface area of 500×500 mm^2 and 8 mm thick. It was evenly cooled on the backside by a cooling water jacket. The temperature of cooling water was maintained automatically at 38°C by a thermostat, which could avoid water condensation on the copper plate and was used to cool the heat flux sensor and to absorb the heat released by the flame. Since copper has a high thermal conductivity, the impinging heat was effectively conducted away.

3.2 Measurement Techniques and Instruments

Experiments were carried out to analyze the structure of the inverse diffusion flame (IDF). The main parameters to be measured in the free jet experiments are the flame temperature and the combustion species. In the IDF impinging jet experiments, the flame temperature, heat flux and combustion species were measured.

3.2.1 Thermocouples

Thermocouples are the most common and simple instrument to measure flame temperature. A thermocouple consists of two dissimilar metallic elements connected to form a closed loop. The temperature difference between the two junctions is obtained by measuring the voltage generated with a high impedance voltmeter [52].

The voltage / temperature relationship for each junction is well known. The thermocouple wires are usually very small and fragile and the junction could suffer from corrosion. So the thermocouple is usually protected by a metal sheath being insulated by aluminum oxide powder inside. However, in our experiments, this was not done since a high frequency response was required. The sheathing will decrease the time response considerably.

In principle, any two different conductors might be used to make a thermocouple. In practice, however, only a few combinations of conductor materials are used. There are eight thermocouples that have been standardized by the American National Standards Institute (ANSI), given letter designations J, T, K, E, N, S, R and B as shown in *Table 1* [53].

Type	Principle Wire Constituents	Temperature Range °C	Standard Tolerance (Reference Junction at 0°C) °C or percentage of °C
J	Iron vs. nickel-copper alloy	0 to 300	±2.2 or ±0.75%
T	Copper vs. nickel-copper alloy	0 to 700	±1 ±0.75%
K	Nickel-chromium alloy vs. nickel-manganese-silicon-aluminum alloy	0 to 1250	±2.2 or ±0.75%
E	Nickel-chromium alloy vs. nickel-copper alloy	0 to 900	±1.7 or ±0.6%
N	Nickel-chromium-silicon alloy vs. nickel-silicon-magnesium alloy	0 to 1250	±2.2 or ±0.75%
S	Platinum-rhodium alloy vs. platinum	0 to 1450	±1.5 or ±0.25%
R	Platinum-rhodium alloy vs. platinum	0 to 1450	±1.5 or ±0.25%
B	Platinum-rhodium alloy vs. platinum-rhodium alloy	670 to 1700	±0.5%

Table 1. Materials and Tolerances for New Thermocouples

An un-coated type B thermocouple with Pt-30%/Rh as the positive lead and Pt-6%/Rh as the negative lead was used in the experiment. As the flame temperature is very high, type B thermocouple is the most suitable one. It has the temperature range of 150°C-1800°C. It is well calibrated by the manufacture (OMEGA) and a voltage to temperature conversion chart is provided. It has the achievable accuracies of 0.2°C to 3°C for the readouts.

3.2.2 Heat Flux Transducer (Vatell HFM-6)

The heat flux transducer used in the experiment is the Heat Flux Microsensor (HFM), which measures the local heat transfer from the flame to the impingement plate. It has a very fast response time of 6±2μs and the minimum sensitivity is 8 μVcm²/W. It was mounted with the impingement plate by using the capture nut shown in *Figure 3.2.1*. The mounting hole was fabricated to the appropriate specifications provided by the manufacturer with ±0.01mm dimensional tolerance to ensure the sensor and the plate surface were in the same alignment. The standard coating for the face of the sensor is zynolyte, which is a high temperature black coating with a 0.94 emissivity. It was recommended that applications involving radiative heat transfer use a coated transducer because the absorption properties are better. The sensor came with a NIST traceable calibration certificate by the manufacturer that provided all of the information necessary to convert the signals from the sensor to their heat flux values and the accuracy was ±3%. The heat flux signals of the transducer were amplified by a low noise, wide-band differential signal conditioning amplifier (Vatell AMP-6) whose gain was set to be 500 with the accuracy of ±1.5%.

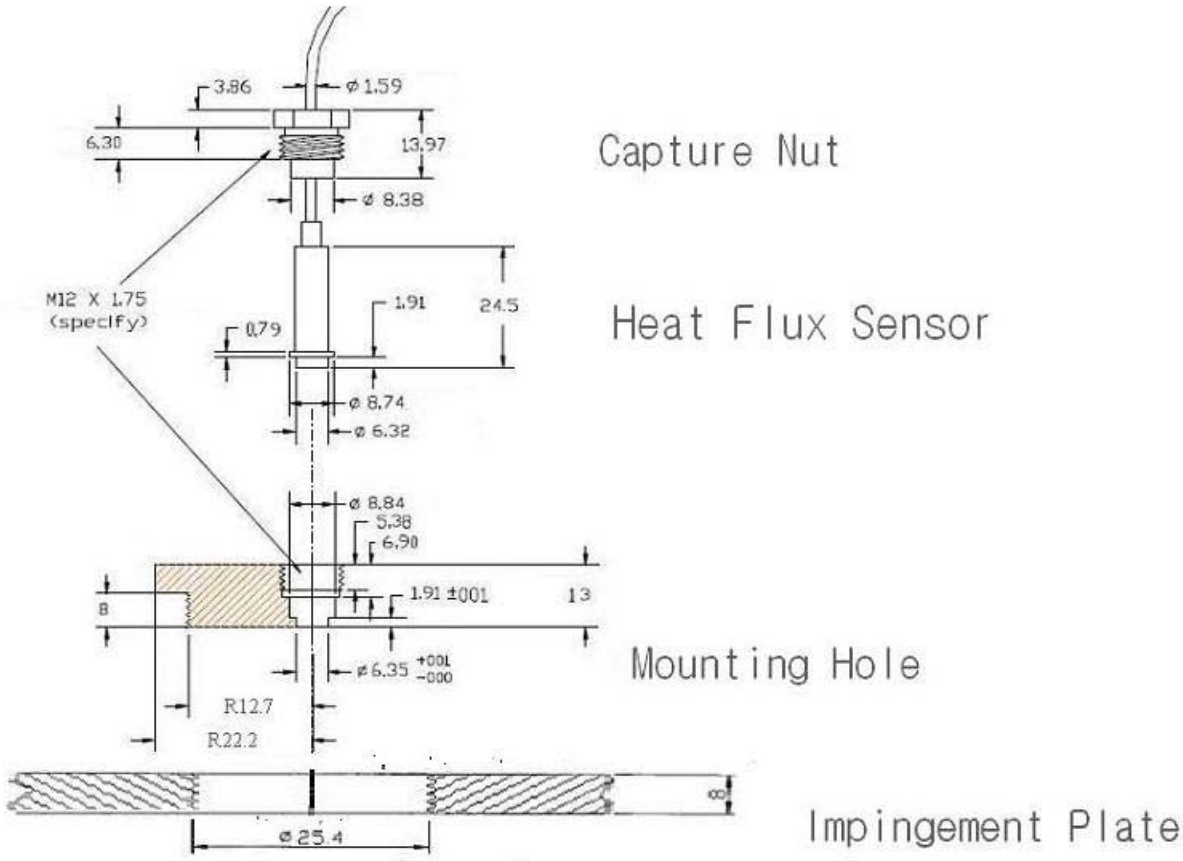

Figure 3.2.1. Installation of heat flux sensor.

3.2.3 Flue-gas Analyzer (Anapol EU-5000)

It was used for measuring the combustion species, including O_2, CO_2, CO, NO and HC. The analyzer used non-dispersive Infrared (NDIR) sensor for measuring the CO_2 and HC concentrations and used electro-chemical sensors for measuring O_2, CO and NO concentrations. The O_2 and CO_2 concentrations were measured in percentage (%) and the CO, NO and HC concentrations in ppm.

The analyzer is calibrated using the corresponding standard zero and span gas each time before the experiments. The ranges and errors for each

species concentration measured using this fuel gas analyzer are shown in *Table 2*.

Species	Range	Error (absolute or relative)
O_2	0.00 to 21.00%	±0.4%
CO_2	0.00 to 20.00%	±0.5% relative
CO	0.00 to 15.00%	±0.5%
NO	0 to 5000ppm	±25ppm
HC	0 to 60000ppm	±5%

Table 2. Ranges and errors for the species concentration measured using the Anapol EU-5000.

3.2.4 Data Acquisition

A Personal Data Acquisition system (Iotch Model/56) was used to record the heat fluxes and flame temperatures simultaneously.

3.3 Experimental Procedures

Experiments were designed to identify the characteristics of an IDF free jet and an IDF impinging jet by carrying out 4 tests. The influences of Reynolds number, equivalence ratio and nozzle to plate distance on the thermal and emission characteristics of the impinging flame were also identified. The fifth test was carried out on investigating a premixed flame for comparison as an impinging jet. *Table 3* shows the ranges of the operating parameters for the tests conducting with the IDF and the premixed flame.

Four values of Re_{air} were chosen: 1500, 2000, 2500 and 3000. At these Reynolds numbers, a premixed flame is able to operate within its flammable range. Flame at the lowest Re_{air} (<1500) was not investigated because the IDF became unstable and combustion was incomplete due to poor entrainment force provided by the air jet. The overall equivalence ratios were chosen from 0.8 to 1.8, so that the flames operated from fuel lean to fuel rich conditions were investigated.

The following sections give detailed descriptions on the experimental procedures.

3.3.1 Free Jet Experiments

For each axial and radial profile in free jet experiments, the distances were varied in the range of 0 mm to 160 mm and 0 mm to 12 mm, respectively.

Tests (1)

Tests (1) were performed by measuring the axial and radial temperature profiles at air Reynolds number, Re_{air}, 1500, 2000, 2500 and 3000, overall equivalence ratio, Φ, equals to 1 using the test rig shown in *Figure 3.1.1*.

Before igniting the flame, it is important to make alignment of these two thermocouples with the centerline of the burner and set the origin (ie., x=0, y=0, z=0) of the flame at the center of the burner. The flame was then ignited. The desired operating conditions were obtained by adjusting the rotatmeters to

control the LPG and compressed air flow rates with the calibrated rotatmeters. The burner was moved along the X and Z direction using the positioning system.

Φ	$\dot{Q}_{air}$ (x10^{-4} m^3/s)	$\dot{Q}_f$ (x10^{-6} m^3/s)	Inverse Diffusion Flame			Premixed Flame	
			Re_{air}	u_{air} (m/s)	u_f (m/s)	Re_P	Condition Selected
0.8	1.08	2.78	1500	3.81	0.05	1076	B
1	1.08	3.47	1500	3.81	0.06	1090	√
1.2	1.08	4.17	1500	3.81	0.08	1104	√
1.4	1.08	4.86	1500	3.81	0.09	1118	√
1.6	1.08	5.56	1500	3.81	0.10	1132	√
1.8	1.08	6.25	1500	3.81	0.12	-	-
2.0	1.08	6.95	1500	3.81	0.13	-	-
2.2	1.08	7.64	1500	3.81	0.14	-	-
2.4	1.08	8.34	1500	3.81	0.15	-	-
0.8	1.44	3.71	2000	5.08	0.07	1435	B
1	1.44	4.63	2000	5.08	0.09	1453	√
1.2	1.44	5.56	2000	5.08	0.10	1472	√
1.4	1.44	6.48	2000	5.08	0.12	1490	√
1.6	1.44	7.41	2000	5.08	0.14	1509	√
1.8	1.44	8.34	2000	5.08	0.15	-	-
2.0	1.44	9.26	2000	5.08	0.17	-	-
2.2	1.44	10.19	2000	5.08	0.19	-	-
2.4	1.44	11.12	2000	5.08	0.20	-	-
0.8	1.79	4.63	2500	6.35	0.09	1794	B
1	1.79	5.79	2500	6.35	0.11	1817	L
1.2	1.79	6.95	2500	6.35	0.13	1840	√
1.4	1.79	8.11	2500	6.35	0.15	1863	√
1.6	1.79	9.26	2500	6.35	0.17	1886	√
1.8	1.79	10.42	2500	6.35	0.19	-	-
2.0	1.79	11.58	2500	6.35	0.21	-	-
2.2	1.79	12.74	2500	6.35	0.23	-	-
2.4	1.79	13.90	2500	6.35	0.26	-	-
0.8	2.15	5.56	3000	7.61	0.10	2152	B
1	2.15	6.95	3000	7.61	0.13	2180	L
1.2	2.15	8.34	3000	7.61	0.15	2208	L
1.4	2.15	9.73	3000	7.61	0.18	2236	√
1.6	2.15	11.12	3000	7.61	0.20	2263	√
1.8	2.15	12.51	3000	7.61	0.23	-	-
2.0	2.15	13.90	3000	7.61	0.26	-	-
2.2	2.15	15.29	3000	7.61	0.28	-	-
2.4	2.15	16.68	3000	7.61	0.31	-	-

'B' – Blow off; 'L' – Flame Lift; '√' - has investigated; '-' – not investigate

Table 3. Operating conditions for the tests conducted with IDF and premixed flame.

Tests (2)

Tests (2) were performed in measuring the exhaust gas of the combustion species at Re_{air}=1500, 2000, 2500 and 3000, Φ=1, using the test rigs shown in *Figure 3.1.2*.

An inverted collector was used to measure the exhaust emission of the flame. The inverted collector was set at a height of 10 mm above the flame tip. The sampled combustion gas collected by the inverted collecter, followed a long flexible tube, in which the gas was cooled by the compressed air. Then it was filtered and introduced into the gas analyzers. The volumetric concentrations of O_2, CO_2, CO and NO were analyzed and recorded simultaneously.

3.3.2 Impinging Jet Experiments

For each axial and radial profile in impinging jet experiment, the distances were varied in the range of 12 mm to 96 mm and 0 mm to 50 mm, respectively.

Tests (3)

Tests (3) were performed measuring the flame temperature and heat fluxes for the range of the operating conditions listed in *Table 3* using the test rig shown in *Figure 3.1.3*. Both stagnation and radial data were recorded. Stagnation heat flux distributions were recorded for all the combination conditions listed in the *Table 3*, but, radial profiles were taken from Φ=0.8-1.8 at 7 nozzle-to-plate distances, H/d_{IDF}=4-10, for analyzing the IDF at Re_{air}=2000

and at 4 nozzle-to-plate distances, H/d_{IDF}=5-8, were analyzed at Re_{air}=1500, 2500 and 3000.

In impinging flame system, the water flow was introduced into the cooling water jacket until it was fully filled to insure that no air was trapped inside. As condensation is a process when the temperature of impingement surface is lower than the dew point of the combustion gases, the vapor in the combustion gases will condense and release energy; condensation should be avoided in the experiment. To achieve this goal, the cooling water was kept at 38°C by the thermostat when it reached a steady state. Such a water-cooling system could cool the heat flux sensor and absorb the heat released by the flame.

The burner was aligned vertically with the heat flux sensor and the thermocouple using the positioning system. The burner was located facing perpendicular to the plate within ±1°. The flame temperature and heat flux were measured at the same time. A computer software, personal data acquisition, was used to record data from the two equipments. The analyzing axial distance was from 20 mm to 130 mm and the radial distance was from 0 mm to 50 mm.

Tests (4)

By replacing the heat flux sensor with the fabricated nut, *tests (4)* were performed to measure the combustion species of the impinging flame jet with Φ=0.8, 1.0, 1.2 and 1.8 at Re_{air}=2000 and 3000 for the IDF. Radial profiles were recorded at 3 nozzle-to-plate distances, H/d_{IDF}=5,7 and 10.

Tests (5)

Tests (4) and *Tests (5)* were repeated using the 9.3 mm round nozzle diameter premixed burner. Stagnation point heat flux distributions were measured at all the combination condition listed in *Table 3.* For Re_P=1453 (Φ=1.0) and 1472 (Φ=1.2), radial heat flux distributions were measured at 7 nozzle-to-plate distances, H/d_P=1.5=4.5 and combustion species concentrations were recorded at 3 nozzle-to-plate distances, H/d_P=1.5, 2 and 4.

Remarks:

1) Lower Re (<1500) was not used because the flame became unstable and combustion was incomplete due to poor entrainment force provided by the air jet.
2) The flame was assumed to be symmetrical about the centerline of the air jet, thus only a half-plane of the flame was measured in the experiments.
3) The time for reaching a steady state for every datum in the same Reynolds number and equivalence ratio was at least 10 seconds. And when there was a change in the Reynolds number or the equivalence ratio, at least five minutes was spent to reach a steady state.
4) At least 480 data were collected in each point of the measurements point and a mean of them represented the value of the parameter in the corresponding position. This could help to reduce the experimental error and obtain more accurate data.

5) It was difficult to adjust the parameters in comparing the two different types of flame, the IDF and the premixed flame. If same velocity were used for the two flames, the fuelling rate would be difference. Therefore, in the study, the fuelling rate and overall equivalence ratio for the two flames were controlled in the same values during comparison.

3.4 Handling of Experimental Data

3.4.1 Determination of Air and Fuel Flow Conditions

In premixed flames, the air and fuel flow rates are determined by the exit Reynolds number and equivalent ratio of the air/fuel mixture before combustion. However, it is very difficult to determine the Reynolds number of the non-premixed flames. In the experiments, the Reynolds number of the IDF was determined by the exit Reynolds number of air, since the air flow rates is more than ten times of the fuel flow rates. The Reynolds numbers, Re_{air} and Re_P, shown in the *Table 3* are defined using the equations of *E3.4.1* and *E3.4.2*, respectively.

$$\mathrm{Re}_{air} = \left(\frac{\rho u (d_{IDF})}{\mu} \right)_{air} \qquad \cdots \textit{For the IDF (E3.4.1)}$$

$$\mathrm{Re}_{P} = \left(\frac{\rho u (d_{P})}{\mu} \right)_{mix} \qquad \cdots \textit{For the premixed flame (E3.4.2)}$$

In the above two equations, d_{IDF} is the effective diameter of the IDF defined as the diameter of the air jet, 6mm, and d_P is that of the premixed flame, which is referred to the nozzle exit diameter, 9.3 mm. In *E3.4.1*, the ρ, u and μ are the density, exit velocity and dynamic viscosity, respectively, of the air at room temperature; and in *E3.4.2*, they are represented to the air/fuel mixture properties before combustion. These mixture properties are calculated using the same method according to Kwok [54].

The equivalence ratio indicated for the IDF, was the overall equivalence ratio of air and fuel before mixing and combustion. The same equation is used to determine the equivalence ratio of the IDF and premixed flame. It was defined as a comparison of the stoichiometric air/fuel ratio to the actual air/fuel ratio (as shown in *E3.4.3*):

$$\Phi = \frac{(A/F)_{stoic}}{(A/F)} \qquad \cdots \textit{For both IDF and premixed flame (E3.4.3)}$$

3.4.2 Calculations of Temperature Correction

The flame temperatures shown in the report were corrected for the radiation effects according to Sato et al. [55]. The calculations are presented as following.

Thermocouple relied on heat transfer from the combustion gases to the thermocouple bead, which is mainly by convection. The assumption is that the bead temperature is the same as the gas temperature. However, an error is

introduced to the system due to radiation from the bead to its surroundings. A heat balance is set up such that:

Convection to the bead = Radiation from the bead

$$h_c(T_g - T) = \varepsilon\sigma(T^4 - T_W^4) \qquad \cdots \textit{(E3.4.4)}$$

Thus,

$$T_g = T + \frac{\varepsilon\sigma}{h_c}(T^4 - T_W^4) \qquad \cdots \textit{(E3.4.5)}$$

E3.4.5 is the correctional term for radiation loss and where T_g is the true gas temperature, T is the measured temperature, T_W is the plate temperature, σ is the Stefan-Boltzmann constant, ε is the thermocouple emissivity and h_c is the convective heat transfer coefficient.

Conduction down the legs of the bead can also play a part but is minimized by inserting a long length of the thermocouple into the gas. And the convective heat transfer coefficient, h_c, is dependent on the local flow conditions and is expressed in terms of Nusselt number correlations [10].

$$Nu = 2 + 0.6\,\mathrm{Re}_{bead}{}^{1/2}\,\mathrm{Pr}^{1/3} \qquad \cdots \textit{(E3.4.6)}$$

Where,

$$Nu = \frac{(h_c)(d_T)}{k} \qquad \cdots \textit{(E3.4.7)}$$

$$\mathrm{Re}_{bead} = \frac{\rho u d_T}{\mu} \qquad \cdots \textit{(E3.4.8)}$$

d_T in the above equations is the diameter of the bulk of the thermocouple. k in *E3.4.7* is the thermal conductivity, while Re_{bead} in *E3.4.8* is the Reynolds number of the gas at the thermocouple and u is assumed to be the average velocity of the exit air jet.

For the total emissivity of the thermocouple bead, the following equation is used as stated by Wu [10],

$$\varepsilon = 9.6 \times 10^{-5} t + 0.056 \qquad \cdots \textit{(E3.4.9)}$$

where t is the measured temperature in degree Celsius.

The fluid properties, Pr, k, r, m and e in *E3.4.6 – E3.4.9* are functions of the temperature as measured correspondingly and they are determined using the method suggested by Borman and Ragland [56].

3.4.3 Heat Flux Data Handling

The heat fluxes presented in the report were the total heat fluxes measured by the heat flux transducer including convection and radiation. In the experiments, stagnation heat flux and radial heat flux distributions were measured and mean values will be shown in this report.

Besides, the area-averaged heat flux and the heat transfer efficiency were obtained by considering the heat flux of a circular area within a radial distance of 50 mm from the stagnation point of the flame.

Area-averaged heat flux

Radial heat fluxes were measured at different non-dimensional nozzle to plate distances. Based on the distribution of the local radial heat fluxes, the area-averaged heat flux ($\bar{\dot{q}}$) can be calculated using the equation, *E3.4.10*.

$$\bar{\dot{q}} = \frac{\iint^{A} \dot{q}\, dA}{A} = \frac{2\pi \int_0^R \dot{q}\, r\, dr}{\pi R^2} \qquad \cdots(E3.4.10)$$

where $\dot{q}$ is the local heat flux and A is the integration area.

The area-averaged heat flux is obtained by integrating the local radial heat flux distributions within a circular zone of 50 mm radius at the central region of the impingement plate. The local heat flux is usually higher in the stagnation region and drops rapidly in the wall jet region. Thus, the average heat transfer decreases if the integration area is increased significantly into the wall jet region. Mahmood [57] has reached the same conclusion that the average heat transfer was greatly dependent on the integration area used.

Heat transfer efficiency

Heat transfer efficiency is defined for evaluation of the efficiency of the burner in transferring energy from the fuel to the impingement plate.

$$\eta(\%) = \frac{Output}{Input} \times 100\% = \frac{\bar{\dot{q}} \times A}{\dot{Q}_f \rho_f LHV} \times 100\% \qquad \cdots(E3.4.11)$$

where Q_f, ρ_f and LHV are the fuel flow rate, density and low heating value, respectively, of the butane gas.

E3.4.11 shows that the heat transfer efficiency is calculated as the percentage of energy from the fuel absorbed by the plate. However, the efficiency is dependent on the total heat flux integrated from the radial distribution, that is, it increases with increasing integration area. Thus, a common area based on a radius of 50 mm is chosen for both area-averaged heat flux and heat transfer efficiency calculation for all operating conditions. The radial distance of 50 mm is chosen because in most cases, the radial heat flux would have decayed by more than 90% over this radial distance. Tuttle et al. [58] defined a heating value fraction and investigated the variation of heating value with the radius of integration for different operating conditions. The concept is similar to that shown in *E3.4.11* except that it is integrated to various radial positions. Their results also show an increase of the heating value fraction with increasing radius of integration.

3.4.4 Combustion Species Data handling

The exhaust emission was corrected to 3 percent of O_2 in the report. Concentrations, corrected to a particular level of O_2 in the product stream, are frequently reported in the literature and used in practice. The purpose of correcting to a specific O_2 level is to remove the effect of various degrees of dilution so that true comparisons of emission levels can be made.

3.5 Reliability of Experimental Results

Fluctuations appear during experiments. To ensure the experimental reliability, one minute was spent to measure the flame temperature and heat flux at each point of the free jet or impinging jet. 8 data were recorded in every seconds, as a result, 480 data for each parameter were collected at each point. Spiegel and Murray [59] stated that if sufficient data points had been collected (usually ≥ 30), the sampling distribution was very nearly a normal distribution. The mean and temperature fluctuations were calculated based on the sample of 480 data point collected at each in-flame location in order to obtain more reliable results. For the species concentration, the values were recorded once the analyzer showed the stable value because it is not very sensible.

An uncertainty analysis was carried out with the method proposed by Kline and McClintock [60]. There are three main types of errors, which are systematic, variable and random errors. The only type of errors that were subject to uncertainty analysis is random errors. Both systematic and variable errors are the domain of the experimenter. One could say that, to an

experimentalist, being able to think about random errors (Ra) is a luxury problem as this implies that all systematic and variable errors have been eliminated.

It is stated that the variable of interest Ra which is a function of N random variable m_i (i= 1,2……N), as following:

$$Ra = f(m_1, m_2, \cdots, m_N)$$

It should be assumed that there is a true value for the measured quantity R. The probability that the true value lies in the interval $Ra - \delta Ra \cdots Ra + \delta Ra$ is p. It is common practice to use probabilities 0.68 or 0.95 which correspond, respectively, to one or two standard deviations of the normal distribution of Ra. To obtain values for the standard deviations, the following equations are used:

$$s_{mt} = \sqrt{\frac{1}{n-1}\sum_{j=1}^{n}(m_i(j) - \bar{m}_i)^2}$$

where $\bar{m}_i$ is the average

$$\bar{m}_i = \frac{1}{n}\sum_{j=1}^{n} m_i(j)$$

For a single measurement of Ra, the uncertainty could be determined by the standard deviation. As a result, using a 95% confidence level, the maximum and minimum uncertainties in free jet flame temperature measurement were 17.3% and 0.23%, respectively, and that in impinging jet flame temperature measurement were 10.4% and 0.97%. The maximum and minimum uncertainties in local heat flux were 14% and 0.2%, respectively.

Chapter 4 Inverse Diffusion Flame – Free Jet

4.1 Flame Observations

The structure and physical appearance of an IDF is significantly different from that of a NDF or a premixed flame as found in the literature. This section gives a detailed analysis on the structure and physical appearance of the IDF as a free jet under Re_{air} of 1500, 2000, 2500 and 3000 at Φ=1. The flames became more distinguishable in dim light so that all observations were performed in a darkened environment.

4.1.1 Flame Structure

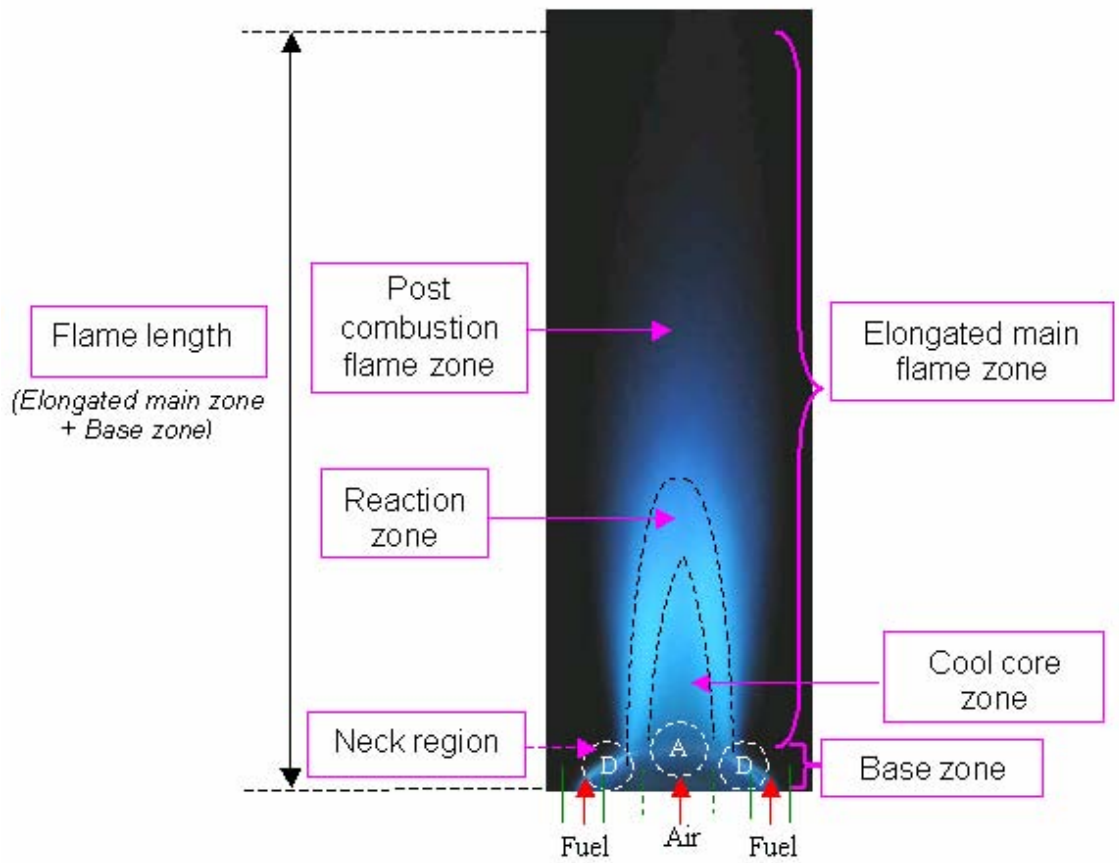

Figure 4.1.1. Schematic of an IDF free jet

Figure 4.1.1 shows the common features observed from the IDF burning LPG within the range of the investigated air and fuel flow rates in this study. The following are some elaborations of *Figure 4.1.1*:

1) The fuel jets are entrained and bent towards the air jet, creating a constricted neck separating the flame into two parts, the base zone and the elongated main flame zone. The sum of the lengths of these two zones is defined as the flame length.
2) The region below the constricted neck is considered as a short base zone. Initial air fuel mixing and combustion occur in the lower regions, A and D. The fuel concentration in A is low, so the gas mixture would be fuel lean. At D, the fuel mixes with air both from the supplied air jet and from entrained air.
3) The upper part is called an elongated main flame zone, which is composed of three characteristic zones:
    I. The cool core zone is enclosed by the shorter dotted line, as shown in the *Figure*. This zone is formed due to the very high velocity of the air jet compared to that of the fuel jets, thus air and fuel are intensely mixing and behave similar to the base zone. In this region, the gas mixture is in fuel lean condition.
    II. The reaction zone is enclosed between the two dotted lines shown in the *Figure*. It is the region where intense premixed combustion occurs after the air and fuel are premixed through the base and cool core zones.

III. The downstream region above the reaction zone is called a post combustion flame zone where the unburned fuel and combustion products produced from the reaction zone diffuse and further react with the ambient air.

From the above elaborations, for a free jet IDF, there is an intense bluish premixed combustion zone (reaction zone) overlapping an inner translucent cool core zone and overlapped by an outer post combustion flame zone at the same time. In addition, the high velocity central air jet creates a low pressure region close to the burner plane. Therefore, the surrounding fuel is entrained towards the edge of the central air jet and the neck region is then formed.

4.1.2 Flame Shape

The flame shapes in Figure 4.1.1, for example, show the physical appearance of the flame, which were recorded using a digital camera. The photos are captured at the shutter speed of 1/50 second and 1/1000 second, respectively. Using the time of exposure of 1/50 second, the images taken could represent the flame shapes directly observed by human eyes, while the time of exposure of 1/1000 second could record the instant appearance of the flame.

(a) Low-speed Shutter with Time Exposure 1/50 Second

Figure 4.1.2 to *Figure 4.1.5* show the flame shape of the free jet IDFs recorded at the low-speed shutter at Re_{air} of 1500, 2000, 2500 and 3000, respectively, with Φ=0.8-2.4. In each case, the air velocity is kept constant while the fuel velocity is increased.

<u>Effects of overall equivalence ratio</u>

By observing the *Figures*, the IDFs being investigated are mainly blue in colour up to Φ=1.4 and Φ=1.6, respectively, for Re_{air}=1500-2000 and Re_{air}=2500-3000, while more brilliant orange flames are observed at higher overall equivalence ratios. It indicates that there is an increase in diffusion combustion at the elongated main flame zone as Φ is further increased at a constant Re_{air} value.

The central air jet causes increased formation of CH and OH within the flame, for which both species yield blue radiation, as evident from the direct flame photos at low level of Φ. As Φ increases, in the post combustion flame zone, the excess unburned fuel undergoing pyrolysis forms the brilliant orange flames, where light hydrocarbon species and eventually carbon conglomerates (soot) are formed. Thus contributes to the characteristic radiation behavior of normal diffusion flames. In *Figure 4.1.2* and *Figure 4.1.3*, brilliant orange flames are also observed at the neck region, which become more obvious as Φ increases. This is due to the weak air-fuel interaction in the base zone at lower air jet Reynolds number. A small portion of fuel is not well mixed with central air, but burns in diffusive mode.

Figure 4.1.2. Direct photos, effects of varying fuel velocity on free jet IDFs at Re_{air}=1500.

Figure 4.1.3. Direct photos, effects of varying fuel velocity on free jet IDFs at Re_{air}=2000.

Figure 4.1.4. Direct photos, effects of varying fuel velocity on free jet IDFs at Re_{air}=2500.

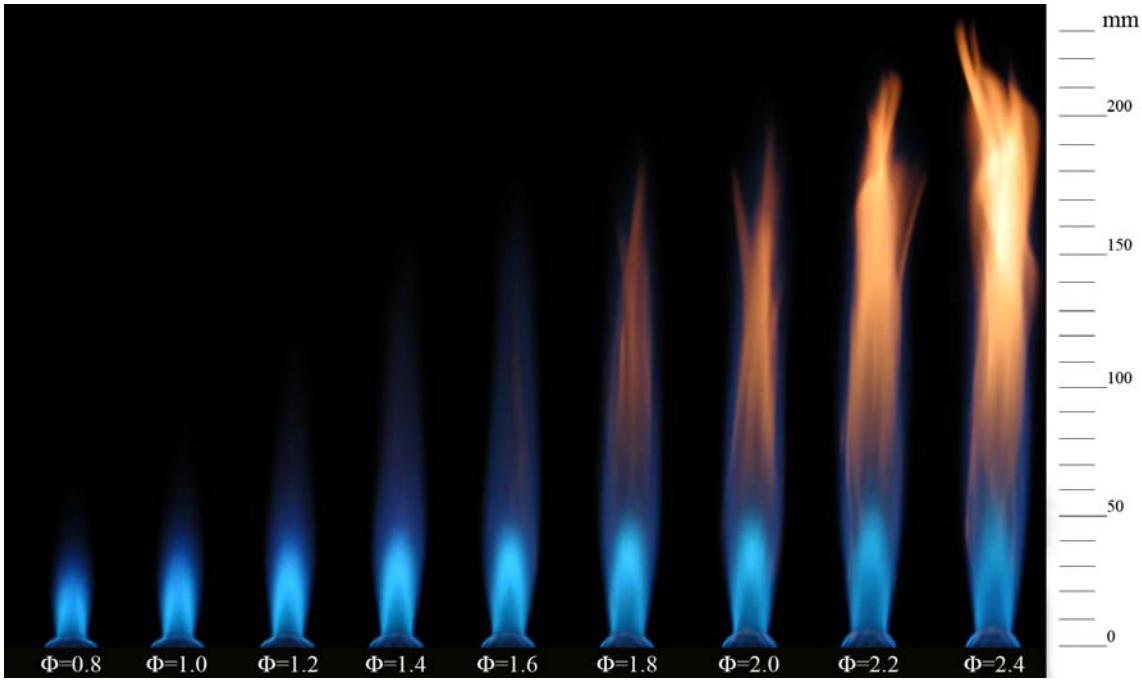

Figure 4.1.5. . Direct photos, effects of varying fuel velocity on free jet IDFs at Re_{air}=3000.

An increase in Φ indicates that more fuel is supplied into the system at a constant air flow rate. Consequently there is an increase in flame length. From *Figure 4.1.2* to *Figure 4.1.5*, at each Re_{air}, when Φ increases, the heights of the base, cool core and the reaction zones increase slightly, while the post combustion flame zone appears to elongate. Also, the constriction effect of the neck region diminishes with increasing Φ. At low level of Φ such as 0.8 and 1.0, the tips of the cool core and the reaction zones are opened due to the high velocity central air jet. The reaction becomes conical and defined as Φ increases.

Effect of the air-Reynolds number

At a constant Φ, increasing Re_{air} indicates increasing both air and fuel flow rates with the same air to fuel ratio. The flame shapes are similar at the four Re_{air} except that due to the stronger air jet flow, there is stronger mixing between the air and the fuel at higher Re_{air}, resulting in more intense combustion, as indicated by less luminous orange flames observed in the diffuse zone and the neck region at higher Re_{air} and constant Φ.

With a decrease in Re_{air}, shorter flame and stronger premixed combustion nature will be found. Again, at low level of Φ such as 0.8 and 1.0, the tips of the cool core and the reaction zones are opened due to the high velocity central air jet. The reaction becomes conical and defined as Φ increases.

(b) High-speed Shutter with Time Exposure 1/1000 Second

The flame shapes shown in *Figure 4.1.6* are recorded at high-speed shutter, except the most right hand side one, which is recorded at low-speed shutter, but all of them are at the same operating condition of Re_{air}=2000 and Φ=1.8.

From the flame shapes recorded at high-speed shutter in *Figure 4.1.6*, the zones defined clearly in the photos recorded at low-speed shutter become blurred. The flow inside the flames is very complex. Different scales of vortexes are found in the elongated main flame zone, leading to the oscillations of the flame. However, the appearance of the base zone recorded by the two speed shutters is similar. This phenomenon is similar to the findings from Sinha et al. [13], they stated that the flow in the base zone was laminar, while the flow in the elongated main flame zone was turbulent. This might due to the intense mixing occurring at the neck region. The fuel and the central air jet in the inner flame zone and the fuel and the ambient air at the flame rim mixed intensely leading to instabilities in the downstream and the vortexes increase in scale as they were convected downstream by the flame flow.

The same flames in *Figure 4.1.3* are shown in *Figure 4.1.7* using the high-speed shutter. Within the range of the Φ being investigated, the flow in the base zone is laminar, while the flow in the elongated main flame zone is turbulent.

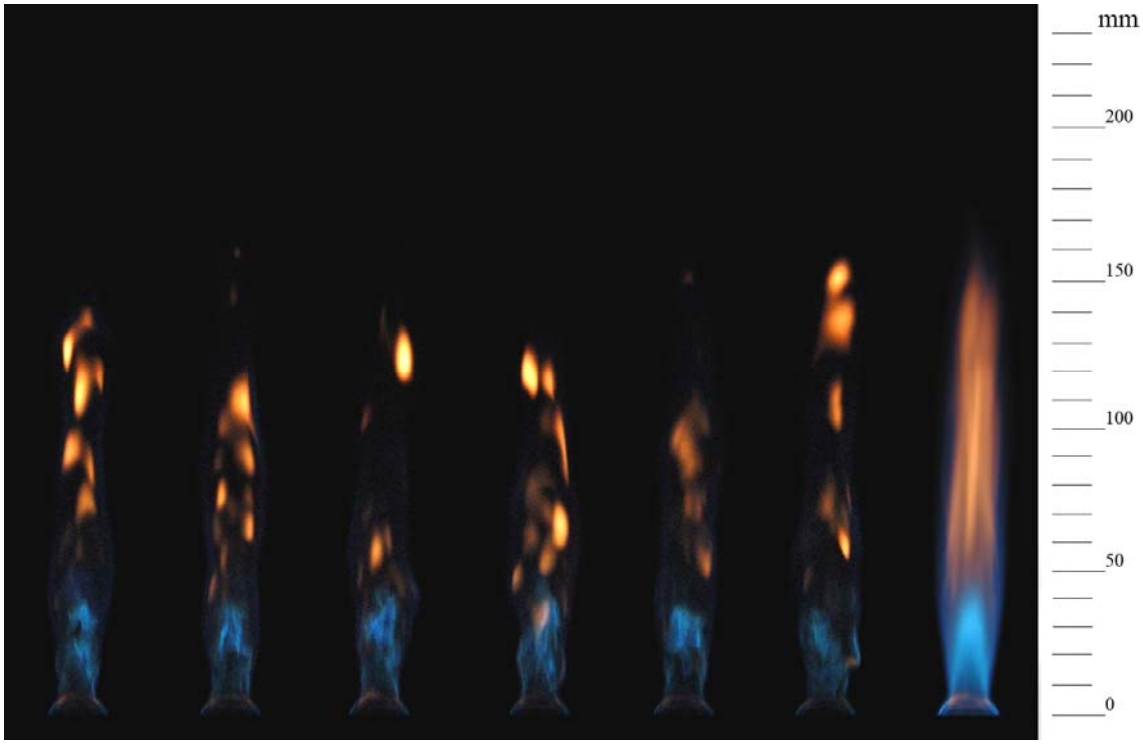

Figure 4.1.6. Direct photos recorded at high-speed shutter on free jet IDFs at Re_{air}=2000 and Φ=1.8.

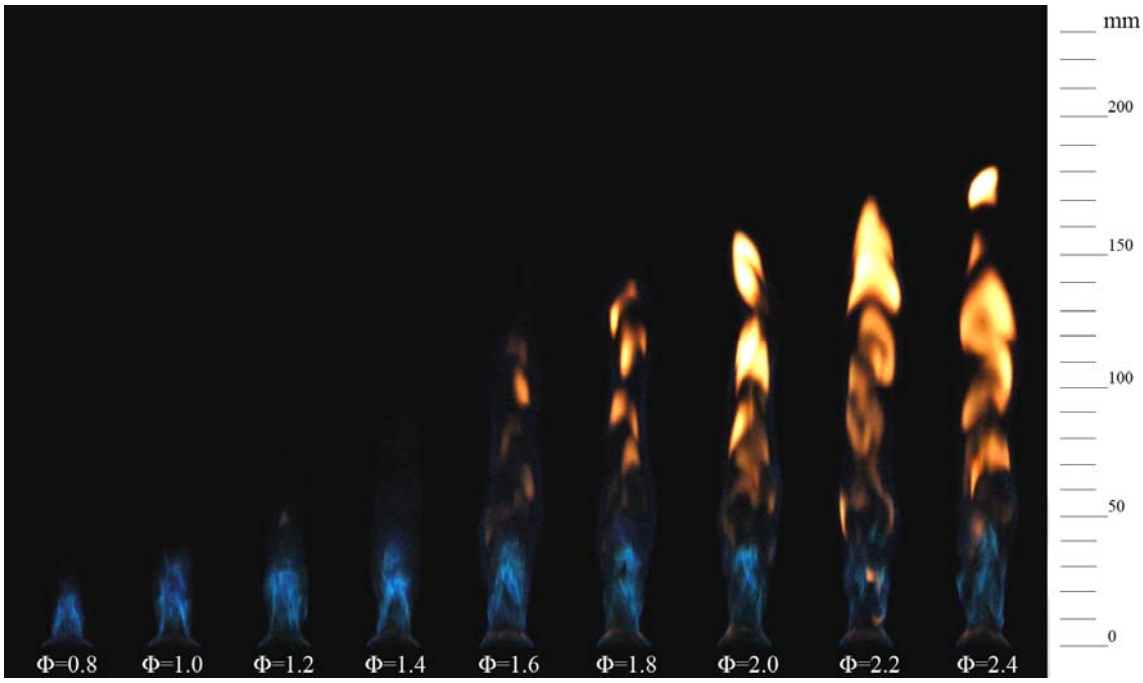

Figure 4.1.7. Direct photos recorded at high-speed shutter of the effects of varying fuel velocity on free jet IDFs at Re_{air}=2000.

4.2 Free Jet Experiments

In the free jet experiments, the axial temperature profiles and the distribution of the flame temperature of an IDF were measured; and the exhaust combustion species concentrations were also measured. The flames of different Re_{air} with Φ=1 were analyzed. The results are presented in the following sections.

4.2.1 Flame Temperatures

Radial and axial temperature profiles were measured with the test rig shown in *Figure 3.1.1*. The temperatures shown in this section are in degree Celsius and have been corrected for the radiation.

(a) Axial Profiles

Axial temperature profiles were measured at the centerline from the axial heights of z=0 mm to z=160 mm at Re_{air}=1500, 2000, 2500 and 3000 and Φ=1.

Figure 4.2.1 shows the effect of the air jet Reynolds number on the axial temperature profile and the corresponding experimental uncertainties. With reference to the flame shapes shown in *Figure 4.1.2* to *Figure 4.1.5*, the four temperature profiles increase steeply from a low initial temperature found in the cool core, progressing to the premixed combustion zone and then entering into an extend region of constant temperature once reaching the heights of the corresponding reaction zones. The profiles begin to decrease at the downstream, where temperature is lost by diffusing to the surrounding. The

uncertainties are low in the in-flame field, while they become high in the post-flame region.

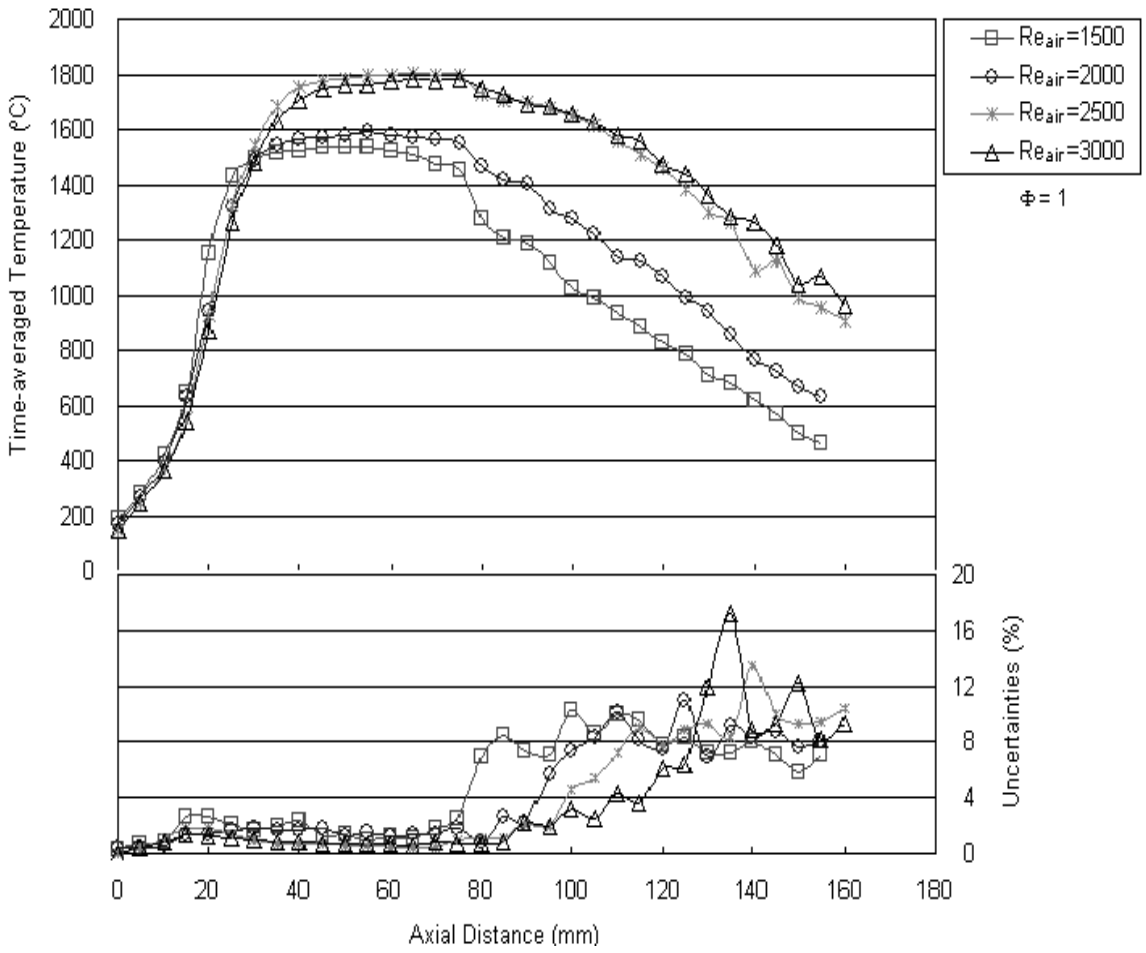

Figure 4.2.1. Comparison of axial temperature profile and uncertainties at the centerline versus Re_{air} with Φ=1, free jet.

As Re_{air} increases, lower initial temperature and higher temperature at the post flame region. The temperature profiles for Re_{air}=2500 and 3000 are very close to each other. It may due to better mixing and combusting for the flame at Re_{air}=2500 or there is more energy lost to the surrounding by radiation in the elongated main flame zone of the flame at Re_{air}=3000.

The maximum axial temperatures for Re_{air} = 1500, 2000, 2500 and 3000 were 1530°C, 1590°C, 1800°C and 1780°C, respectively, located at the heights of 45 mm, 55 mm, 65 mm and 75 mm.

(b) Radial Profiles

The radial temperature profiles analyzed in this section are chosen at the heights of 20 mm to 120 mm with 20 mm intervals; and radial distance of 0 mm to 12 mm, for Re_{air}=1500, 2000, 2500 and 3000 and Φ=1.

Figure 4.2.2 shows the radial profiles at the heights of 10 mm, and then from 20 mm to 120 mm with a vertical interval of 20 mm, for Re_{air}=2000. It is found that the radial profile at z=10 mm shows effect of the cool core near the centerline of the flame. The temperature then enters a steep increasing gradient region as the enveloped reaction zone is approached and it abruptly drops once past the flame rim. The temperature difference from the centerline to the maximum is about 900°C. When z increases, the temperatures near the centerline increase and the profiles become bell-shaped which indicates the end of the intense combustion at z=80 mm. Further increase of the radial distance, the temperature profile becomes flatter with lower peak temperature at the centerline.

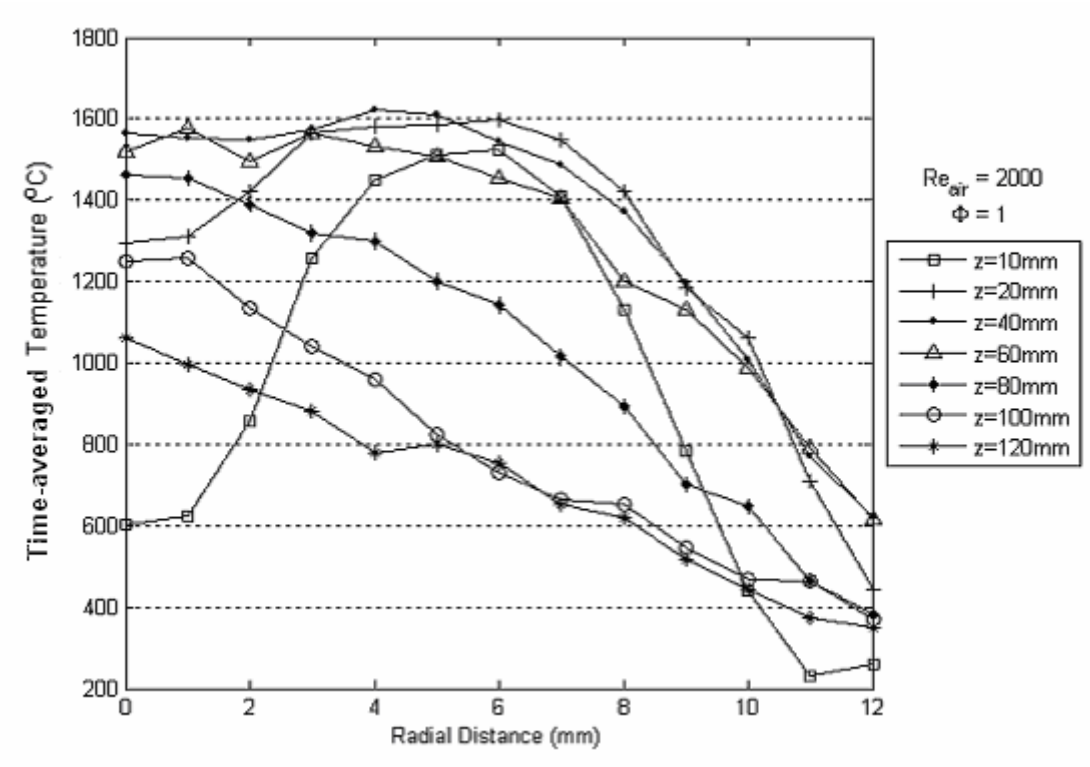

Figure 4.2.2. Radial temperature profiles at different flame heights, Re_{air}=2000, Φ=1, free jet.

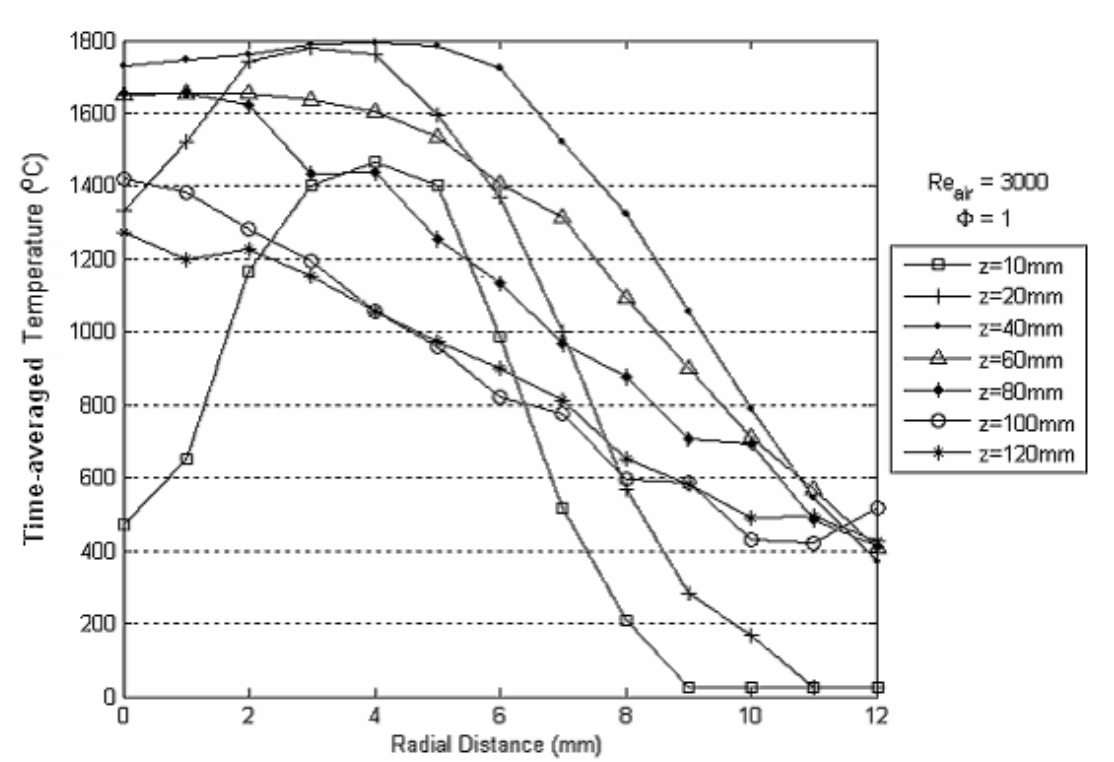

Figure 4.2.3. Radial temperature profiles at different flame heights, Re_{air}=3000, Φ=1, free jet.

Figure 4.2.3 shows the case at Re_{air}=3000 and Φ=1. The radial temperature profiles at the corresponding heights are similar to those in Re_{air}=2000. The temperatures at z=10 mm and z=20 mm show that the effect of the central cool core is more evident compared to that at Re_{air}=2000, while combustion occurs closer to the centerline and lower temperatures are measured at the edge of the flame. This is due to the increased entrainment effect on the fuel towards the centerline as Re_{air} increases; and at the same time, the entrainment on the cool ambient air is also increased.

Higher maximum temperature is recorded at increasing Re_{air}. The maximum temperatures are found at z=40 mm for each Re_{air}, which are 1608°C, 1709°C, 1768°C and 1794°C respectively for Re_{air}=1500, 2000, 2500 and 3000. Besides, the first bell-shaped profile is found at the heights of 40 mm, 60 mm, 80 mm, 100 mm, respectively, which indicates the increasing height of the reaction zones as Re_{air} increases.

Effect of the cool core is similar (*Figure 4.2.4)* for the four Re_{air} at z=10 mm. At Re_{air}=1500 and 2000, the peak temperatures usually distribute at larger radial distances when compared to Re_{air}=2500 and 3000. When Re_{air}=1500 increases to Re_{air}=2000, there is more fuel supplied to better mix with air. Thus, more intense combustion occurs resulting in higher temperatures. When Re_{air} increases to 2500 and 3000, the higher entrainment force provided by the increased central air jet velocity attracts fuel to combust closer to the centerline.

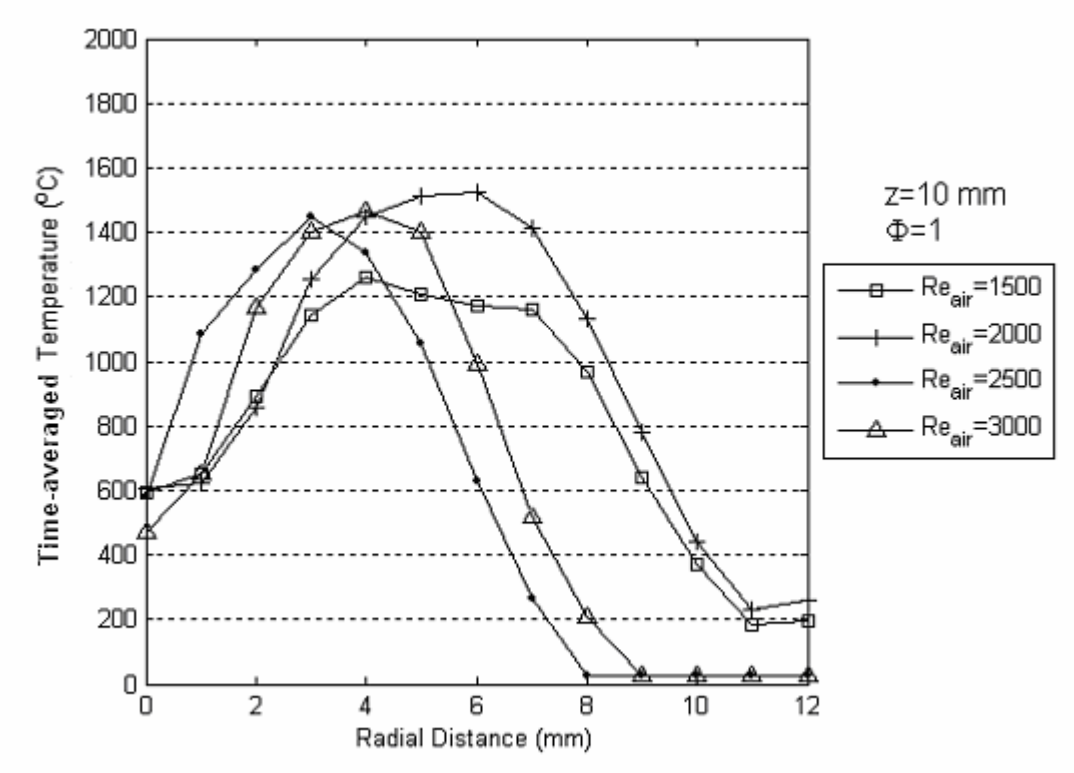

Figure 4.2.4. Radial temperature profiles at different Re_{air}, at z=10mm, Φ=1, free jet.

(c) Contour Plot of Flame Temperature

Figures 4.2.5 to *4.2.8* display the contour plots of the flame temperature for the IDFs at Re_{air} from 1500 to 3000 and Φ=1. As the contour lines are at an interval of 200°C, the four *Figures* show the basic flame temperature distributions.

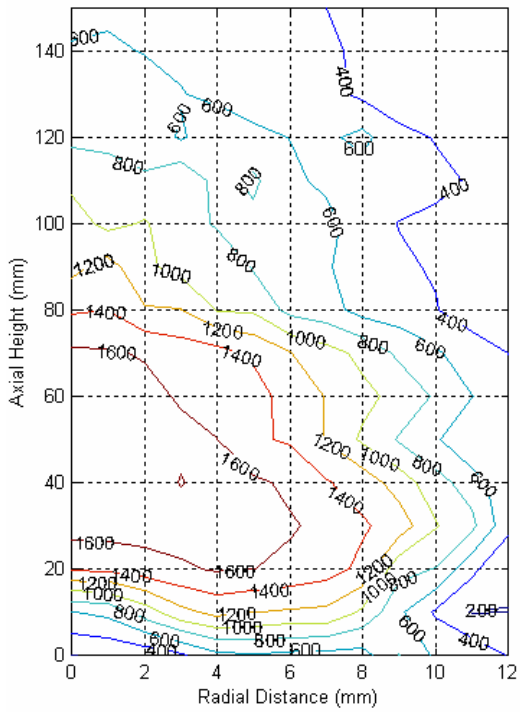

Figure 4.2.5. Contour plot of flame temperature for Re_{air}=1500, Φ=1

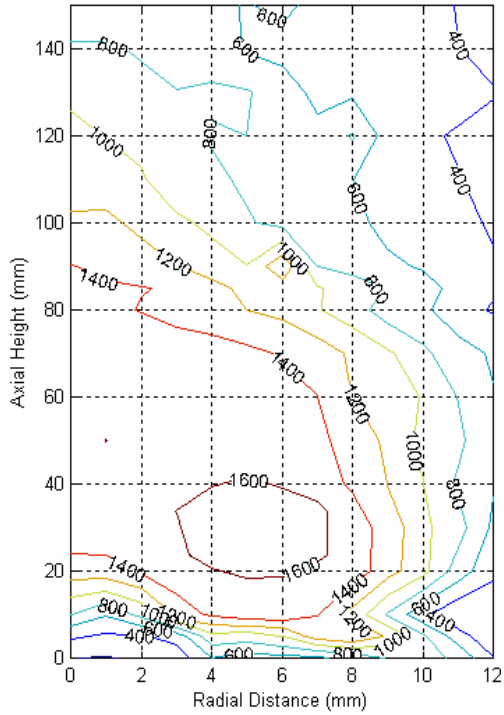

Figure 4.2.6. Contour plot of flame temperature for Re_{air} =2000, Φ=1

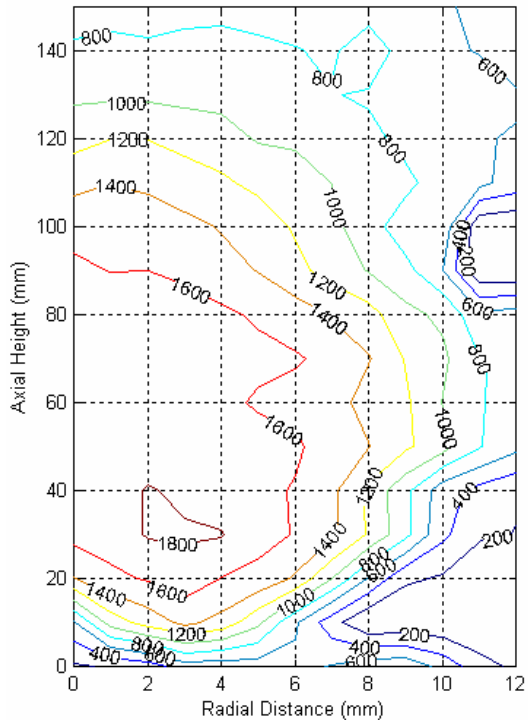

Figure 4.2.7 Contour plot of flame temperature for Re_{air} =2500, Φ=1

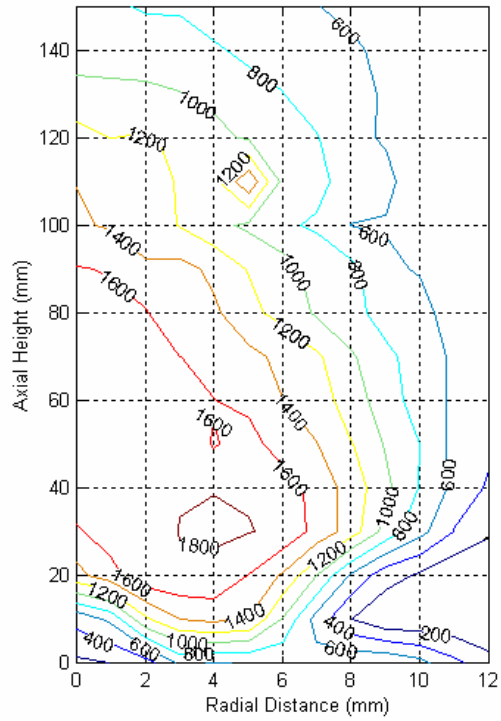

Figure 4.2.8 Contour plot of flame temperature for Re_{air} =3000, Φ=1

From the contour plots, at low flame heights (flame height < 10 mm), the cool core zone can be observed at each Re_{air}, while higher temperatures are located at the edge of the flame (radial distance ≈ 6-7 mm). This is because fuel cannot diffuse into the center of the flame at low flame heights. At the shear layers in between the air and fuel flows, the fuel is mixed with the air to form a combustible mixture close to stoichiometric composition and reacts. Hence, lean combustion occurs towards the centerline while rich combustion occurs near the fuel ports. As a result, there is brilliant orange flames at the neck region as observed from the direct photos shown in the previous sections.

A comparison of *Figure 4.2.5* to *Figure 4.2.8* shows that the 1400°C temperature contour expands in the axial direction and contractes in the radial direction with increasing Re_{air} due to the higher velocity of the air jet, as well as increased fuel supply at higher Re_{air}. The entrainment of the ambient air also increases with increasing Re_{air}, which can be observed from the 400°C temperature contours.

4.2.2 Exhaust Combustion Species

The concentrations of the combustion productss were measured for four Reynolds numbers. The data were corrected to 3 percent of O_2 at dry conditions and are presented in a bar chart shown in *Figure 4.2.9*.

It is observed, from the bar chart, that the O_2 and CO_2 concentrations are similar for all Re_{air}; the peak value was 14.9% and 2.8%, respectively, both found at Re_{air}=3000. The NO concentration increases with the increase in Re_{air}. The maximum NO concentration is 24.7 ppm found at Re_{air}=3000, while the minimum value is 9.1 ppm found at Re_{air}=1500. The CO emissions are nearly zero in the exhaust, except that, there is 0.74% of CO measured in the flame at Re_{air}=3000.

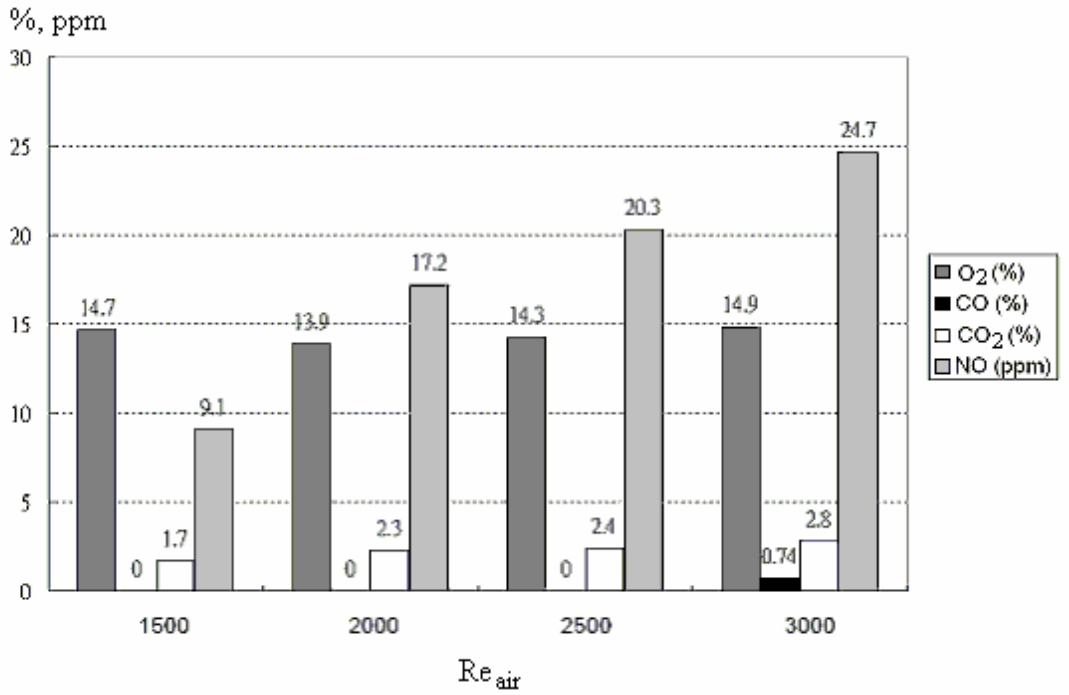

Figure 4.2.9. The exhaust emission of the O_2, CO_2, CO and NO concentrations for the Re_{air}=1500, 2000, 2500 and 3000.

The NO and CO in the flame at Re_{air}=3000 are the highest among the four selected Re_{air}. This can be explained as follows. Refer to *Figure 4.1.5*, the tip of the cool core and the reaction zone are opened and the flame is hollow in structure at Re_{air}=3000. Since the velocity of the central air jet is the highest at Re_{air}=3000 among the Re_{air} investigated, the most intense mixing and the most effective air entrainment lead to the higher temperatures in the flame. The axial temperature profiles at Re_{air}=2500 and Re_{air}=3000 are similar, but higher temperatures are found in the radial direction at Re_{air}=3000, as observed in *Figure 4.2.7* and *Figure 4.2.8*, thus more NO is formed near to the flame edges and the highest exhaust NO concentration is obtained. However, the high velocity of the air jet forces the unburned fuel to react in the downstream of the flame with insufficient air. Therefore, the exhaust emission of CO is also high at Re_{air}=3000.

4.3 Summary

The flame structure of the CAP IDF as a free jet, (within the operating condition being investigated), is divided into a base zone and an elongated main flame zone separated by a neck region formed by the low pressure created by the central high momentum air jet. In the elongated main flame zone, a reaction zone with premixed combustion is found enclosing a cool core zone, which is enclosed by a post combustion flame zone at the same time. The zones characteristics can be identified by color of the flame and also the time-averaged temperature distributions.

The flame length and the heights of the base zone, cool core zone and the post combustion flame zone increase when Φ increases. The photos of the flames reveal that more brilliant orange flames in the post combustion flame zone and the neck region at higher level of Φ with lower Re_{air}. It can be explained that, at constant value of Re_{air}, increase in Φ results in more fuel is present in the post combustion zone; while at constant Φ, decrease in Re_{air} results in reducing the mixing rate between the air and fuel. Thus, rich and incomplete combustion would be expected to occur.

When high-speed shutter of 1/1000 second exposure time is used to record the flame images, complex flows are found at the elongated main flame zone. The intense mixing at the neck region leads to the instabilities in the downstream of the flame, where increasing scale of vortexes are advent. By observing the flame images, it is believed that the flow in the base zone is laminar, while the flow in the elongated main flame zone is turbulent.

In both axial and radial directions, as Re_{air} increases, the temperature at the same coordinates in the flames increases. This effect is more significant in the axial direction. It is also found that the emissions of free jet IDFs are low. The CO concentration is small, except of the case Re_{air}=3000, and the NO concentration is about 20 ppm in the exhaust products.

Chapter 5 Inverse Diffusion Flame – Impinging Jet

5.1 Flame Observations

When the IDF impinges on a horizontal flat plate, the flame flow will be affected and different physical appearance will be observed. This section gives a detailed description in the structure and physical appearance of the IDF as an impinging jet under different operating conditions. The effects of the impingement plate on the flame shape are compared with respect to that in the free jet.

5.1.1 Flame Structure

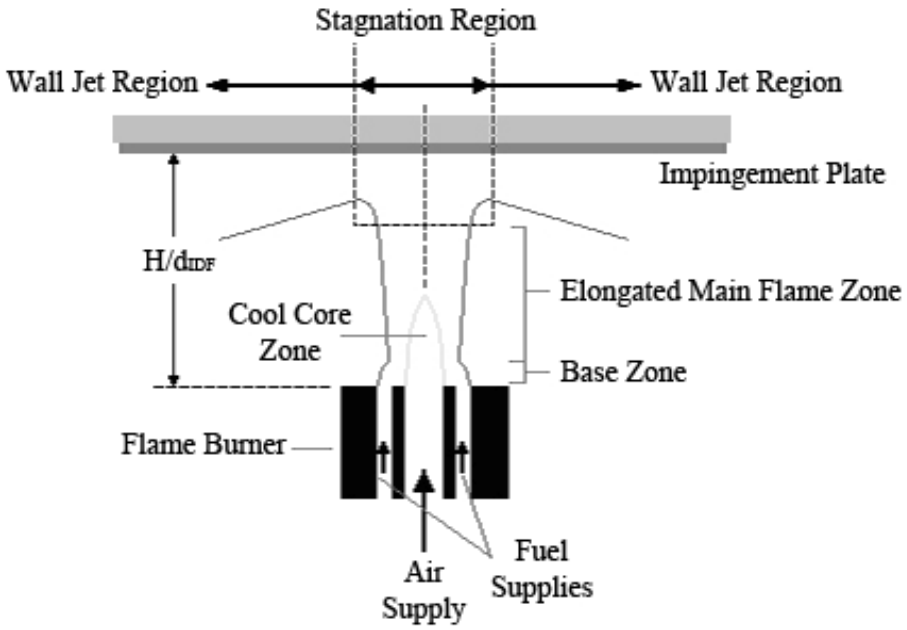

Figure 5.1.1. Schematic of an IDF as an impinging jet

Figure 5.1.1 shows the structure of an impinging IDF jet schematically. It can be observed that, when an IDF is impinging on a horizontal plate, the part of the flame below the plate is little affected. The 4 zones, namely, the base zone, the elongated main flame zone, the cool core zone and the reaction zone, can be observed if the nozzle-to-plate distance (H/d_{IDF}) is larger than the corresponding heights of each zone.

Two main regions are defined for the flame impinging on the plate. The first is called the stagnation region, where the flame just reaches the plate before distortion. The second is the part of the flame above the plate, which is highly distorted and spreads horizontally along the plate, forming the wall jet region as shown in the figure.

5.1.2 Flame Shape

The same method used for describing the flame shape of the free jet is applied for the impingement jet. All observations were performed in a darkened environment. The low-speed and high-speed shutters with time of exposure of 1/10 second and 1/1000 second, respectively, were selected to record the flame shapes.

(a) Low-speed Shutter with Time Exposure of 1/10 Second

Figure 5.1.2 to *Figure 5.1.5* show the shape of the impinging flame jet recorded using the low-speed shutter at Re_{air}=1500, 2000, 2500 and 3000, respectively, with Φ=0.8-2.4. The following discussion include the effects of Φ, Re_{air} and H/d_{IDF} on the shape of the impinging flame jet; and comparisons with the corresponding free jet flames shown in *Figure 4.1.2* to *Figure 4.1.5* in *Chapter 4*.

<u>Effects of overall equivalence ratio</u>

Figures 5.1.2 to *5.1.5* show the flame shape with the impingement plate located at a distance of 42 mm above the nozzle of the IDF burner, corresponding to H/d_{IDF} of 7, for Re_{air} of 1500, 2000, 2500 and 3000, respectively. For Φ=0.8 at each Re_{air}, the visible flame is not yet touching the plate. For Φ=1.0 to 1.8, the visible flame is touching the plate, and the tip of the intense premixed combustion zone is getting closer and closer to the plate. At higher values of Φ, the intense premixed combustion zone directly impinges on the plate.

When Φ increases from 0.8 to 2.4, more brilliant orange flames are observed in the neck region (same observation as found in the free jet) and at the boundary layer between the stagnation and the wall jet region. This indicates that the fuel reaches the impingement plate before spreading to the wall jet region. The fuel accumulates at the boundary layer and reacts with the ambient air to form a ring of a small diffusion flame. More fuel burns in diffusive mode at the flame edge when Φ is increased.

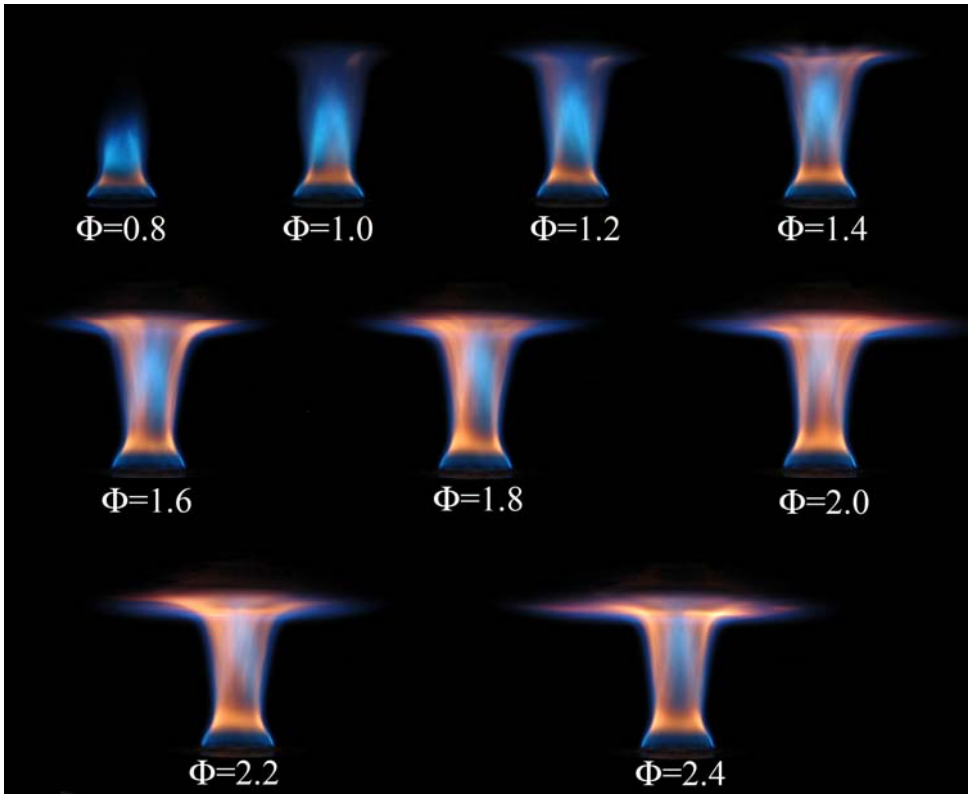

Figure 5.1.2. Direct photos, effects of varying fuel velocity on impinging jet IDFs at Re_{air}=1500 and H/d_{IDF}=7.

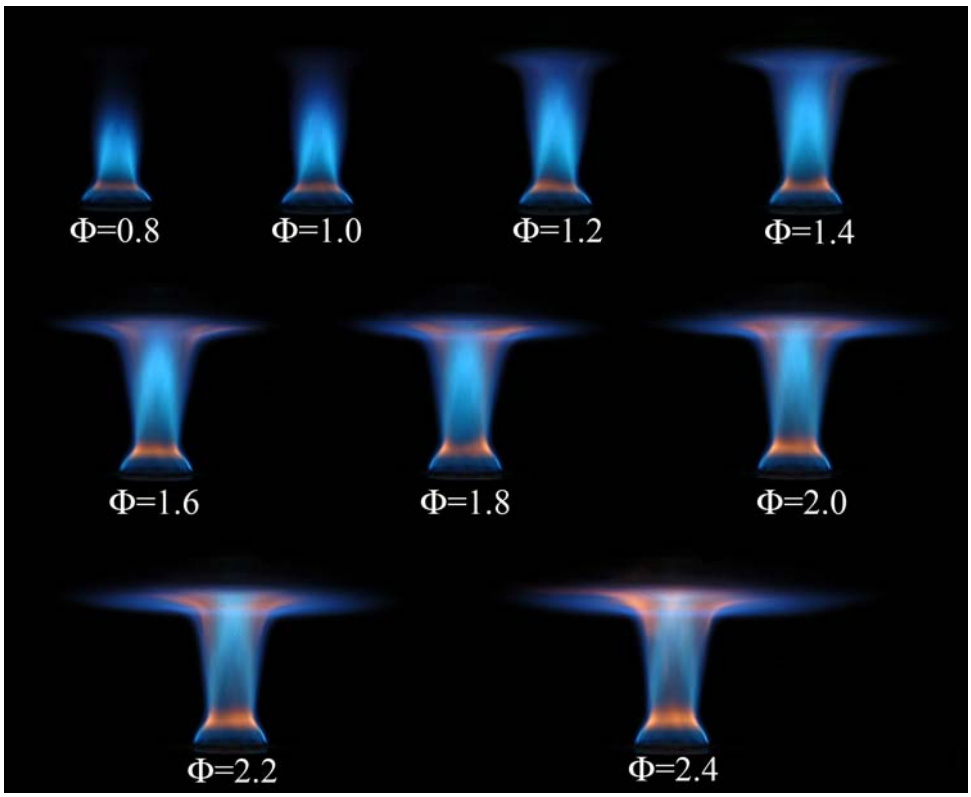

Figure 5.1.3. Direct photos, effects of varying fuel velocity on impinging jet IDFs at Re_{air}=2000 and H/d_{IDF}=7.

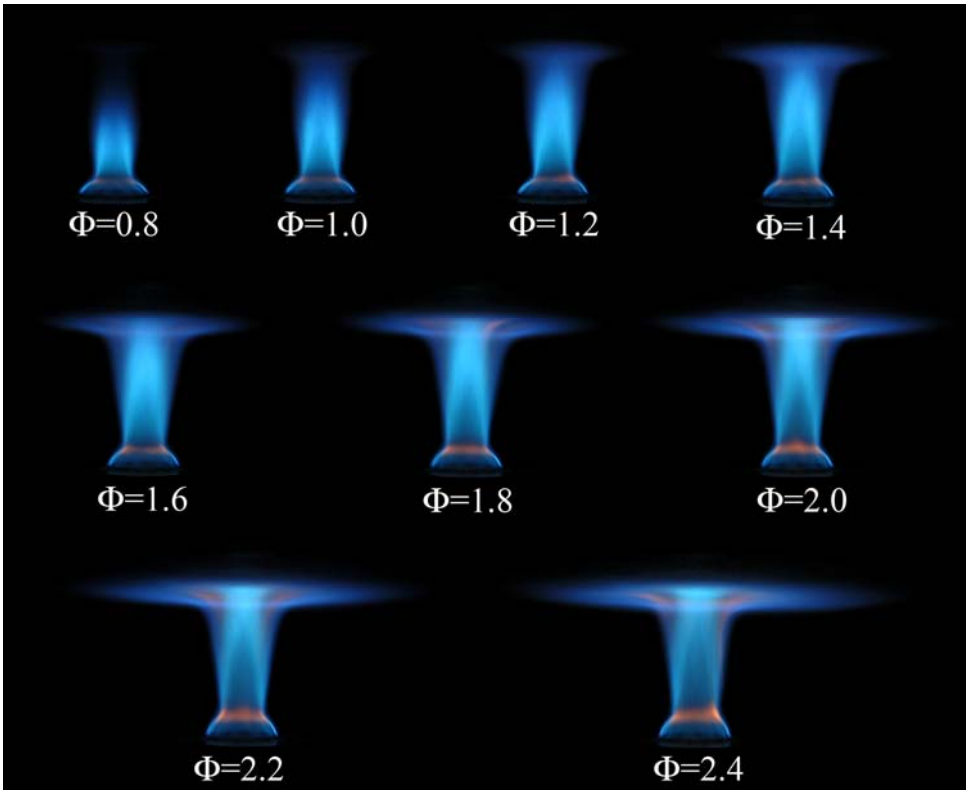

Figure 5.1.4. Direct photos, effects of varying fuel velocity on impinging jet IDFs at Re_{air}=2500 and H/d_{IDF}=7.

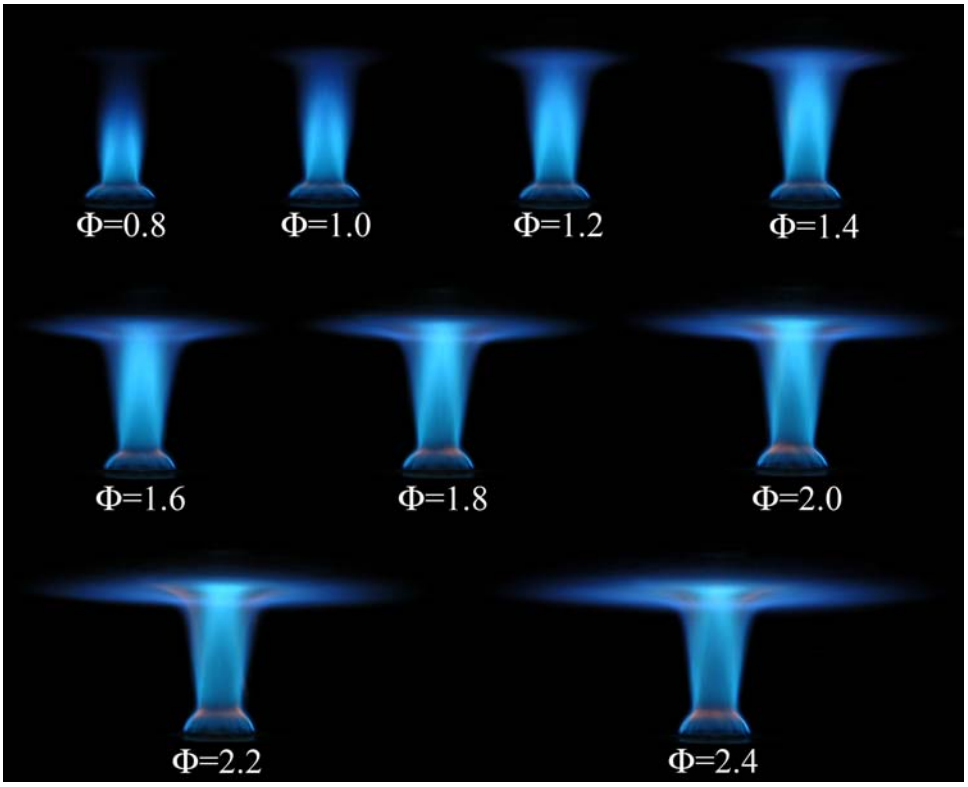

Figure 5.1.5. Direct photos, effects of varying fuel velocity on impinging jet IDFs at Re_{air}=3000 and H/d_{IDF}=7.

There is increasing contact between the visible flame and the plate as Φ is increased. The flame thins out along the plate, which helps to get the flame into contact with secondary air. The impinging flames are blue in colour at the wall jet regions even at Φ= 2.4 for Re_{air}=2000, 2500 and 3000. Comparison of the free jet flame with the corresponding impinging flames at Φ=2.4, reveals improved air fuel mixing for the impinging flame, as reflected in the colours of the two flames: the free jet flame is mainly yellow while the impinging flame is almost completely blue.

Of the four Re_{air} investigated, the IDFs at Re_{air}=1500 show a flame structure slightly different from the other Re_{air}. The blue reaction zone is totally enclosed by the normal diffusion flame at the edge of the flame at higher values of Φ. It can be explained that due to the low velocity of the central air jet, the inducement force is weak at the neck region, and at the same time, the presence of the impingement plate causes fuel accumulation to begin appear at Φ=1.2. Further increase in Φ intensifies the accumulation of fuel and diffusion combustion occurs expanding from the boundary between the stagnation and the wall jet regions to the flame edge in the elongated main flame zone.

Effect of air-Reynolds number

As found in the free jet investigations, an increase in Re_{air} at a constant Φ leads to longer flame length. Therefore, the contact between the visible flame and the plate increases when Re_{air} is increased. Again, increase in the Re_{air} leads to increase in the mixing rate of the air and fuel, thus, less brilliant orange flames are observed. The flames are almost blue at Re_{air}=2000 and 3000.

Effect of nozzle-to-plate distance

Figure 5.1.6 shows the IDF of Re_{air}=2000 and Φ=1.8 striking on the plate at H/d_{IDF} of 3 to 8. The *Figure* shows that at H/d_{IDF}=3, the inner air jet strikes against the centre of the plate. At higher H/d_{IDF}, the premixed reaction zone strikes the centre of the plate. At H/d_{IDF}=8, the tip of the premixed flame zone fails to reach the center of the plate. Also, as H/d_{IDF} is increased, there is less contact area between the visible flame and the plate.

The direct photos of the impinging jet IDFs reveal that, the overall equivalence ratio, the air-Reynolds number and also the nozzle-to-plate distance plays an important role in affecting the heat transfer between the flame and the plate as well as the heat flux distribution on the plate.

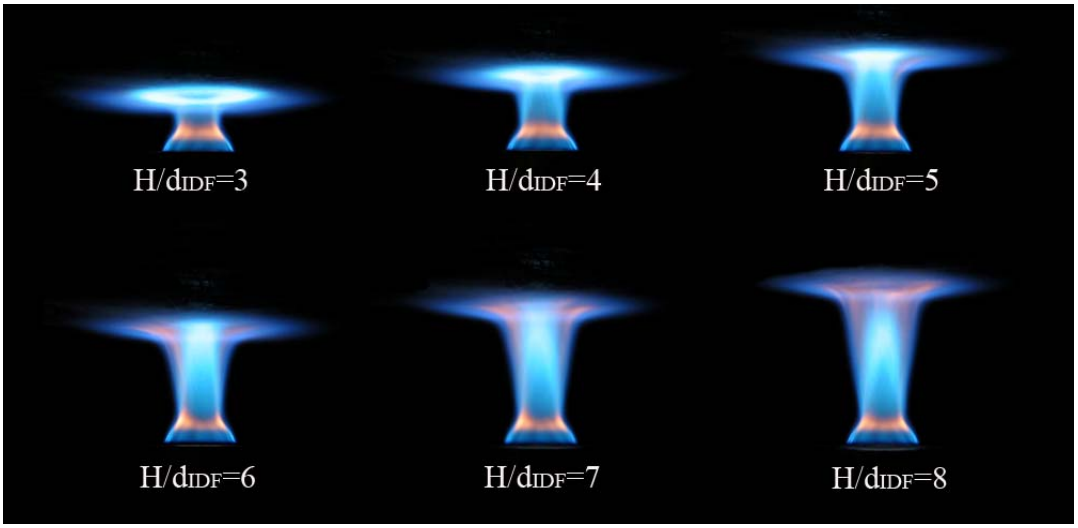

Figure 5.1.6. Direct photos, effects of varying H/d_{IDF} on impinging jet IDFs at Re_{air}=2000 and Φ=1.8.

(b) High-speed Shutter with Time Exposure 1/1000 Second

Figure 5.1.7 shows the flame shapes recorded at high-speed shutter at Re_{air}=2000, Φ=1.8 and H/d_{IDF}=7. The complex flow and the blurred zones are observed. Since the impingement plate is placed at a distance of 42 mm apart from the burner, the vortexes cannot increase in scale as there is limited space.

Figure 5.1.7. Direct photos of flame shapes recorded at high-speed shutter on impinging jet IDFs at Re_{air}=2000, Φ=1.8 and H/d_{IDF}=7.

5.2 Impinging Jet Experiment

In the impinging jet experiments, flame temperature, heat flux and combustion species concentrations were measured at Re_{air}=1500, 2000, 2500 and 3000 with different Φ and H/d_{IDF}. Stagnation point and radial profiles were measured for the flame temperature and heat flux with the test rig shown in *Figure 3.1.3*. Stagnation point profiles were measured for Φ=0.8-2.4 for the four selected Re_{air} with H/d_{IDF}=2-16, while radial profiles were measured for Φ=0.8-1.8 with H/d_{IDF}=4-10, at Re_{air}=2000 and H/d_{IDF}=5-8 at Re_{air}=1500, 2500 and 3000. Radial profiles of combustion species concentrations were measured at Re_{air}=2000 and 3000 with Φ=0.8, 1.0, 1.2, 1.8 and H/d_{IDF} of 5, 7 and 10. The results are shown in the following sections.

5.2.1 Impinging Flame Temperature

In the impinging jet experiment, the flame temperature was measured at 2 mm below the plate. In this section, it can be divided into 2 parts: the temperature distribution at the stagnation point and the temperature distribution from the centerline radially outward along the wall jet region. Both effects of the Re_{air} and Φ are examined on the stagnation point and radial temperature distributions; the effects of H/d_{IDF} on the radial temperature distribution are also analyzed.

(a) Stagnation Point Temperature Distributions

The mean temperature and temperature fluctuation at the stagnation point were measured at different nozzle to plate distances. The temperature fluctuation profiles are similar at different Re_{air} and Φ. Taking the stagnation point profile for Re_{air}=2000 and Φ=1.0 as an example (see *Figure 5.2.1),* in which the temperature fluctuations are high at the two extremes of the investigated H/d_{IDF}, $H/d_{IDF} \leq 4$ and $H/d_{IDF} \geq 13$, while low and quite constant in the intermediate range of $4<H/d_{IDF}<13$. At low level of H/d_{IDF}, the cool core might impinge on the stagnation point while at high level of H/d_{IDF}, the tail of the flame might impinge on the stagnation point, both leads to higher temperature fluctuations, for the case Re_{air}=2000 and Φ=1. In the intermediate range, the main reaction zone of the flame, which is more stable, impinges on the stagnation point.

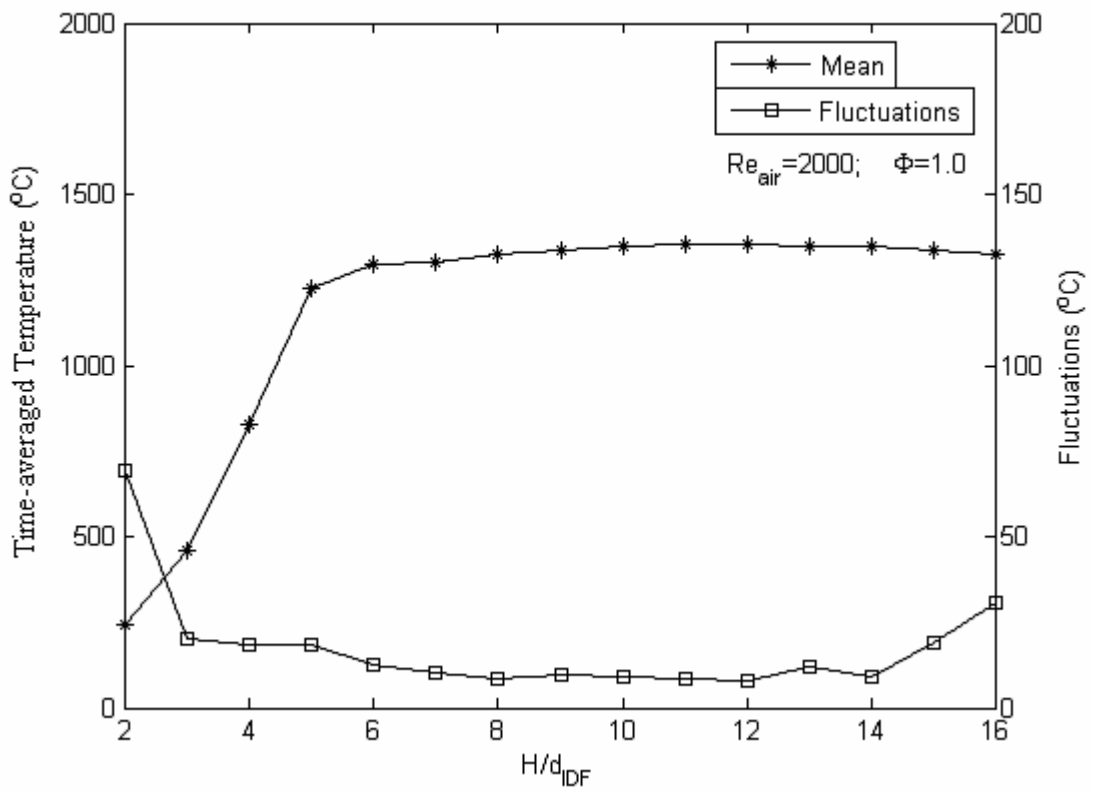

Figure 5.2.1. Stagnation point temperature and fluctuations profiles for Re_{air}=2000, Φ=1.0.

Compare with the free jet, the mean temperature of the impingement IDF shows a more constant profile, instead of a decreasing profile as found in the free jet (refer to *Figure 4.2.1*), at $H/d_{IDF}>12$, which is equivalent to z=72 mm in the free jet. At the same time, higher fluctuations of the stagnation point temperature are found near to the cool core zone of the impingement jet while lower fluctuations are observed in the free jet.

Figure 5.2.2 to *Figure 5.2.5* show the mean stagnation temperature profiles at Φ=0.8-2.4 for Re_{air}=1500, 2000, 2500 and 3000, respectively. At Φ=0.8 and Φ=1.0, the stagnation point temperatures are low for each of the Re_{air}. By referring to *Figure 5.1.2* to *Figure 5.1.5*, the flames are short and the tip of the reaction zone during these operating conditions is opened, thus, the central air jet cools the flame mixture at the stagnation point. Moreover these flames are cooler because they are basically fuel lean.

From Φ=1.2 to Φ=1.6, the profiles shift upwards for each Re_{air}, since the tip of the reaction zone is developing to be conical and strikes at the stagnation point with the increase in fuel supplied at constant air flow rate. The flames are hotter because the partially premixed reaction zones are close to stoichiometric combustion condition.

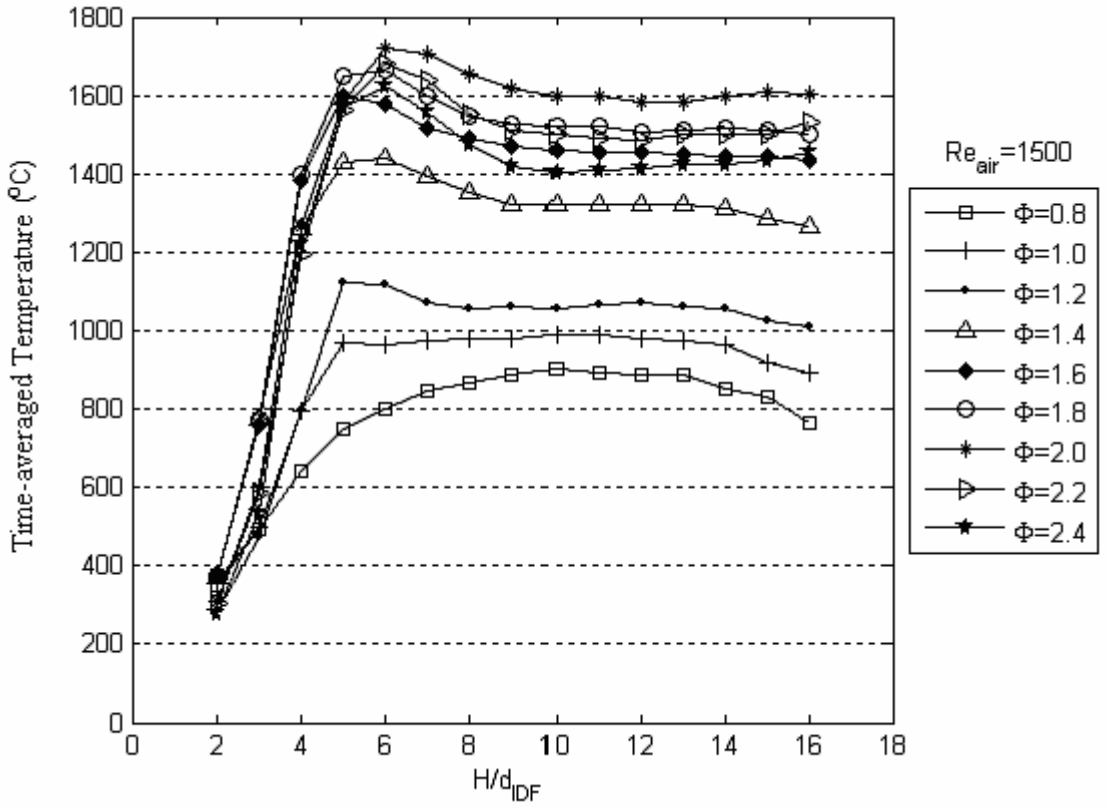

Figure 5.2.2. Stagnation point temperature profiles at different Φ for Re_{air}=1500.

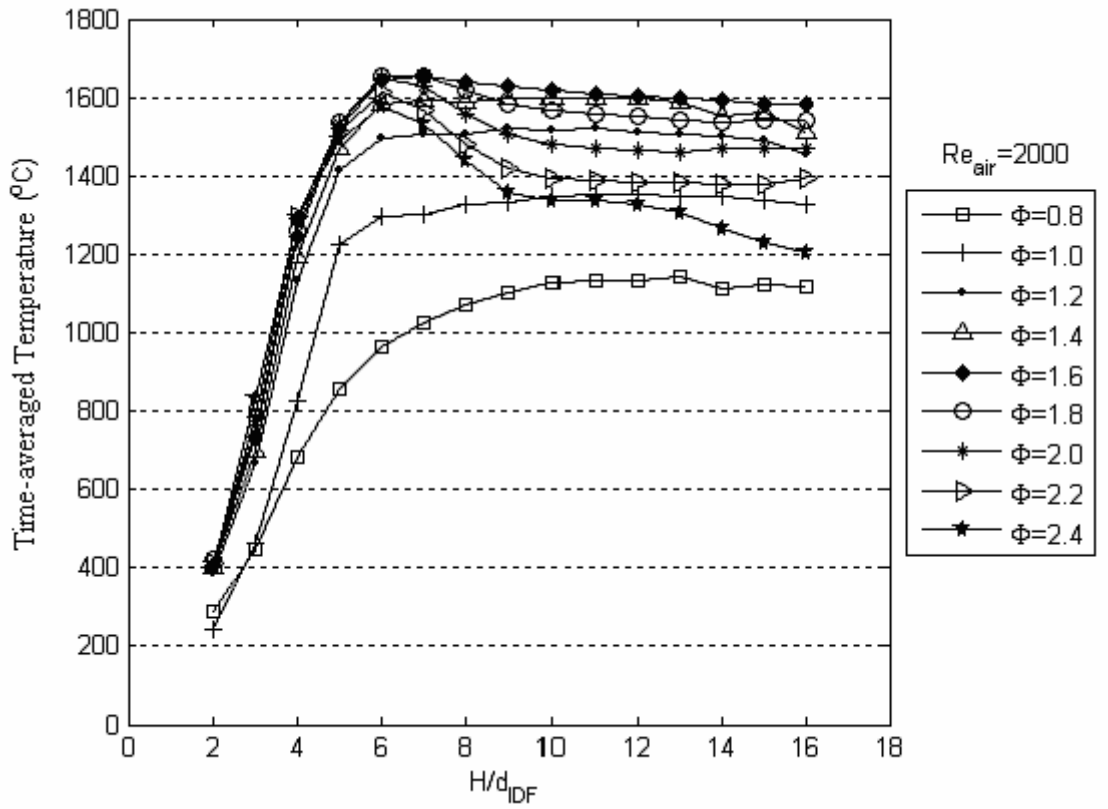

Figure 5.2.3. Stagnation point temperature profiles at different Φ for Re_{air}=2000.

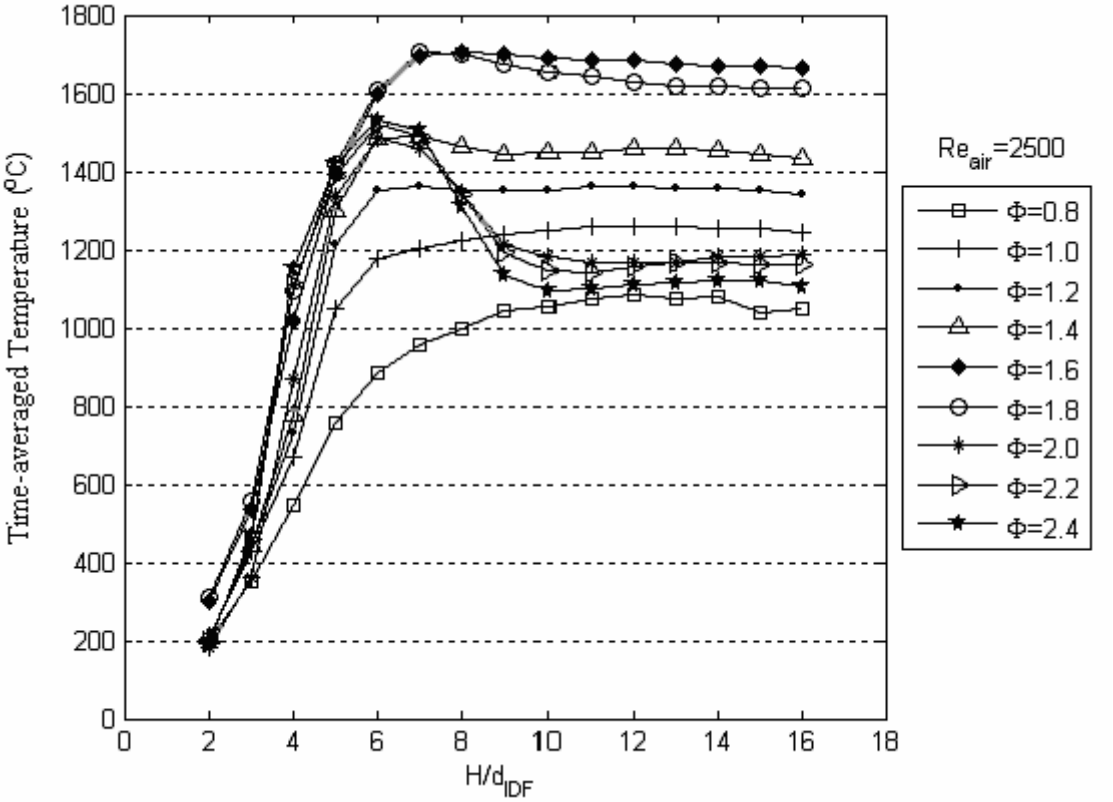

Figure 5.2.4. Stagnation point temperature profiles at different Φ for Re_{air}=2500.

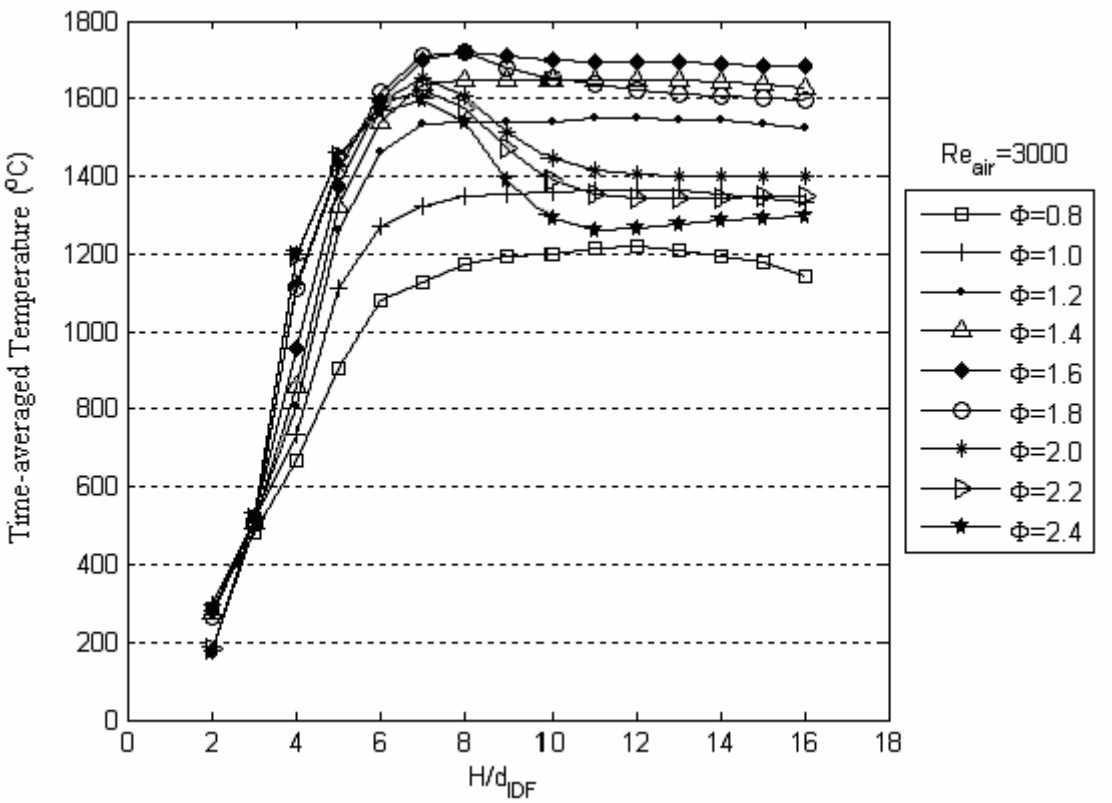

Figure 5.2.5. Stagnation point temperature profiles at different Φ for Re_{air}=3000.

For Re_{air}=2000, 2500 and 3000, the maximum stagnation point temperature profile is found at Φ=1.6. When Φ is further increase (Φ=1.8-2.4), the profiles shift downwards with more obvious temperature drop at the downstream beyond the peak values as Re_{air} increases. It can be explained that, at fixed air flow rate, the fuel and air are mixed and burned in the partially premixed reaction zone. However, with increase in Φ, there is initially an increase in combustion intensity in the partially premixed combustion zone, leading to an increase in temperature and heat flux. However, beyond a certain level of Φ, there is excessive fuel for combustion in the partially premixed zone. Part of the fuel will be burned in the downstream with entrained air, leading to lower temperature and hence lower heat flux.

For Re_{air}=1500, the maximum stagnation point temperature profile is found at Φ=2.0. In this case, with constant values of Φ, the fuel jets momentum and the air jet momentum are the lowest among the considered Re_{air}. And the flame length at Re_{air}=1500 is also the shortest when compared to the others. Therefore, at Φ=1.8 and 2.0, instead of cooling, the less amount of unburned fuel may react with the ambient air at the larger spacing between the flame tip and the plate. However, when Φ is further increased to 2.2 and 2.4, the fuel in the post-combustion flame zone increases and reacts with insufficient air, which cools the flame temperature at the stagnation point.

Comparing with the axial profiles in the free jet IDFs (refer to *Figure 4.2.2*), the flame temperature under impinging is lower than that under free jet. This is due to the quenching effect of the presence of the cooled copper impingement plate. The flame is cooled when it is impinged on the plate.

Base on the stagnation point temperature investigations, flames with Φ in the range of 0.8 to 1.8, and H/d_{IDF} in the range of 4 to 10, at Re_{air}=2000 were selected for investigation of the radial temperature distribution. The selected range of H/d_{IDF} covers the range of the stagnation point temperature profiles which is more intense (the plate is impinged by the intense combustion region of the flame). The range of H/d_{IDF} is reduced to 5 to 8, for Re_{air}=1500, 2500 and 3000. Tests were carried out for further investigation of the effects of the Re_{air} on the radial temperature distributions. The four selected heights represent the heights of the reaction zone for the IDFs operating at Φ=0.8-1.8, as shown in *Figure 4.1.2* to *Figure 4.1.5*.

(b) Radial Temperature Distributions

In the radial temperature profiles, the trends of the temperature fluctuation can be divided into two main groups as shown in *Figure 5.2.6* and *Figure 5.2.7*. The former Figure shows an instable increasing fluctuation temperature profile, while the latter Figure shows an instable decreasing fluctuation temperature profile.

The fluctuation is more instable in the radial temperature profiles as compare to the stagnation point temperature profiles. Within the range of H/d_{IDF} being studied, the increasing fluctuation temperature profiles are found at the H larger than the height of the cool core zone and the steepest increasing gradient occurs when the reaction zone touches the impingement plate at the centerline. On the other hand, the decreasing fluctuation temperature profiles are found when the cool core zone is close to or impinges on the impingement plate.

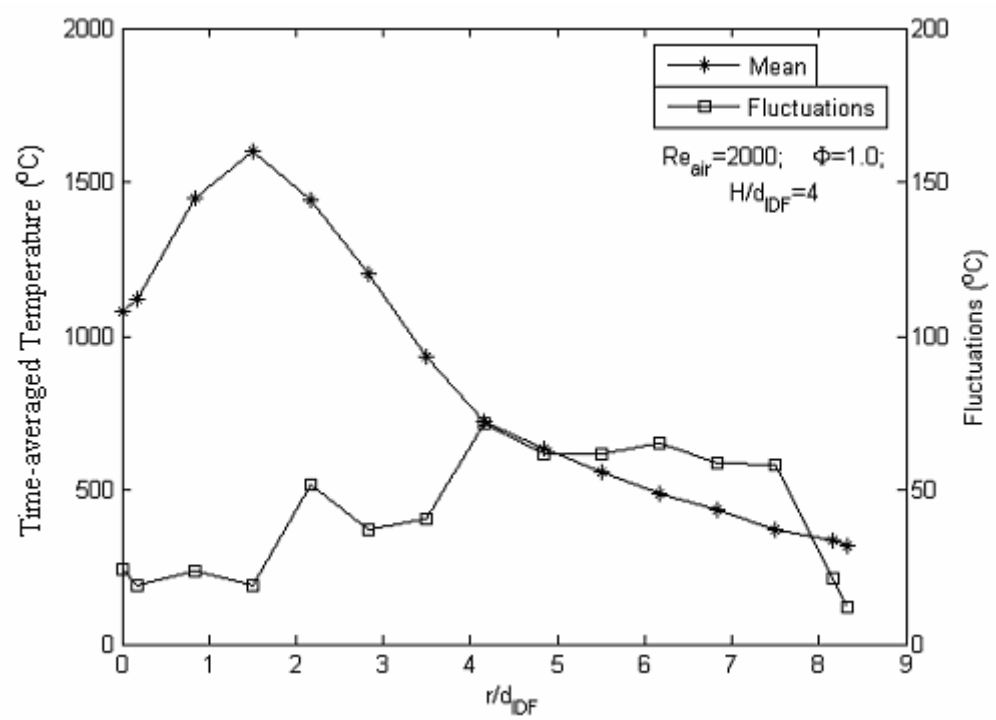

Figure 5.2.6. Radial temperature and fluctuations profiles for Re_{air}=2000, Φ=1.0 and H/d_{IDF}=4.

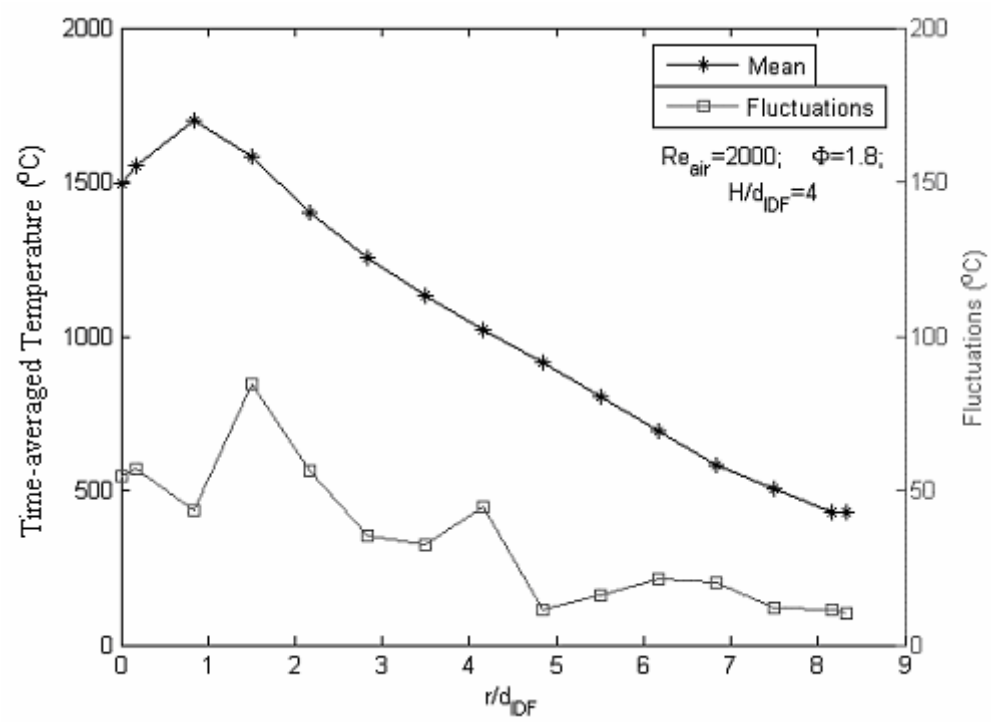

Figure 5.2.7. Radial temperature and fluctuations profiles for Re_{air}=2000, Φ=1.8 and H/d_{IDF}=4.

The radial temperature profiles are shown in *Figure 5.2.8* to *5.2.20* to investigate the effect of H/d_{IDF}, Re_{air} and Φ on the radial temperature distributions. In *Figure 5.2.8* to *Figure 5.2.13*, the Re_{air} is fixed at 2000 for comparing the effect of nozzle-to-plate distance and the overall equivalence ratio on the radial temperature distributions. In the other Figures, the effects of these two parameters at Re_{air} of 1500, 2500 and 3000 were investigated.

The effects of the H/d_{IDF} on the radial temperature distribution are shown in *Figure 5.2.8* and *Figure 5.2.9* at Re_{air}=2000 for Φ=0.8 and Φ=1.8, respectively. These two are typical cases; the first one corresponds to a fuel lean flame while the other corresponds to a fuel rich flame. H/d_{IDF} is varied from 4 to 10, corresponding to the nozzle-to-plate distance from 24 mm to 60 mm.

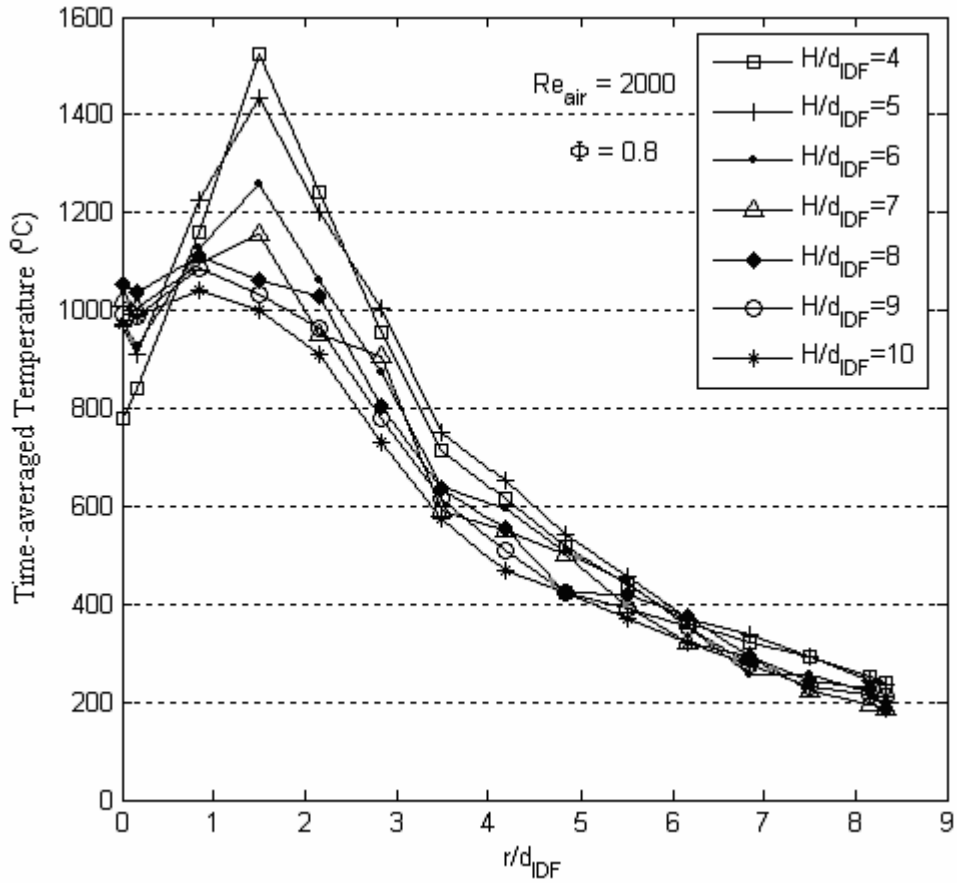

Figure 5.2.8. Radial temperature profiles at different H/d_{IDF} for Re_{air}=2000 and Φ=0.8.

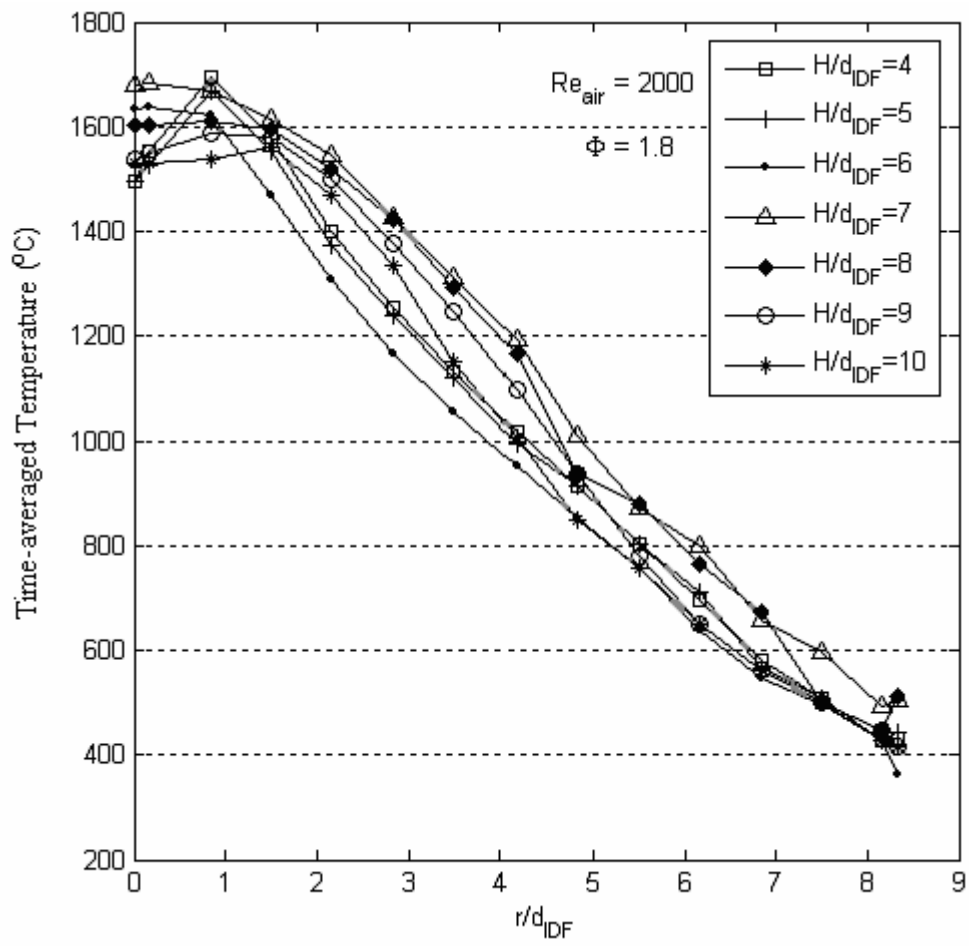

Figure 5.2.9. Radial temperature profiles at different H/d_{IDF} for Re_{air}=2000 and Φ=1.8.

At the lower value of Φ (Φ=0.8), the temperature is around 800°C to 1000°C at the centerline and increases to a peak value in the region of r/d_{IDF} of 1.0 to 2.0 and then drops gradually radially outwards. The maximum peak temperature occurs at H/d_{IDF} of 4; and the lowest peak temperature occurs at H/d_{IDF} of 10. The radial temperature profiles tend to flatten and the temperature decreases at increasing level of H/d_{IDF}.

At Φ=0.8, the flame has a hollow core with intense combustion occurring at the periphery of the cool core. Thus the maximum temperature does not occur at the centerline. The flame is short, thus at higher nozzle-to-plate distance, the combustion products strike the plate and the temperature becomes lower. The radial drop in the temperature is a characteristic of the impinging flame: the gas cools down as it spreads along the plate.

In *Figure 5.2.9*, at the higher value of Φ (Φ=1.8), the temperature is around 1500°C to 1700°C at the centerline; being the highest at H/d_{IDF} of 7. At H/d_{IDF} of 4 and 5, the peak temperature is much higher than the centerline temperature and occurs at a small distance from the centerline. At H/d_{IDF} of 6, 7 and 8, the peak temperature occurs at the centerline, and the temperature drops with the radial distance.

At Φ=1.8, there is an increase in flame length and intensity of combustion. The radial gas temperatures are significantly higher than those at Φ=0.8, due to the increased fuelling rate. A minor cool core effect is observed at H/d_{IDF}=4 and 5. When H/d_{IDF} increases from 6 and 7, the flame temperature increases along the radial direction, and the temperature decreases again at H/dI_{DF} of 8. This indicates that the tip of the reaction zone is approaching and strikes at the stagnation point at around H/d_{IDF} of 7. Further increase in H/d_{IDF}, the temperature profiles shift downwards, which indicate the flame temperature is lower at the post-combustion flame zone.

Figure 5.2.10 to *Figure 5.2.13* show the effects of the Φ on the radial temperature distribution for Re_{air}=2000 at H/d_{IDF}=4, H/d_{IDF}=5, H/d_{IDF}=7 and H/d_{IDF}=10, respectively. . In each case, Φ was varied from 0.8 to 1.8.

In each Figure (*Figure 5.2.10* - *Figure 5.2.13*), at fixed H/d_{IDF}, the radial profiles shift upwards when Φ is increased from 0.8 to 1.4, which is due to the increase in the fueling rate at higher level of Φ under a fixed Re_{air}. When Φ increases to 1.6 and 1.8, the temperature profiles might not shift upwards, but rather, spread more even radially, indicating that part of the fuel is consumed after the flame impinged on the plate. The Figures also shows that the cool core effect is more intense at lower level of Φ, and the cool core effect is more intense at lower level of H/d_{IDF}.

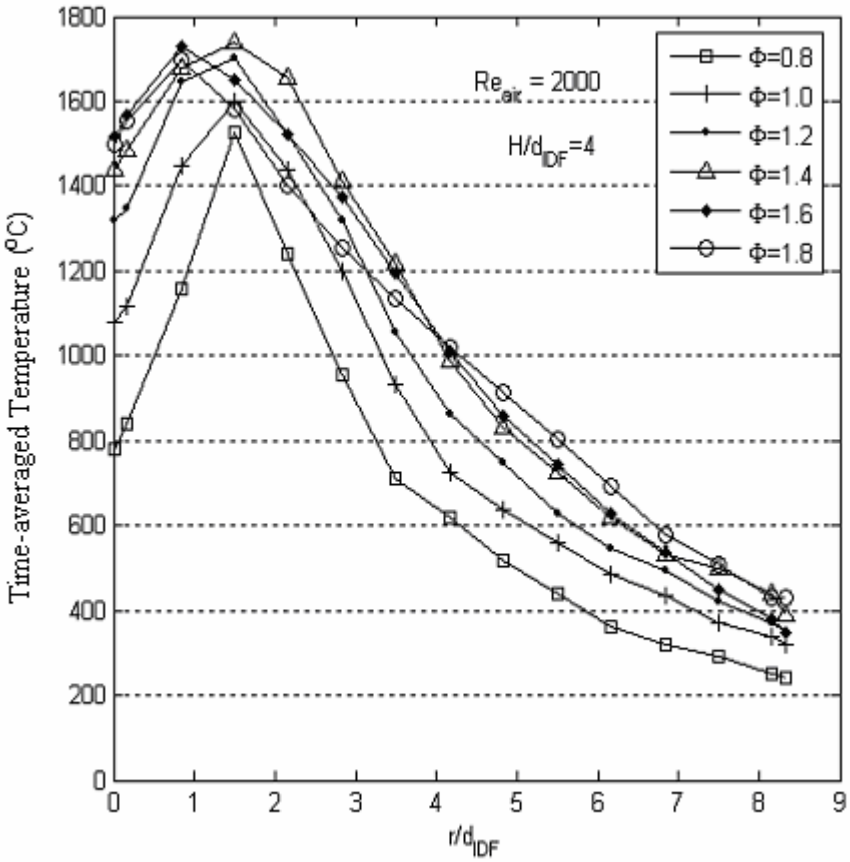

Figure 5.2.10. Radial temperature profiles at different Φ for Re_{air}=2000 and H/d_{IDF}=4.

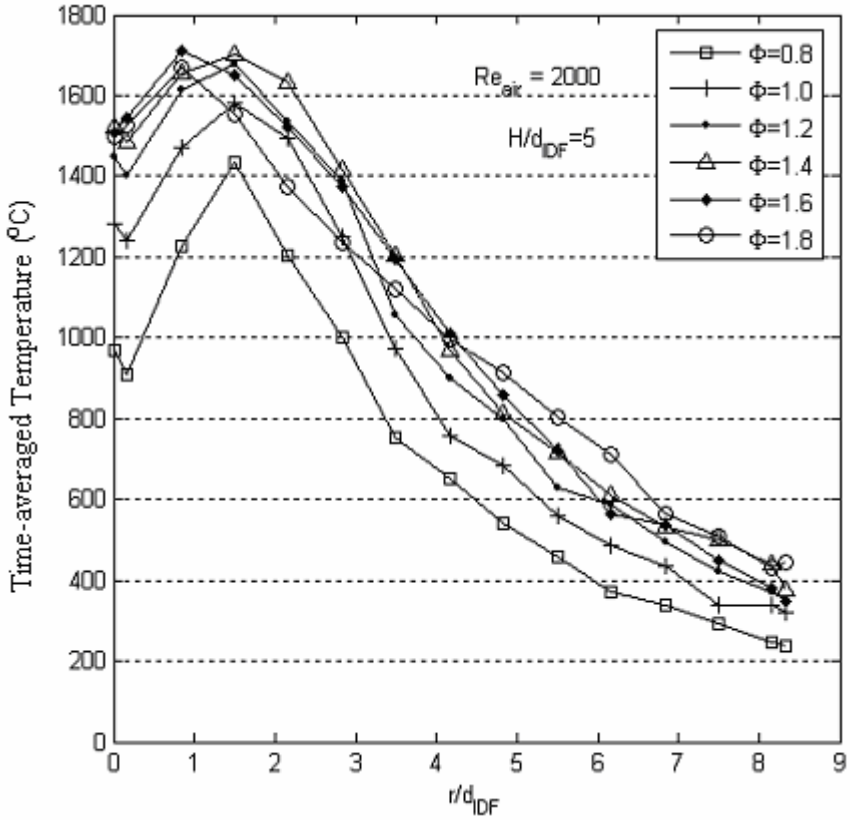

Figure 5.2.11. Radial temperature profiles at different Φ for Re_{air}=2000 and H/d_{IDF}=5.

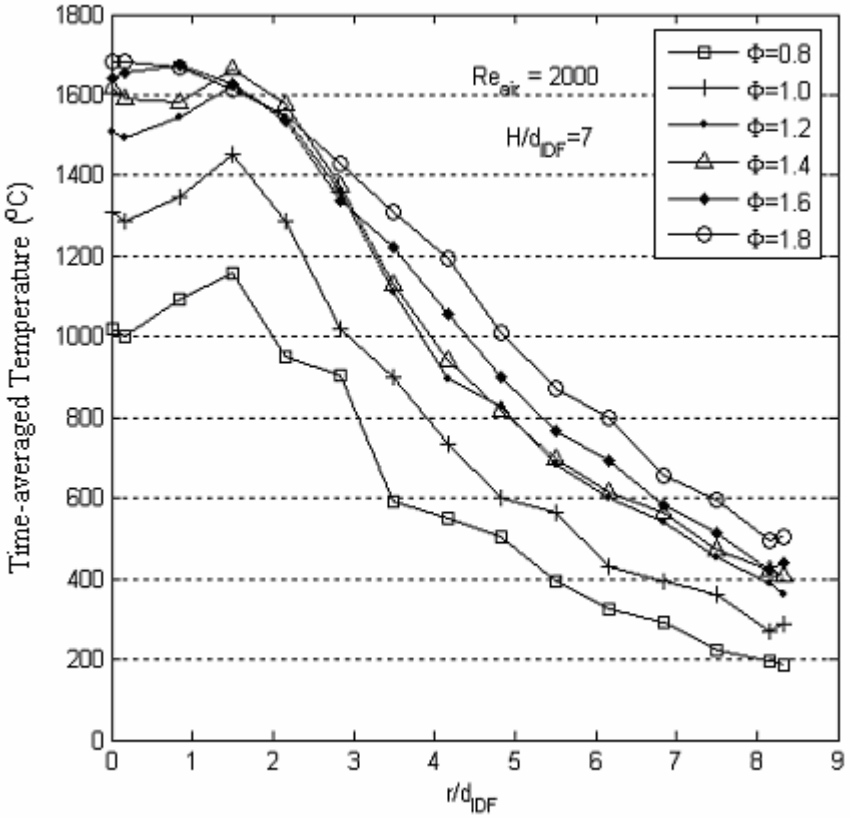

Figure 5.2.12. Radial temperature profiles at different Φ for Re_{air}=2000 and H/d_{IDF}=7.

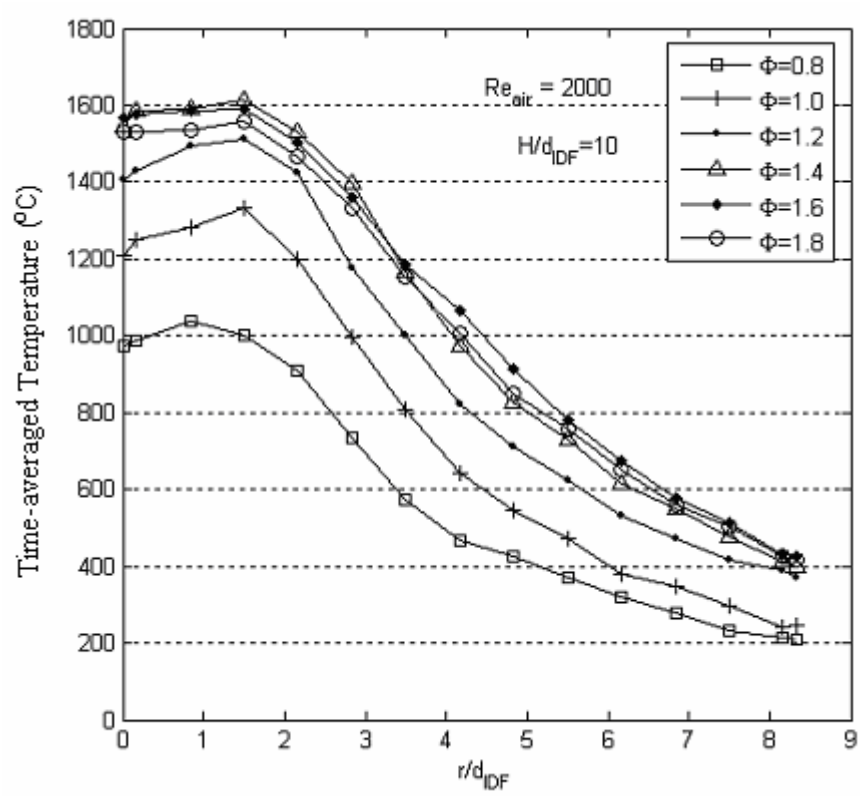

Figure 5.2.13. Radial temperature profiles at different Φ for Re_{air}=2000 and H/d_{IDF}=10.

However, in *Figure 5.2.13*, at H/d_{IDF}=10, the nozzle to plate distance is larger than the partially premixed combustion zone and hence the post combustion products strikes on and spread along the plate. In the range of investigated Φ, slightly lower flame temperature is measured near the stagnation point. The temperature then increases to a maximum and decreases along the impingement plate. This indicates that, the heat generated in the reaction zone is diffused radially in the wall jet region through the post combustion products of the flame.

Figure 5.2.14 and *Figure 5.2.15* show the cases of the effects of H/d_{IDF} on the radial temperature distribution for Re_{air}=1500 and 3000, respectively at Φ=0.8. And, *Figure 5.2.16* and *Figure 5.2.17* show the corresponding results with Φ=1.8. The general results are similar to those shown in *Figure 5.2.8* and *Figure 5.2.9* for Re_{air}=2000. However, with increase in the Re_{air} at constant values of Φ=0.8 and Φ=1.8, the effect of the H/d_{IDF} become more insignificant on the radial temperature distributions in the wall jet region. Besides, at constant values of Φ and H/d_{IDF}, the radial temperature distributions increase with Re_{air} increases, due to increased fuelling rate.

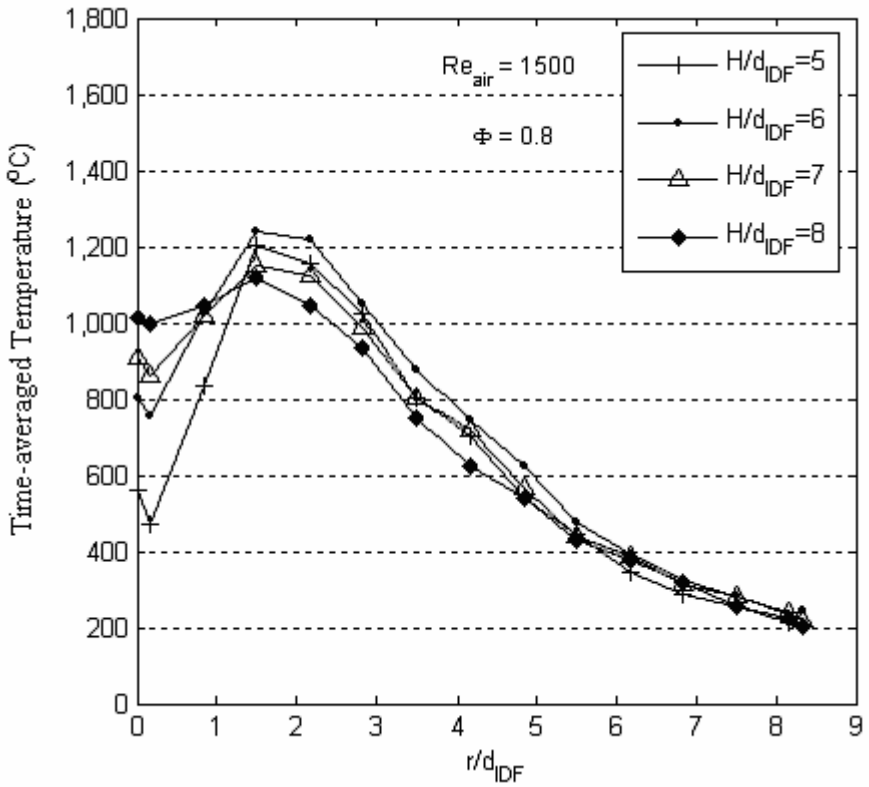

Figure 5.2.14. Radial temperature profiles at different H/d_{IDF} for Re_{air}=1500 and Φ=0.8.

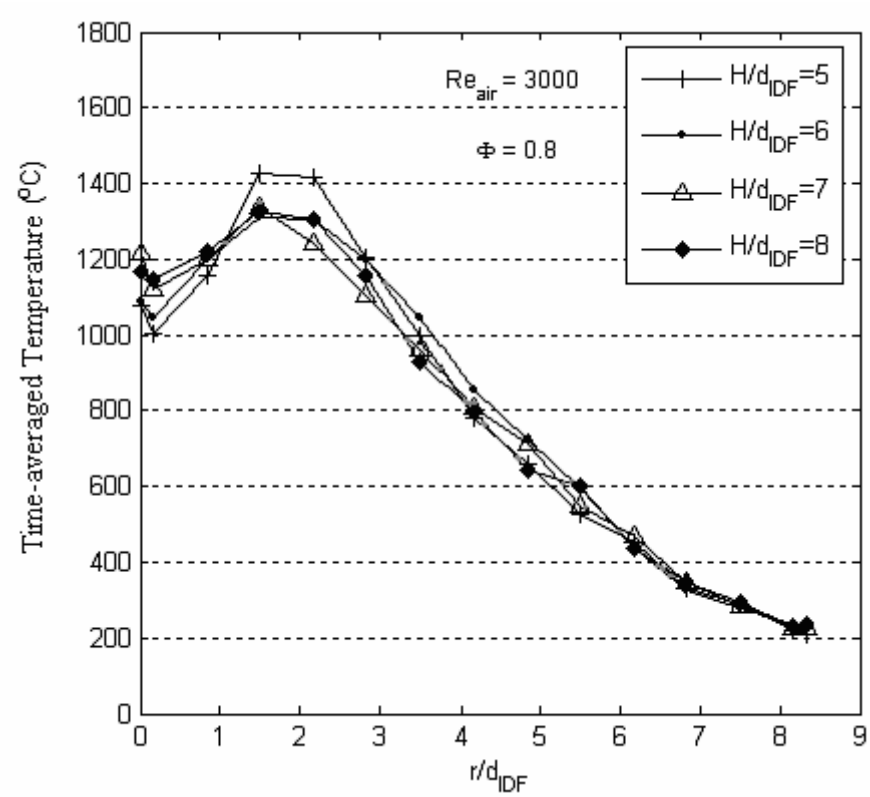

Figure 5.2.15. Radial temperature profiles at different H/d_{IDF} for Re_{air}=3000 and Φ=0.8.

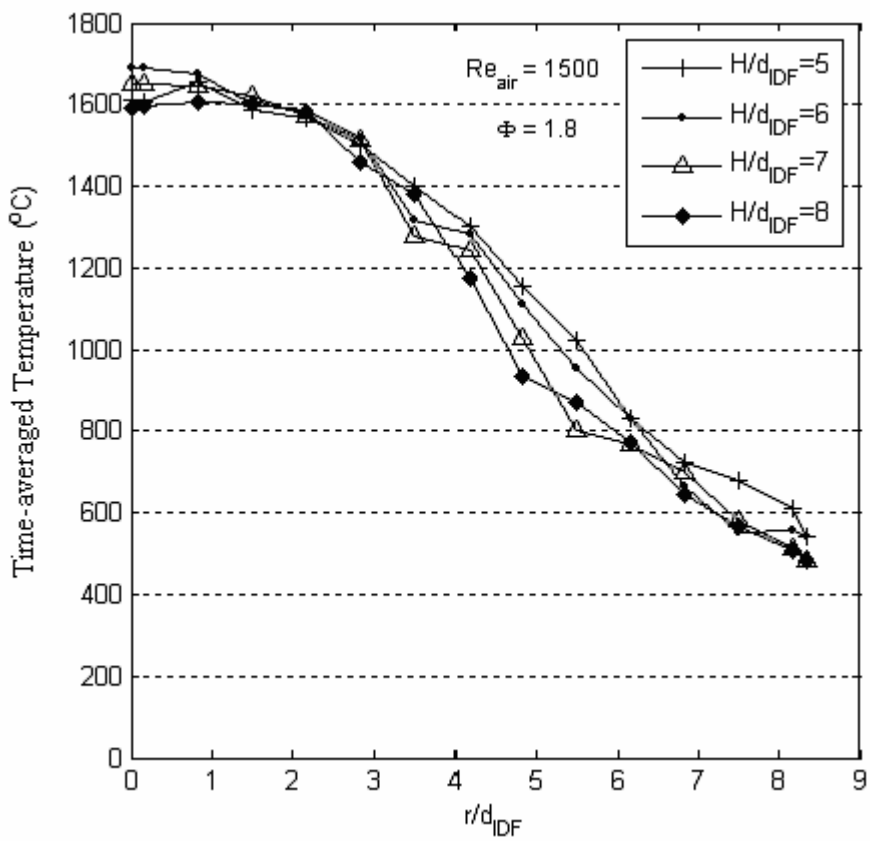

Figure 5.2.16. Radial temperature profiles at different H/d_{IDF} for Re_{air}=1500 and Φ=1.8.

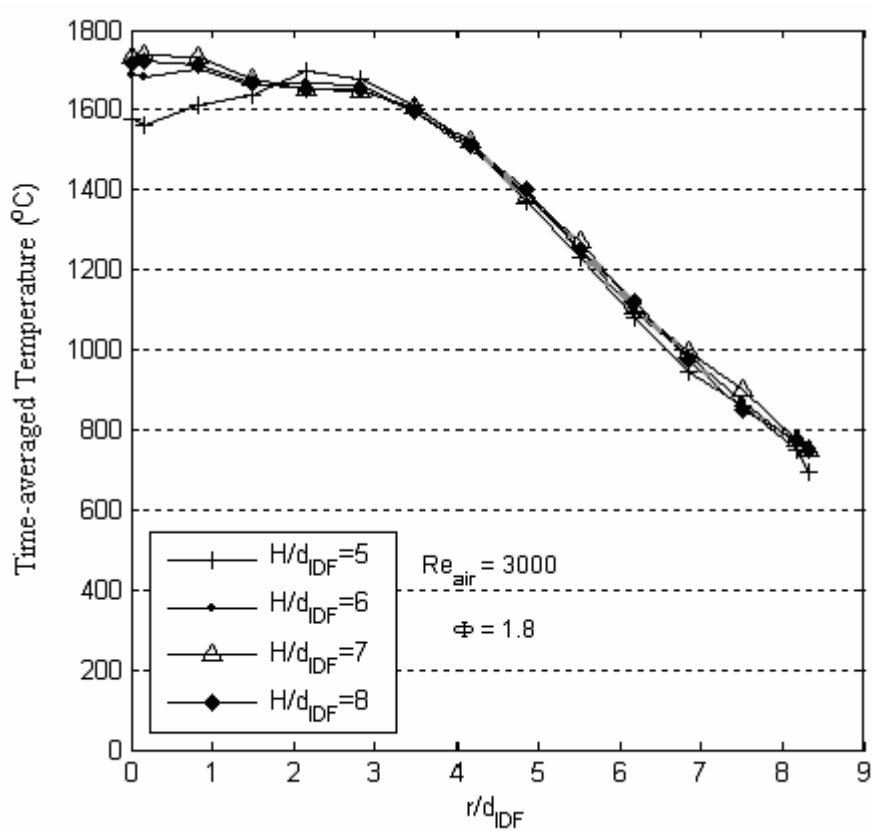

Figure 5.2.17. Radial temperature profiles at different H/d_{IDF} for Re_{air}=3000 and Φ=1.8.

The radial temperature distributions at different Φ for Re_{air}=1500, 2500 and 3000 at H/d_{IDF}=7 are shown in *Figure 5.2.18* to *Figure 5.2.20*, respectively. The corresponding result for Re_{air} of 2000 is shown in Figure 5.2.12.

In the *Figures,* in each case, at a fixed Re_{air}, the radial temperature profiles shift upwards with increasing Φ. Moreover, at a fixed Φ, the larger of the Re_{air}, the higher the radial temperature distributions will be; which reflects better mixing between the air and fuel due to the increase in entrainment effect at higher level of Re_{air}.

From the above results examined for the IDFs, H/d_{IDF}, in the range being investigated, has less significant effect on the radial temperature distribution when compared to the parameters of Re_{air} and Φ.

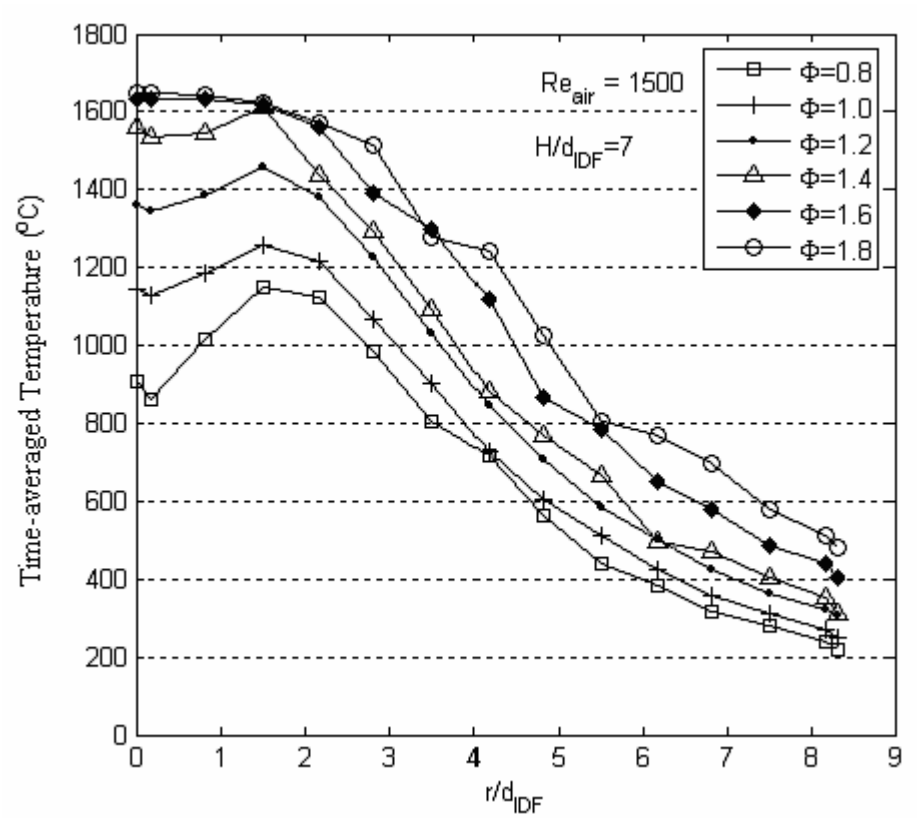

Figure 5.2.18. Radial temperature profiles at different Φ for Re_{air}=1500 and H/d_{IDF}=7.

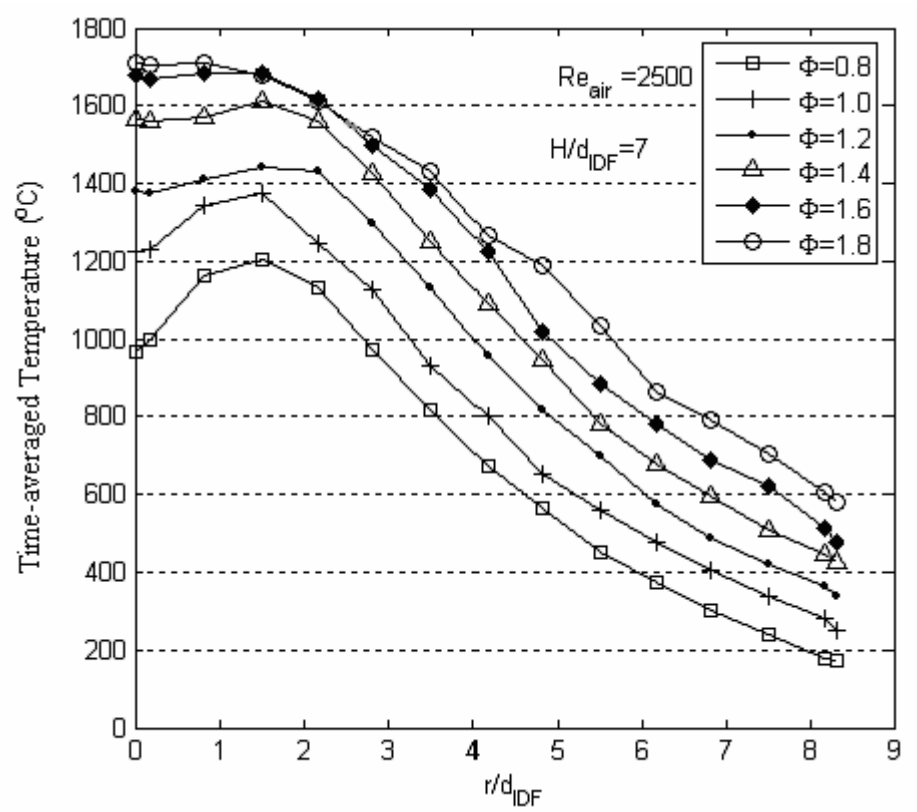

Figure 5.2.19. Radial temperature profiles at different Φ for Re_{air}=2500 and H/d_{IDF}=7.

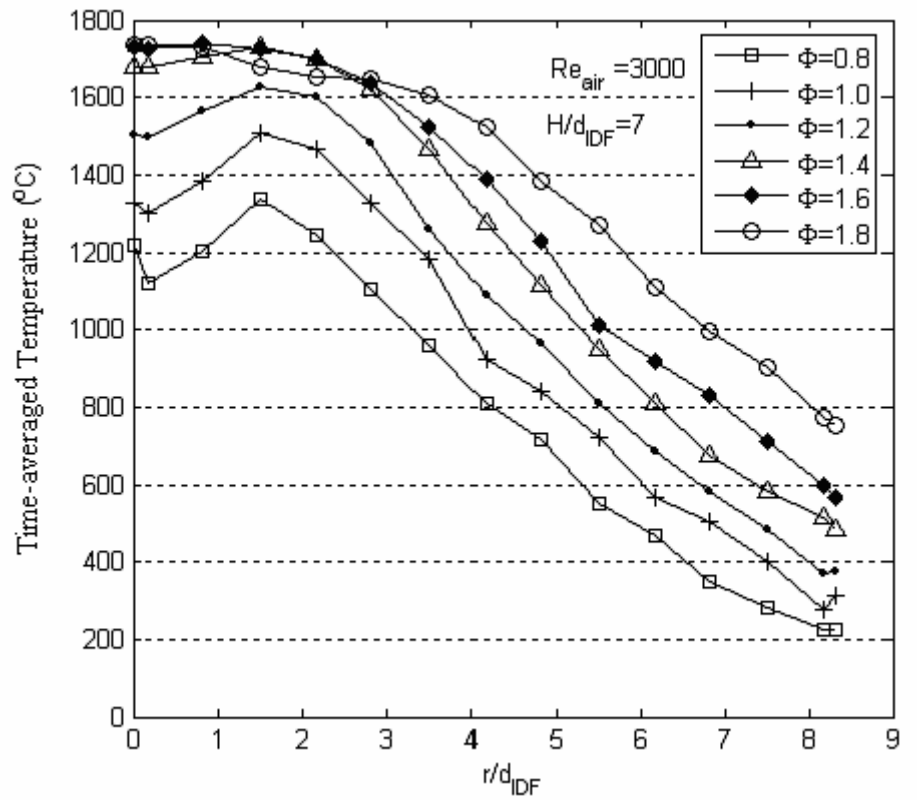

Figure 5.2.20. Radial temperature profiles at different Φ for Re_{air}=3000 and H/d_{IDF}=7.

5.2.2 Heat Flux

The heat fluxes measured in the experiments were the total heat flux induced by convection and radiation. Both stagnation point and radial heat flux distributions were measured at the same operating conditions and measuring locations for the temperature measurement.

This section is divided into 2 parts: the heat flux distribution at the stagnation point and the heat flux distribution from the centerline along the wall jet region. Again, the effects of the H/d_{IDF}, Re_{air} and Φ are examined on the stagnation point and radial heat flux distribution.

(a) Stagnation Point Heat Flux Distributions

The local heat flux is affected by the upstream combustion conditions. For this reason, the stagnation point heat flux was measured for different nozzle-to-plate distance to identify the effective range of it for further investigation. The results for the IDF for Re_{air}=1500, 2000, 2500 and 3000 with different Φ and H/d_{IDF} are shown in *Figure 5.2.21 – Figure 5.2.24*, respectively. The stagnation point heat flux was measured from H/d_{IDF}=2 to H/d_{IDF}=16 at 6 mm interval.

The results obtained for each Re_{air} are similar. With Φ increasing from 0.8 – 2.4, there is an increasing amount of fuel burn in the flame. There is also an increase in flame length of the corresponding open flame, as shown in *Figure 4.1.2* to *Figure 4.1.5*.

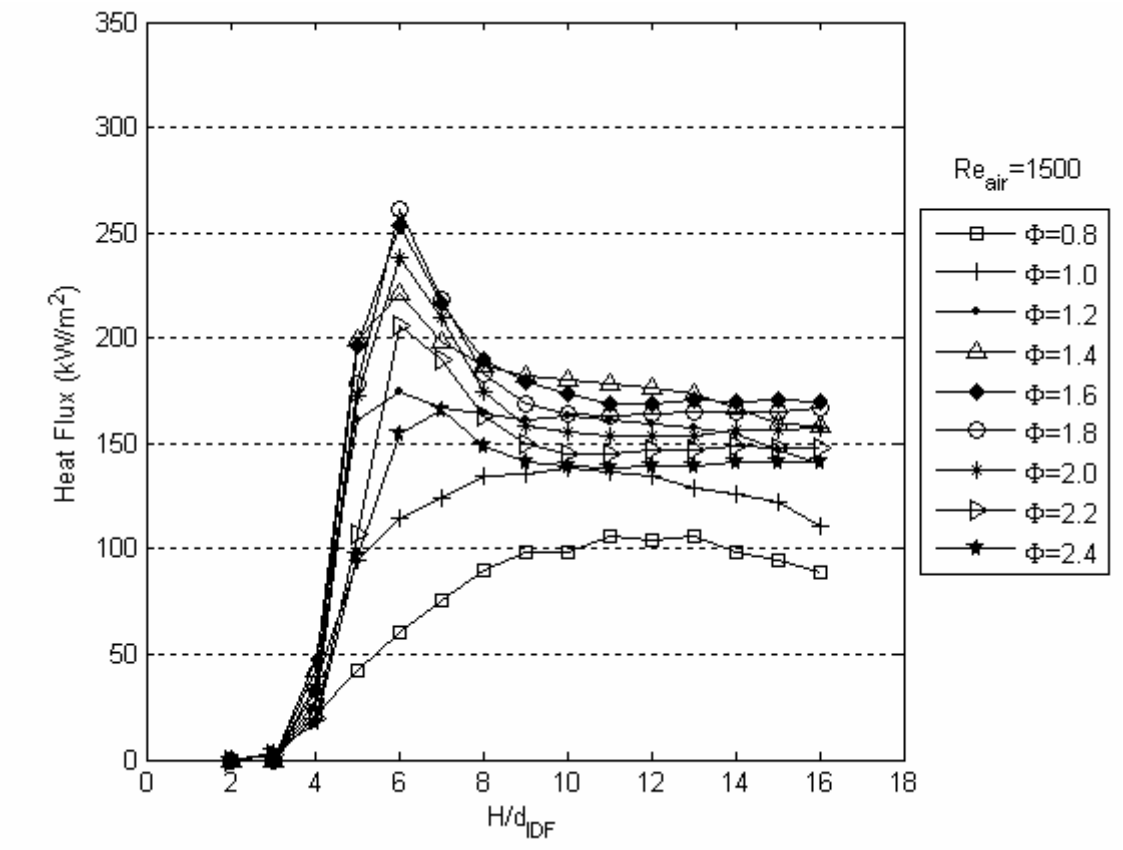

Figure 5.2.21. Stagnation point heat flux profiles at different Φ for Re_{air}=1500.

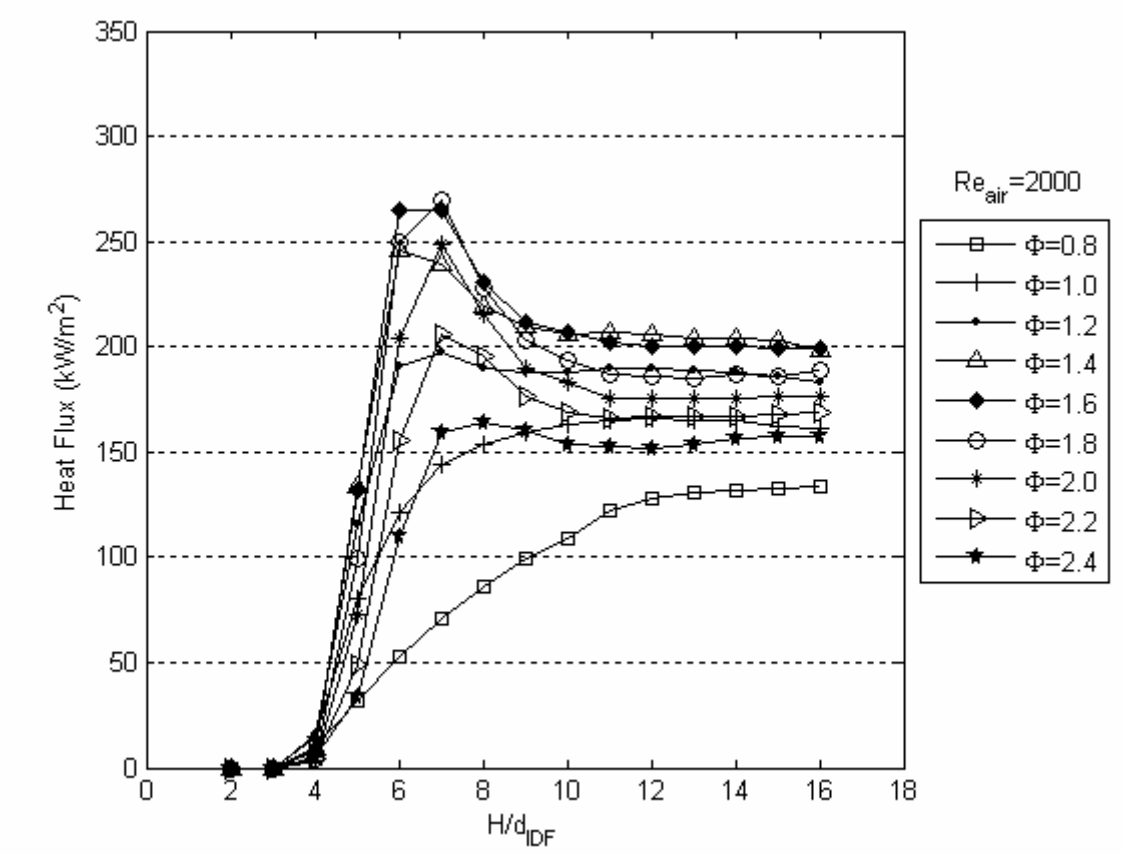

Figure 5.2.22. Stagnation point heat flux profiles at different Φ for Re_{air}=2000.

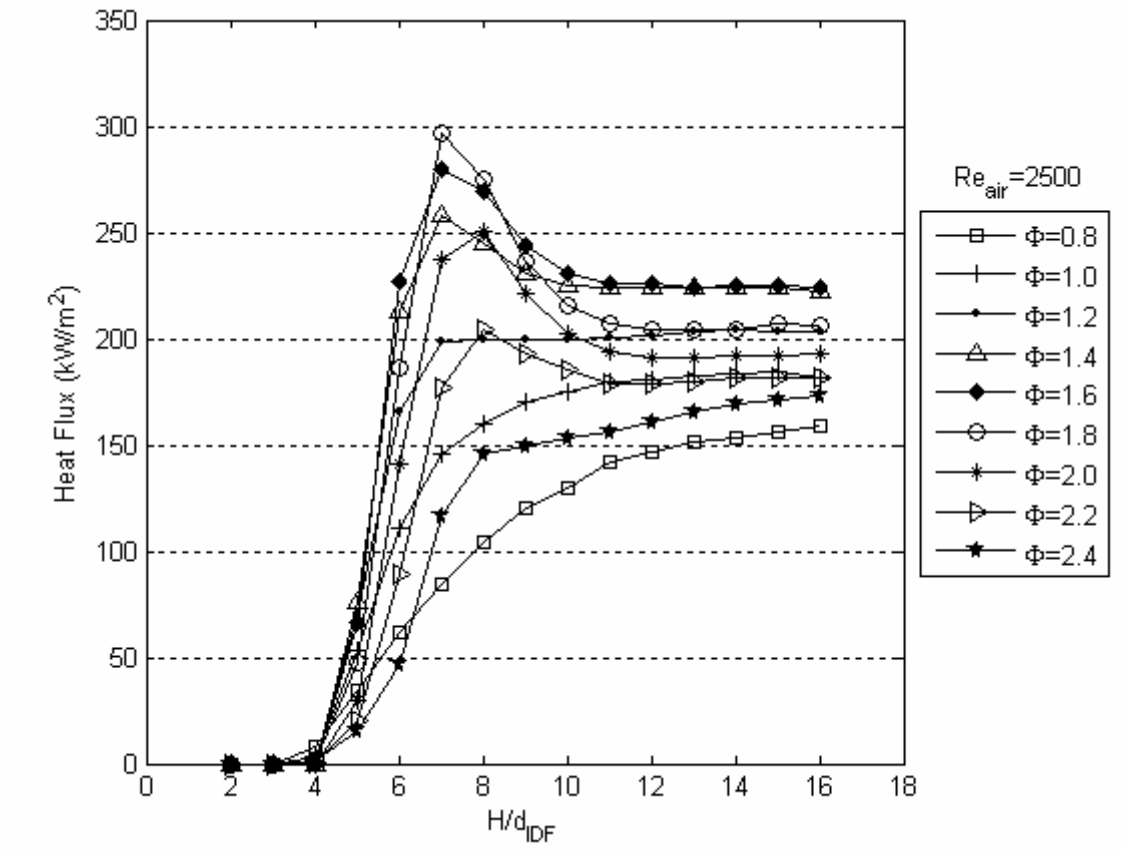

Figure 5.2.23. Stagnation point heat flux profiles at different Φ for Re_{air}=2500.

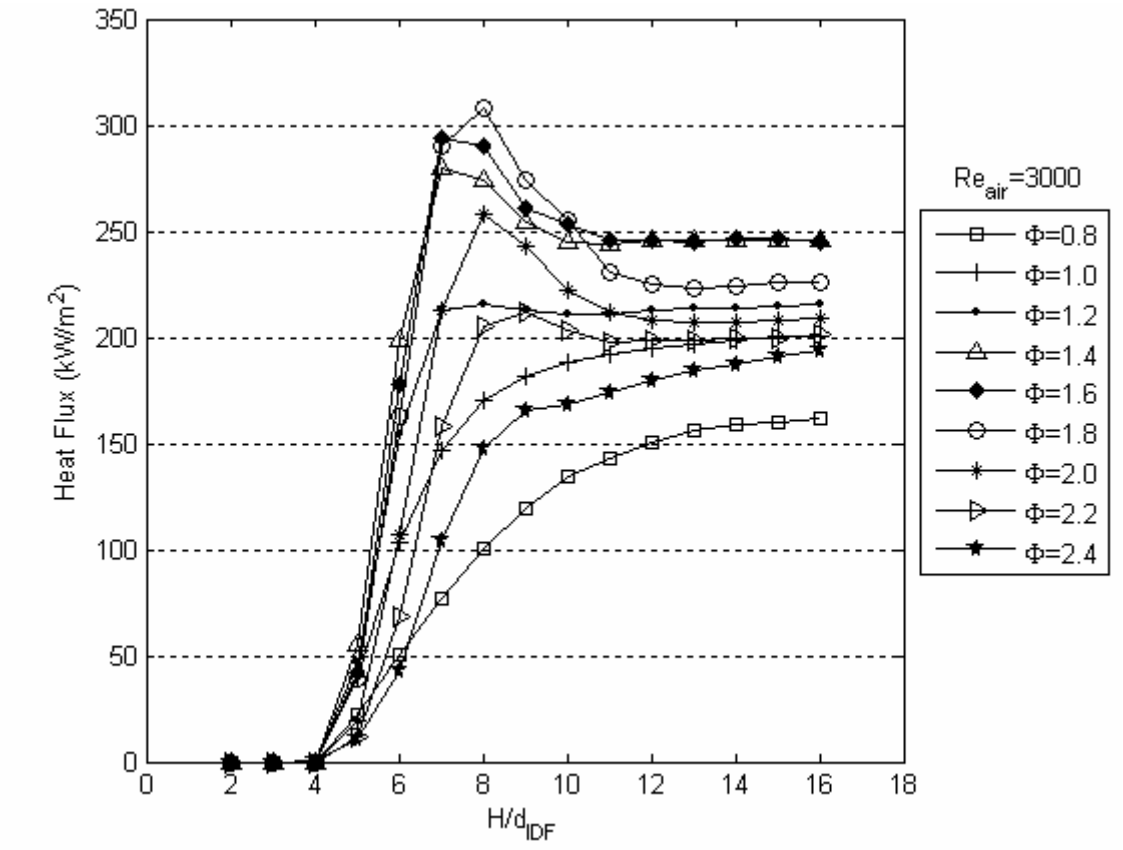

Figure 5.2.24. Stagnation point heat flux profiles at different Φ for Re_{air}=3000.

Figure 5.2.21 to Figure 5.2.24 show that the stagnation point profiles can be divided into three groups at each value of the Re_{air}. The first group corresponds to Φ=0.8-1.0; the second group for Φ=1.2-1.8 and the third group for $\Phi>1.8$. For the first group, the stagnation point heat flux increases as H/d_{IDF} is increased. For the second group, the stagnation point heat flux increases to a peak value and then drops to a lower, steady value as H/d_{IDF} is increased. The peak heat flux is higher at higher Φ, and occurs at lower H/d_{IDF}. For the third group, the stagnation point heat flux also increases to a peak value and then drops to a lower, steady value as H/d_{IDF} is increased. However, the peak heat flux is lower at higher Φ, and occurs at higher H/d_{IDF}. For the last two groups, the peak flux occurs in the range of H/d_{IDF}=5-8 while the steady values occur at about H/d_{IDF}=10. These results are similar to those reported in [2].

The results can be explained with reference to the flames shown in *Figure 5.1.2* to *Figure 5.1.5* for Re_{air}=1500, 2000, 2500 and 3000, respectively. At Φ=0.8, the visible flame is not touching the plate at H/d_{IDF}=7. The central air jet draws in the fuel to burn along the periphery of the air jet. The air jet in this case is penetrating through the flame and thus causes a cool core effect. If the plate is at a small distance from the nozzle, the stagnation point will be struck by the cool air, giving a low stagnation point heat flux. However, the influence of the air jet decreases while the influence of the hot gas increases as the nozzle-to-plate distance is increased, which leading to increase stagnation point heat flux as H/d_{IDF} is increased. The stagnation point heat flux at Φ=0.8 increases to a maximum value at H/d_{IDF} of around 13 and remains rather constant thereafter. The situation is almost the same for Φ=1.0 except that the stagnation point heat

flux is higher than the case of Φ=0.8 because more fuel is burned, and it increases to a peak value at about H/d_{IDF}=11 and remains rather constant thereafter.

For flames of Φ=1.2 to 2.4, the fuel jets are entrained by the air jet and burn to form a bright premixed flame overlapped with a diffusion flame at sufficiently high level of Φ. However, this entrainment weakens at higher level of Φ when the fuel jet velocity becomes higher. The visible flame impinges on and spreads along the plate. Each flame consists of a premixed combustion zone enclosing a cool zone of air. The premixed combustion zone extends in height with an increase in Φ due to the weakened entrainment effect. Thus the tip of the premixed combustion zone reaches the impingement plate at higher H/d_{IDF} as Φ is increased and finally the cool core starts to impinge on the plate at sufficiently high level of Φ. There are two mechanisms affecting the heat flux at the stagnation point. At lower level of Φ, more fuel is entrained into the premixed combustion zone as Φ is increased, creating higher flame temperature and thus increasing heat flux at the stagnation point. At higher level of Φ, further increase in Φ will reduce fuel entrained due to increased momentum of the fuel jets, causing a cooler premixed flame and decreasing heat flux at the stagnation point. In each case, the heat flux drops at higher H/d_{IDF} because the plate is at a higher position than the position of the tip of the premixed combustion zone. The steady heat flux region at H/d_{IDF} larger than 10 is due to the existence of a fairly constant temperature region beyond the premixed combustion zone of the IDF.

Figure 5.2.21 to *Figure 5.2.24* can also be divided into three zones based on the H/d_{IDF} values. At $H/d_{IDF} \leq 4$, the stagnation point heat flux is very low because it is in contact with the cool air, as reflected in the flames with H/d_{IDF} =3 and 4 in *Figure 5.1.6*. For H/d_{IDF} =5 to 10, the heat flux increases subsequently to a peak value and then drops to a steady state value. For H/d_{IDF} >10, the stagnation point remains rather steady on further increase to H/d_{IDF}=16, the largest H/d_{IDF} value being considered in this study.

Comparing with Figure 5.2.2 to Figure 5.2.5, the maximum stagnation point heat flux at any Φ occurs with the maximum stagnation point temperature correspondingly at the similar H/d_{IDF}. However, the stagnation point flame temperature decreases gradually after reaching the peak value, while the stagnation point heat flux drops obviously once after reaching the peak value. In other words, after the peak value, the heat transfer to the plate is limited even there is still a high flame temperature. The heat flux is affected by the gas temperature as well as other parameters, for example, the convective heat transfer coefficient. In such case, the drop in heat flux is due to the weakened convective heat transfer coefficient rather than the gas temperature.

(b) Radial Heat Flux Distributions

Base on the stagnation point heat flux investigations, radial heat flux profiles were measured at Φ=0.8-1.8 for H/d_{IDF}=4-10, at Re_{air}=2000. Further investigations were also carried out for Re_{air} of 1500 and 3000 at Φ=1.8 for H/d_{IDF} =5-8. The results are shown in Figure 5.2.55 to 5.2.34.

Figure 5.2.25 shows the radial heat flux profiles and the corresponding experimental uncertainties, for the case of Re_{air}=2000 and Φ=1.8, at seven different nozzle-to-plate distances corresponding to H/d_{IDF} of 4 to 10. The corresponding flame images are shown in *Figure 5.1.6*.

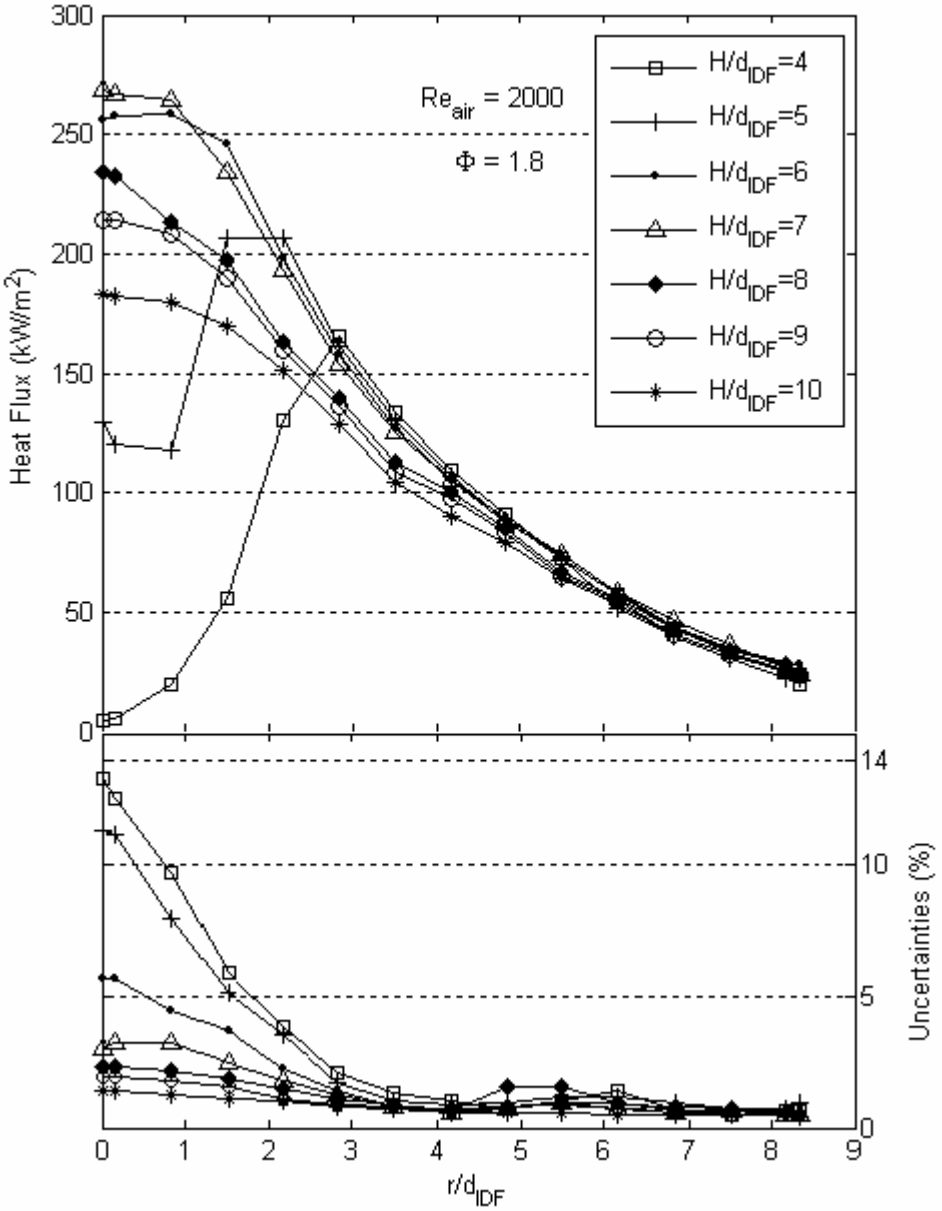

Figure 5.2.25. Radial heat flux profiles and uncertainties at different H/d_{IDF} for Re_{air}=2000 and Φ=1.8.

The radial heat flux profiles for H/d_{IDF}=4 and 5 has a peak value some distance away from the stagnation point. The heat flux is about 23 kW/m^2 and 118 kW/m^2 at r/d_{IDF}=1, but increases steeply to the maximum value of 163 kW/m^2 and 206 kW/m^2 at r/d_{IDF}=2, respectively. For this flame, the cool core impinges at the stagnation point while the bright premixed combustion zone impinges at about r/d_{IDF}=2, and the rest of the flame is forced to spread along the plate. The radial heat flux then drops once the peak value is reached because the flame is spreading radially outwards and becomes cooler and cooler. It is cooled on one side by the plate and on the other side by the ambient air, thus the heat transferred to the plate drops quickly.

When H/d_{IDF} is increased to 6 and 7, the stagnation point heat flux also increases. The peak flux occurs close to the stagnation point for H/d_{IDF}=6, and occurs at the stagnation point for H/d_{IDF}=7. This indicates that the bright premixed combustion zone is impinging close to the stagnation at H/d_{IDF}=6 and impinging at the stagnation point at H/d_{IDF}=7. The radial profiles are bell shaped in both cases.

At H/d_{IDF}=8, 9 and 10, the maximum heat flux also occurs at the stagnation point but the value is much lower than those at H/d_{IDF}=6 and 7, because the premixed combustion zone is at some distance below the impingement plate as the nozzle-to-plate distance is increased, and thus the stagnation point is impinged by the cooler combustion gases. The radial heat flux drops rapidly in the radial direction and its local radial heat flux in the wall jet region is even lower than that at H/d_{IDF}=5. It can be observed that the radial heat flux profile shifts downwards as H/d_{IDF} increasing from 8 to 10.

Thus, at H/d_{IDF} of 4 and 5, the nozzle-to-plate distance is too small for full development of the premixed combustion zone. Some unburned air and fuel would be forced to the wall jet region and further react in the wall jet region. When H/d_{IDF} is increased, there is sufficient space for the intense combustion to occur near to the center of the impingement plate. Consequently, local heat flux near the centerline increases and a bell-shaped profile would be obtained. If H/d_{IDF} is further increased, the wall jet region is reduced, indicating that the plate is heated by the combustion products from the reaction zone and the maximum radial heat flux is found at the stagnation point but the local heat flux is lower because of the cooler flame temperature along the radial profile.

It can be observed that under every considered flame operating conditions, the nozzle-to-plate distance for H/d_{IDF}=4 to 10 influences the radial heat flux profile mainly in the early wall jet region. Large experimental uncertainties are obtained at the centerline. The uncertainties become very high when H/d_{IDF} is decreased. At $r/d_{IDF} \geq 4$, the seven profiles for both heat flux and experimental uncertainties are close to each other.

Figure 5.2.26 to *Figure 5.2.28* show the radial heat flux distributions at lower overall equivalence ratios of 0.8, 1.0 and 1.2, respectively. Comparing with *Figure 5.2.25*, the lower the overall equivalence ratio, the lower the heat fluxes are obtained due to the lower fueling rate. Again, the heat flux distribution in the wall jet region is quite similar for the seven profiles.

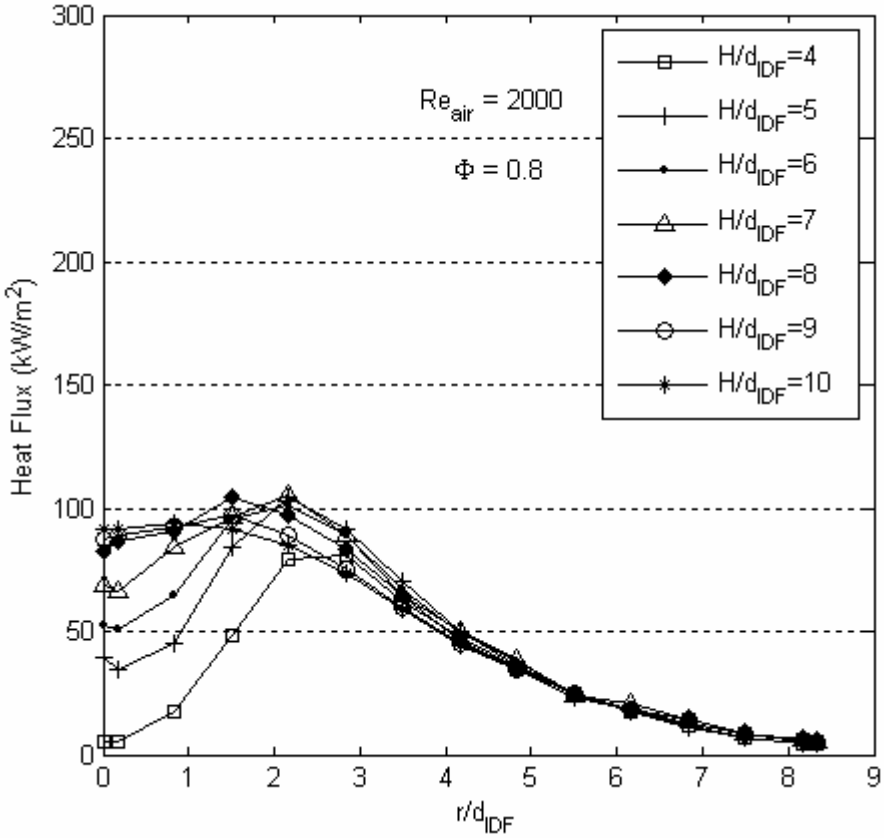

Figure 5.2.26. Radial heat flux profiles at different H/d_{IDF} for Re_{air}=2000 and Φ=0.8.

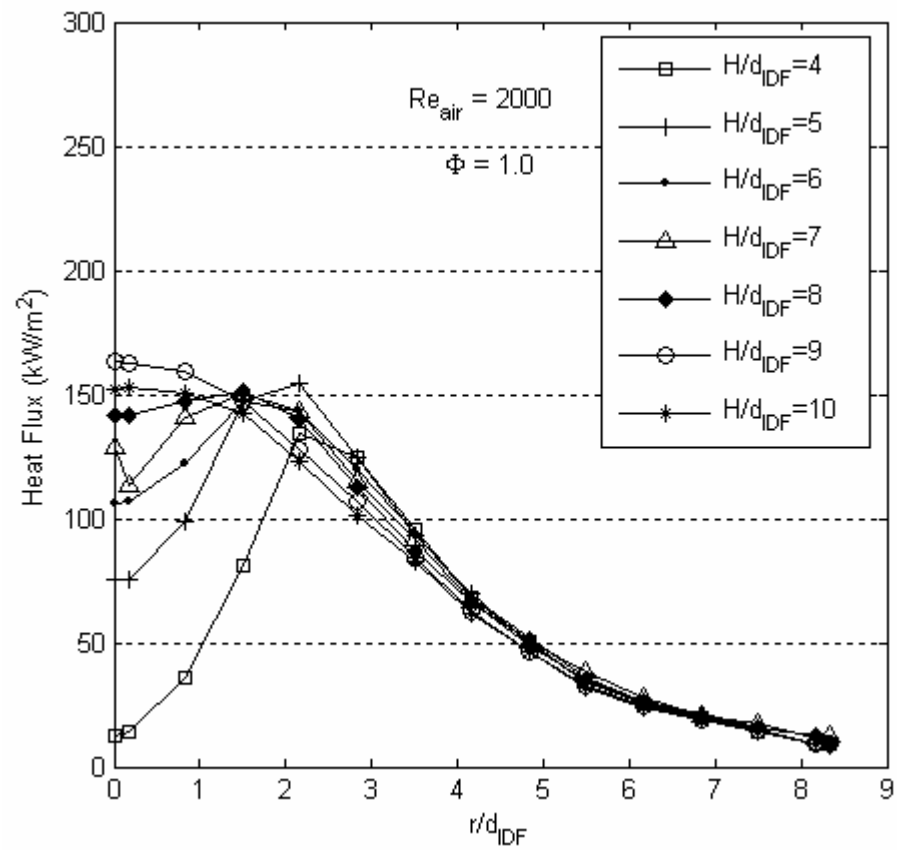

Figure 5.2.27. Radial heat flux profiles at different H/d_{IDF} for Re_{air}=2000 and Φ=1.0.

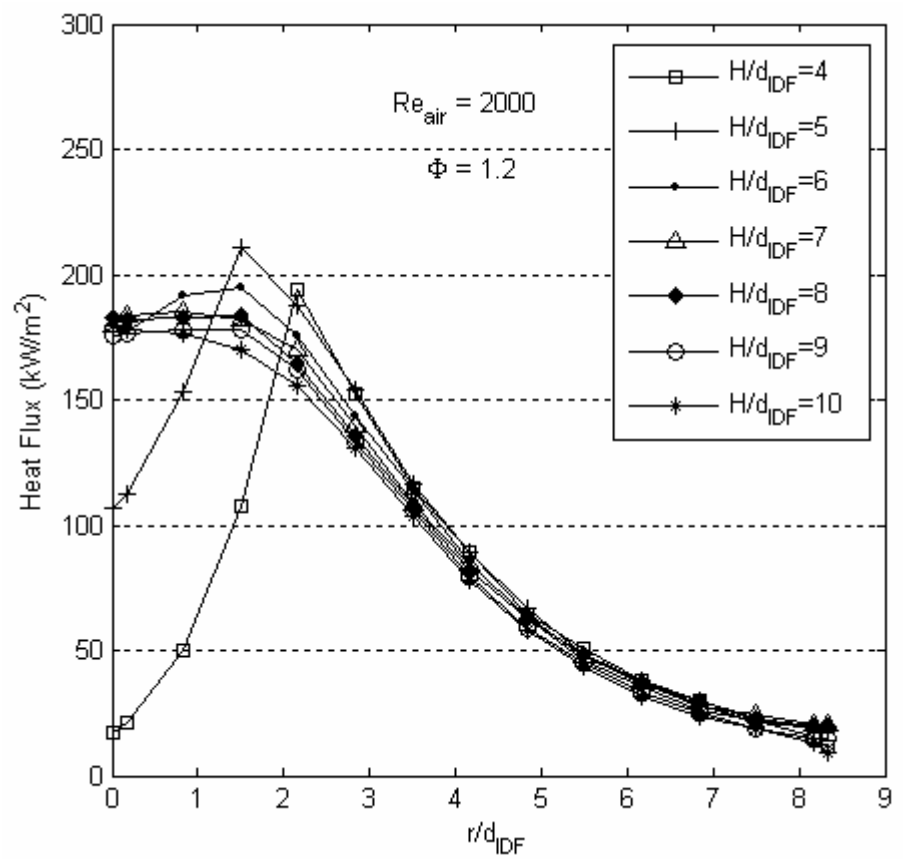

Figure 5.2.28. Radial heat flux profiles at different H/d_{IDF} for Re_{air}=2000 and Φ=1.2.

The effects of the overall equivalence ratio on the radial heat flux distribution are shown in *Figure 5.2.29* to *Figure 5.2.32* for H/d_{IDF}=4, 5, 7 and 10, respectively. The trends of the radial heat flux profiles correspond with those of the radial flame temperature profiles (see *Figure 5.2.10-Figure 5.2.13*).

Figure 5.2.29 shows that the cool core effect is very significant at H/d_{IDF}=4. It occurs for Φ=0.8-1.8. The cool core effect diminishes gradually at higher level of H/d_{IDF}. In Figure 5.2.29 (H/d_{IDF}=4) and Figure 5.2.30 (H/d_{IDF}=5), the cool core effect is observed for all the flames in the range of Φ=0.8-1.8. In Figure 5.2.31 (H/d_{IDF}=7), the cool core effect is observed in flame with low level of Φ. In Figure

5.2.32 (H/d_{IDF}=10), the cool core effect is not observable. In Figure 5.2.31, at H/d_{IDF}=7, the peak heat flux occurs at Φ=1.8 at the centerline, indicating that in the flame with Re_{air}=2000 and Φ=1.8, the tip of the partially premixed combustion zone touched the plate at H/d_{IDF}=7; thus, in Figure 5.2.32, with a higher H/d_{IDF} of 10, the plate is impinged by combustion products and the six heat flux profiles shift downwards compared to those at H/d_{IDF}=7.

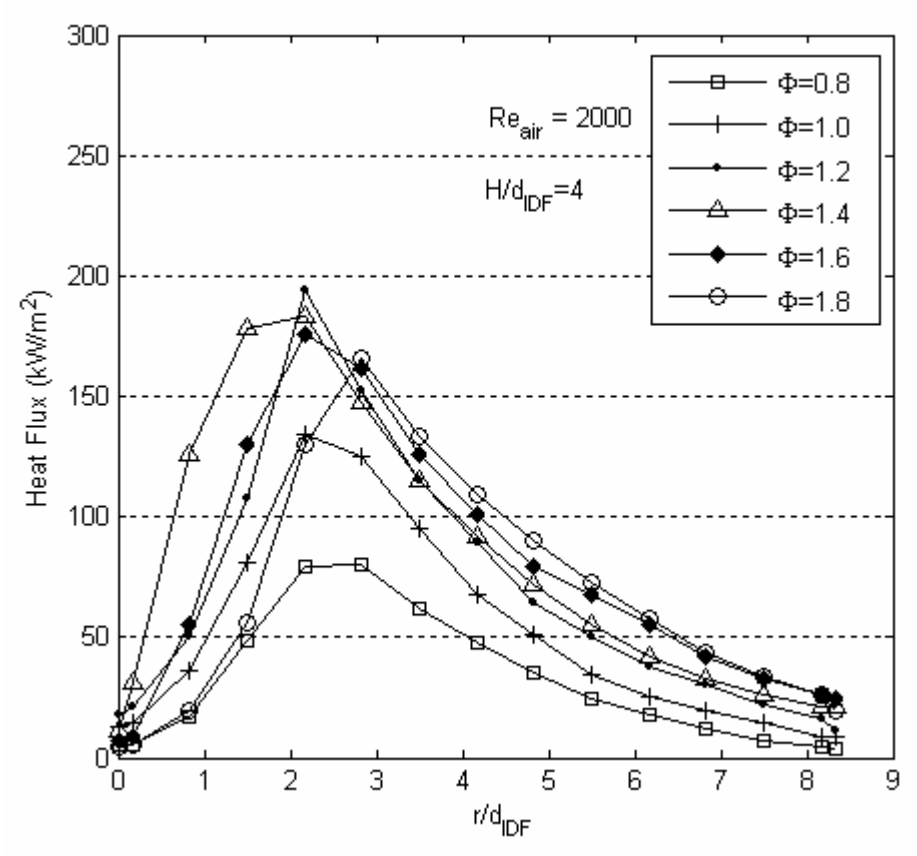

Figure 5.2.29. Radial heat flux profiles at different Φ for Re_{air}=2000 and H/d_{IDF}=4.

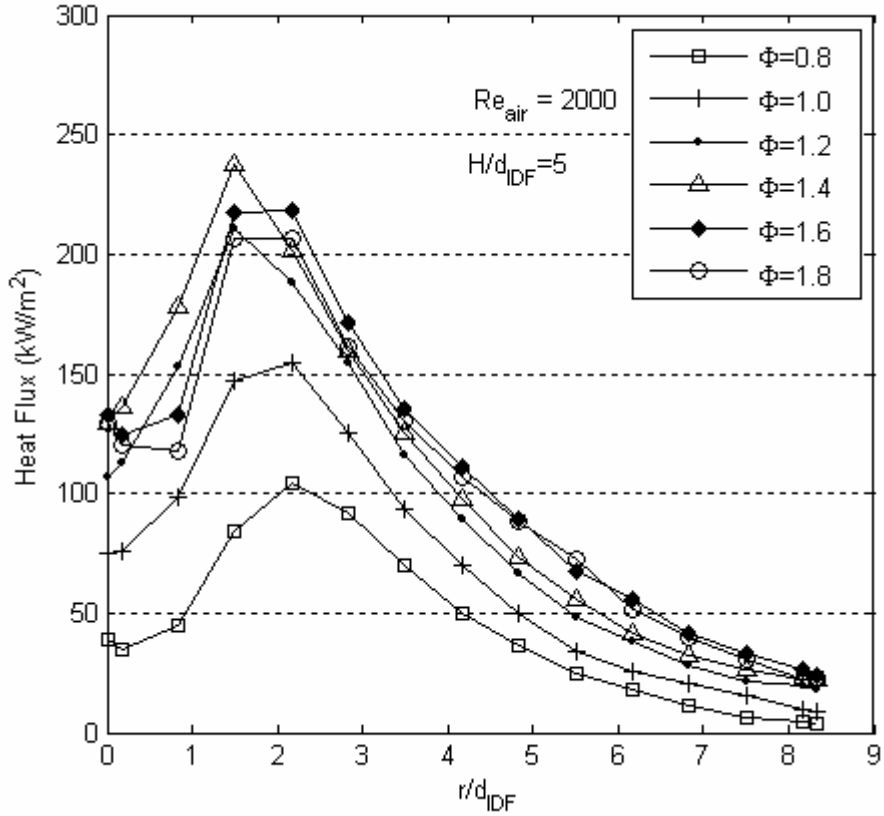

Figure 5.2.30. Radial heat flux profiles at different Φ for Re_{air}=2000 and H/d_{IDF}=5.

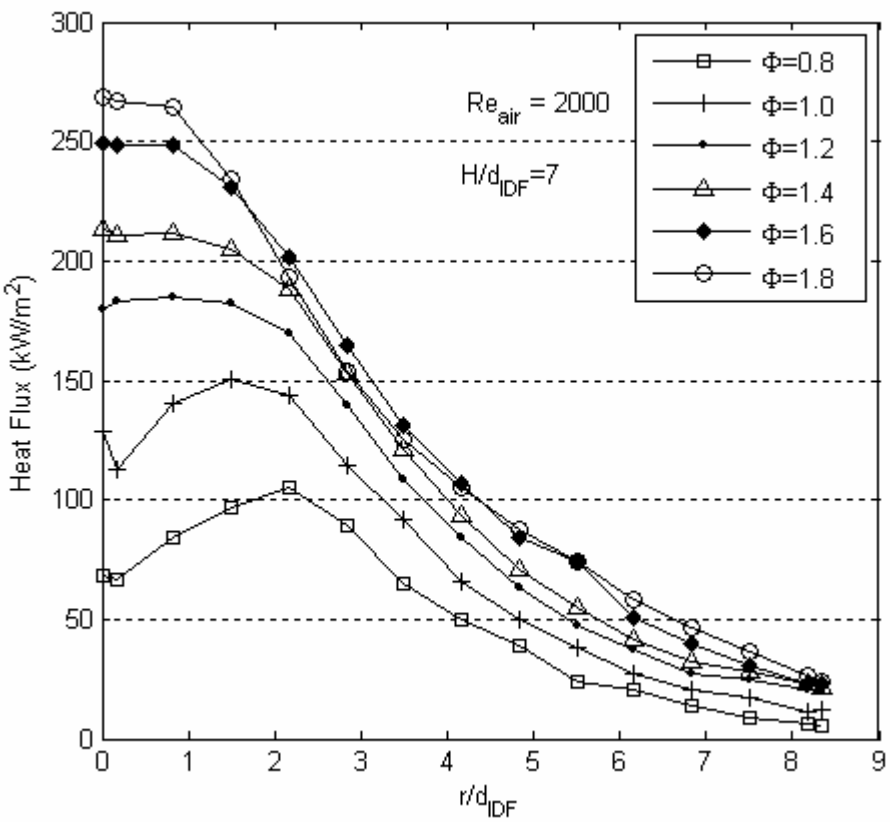

Figure 5.2.31. Radial heat flux profiles at different Φ for Re_{air}=2000 and H/d_{IDF}=7.

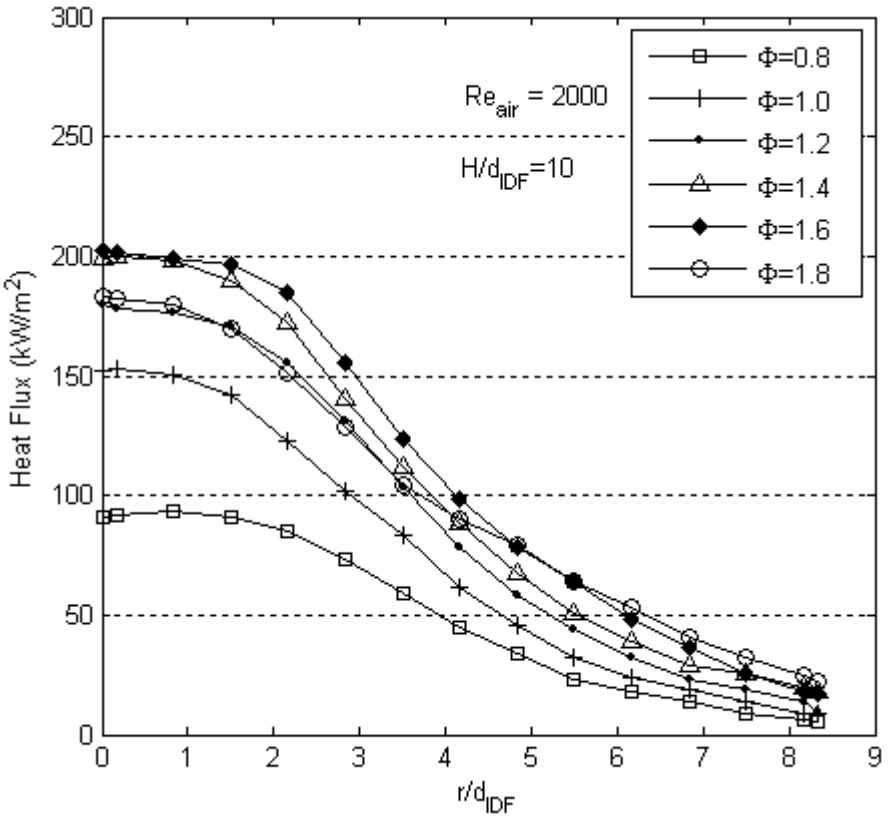

Figure 5.2.32. Radial heat flux profiles at different Φ for Re_{air}=2000 and H/d_{IDF}=10.

Figure 5.2.33 and *Figure 5.2.34* show the radial heat flux distributions at a lower and higher Re_{air} of 1500 and 3000 at Φ=1.8. The corresponding results at Re_{air}=2000 are shown in Figure 5.2.25. With the same Φ, an increase in Re_{air} implies increase in both the air flow rate and the fuelling rate. Thus the flames associated with Re_{air} of 1500 are shorter and less intense. In such case, the cooler core effective is not obvious and the heat fluxes are lower. On the contrary, the heat fluxes are higher due to the higher fueling rate supplied at Re_{air}=3000, and the cool core effect is also obvious. Again, the heat flux distributions in the wall jet region are quite similar for the four profiles at different Re_{air}.

From the above comparisons, it can be concluded that Re_{air} and Φ will affect the fueling rate and thus the level of heat flux. In the stagnation point region, the heat flux distributions are affected by Re_{air} and Φ, as well as the nozzle-to-plate distance. However in the wall jet region, the heat flux distributions are affected by Re_{air} and Φ, but only slightly by the nozzle-to-plate distance.

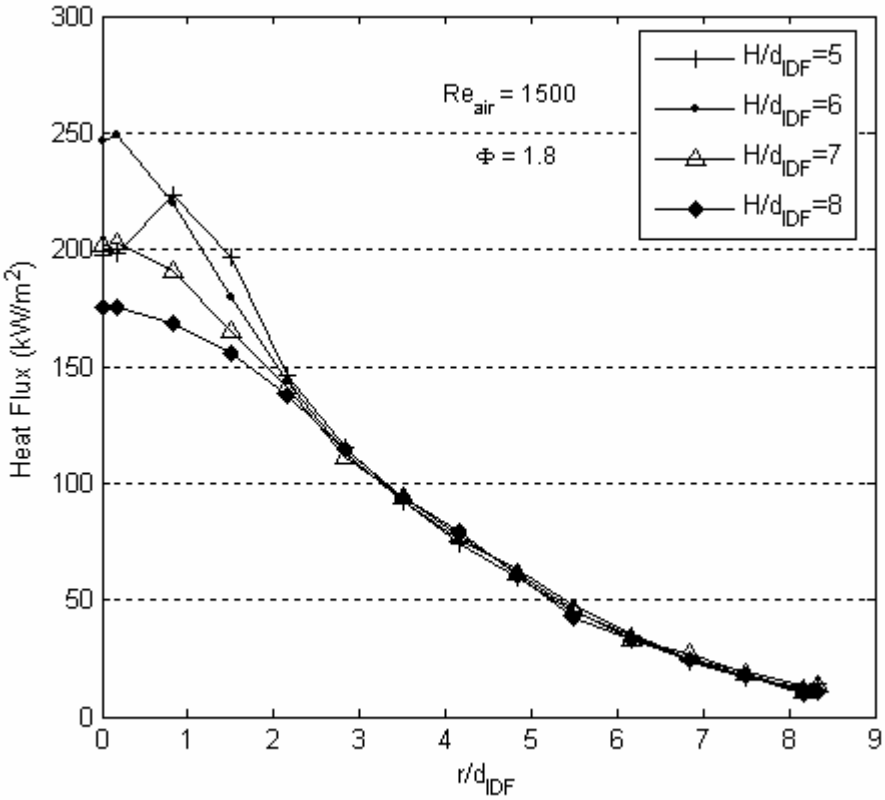

Figure 5.2.33. Radial heat flux profiles at different H/d_{IDF} for Re_{air}=1500 and Φ=1.8.

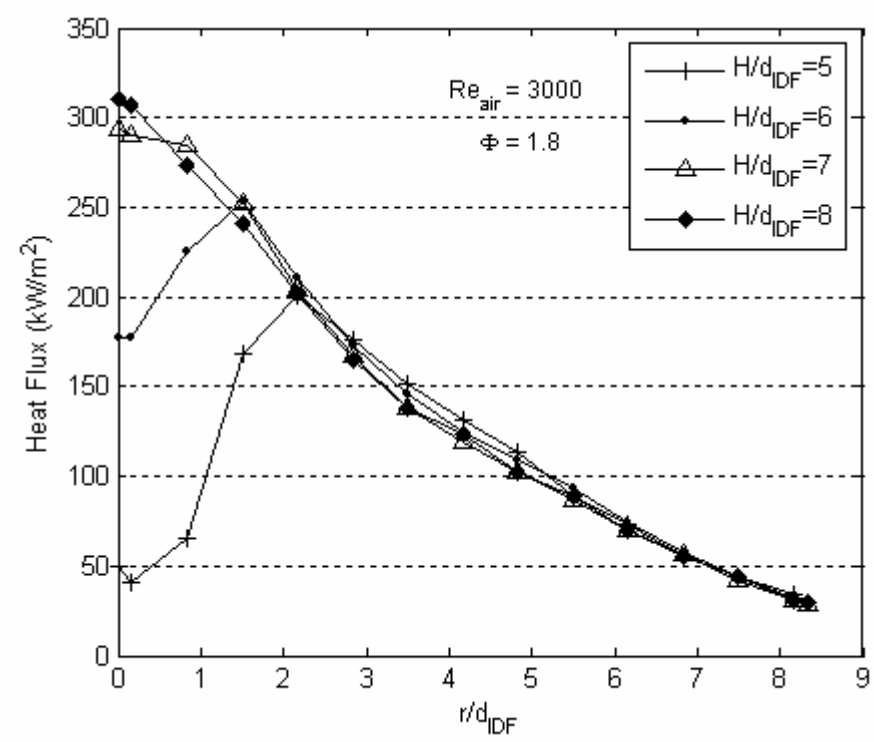

Figure 5.2.34. Radial heat flux profiles at different H/d_{IDF} for Re_{air}=3000 and Φ=1.8.

5.2.3 Combustion Species Concentration

The concentration of the combustion species, including O_2, CO_2, CO, NO and HC were measured for further investigation with the radial heat flux distribution and the radial flame temperature, using the test rig in *Figure.3.1.3*. Combustion species were sampled through a tap with 1.5 mm diameter at the center of the impingement plate. A flue-gas analyzer (Anapol EU-5000) was used for measuring the species concentrations. The O_2, CO_2, and CO concentrations were measured in percentage (%) and the NO and HC concentration were in parts per million (ppm).

Experiments were conducted for Re_{air} of 2000 and Re_{air} of 3000, and for each Re_{air}, measurements were carried out at H/d_{IDE} of 5, 7 and 10. In each case, the overall equivalence ratio of the flame was varied from 0.8 to 1.8. The results are shown in Figures 5.2.35 to 5.2.43 for Re_{air} of 2000; and in *Figures 5.2.44* to 5.2.52 for Re_{air} of 3000.

The radial concentration profiles of the combustion species at H/d_{IDF}=5,7 and 10 are similar in shape for Re_{air} 2000 and Re_{air} of 3000. In this section, we will look into the results of Re_{air}=2000, and discuss on the effects of the Φ and H/d_{IDF} on the distributions of the combustion species. There will then be a comparison with the results obtained at Re_{air}=3000 to analyze the effect of Re_{air}.

(a) Combustion Species Concentration, Re_{air}=2000

Figure 5.2.35 to *Figure 5.2.37* show the radial concentration profiles of O_2 and CO_2 at H/d_{IDF}=5, 7 and 10, respectively. In the Figures, it can be observed that with increase in Φ, the O_2 profiles shift downwards while the CO_2 profiles shift upwards. This is because at higher values of Φ, as more fuel is supplied to the flame, more O_2 will be consumed, leading to the increase in the CO_2 concentration. At H/d_{IDF} of 5, for each O_2 concentration profile, there is a drop in O_2 concentration in the stagnation region and then an increase in concentration in the wall jet region. Thus the combustion intensifies in the stagnation region but in the wall jet region, there is a gradual dilution of the combustion products by ambient air. The opposite effect occurs to the CO_2 profiles. At H/d_{IDF} of 10, the initial drop of O_2 concentration disappears except for the case of Φ=1.8; there is a continuous increase of O_2 concentration for each profile.

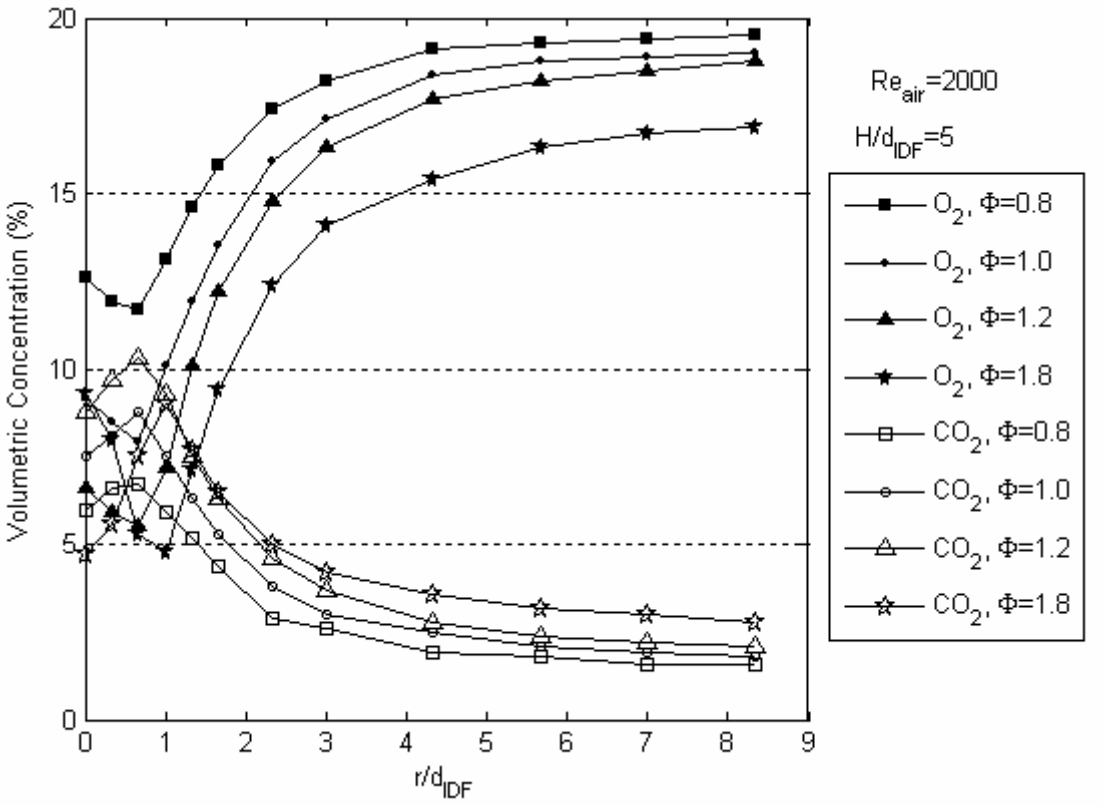

Figure 5.2.35. Distributions of the concentrations of O_2 and CO_2 under different Φ at Re_{air}=2000 and H/d_{IDF} =5.

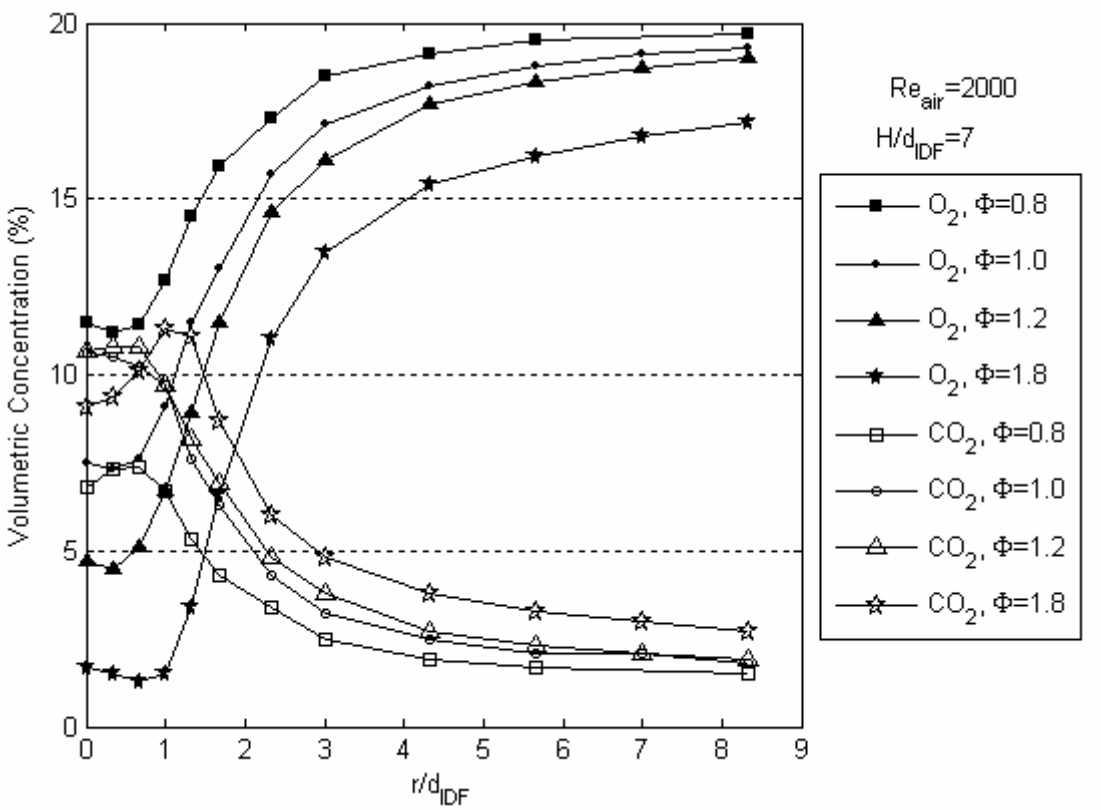

Figure 5.2.36. Distributions of the concentrations of O_2 and CO_2 under different Φ at Re_{air}=2000 and H/d_{IDF} =7.

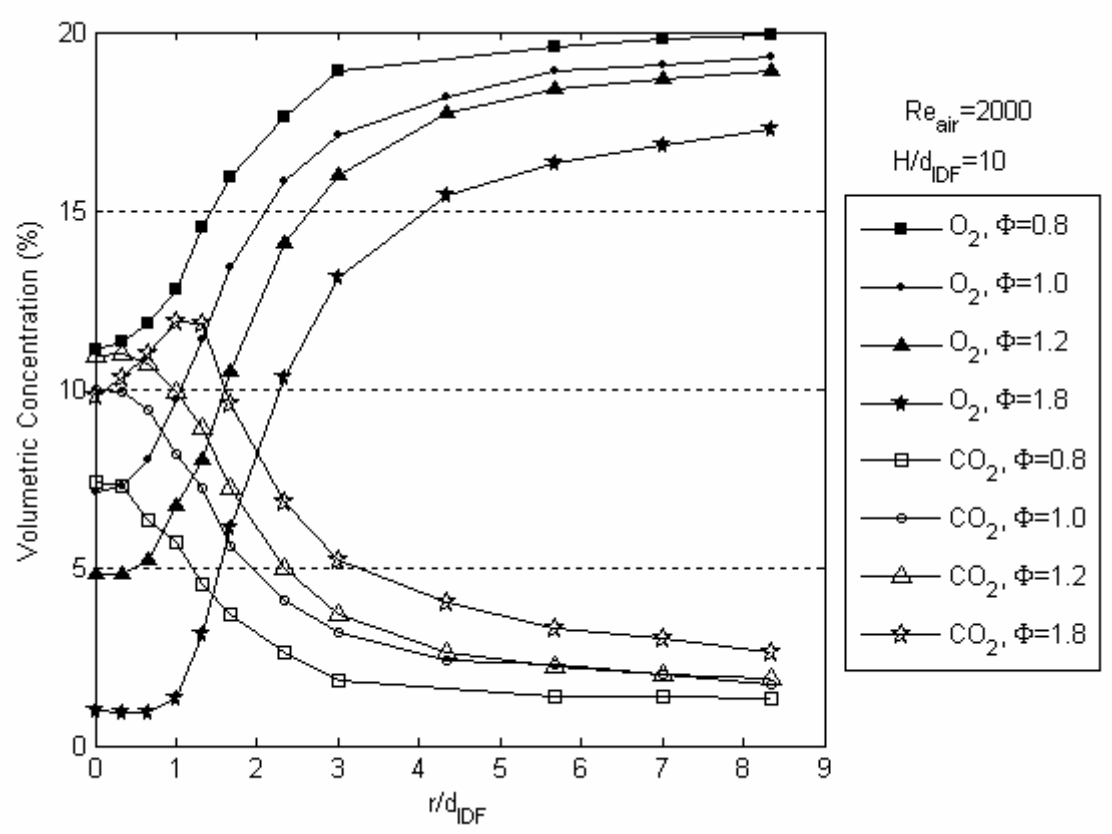

Figure 5.2.37. Distributions of the concentrations of O_2 and CO_2 under different Φ at Re_{air}=2000 and H/d_{IDF} =10.

In *Figure 5.2.35* (H/d_{IDF}=5), the CO_2 concentrations are lower at the centerline, they increase gradually to peak values at r/d_{IDF}=0.7 for Φ=0.8–1.2, and at r/d_{IDF}=1 for Φ=1.8. Beyond these locations, the CO_2 profiles decrease exponentially. The contrary trends are found for the O_2 profiles. Comparing with the radial heat flux distributions shown in Figure 5.2.30, the radial heat flux profiles of the corresponding Φ increase from the centerline to peak values at around r/d_{IDF}=2 and then decrease also exponentially subsequently. The O_2 concentration profiles indicate that intense combustion occurs at r/d_{IDF}=0.7 for Φ=0.8 – 1.2 and at r/d_{IDF}=1 for Φ=0.8. The peak flux appears in the downstream of the most intense combustion region.

When H/d_{IDF}=7 (see *Figure 5.2.36*), the lowest O_2 concentrations occur at r/d_{IDF}=0.3 for Φ=0.8–1.2 and r/d_{IDF}=0.7 for Φ=1.8. The location of intense combustion appears to shift towards the centerline as H/d_{IDF} increases. Referring to the corresponding radial heat flux distributions (*Figure 5.2.31*), the maximum heat flux occurs at r/d_{IDF} of 2, 1.5, 0.8 and 0.8 respectively for Φ of 0.8, 1.0, 1.2 and 1.8. When H/d_{IDF} is further increased to 10, the lowest O_2 concentrations are found at the centerline, while the maximum heat fluxes also occur at the stagnation point.

Therefore, it can be concluded that both Φ and H/d_{IDF} influence the heat transfer mainly at the stagnation region. At lower value of H/d_{IDF}, the maximum heat flux occurs at the downstream of the intense combustion region, which may due to the effect of the cool core. The heat generated by the intense combustion is cooled down by the cool core at the upstream. When H/d_{IDF} increases, the effect of the cool core decreases. Therefore, the intense combustion region and the maximum heat flux occur at the same location.

Figure 5.2.38 – Figure 5.2.40 show the CO concentrations with different Φ at H/d_{IDF}=5, 7 and 10, respectively. It is observed that the CO concentration increases when Φ is increased, which is due to the increase in the fuelling rate at a fixed air flow rate. The CO concentration at Φ=1.8 is especially high and the CO concentration profiles at Φ=0.8, 1.0 and 1.2 decrease with increase of H/d_{IDF}. It is because at Φ=1.8, the combustion is fuel rich as there is insufficient air supplied from the central air jet and from the entrained atmospheric air to support complete combustion. Also when the H/d_{IDF} is low, the plate impedes mixing of the air and

fuel, leading to a higher level of CO due to local rich combustion. At higher level of H/d_{IDF}, there is more headroom for mixing of the air and fuel, leading to lower level of CO due to leaner combustion conditions. In all cases, in the wall jet region, the CO formed during rich combustion is converted into CO_2. There is practically no CO beyond r/d_{IDF} of 7.

In *Figure 5.2.38* (H/d_{IDF}=5), the radial CO concentrations decrease from the stagnation point for Φ=0.8–1.2, while it increases from 4.3% to 4.8% at the centerline to r/d_{IDF}=0.7 for Φ=1.8. For Φ=0.8–1.2, the higher concentrations of CO at the stagnation are the result of incomplete combustion, while CO is converted into CO_2 in the early wall jet region. For Φ=1.8, as fuelling rate and fuel momentum both increase, there is reduced entrainment of the fuel towards the central air jet, resulting in poorer mixing of the air and fuel. Thus, more fuel accumulates at a small radial distance away from the stagnation point, leading to higher CO concentration upon combustion. The CO formed is also gradually converted into CO_2 in the wall jet region.

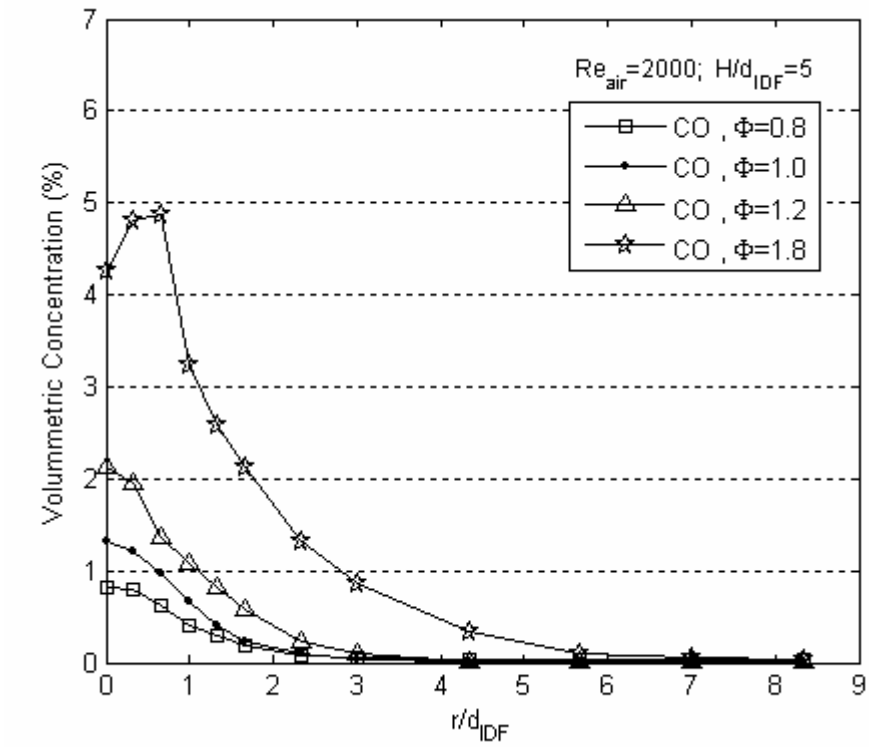

Figure 5.2.38. Distribution of the concentration of CO under different Φ at Re_{air}=2000 and H/d_{IDF} =5.

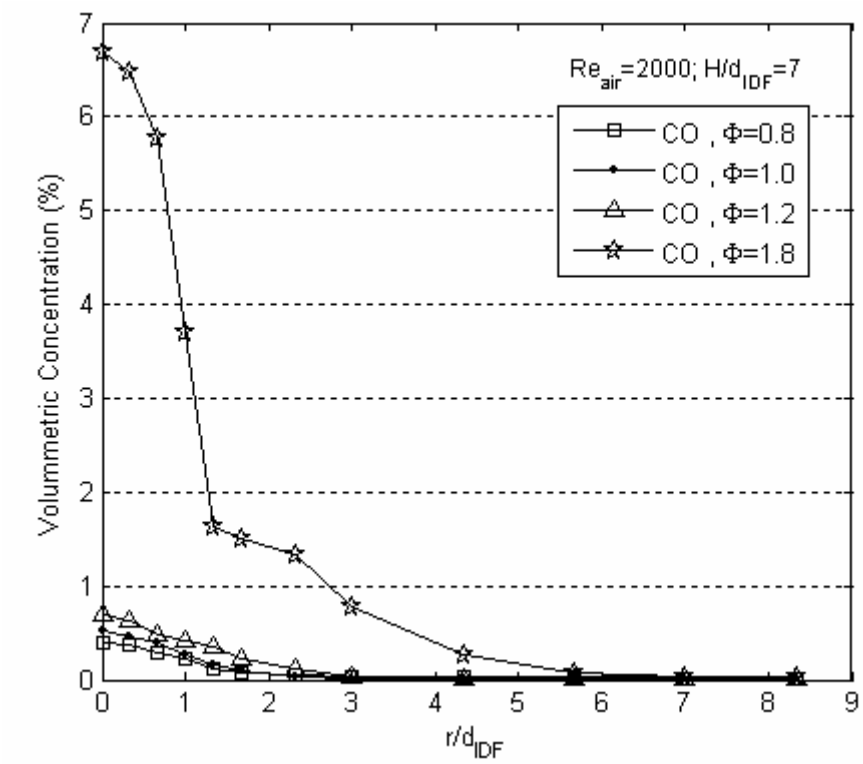

Figure 5.2.39. Distribution of the concentration of CO under different Φ at Re_{air}=2000 and H/d_{IDF} =7.

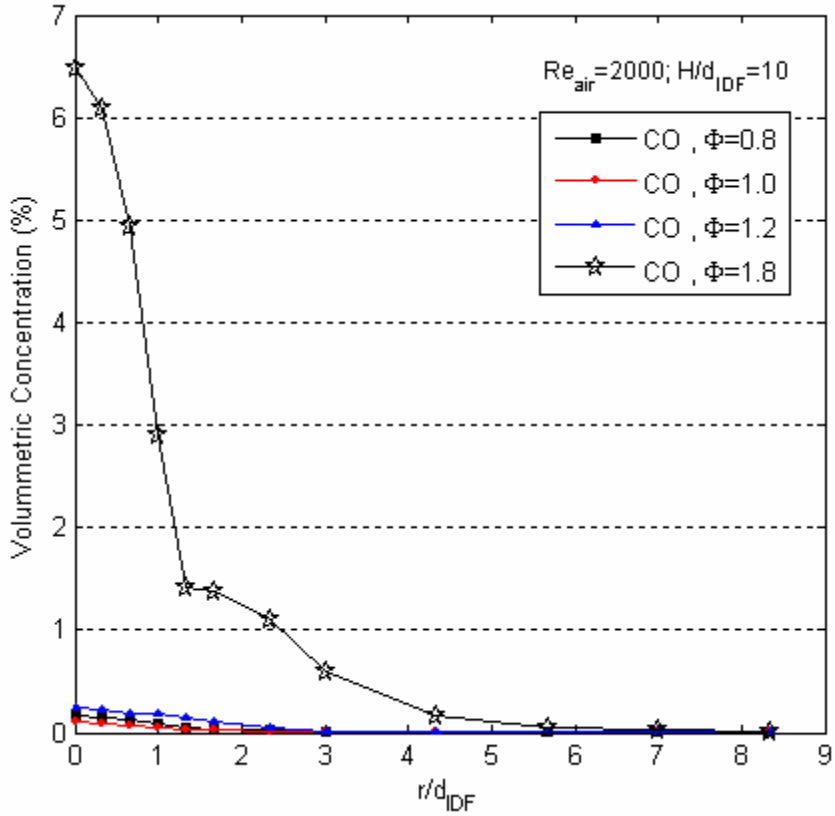

Figure 5.2.40. Distribution of the concentration of CO under different Φ at Re_{air}=2000 and H/d_{IDF} =10.

In *Figure 5.2.39* and *Figure 5.2.40*, the lower concentrations of CO profiles for Φ=0.8–1.2 are due to the more complete combustion as indicated by the lower O_2 concentration measured at the corresponding locations. It is the same reason for the decrease in CO concentration for Φ=1.8 when H/d_{IDF} increases from 7 to 10. The high CO concentration profiles at Φ=1.8, H/d_{IDF}=7, is due to rich combustion. In addition, the cold impingement plate may have the quenching effect, which also increases the CO emission [23].

The radial HC concentration distributions are shown in *Figure 5.2.41* to *Figure 5.2.43*.

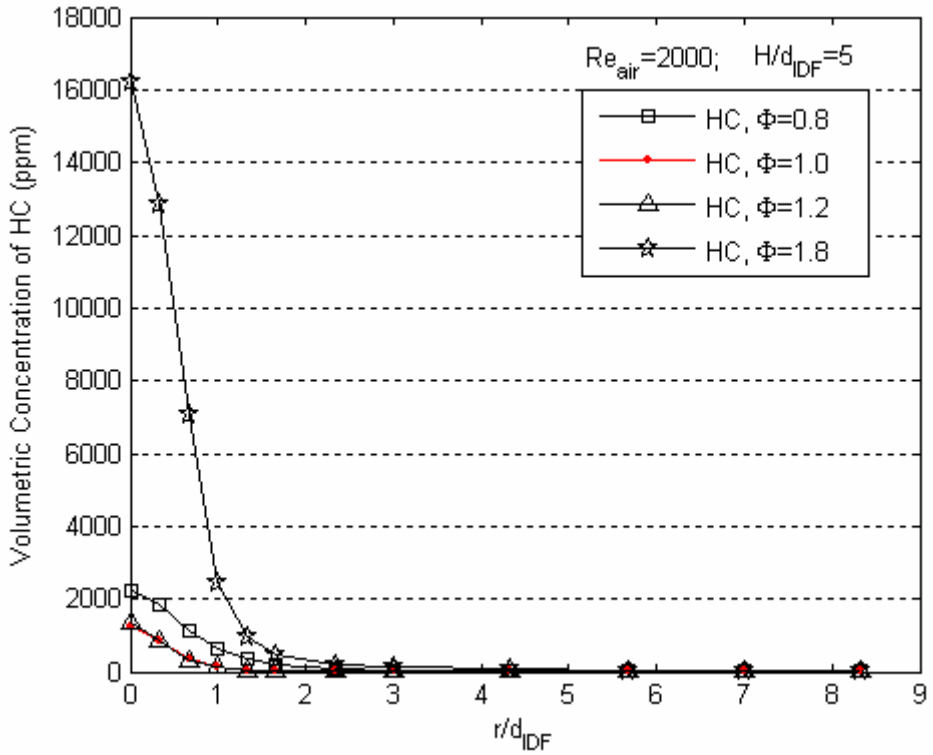

Figure 5.2.41. Distribution of the concentration of HC under different Φ at Re_{air}=2000 and H/d_{IDF} =5.

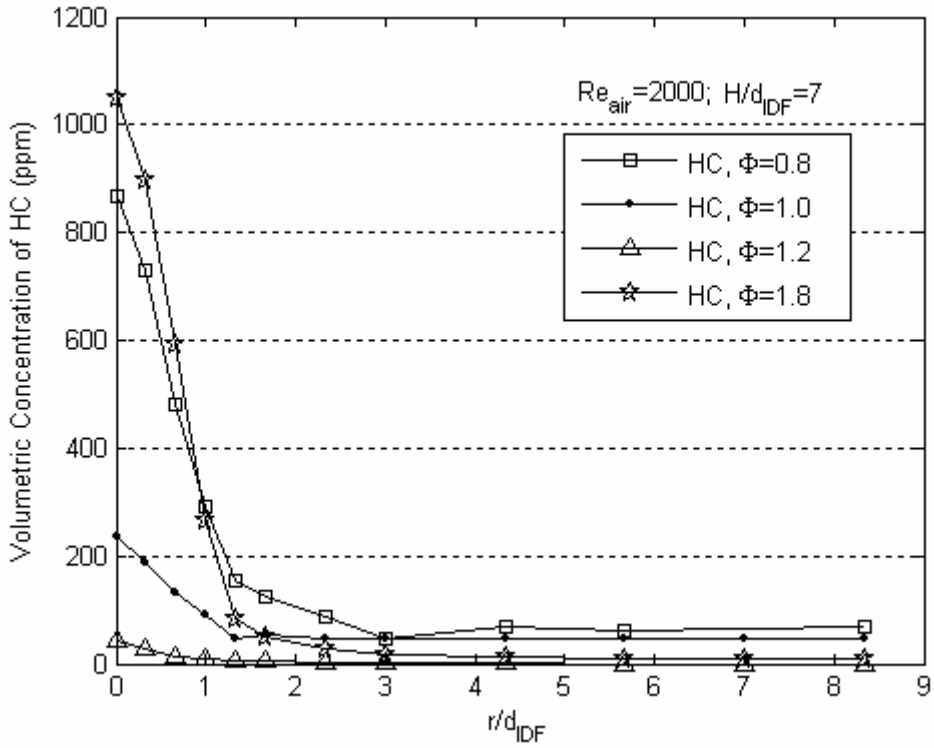

Figure 5.2.42. Distribution of the concentration of HC under different Φ at Re_{air}=2000 and H/d_{IDF} =7.

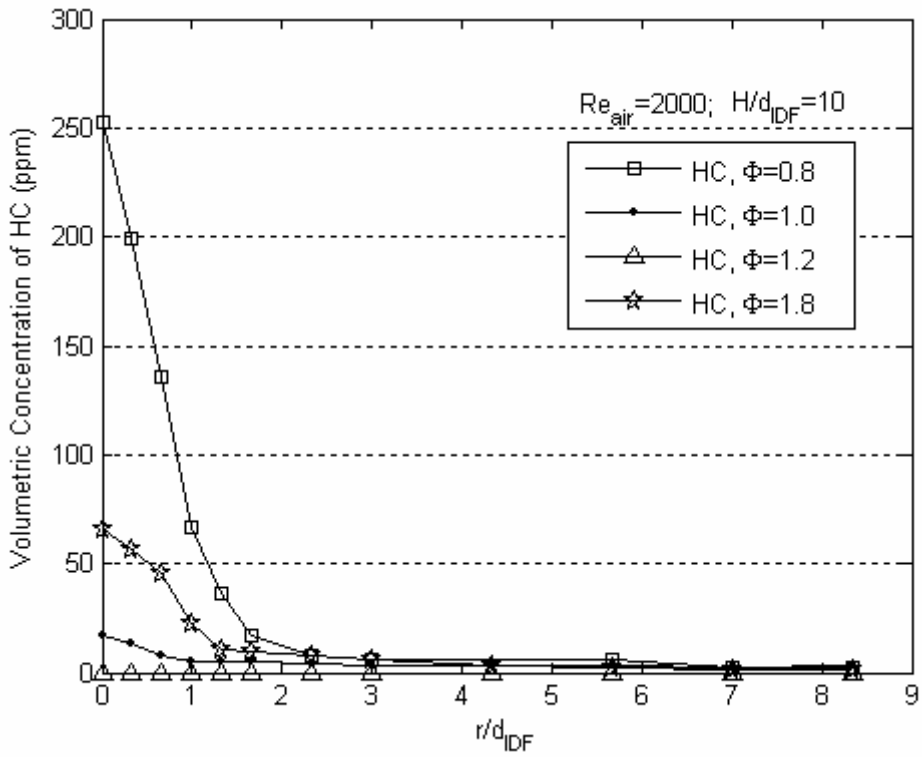

Figure 5.2.43. Distribution of the concentration of HC under different Φ at Re_{air}=2000 and H/d_{IDF} =10.

At H/d_{IDF}=5, very high HC concentration occurs at the stagnation point and a sharp decrease happens thereafter. The measured concentrations of HC at the stagnation point are 2200ppm, 1200ppm 1300ppm and 16000ppm for Φ=0.8, 1.0, 1.2 and 1.8, respectively. At r/d_{IDF}=2.3, the HC concentrations drop to 84ppm, 17ppm, 14ppm and 200ppm correspondingly. The relatively high concentration measured along the plate at Φ=0.8 is evident that the fuel is forced to impinge and spread along the plate by the air jet. Also, the flame at Φ=1.8 processes a very intense combustion under the region at r/d_{IDF}≤2.3. Since the fuel is too rich, the unburned fuel is also forced to spread along the plate as there is 40ppm recorded at r/d_{IDF}=8.3. For the flame at Φ=1.0 and Φ=1.2, lower HC concentration is found at r/d_{IDF}=2.3 with Φ=1.2. This indicates that, the flame at Φ=1.2 is more complete in combustion than that at Φ=1.0.

When H/d_{IDF} increases to 7 and 10, the stagnation point HC concentrations decrease obviously when compared to those at H/d_{IDF}=5. In general, the HC concentrations at r/d_{IDF}=2.3 also decrease with increasing H/d_{IDF}. However, at Φ=0.8, there is still 84ppm of HC recorded at such radial distance, which again shows that unburned fuel is located along the plate surface. Among the investigated values of Φ, the most complete combustion occurs at Φ=1.2. It is because it has the lowest HC concentration profile at H/d_{IDF}=7 and even zero HC concentration is recorded at H/d_{IDF}=10. Therefore, all the fuel for the flame at Φ=1.2 reacts with the central air supplied and also the secondary air along the impingement plate.

It is interesting to look at the HC concentration profiles for Φ=0.8 and Φ=1.8 under the three levels of H/d_{IDF}. The HC concentration in each case decreases as H/d_{IDF} becomes larger. However, at H/d_{IDF}=5, the HC concentration profile of Φ=1.8 is much higher that the profile at Φ=0.8. The two profiles are close to each other at H/d_{IDF}=7. At H/d_{IDF}=10, the HC concentrations are higher at Φ=0.8. This is an indicating that at H/d_{IDF}=5, the higher fuelling rate at Φ=1.8 causes more fuel to impinge on the plate due to lack of space for flame development. While at H/d_{IDF}=10, there is enough headroom for mixing of the air and fuel and subsequent combustion. Thus the HC concentration is very low for the case of Φ=1.8. At Φ=0.8, there is a cool core formed with fuel burning at the periphery of the air jet. Air and fuel mixing is poorer to the lower air and fuel flow rates associated with the lower overall equivalence ratio at a fixed Re_{air} of 2000. This might have resulted in a higher HC concentration than the other three.

The NO concentration distributions are shown in *Figure 5.2.44* to *Figure 5.2.46.* At Φ=0.8, there is less than 1ppm of NO as observed in the Figures. This is due to the cooler, fuel-lean flames. For Φ=1.0, less than 1ppm NO concentration is again observed in *Figure 5.2.44*. This is again because of the low flame temperature at this operating condition.

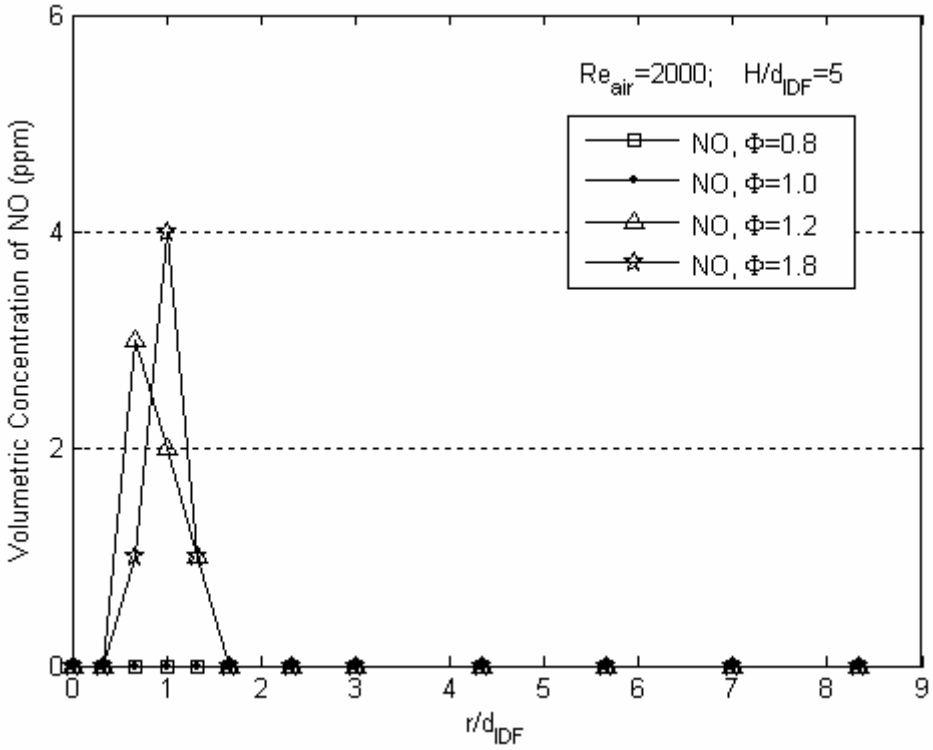

Figure 5.2.44. Distribution of the concentration of NO under different Φ at Re_{air}=2000 and H/d_{IDF} =5.

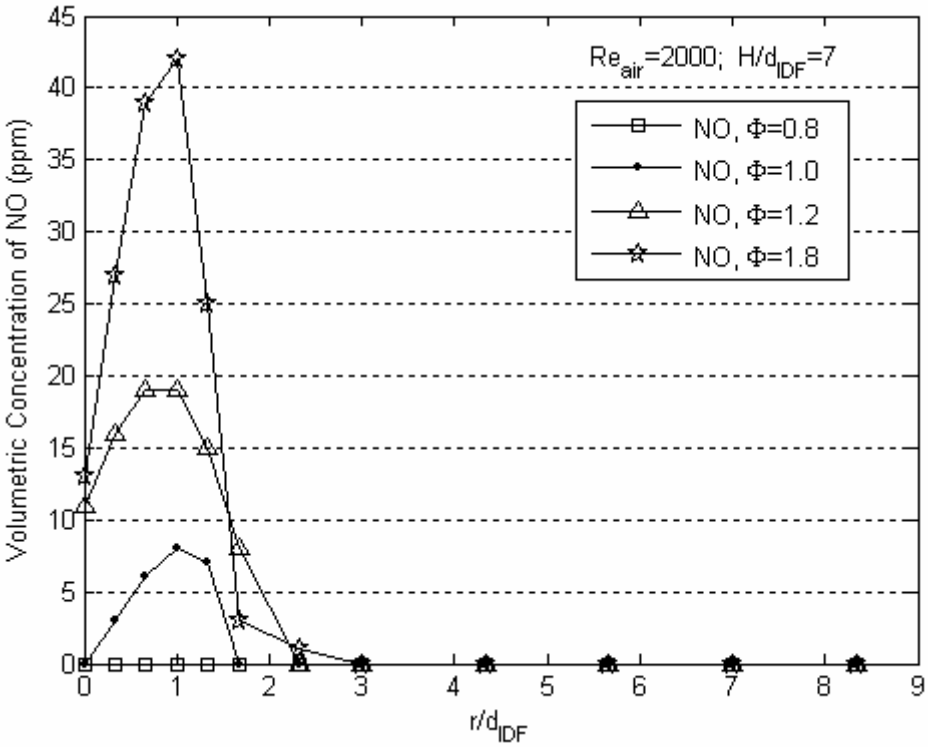

Figure 5.2.45. Distribution of the concentration of NO under different Φ at Re_{air}=2000 and H/d_{IDF} =7.

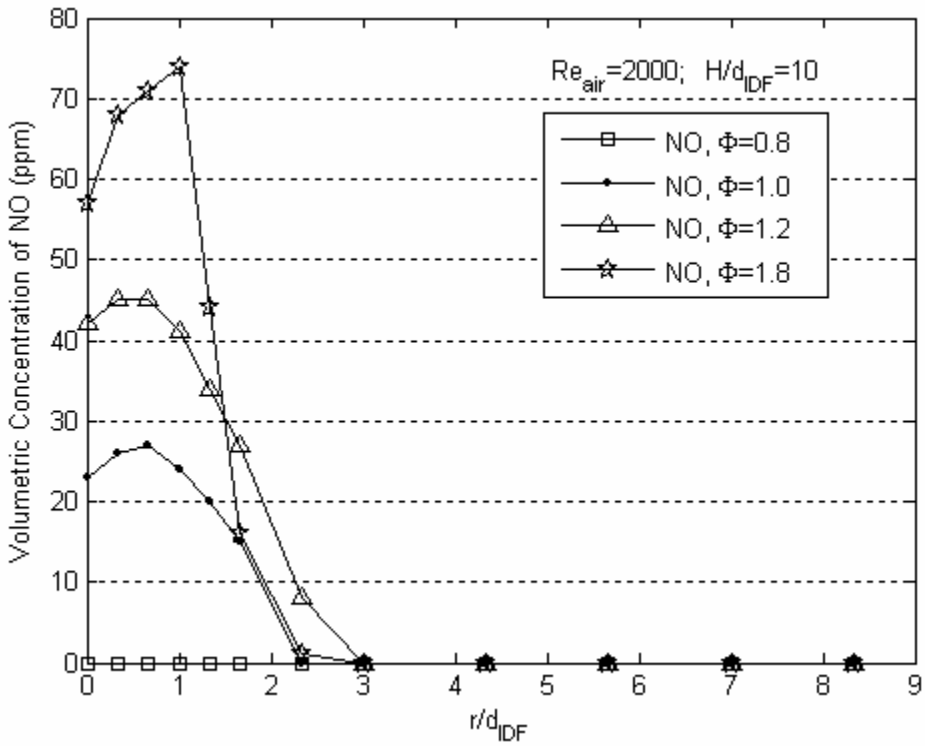

Figure 5.2.46. Distribution of the concentration of NO under different Φ at Re_{air}=2000 and H/d_{IDF} =10.

The NO concentration increases with Φ, or when H/d_{IDF} is increased. From the radial flame temperature profiles, it can be observed that the flame temperature increases with Φ. As a result, NO concentration increases. Besides, the stagnation point flame temperature distributions show that the temperature is still high in the post-combustion flame zone. Thus, the higher NO concentration measured at higher value of H/d_{IDF} is due to the increase in the residence time.

At H/d_{IDF}=5, basically all measured NO concentrations are very low, since the whole flame is cool as it spreads along the plate. At H/d_{IDF}=7 and 10, NO is detected only in the region up to r/d_{IDF}=3. The NO concentration is higher at higher level of Φ and higher H/d_{IDF}, as explained. In all cases, the NO concentrations are low, thus, the NO concentration is less than 1ppm in the wall jet region due to dilution effect.

The Figures also show that the peak NO concentration occurs at the region of the most intense combustion as indicated by the corresponding O_2 concentration.

(b) Combustion Species Concentration, Re_{air}=3000

The combustion species concentrations were also measured at Re_{air}=3000 for examining the effect of the Re_{air}. The results are shown in *Figure 5.2.44* to *Figure 5.2.52*. The trend of each combustion species at the three investigated values of H/d_{IDF} are similar to those obtained at Re_{air}=2000.

Figure 5.2.47 – Figure 5.2.49 show the O_2 and CO_2 concentrations at different Φ for Re_{air}=3000 at H/d_{IDF}=5, 7 and 10, respectively. Comparing with those at Re_{air}=2000, the O_2 concentration is higher at the stagnation point but lower in the wall jet region. The contrary is observed from the CO_2 concentration profiles. At higher Re_{air} and at the same Φ, there is an increase in both air flow rate and fuel flow rate. Thus there is an extension of the cool core. Combustion occurs at a higher height, leading to higher level of oxygen concentration at the stagnation point (less combustion at the stagnation point) and lower oxygen concentration in the wall jet region (combustion occurs along the wall jet region).

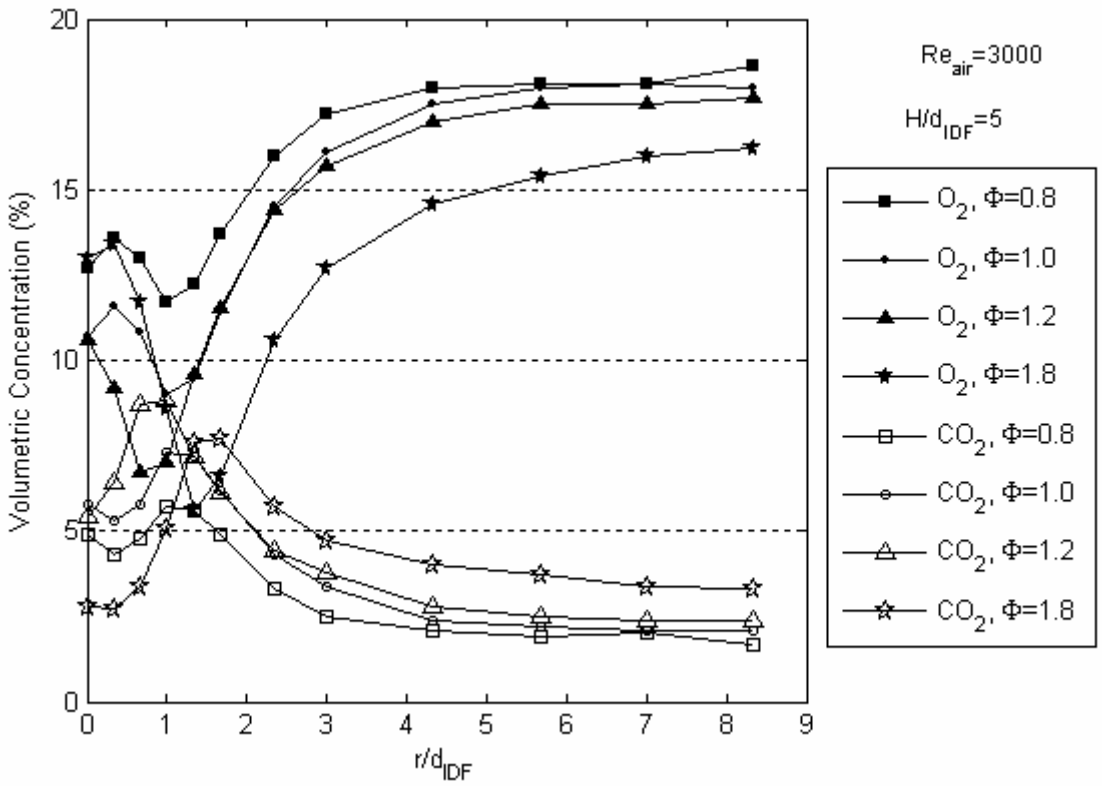

Figure 5.2.47. Distributions of the concentrations of O_2 and CO_2 under different Φ at Re_{air}=3000 and H/d_{IDF} =5.

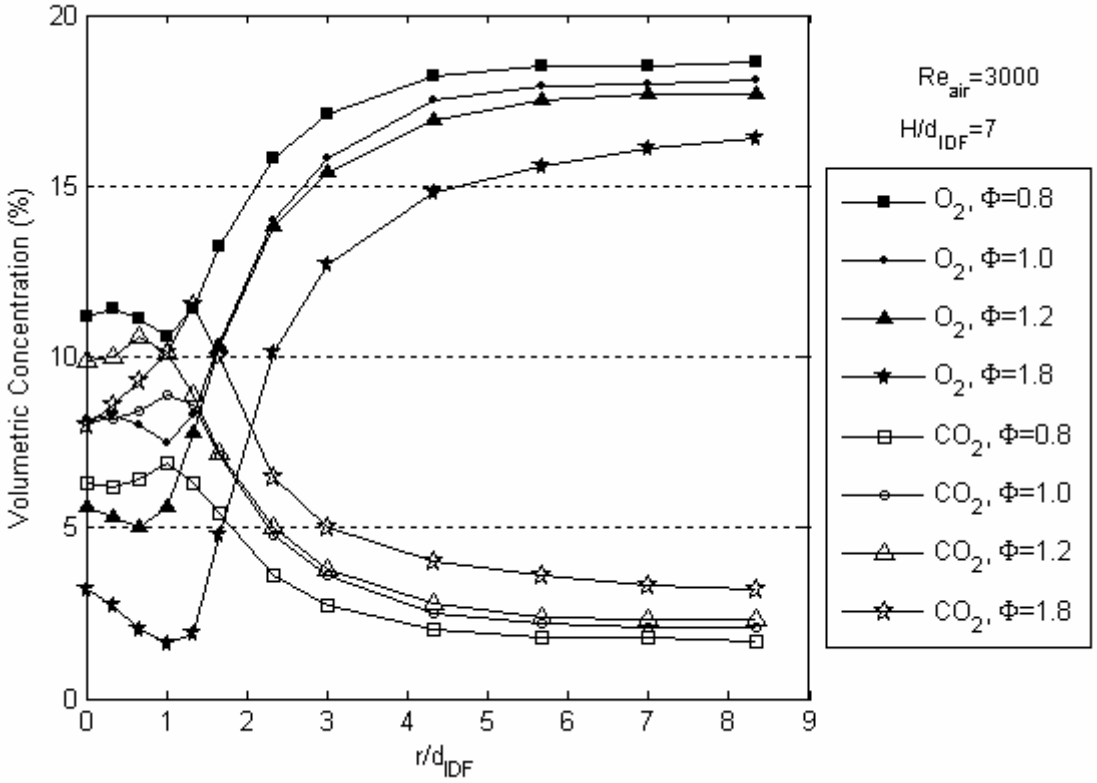

Figure 5.2.48. Distributions of the concentrations of O_2 and CO_2 under different Φ at Re_{air}=3000 and H/d_{IDF} =7.

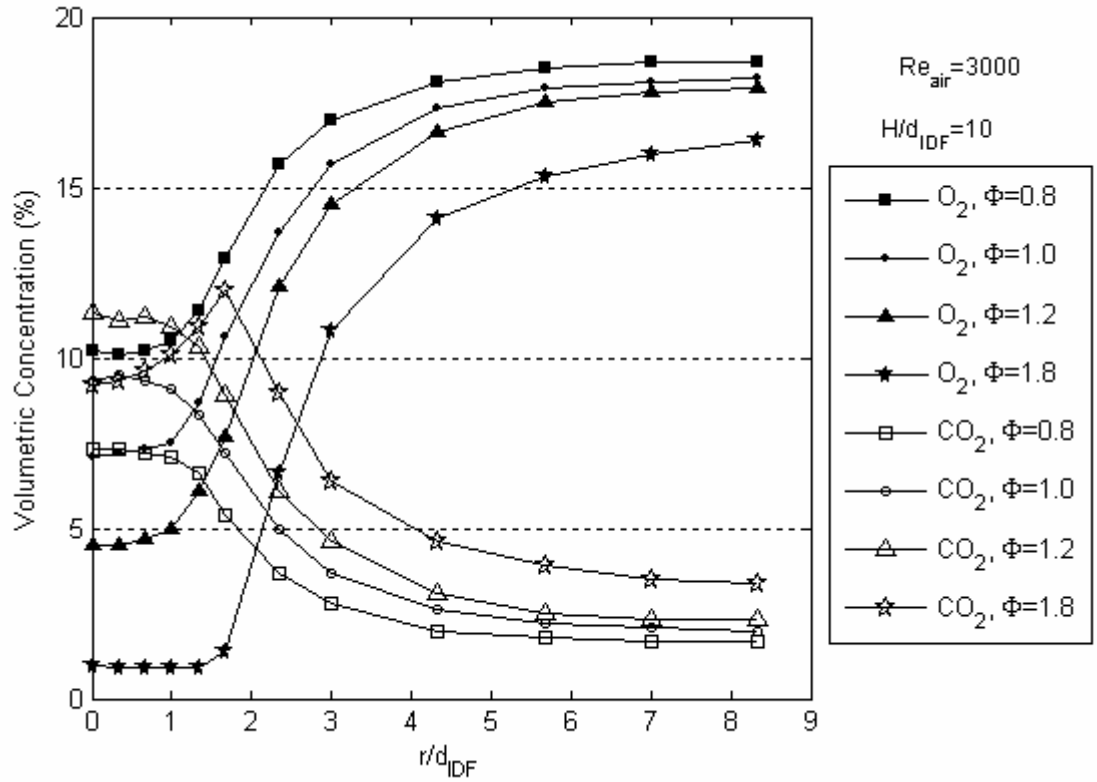

Figure 5.2.49. Distributions of the concentrations of O_2 and CO_2 under different Φ at Re_{air}=3000 and H/d_{IDF} =10.

Figure 5.2.50 – Figure 5.2.52 show the CO concentration distributions at Re_{air}=3000. At Φ=0.8, 1.0 and 1.2, the CO concentration increases as Re_{air} increases. However, there is practically no CO beyond r/d_{IDF} of 8 at Re_{air} of 3000 while the same occurs beyond r/d_{IDF} of 7 at Re_{air} of 2000. Thus due to the longer cool core and longer flame, there is more combustion along the plate at Re_{air} of 3000. It also takes longer distance to ensure complete mixing of air and fuel. Hence at the stagnation point region, there tends to be more incomplete mixing at Re_{air} leading to higher CO concentrations.

However, at Re_{air}=3000 and Φ=1.8, lower CO concentration is found near the stagnation point at H/d_{IDF}=5 and H/d_{IDF}=7, while higher values occur thereafter as compared to those values at Re_{air}=2000. At Φ=1.8, the fuel jet momentum is relatively high and the cool core becomes longer; there is less combustion occurring at the stagnation point region at Re_{air} of 3000, leading to a lower value of CO concentration. As refer to the stagnation point flame temperature distribution, lower flame temperature is found at the two values of H/d_{IDF} at Re_{air}=3000.

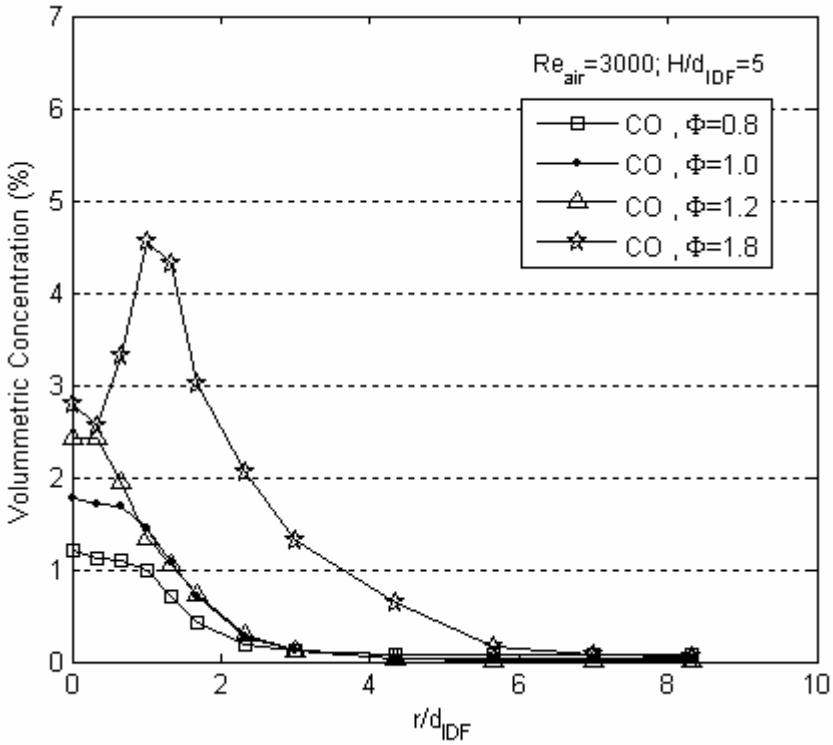

Figure 5.2.50. Distribution of the concentration of CO under different Φ at Re_{air}=3000 and H/d_{IDF} =5.

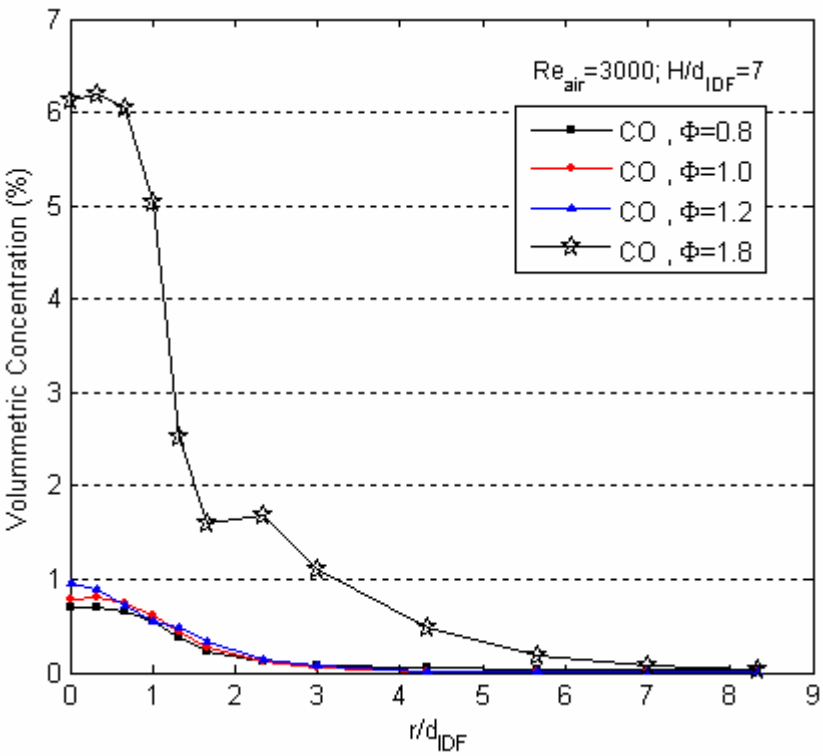

Figure 5.2.51. Distribution of the concentration of CO under different Φ at Re_{air}=3000 and H/d_{IDF} =7.

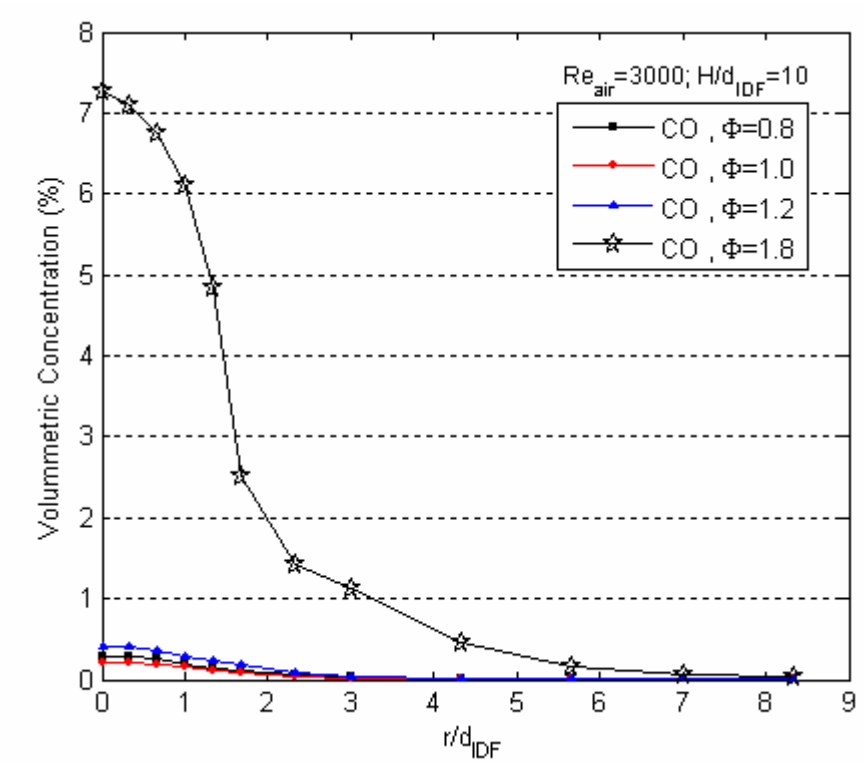

Figure 5.2.52. Distribution of the concentration of CO under different Φ at Re_{air}=3000 and H/d_{IDF} =10.

From *Figure 5.2.53* – *Figure 5.2.55*, the HC concentration also increases with Re_{air} is increased. Under the considered operating conditions, the HC concentration is higher from the stagnation point along the impingement plate. This indicates that although the flame temperature and the heat flux increase with Re_{air} at constant Φ, which are due to the increase in the supplied fuel flow rate, however there is more unburned fuel accumulates at the stagnation region and the wall jet region. Therefore, again, the HC concentration shows the more incomplete combustion at the stagnation point at Re_{air}=3000. Comparing Figure 5.2.55 (Re_{air}=2000, H/d_{IDF}=10) with Figure 5.2.43 (Re_{air}=2000, H/d_{IDF}=10), there is more unburnt HC along the wall jet region in the latter case.

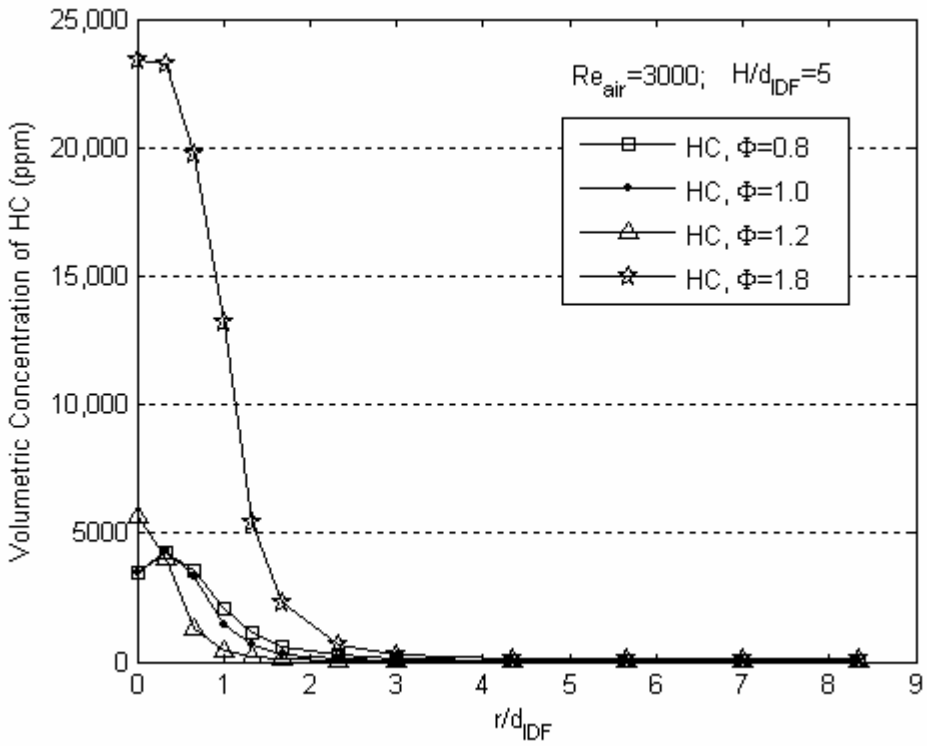

Figure 5.2.53. Distribution of the concentration of HC under different Φ at Re_{air}=3000 and H/d_{IDF} =5.

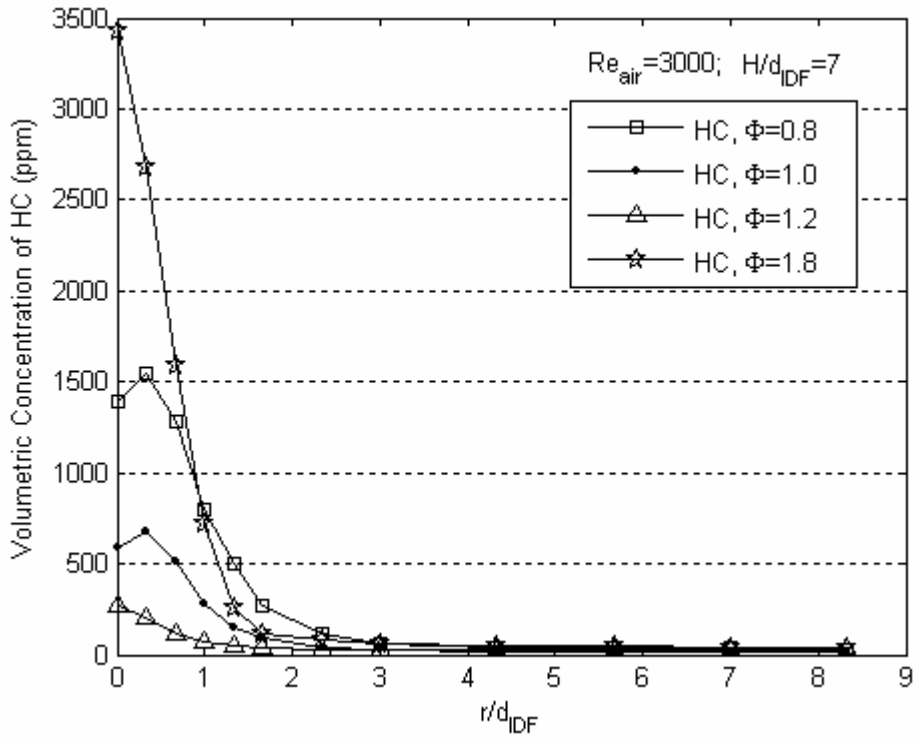

Figure 5.2.54. Distribution of the concentration of HC under different Φ at Re_{air}=3000 and H/d_{IDF} =7.

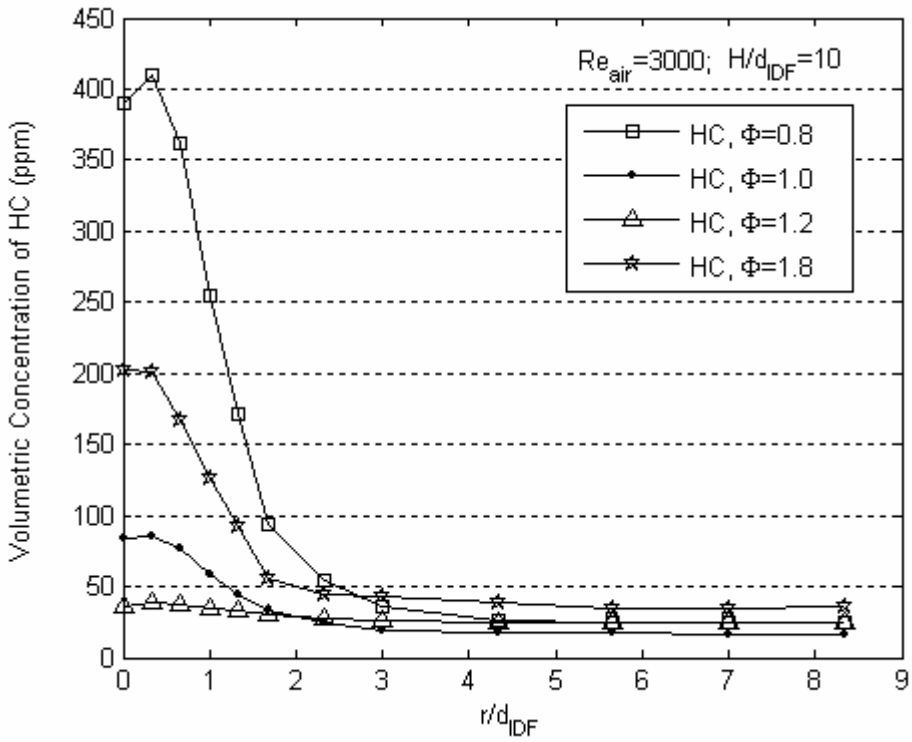

Figure 5.2.55. Distribution of the concentration of HC under different Φ at Re_{air}=3000 and H/d_{IDF} =10.

In *Figure 5.2.56 – Figure 5.2.58*, it is observed that the NO concentration is lower at the stagnation point, but it decays slower in the wall jet region, at Re_{air}=3000. It is again due to the fact that at the same H/d_{IDF}, at a higher Re_{air}, less fuel is burned in the flame up to the stagnation point region and more fuel is burned in the wall jet region. The radial flame temperature distribution shows higher flame temperature for Re_{air}=3000, which corresponds with the higher NO concentration in the wall jet region.

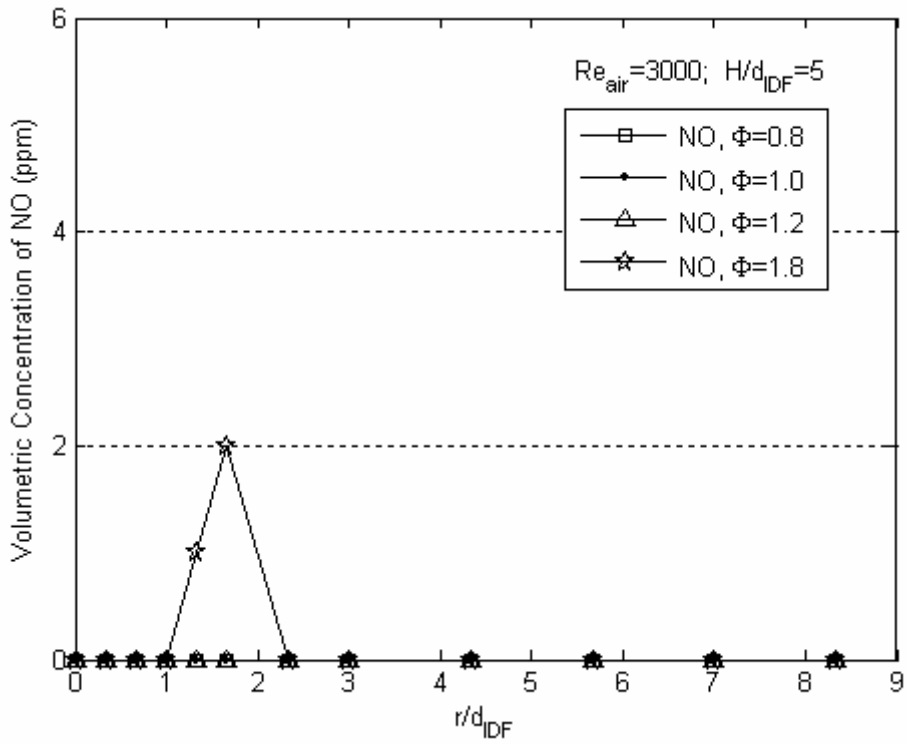

Figure 5.2.56. Distribution of the concentration of NO under different Φ at Re_{air}=3000 and H/d_{IDF} =5.

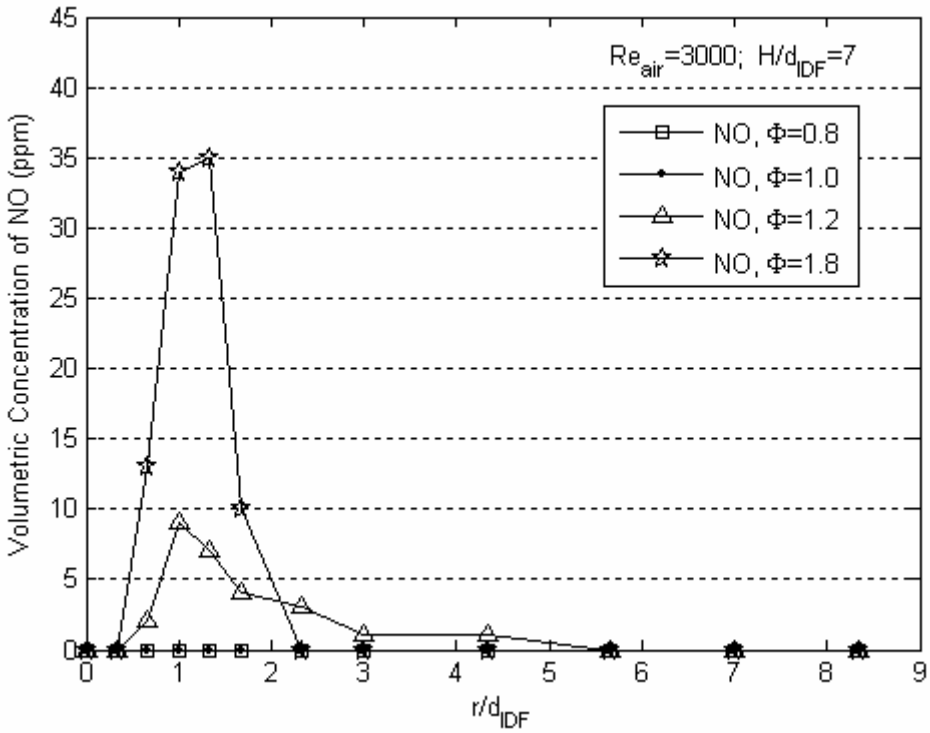

Figure 5.2.57. Distribution of the concentration of NO under different Φ at Re_{air}=3000 and H/d_{IDF} =7.

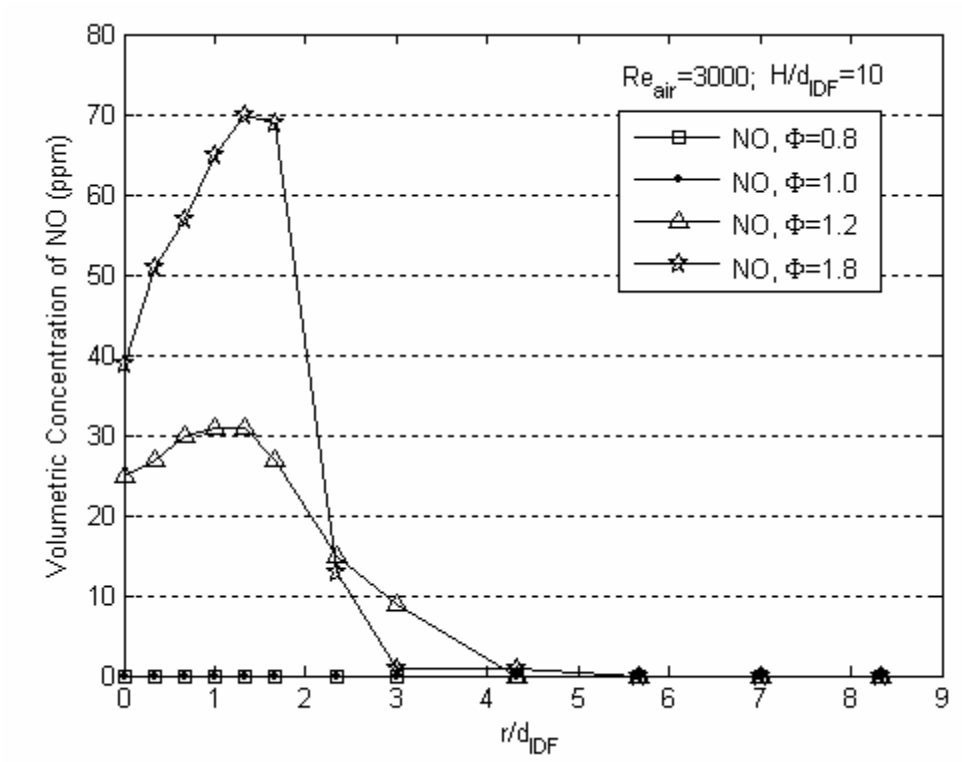

Figure 5.2.58. Distribution of the concentration of NO under different Φ at Re_{air}=3000 and H/d_{IDF} =10.

5.3 Area-averaged Heat Flux

The area-averaged heat flux was obtained by considering the heat flux of a circular area within a radial distance of 50 mm from the stagnation point of the flame. Based on the distribution of the local radial heat fluxes, the area-averaged heat flux can be calculated using the equation, *E3.4.10* shown in *Chapter 3*.

The effects of H/d_{IDF} and Φ on the area-averaged heat flux can be observed at *Figure 5.3.1* with Re_{air}=2000. The Six profiles at different Φ are similar for each H/d_{IDF} from 4 to 10: there is always a peak value at some intermediate H/d_{IDF}. Low area-averaged heat flux are found at H/d_{IDF}=4 and all of the profiles decrease

from H/d_{IDF}=8. Therefore, heat is transferred to the plate more significantly when $5 \leq H/d_{IDF} \leq 8$ at the investigated Φ and Re_{air}=2000.

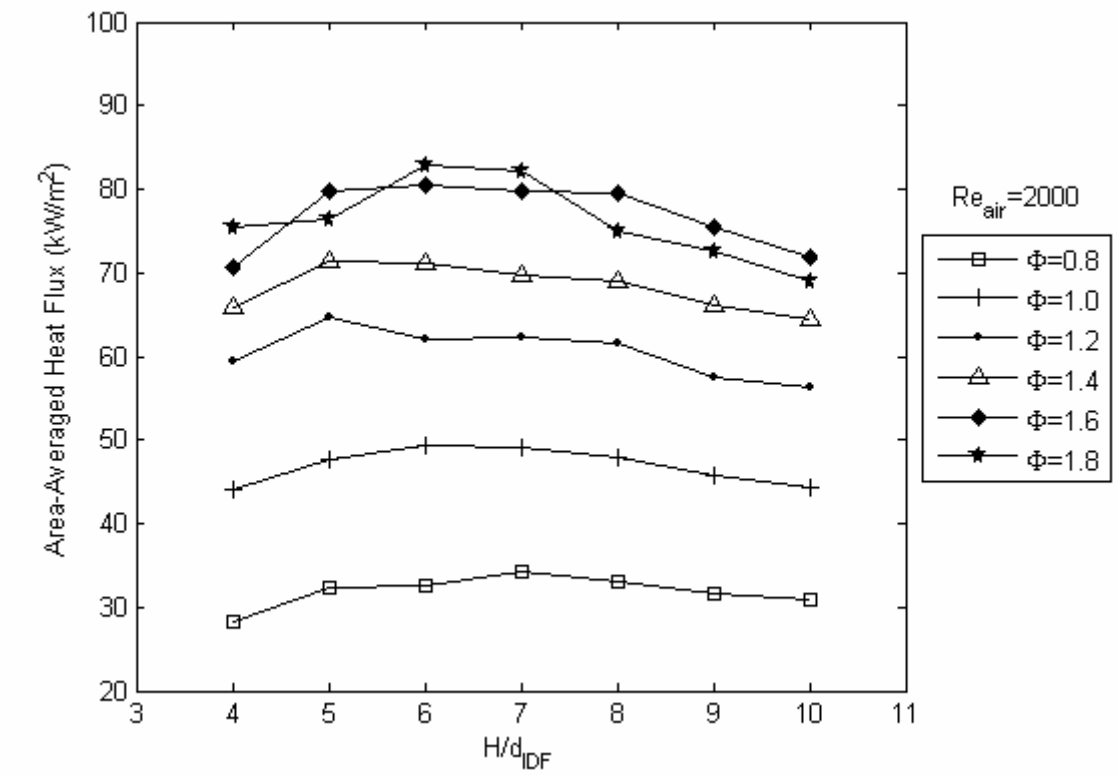

Figure 5.3.1. Variation of area-averaged heat flux with H/d_{IDF} and Φ at Re_{air}=2000.

Besides that, in *Figure 5.3.1*, with increase in Φ, the profiles shift upwards until Φ=1.6. At fixed Re_{air} of 2000, an increase in Φ corresponds to an increase in the fuelling rate, which should lead a corresponding increase in the area-averaged heat flux.

However, the curves for Φ=1.6 and Φ=1.8 have certain degree of overlap with each other, which means that the extra fuel provide at Φ=1.8 is not converted into useful heat flux. It can be explained from the flame images shown in *Figure 5.1.3*. At Φ=1.8, more brilliant orange flame is observed at the boundary between the stagnation and the wall jet regions and there is more contact area between the visible flame and the plate. Thus, more heat may loss to the surrounding due to the radiation of the brilliant orange diffusion flame. At the same time, more heat may be transferred to the wall jet region beyond the integration area. However, this factor might not be an important one as the area-averaged heat flux is still lower at H/d_{IDF} of 10, which should have provided sufficient headroom for the flame to develop and the heat to be transferred to the plate.

Figure 5.3.2 – *Figure 5.3.5* present the effect of Re_{air} and Φ on the area-averaged heat flux, for H/d_{IDF}=5, 6, 7, and 8, respectively. The profiles in the four Figures are similar due to the insignificant effect of H/d_{IDF} on the area-averaged heat flux at $5 \leq H/d_{IDF} \leq 8$. In the *Figures*, in general, the area-averaged heat flux increases with increasing Φ and Re_{air}. An increase in the Re_{air} at fixed Φ means increase in both air and fuel supplies, so that there is an increase in the fueling rate and hence the area-averaged heat flux increases. Thus, the profiles shift upwards when Re_{air} is increased. On the other hand, an increase in the Φ at fixed Re_{air} means increase in the fuel flow rate while the air supply remains unchanged. Again, there is an increase in the fueling rate which leads to an increase in the area-averaged heat flux.

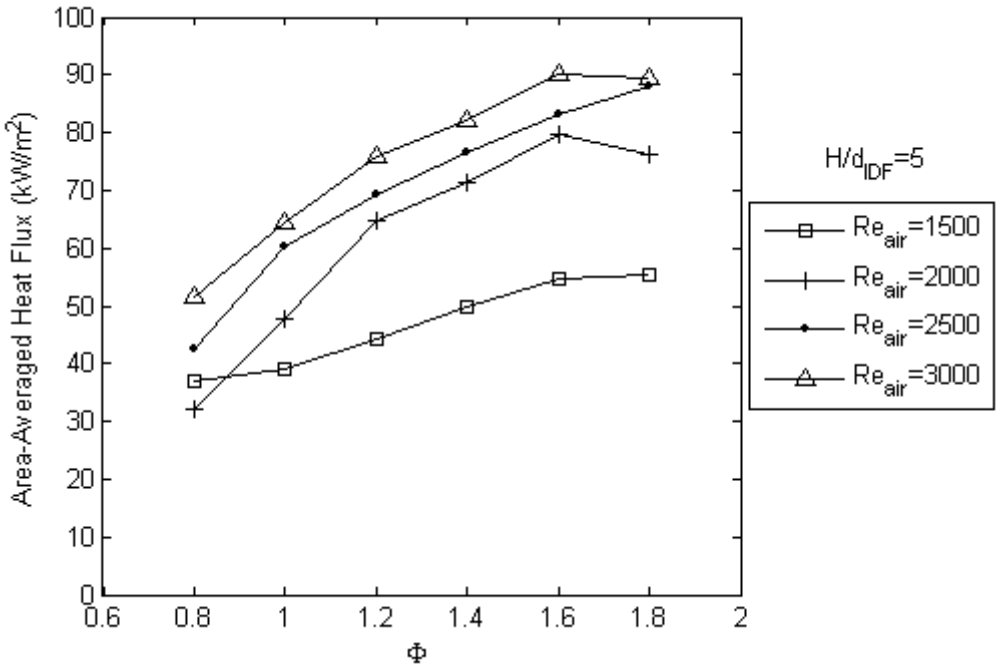

Figure 5.3.2. Variation of area-averaged heat flux with Φ and Re_{air} at $H/d_{IDF}=5$.

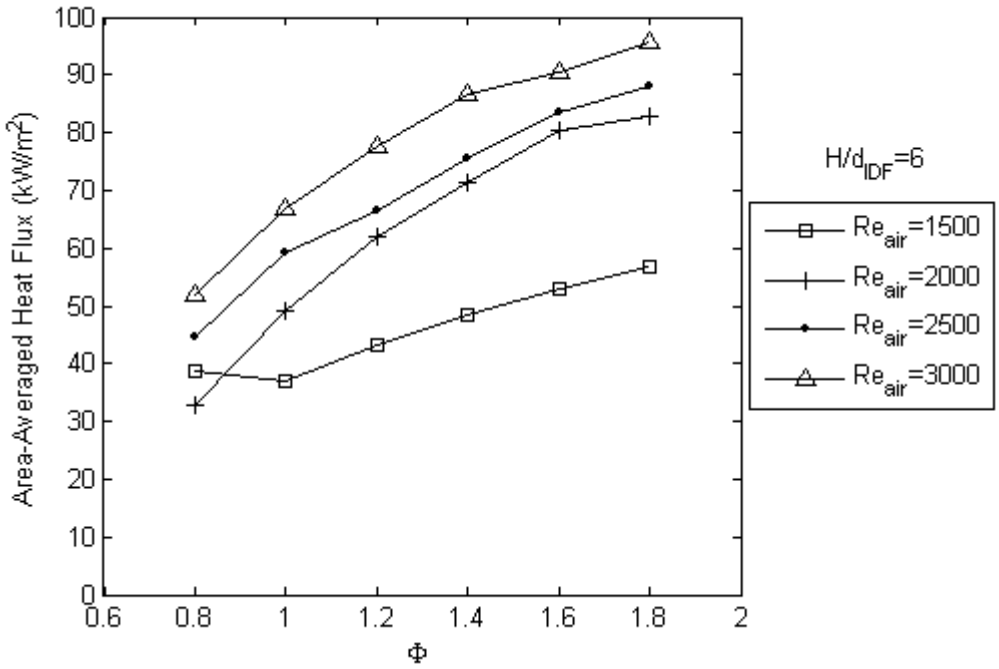

Figure 5.3.3. Variation of area-averaged heat flux with Φ and Re_{air} at $H/d_{IDF}=6$.

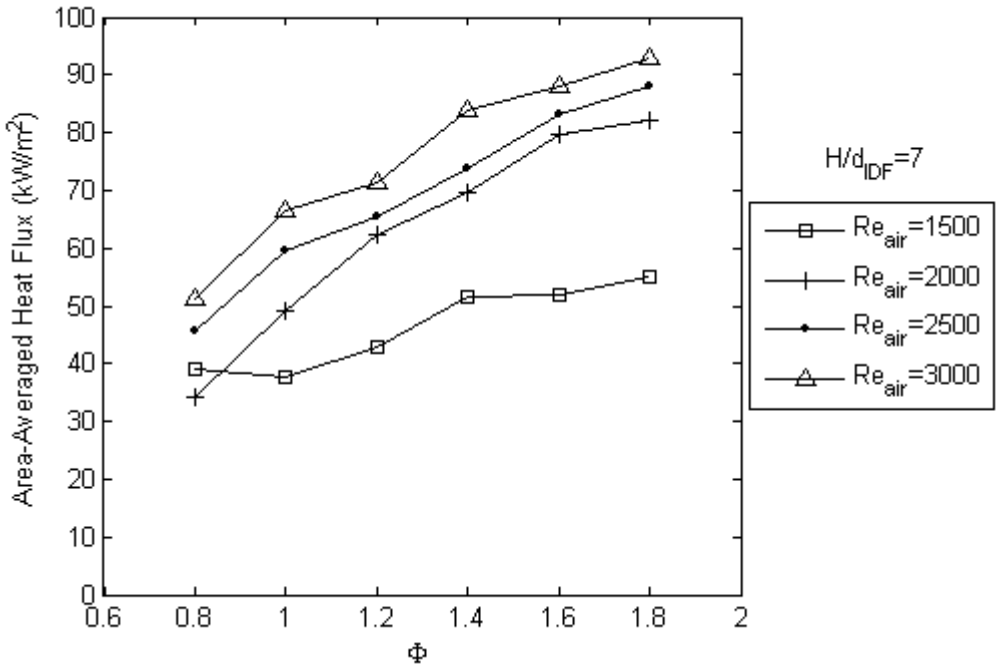

Figure 5.3.4. Variation of area-averaged heat flux with Φ and Re_{air} at $H/d_{IDF}=7$.

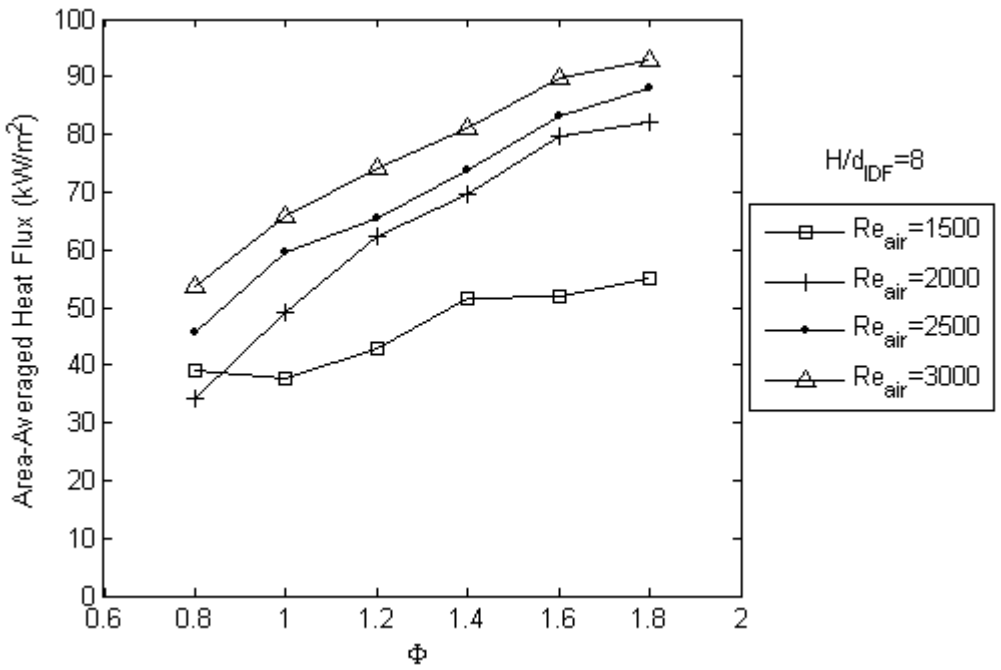

Figure 5.3.5. Variation of area-averaged heat flux with Φ and Re_{air} at $H/d_{IDF}=8$.

However, there is an exceptional case indicated in the above Figures. The profiles at Re_{air}=1500 is different from the others. The area-averaged heat fluxes are particularly lower. At Re_{air}=1500, the area-averaged heat flux at the fuel lean condition of Φ=0.8 is higher than that at Φ=1.0 for H/d_{IDF}=6, 7 and 8. Also at Φ=0.8, higher area-averaged heat flux is found at Re_{air}=1500 when compared to that at Re_{air}=2000. As mentioned in the previous section, according to the HC concentration measurement, the fuel is forced to impinge and spread along the impingement plate by the air jet for the flame at Φ=0.8 at Re_{air}=2000 and 3000. Also, more fuel is accumulated along the plate at lower Re_{air} (Re_{air}=2000). Therefore, it is believed that most of the fuel is burnt near the impingement plate, hence higher area-averaged heat flux is obtained at Re_{air}=1500 and Φ=0.8.

5.4 Heat Transfer Efficiency

The heat transfer efficiency, as defined in *E3.4.11* in Chapter 3, is more useful in indicating the effectiveness of energy transferred from the fuel to the impingement plate. Again, the heat transfer efficiency was obtained by considering the heat flux of a circular area within a radial distance of 50 mm from the stagnation point of the flame.

The effects of H/d_{IDF} and Φ on the heat transfer efficiency are shown in *Figure 5.3.6* with Re_{air}=2000. The Six profiles at different Φ are similar for each H/d_{IDF} from 4 to 10: there is always a peak value at some intermediate H/d_{IDF}. Low heat transfer efficiency are found at H/d_{IDF}=4 and all of the profiles decrease from

H/d_{IDF}=8. Therefore, heat is transferred to the plate more effective when $5 \leq H/d_{IDF} \leq 8$ at the investigated Φ and Re_{air}=2000.

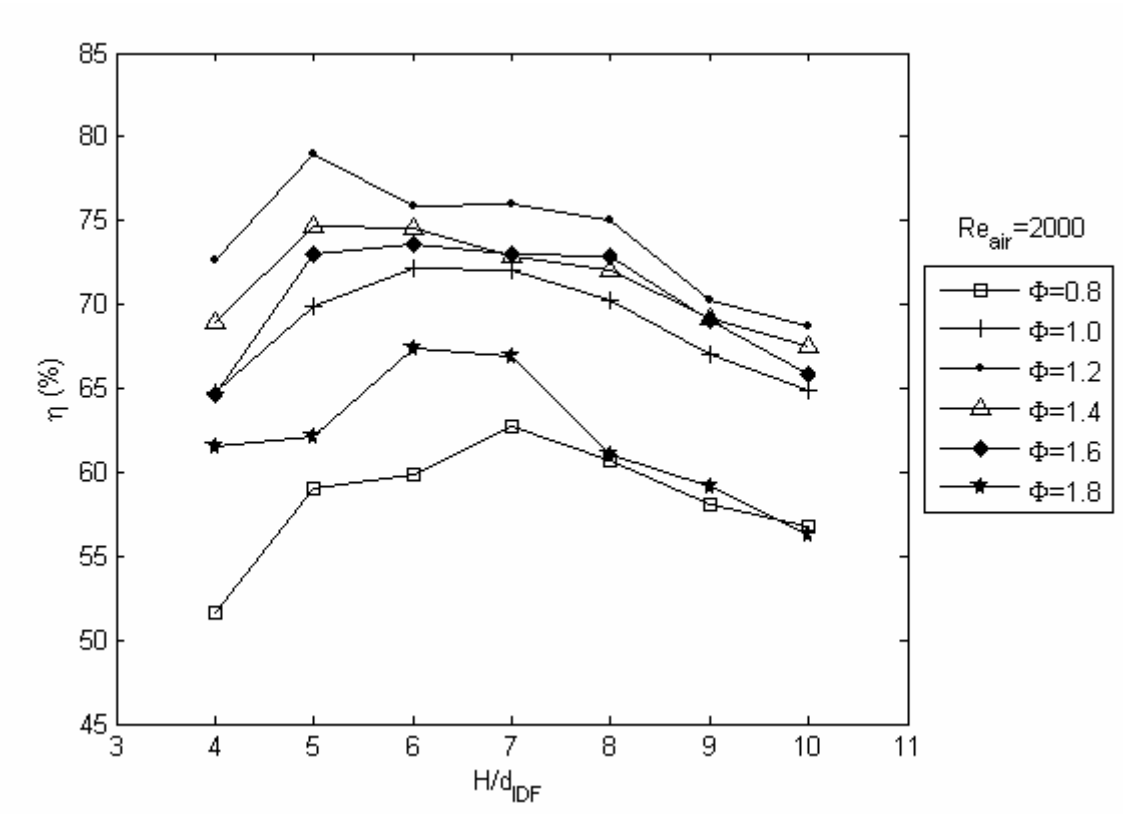

Figure 5.4.1. Variation of heat transfer efficiency with H/d_{IDF} and Φ at Re_{air}=2000.

When compare to *Figure 5.3.1*, the shapes of the six profiles are the same at each corresponding values of Φ, but the effect of Φ on the heat transfer efficiency is different from that on the area-averaged heat flux. By observing from *Figure 5.4.1*, the heat transfer efficiency increases when Φ is increased from 0.8 to 1.2. At the profiles of Φ=1.2, it shows the highest values of heat transfer efficiency, while it achieves 79% at H/d_{IDF}=5. The efficiency then decreases when Φ is further increased.

The curves for the heat transfer efficiency at Φ=1.4 and Φ=1.6 have certain degree of overlap with each other, although higher area-averaged heat flux is obtained at Φ=1.6 as shown in *Figure 5.3.1*. It means that the extra heat flux obtained at Φ=1.6 is not increase in the same proportion with the extra fuel provided. It can be again explained that at Φ=1.6, more heat may loss to the surrounding due to the radiation of the brilliant orange diffusion flame. When Φ is further increase to 1.8, such heat loss becomes more significant, thus, low values of both area-averaged heat flux and heat transfer efficiency are obtained.

Figure 5.4.2 – Figure 5.4.5 show the variation of the efficiency with Re_{air} and Φ for the four H/d_{IDF}=5, 6, 7 and 8, respectively. The results are very similar for each H/d_{IDF}. For Re_{air}=2000 – Re_{air}=3000, in general, the heat transfer efficiency is the highest for Re_{air}=2000 at Φ=1.0–1.8. At Φ=0.8, the heat transfer efficiency at Re_{air}=2000 drops below those at higher Re_{air}. At Re_{air}=2000, the maximum heat transfer efficiency occurs around Φ=1.2 and drops on both ends. At Re_{air}=2500, the maximum heat transfer efficiency occurs around Φ=1.0. At Re_{air}=3000, the maximum heat transfer efficiency occurs at either Φ=0.8 or Φ=1.0. Thus the maximum heat transfer efficiency shifts towards lower Φ as Re_{air} is increased from 2000 to 3000.

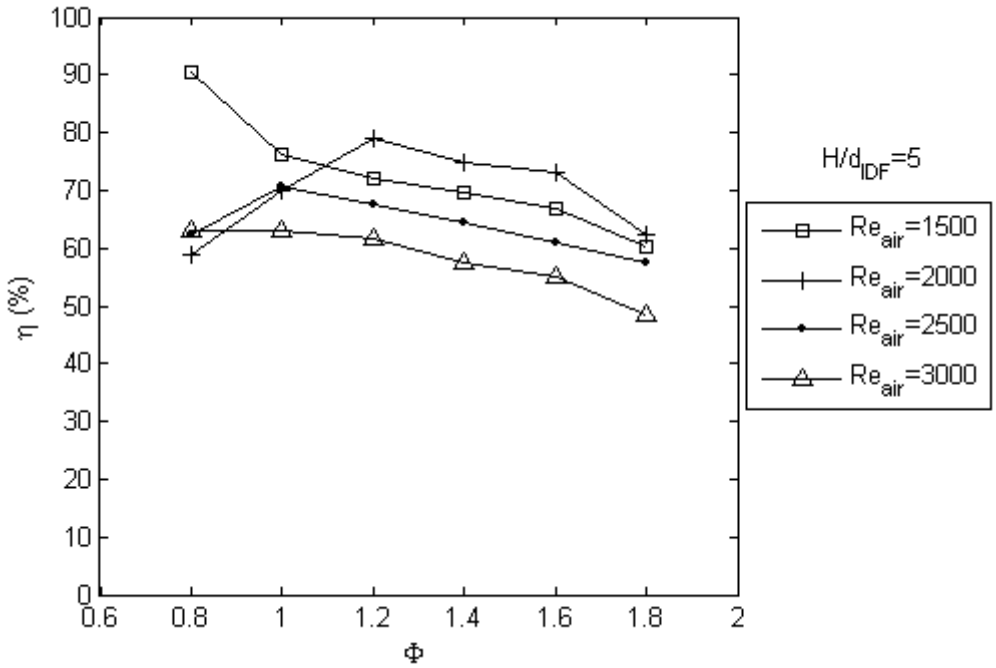

Figure 5.4.2. Variation of heat transfer efficiency with Φ and Re_{air} at $H/d_{IDF}=5$.

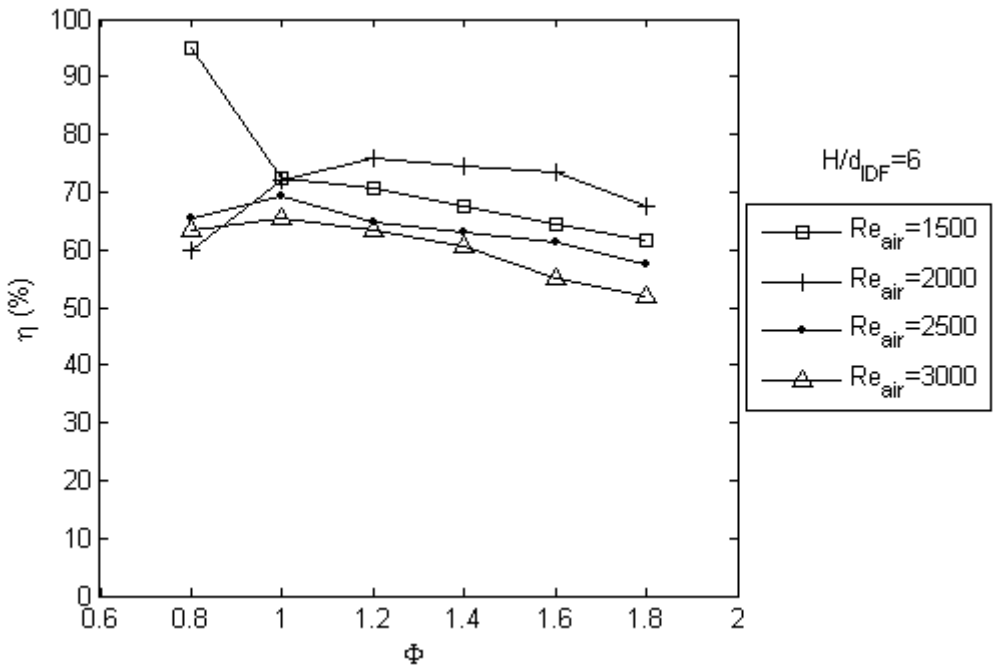

Figure 5.4.3. Variation of heat transfer efficiency with Φ and Re_{air} at $H/d_{IDF}=6$.

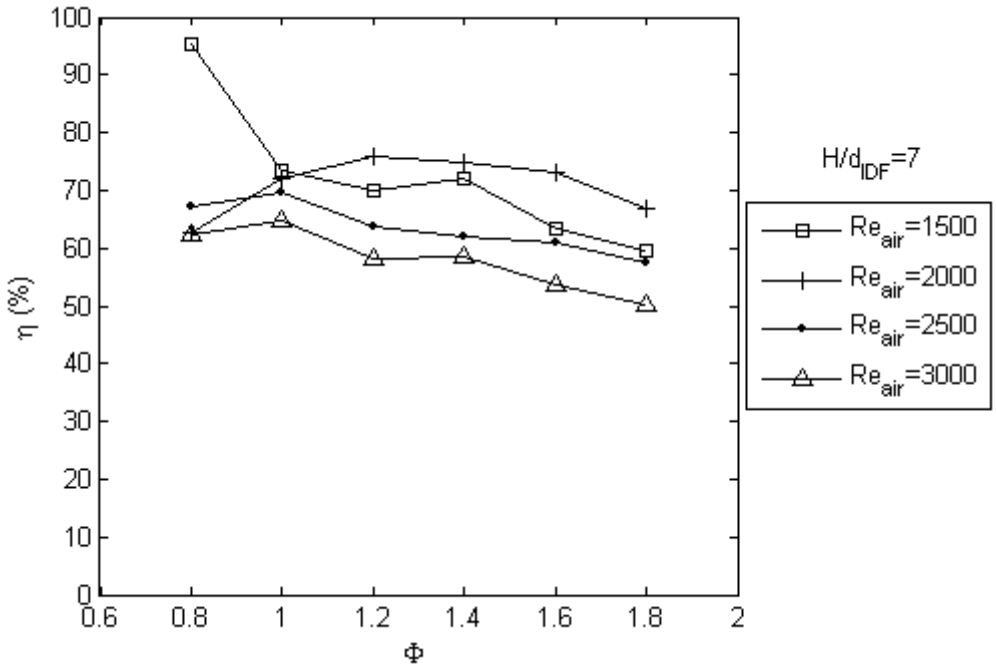

Figure 5.4.4. Variation of heat transfer efficiency with Φ and Re_{air} at $H/d_{IDF}=7$.

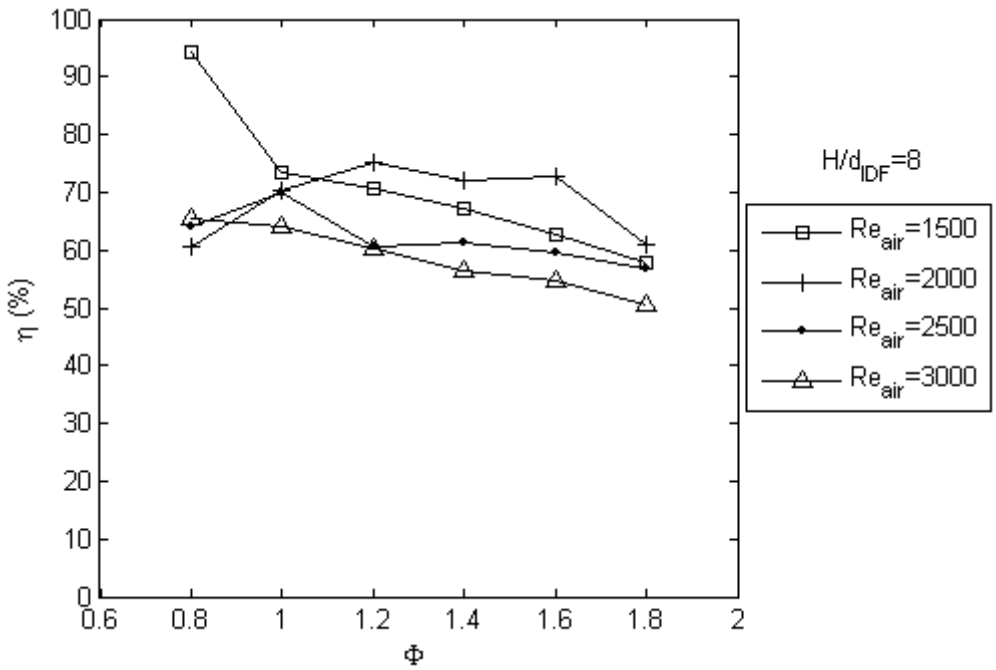

Figure 5.4.5. Variation of heat transfer efficiency with Φ and Re_{air} at $H/d_{IDF}=8$.

Again from the *Figures*, for Re_{air}=2000 – Re_{air}=3000, the results are more orderly for Φ=1.2 to 1.8. Under this range of overall equivalence ratio, the heat transfer efficiency is always the highest at Re_{air}=2000 and decreases as Re_{air} is increased. There is also a tendency of decreasing heat transfer efficiency with increasing Φ within this range of value. These trends agreed with results in literature for premixed flames [37,41]. One of the major reasons of dropping efficiency with Re_{air} and Φ is due to energy transferred beyond the integration area. As these two parameters are increased in the range of values being investigated, there is an increase in flame length and increase contact with the impingement plate in the wall jet region. Since an area is chosen for integration, some of the energy transferred beyond the chosen area will not be taken into account. As Re_{air} and Φ are increased, there is increasing amount of energy transferred beyond the integrated area which results in decreasing efficiency.

The profiles of the exceptional case at Re_{air}=1500 shown in the four *Figures* indicating a peak heat transfer efficiency with value over 90% locates at Φ=0.8, which then drops to about 70% at Φ=1.0 and continues decrease with further increase in Φ. At Φ>1.0, it has the values in between those obtained at Re_{air}=2000 and Re_{air}=2500. The case at Re_{air}=1500 and Φ=0.8 has the area-averaged heat flux less than 40kW/m^2, but it has a very high thermal efficiency, because the fuel is forced to the impingement plate and combustion occurs along it.

5.5 Summary

When the IDF is under impinging, the part of the flame below the horizontal flat plate is not much affected. The structure of the flame impinged on the plate can be divided into 2 parts: a stagnation region, where the flame just reaches the plate before distortion; and a wall jet region, where the part of the flame above the plate is highly distorted and spread horizontally along the plate.

Basically, both of the flame temperature and the heat flux of the impinging IDF increases with either Re_{air} or Φ ($0.8 \leq \Phi \leq 1.6$) is increased, because the increase in these two parameters means the fueling rate is increased. For the stagnation point distributions, the maximum stagnation point heat flux at any Φ occurs with the maximum stagnation point temperature correspondingly at the similar H/d_{IDF}. However, the stagnation point flame temperature decreases gradually after reaching the peak value, while the stagnation point heat flux drops obviously once after reaching the peak value. In other words, after the peak value, the heat transferred to the plate is limited even there is still a high flame temperature. The heat flux is affected by the gas temperature as well as other parameters, for example, the convective heat transfer coefficient. In such case, the drop in heat flux is due to the weakened convective heat transfer coefficient rather than the gas temperature.

For the radial distributions, both of the flame temperature and the heat flux are low near the centerline when either Φ or H/d_{IDF} is low, which indicate the effect of the central cool core zone. When H/d_{IDF} increases, at fixed value of Φ, the flame temperature and the heat flux near the centerline increase and the radial profile becomes bell-shaped. The temperature and the heat flux distributions are affected by the nozzle-to-plate distance near the centerline, but only slightly affected in the wall jet region.

Besides that, in the combustion species analysis in the impinging IDF, when either Re_{air} or Φ is increased, the O_2 concentration decreases while the CO_2, CO and NO concentrations increases. That means, when there is more fuel supplied ($0.8 \leq \Phi \leq 1.2$), more O_2 is consumed and more intense combustion occurs leading to produce high flame temperature, hence high level of NO. However, the combustion becomes more incomplete when Φ=1.8 as there is insufficient O_2. Therefore, CO concentration increases due to the dissociation of CO_2 increases under high flame temperature. In any radial profiles, the intense combustion is indicated by the lowest value of O_2 level, where the highest values of NO, CO_2 and CO levels were found. Such findings are agreed with Sze [2].

The concentration of HC evident that the fuel is forced to impinge and spread along the plate by the air jet for the flame at Φ=0.8 and more fuel is accumulated along the plate at lower Re_{air} (Re_{air}=2000). When the fuel is too rich (Φ=1.8), the unburned fuel is also forced to spread along it. The HC concentration shows that the flame at Φ=0.8 is processing a very incomplete combustion, while the most complete combustion is occurred at Φ=1.2.

Both Φ and H/d_{IDF} influence the heat transfer mainly at the stagnation region. At low value of H/d_{IDF}, the maximum heat flux occurs at the downstream of the intense combustion region indicated by the O_2 and CO_2 concentration profiles. This may due to the effect of the cool core. When H/d_{IDF} increases, the effect of the cool core decreases. Therefore, the intense combustion region and the maximum heat flux occur at the same location.

In general, the calculated area-averaged heat flux increases with Re_{air} and Φ since both imply an increase in the fueling rate. However, there is little variation of the area-average heat flux with H/d_{IDF} for the range of H/d_{IDF} from 5 to 8. The value at Re_{air}=1500 and Φ=0.8 is at a high level in an unexpected way. According to the HC concentration measurement, the fuel is forced to impinge and spread along the impingement plate by the air jet, thus, more fuel is burnt near the plate.

For the range of Φ investigated and at Re_{air}=2000 to 3000, the heat transfer efficiency has a peak value at Re_{air}=2000 and Φ=1.2. At higher Re_{air} and at higher Φ, the heat transfer efficiency decreases. One of the main reasons of the drop in heat transfer efficiency is due to the heat escaped beyond the integration area used for the evaluation of the heat transfer efficiency.

As a result, for the investigated operating conditions of the impinging IDF, the flame at Re_{air}=2000 and Φ=1.2 burnt in a most complete combustion with the least pollutant emissions and also has the best heat transfer efficiency.

Chapter 6 Premixed Flame

This chapter contains two main sections. The first section is showing the results obtained from both free and impinging premixed flame jet experiments. The effects of the parameters, Re_p, Φ and H/d_p, on the flame shape, stagnation point and radial distributions of the temperature and heat flux and radial combustion species concentration are provided. In addition, the area-averaged heat flux and the heat transfer efficiency of the impinging flame system are presented. A comparison of the flame performance between the IDF and the premixed flames at the same flow rates of air and fuel supplies is given in the second section.

6.1 Premixed Flame Jet

Premixed flames operating at Φ = 0.8– 1.6 were analyzed experimentally under four fixed flow rates of air supply: Q_{air} = 1.08x10^{-4} m^3/s, 1.44x10^{-4} m^3/s, 1.79x10^{-4} m^3/s and 2.15x10^{-4} m^3/s, corresponding to Re_{air} = 1500, 2000, 2500 and 3000, respectively for the IDF. As shown in the column of “Condition Selected” in *Table 3*, the premixed flame was blown off at Φ = 0.8 at all the four flow rates of air supply. When the flow rate of air supply was increased to Q_{air} = 1.79x10^{-4} m^3/s, the flame was lift at Φ = 1.0, and flame lift occurred at Φ = 1.0 and Φ = 1.2 when it was further increased to Q_{air} = 2.15x10^{-4} m^3/s.

Different flame shapes were analyzed by images taken with a digital camera of the free and also impinging premixed flame jets. In impinging jet experiments, stagnation point heat flux distributions were measured at Φ = 1.0–1.6 for Q_{air} = 1.08x10^{-4} m^3/s and 1.44x10^{-4} m^3/s; Φ = 1.2– 1.6 for Q_{air} = 1.79x10^{-4} m^3/s; and Φ = 1.4 – 1.6 for Q_{air} = 2.15x10^{-4} m^3/s. For Re_P = 1453 (Φ = 1.0) and 1472 (Φ = 1.2), corresponding to Re_{air} = 2000 at Φ = 1.0 and Φ = 1.2 in the IDF, radial heat flux distributions were measured at 6 nozzle-to-plate distances, H/d_P = 1.5 and 4 with 0.5 intervals, whereas combustion species concentrations were recorded at 3 nozzle-to-plate distances, H/d_P = 1.5, 2 and 4.

6.1.1 Flame Shape Observations

(a) Free Flame Jet

Low speed shutter was first used with the time exposure of 1/50 second in taking photos of the flame. *Figure 6.1.1* shows the premixed flame at Φ = 1.0 – 1.6 with fixed air flow rates of Q_{air} = 1.08x10^{-4}m^3/s and 1.44x10^{-4}m^3/s, which are corresponding to Re_{air} = 1500 and 2000 in the IDF respectively. Figure 6.1.2 shows the premixed flame at Φ = 1.2 – 1.6 and Φ = 1.4 – 1.6 with fixed air flow rates Q_{air} = 1.79x10^{-4}m^3/s and 2.15x10^{-4}m^3/s, respectively, which are corresponding to Re_{air} = 2500 and 3000 in the IDF.

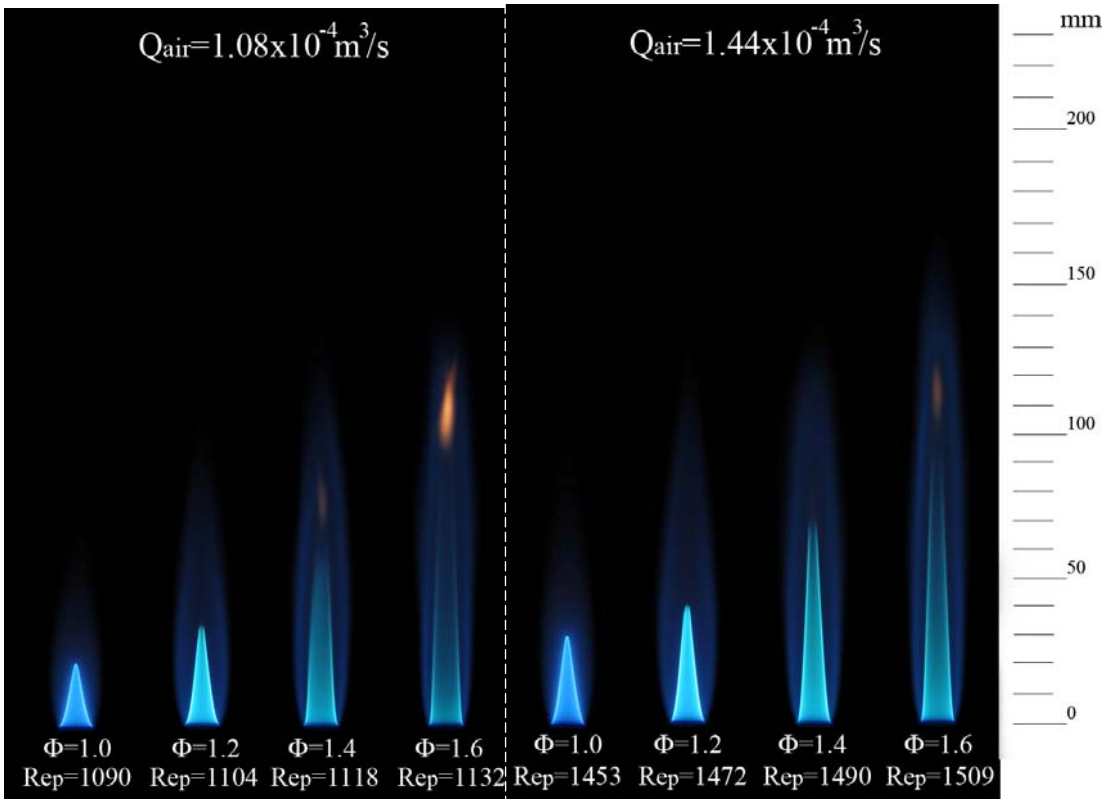

Figure 6.1.1. Direct photos, effects of varying fuel velocity on free jet premixed flame at fixed air flow rates Q_{air} = 1.08x10^{-4}m^3/s and 1.44x10^{-4}m^3/s.

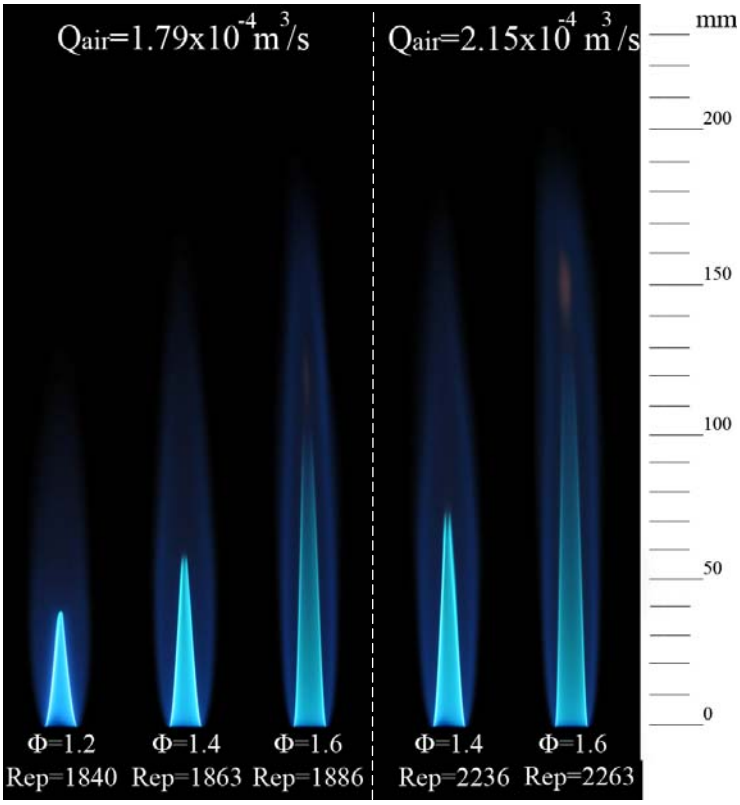

Figure 6.1.2. Direct photos, effects of varying fuel velocity on free jet premixed flame at fixed air flow rates Q_{air} = 1.79x10^{-4}m^3/s and 2.15x10^{-4}m^3/s.

As seen in the Figures, the premixed flame consists a thin layer of reaction zone appeared as a sharp boundary between the inner unburned gas and the outer burned gas. The reaction zone is conical in shape at Φ = 1.0 and 1.2, but the tip of the zone is opened when Φ is further increased. It is lengthened when either Φ or Q_{air} is increased. At constant Q_{air} with increasing Φ or at constant Φ with increasing Q_{air}, the fuelling rate is increased, thus, the flame length also increases. Also, brilliant orange flame is observed at the region above the tip of the reaction zone when Φ = 1.6 for the four fixed flow rates of air supply.

Figure 6.1.3 shows the premixed flame recorded at high-speed shutter with time exposure of 1/1000 second at Φ = 1.0 – 1.6 and $Q_{air} = 1.44 \times 10^{-4} m^3/s$. Compare to the flame shapes recorded at low-speed shutter as shown in *Figure 6.1.1,* the appearance of the premixed flame recorded at the two speed shutters is slightly different. The reaction zone is still stable as recorded at the high-speed shutter, while the edge of the flame is wrinkled, which becomes more significant as Φ increases. This phenomenon is similar to the findings of Hargrave et al [4], i.e. the flame flicker. They stated that it is attributed to the development of a vortex ring in the shear layer of the flame, which increases in scale as it is carried downstream by the main flow.

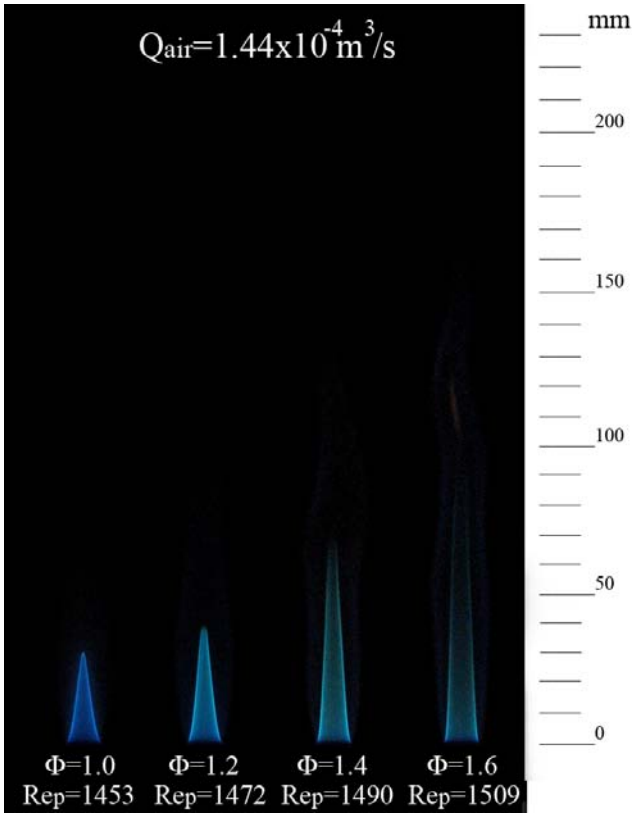

Figure 6.1.3. Direct photos recorded at high-speed shutter of the effects of varying fuel velocity on free jet premixed flame at Q_{air} = 1.44x10^{-4} m^3/s.

(b) Impinging Flame Jet

Figure 6.14 and *Figure 6.1.5* show the flame shapes of the premixed flame jet impinging upward onto a horizontal plate at H/dp of 1.5, 2, 3 and 4 with Re_p = 1453 and Φ = 1.0, and Re_p = 1472 and Φ=1.2, respectively. The two premixed flames are operated at the same flow rate of air supply, Q_{air} = 1.44x10^{-4}m^3/s. In these two cases, inner part of the reaction zone of the flame is impinging upon the stagnation point at H/dp = 1.5 and 2, tip of the reaction zone is impinging at the stagnation point at H/dp = 3, whereas tip of the reaction zone is unable to reach the stagnation point of the impingement plate at H/dp = 4. It

is also observed that, when Φ is increased from 1.0 to 1.2, the reaction zone is slightly lengthened, and the contact area between the premixed flame and the impingement plate is increased significantly.

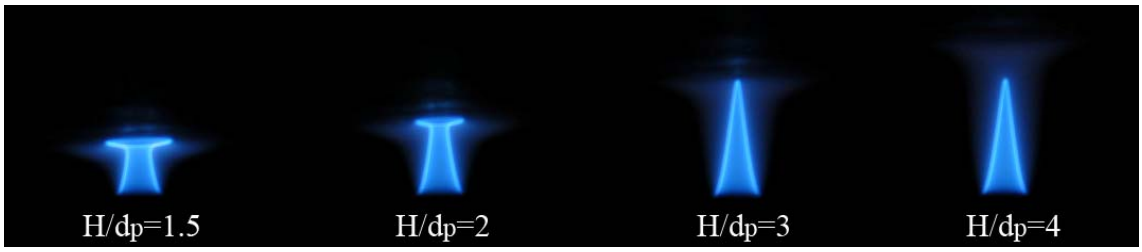

Figure 6.1.4. Direct photos, effects of varying H/d_p on impinging premixed flame jet at Re_p = 1453 and Φ = 1.0 (with constant Q_{air} = 1.44x10^{-4}m^3/s).

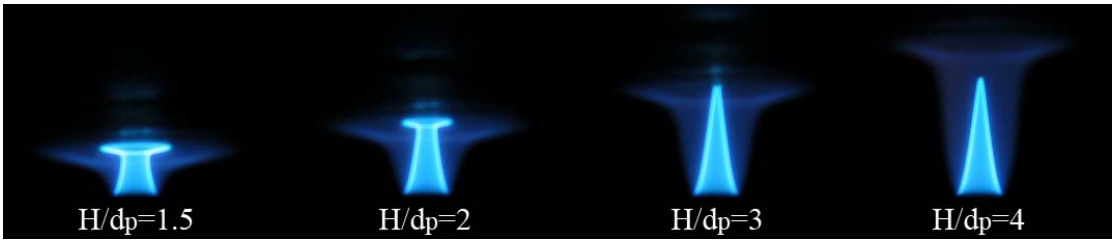

Figure 6.1.5. Direct photos, effects of varying H/d_p on impinging premixed flame jet at Re_p = 1472 and Φ = 1.2(with constant Q_{air} = 1.44x10^{-4}m^3/s).

6.1.2 Impinging Flame Temperature

(a) Stagnation Point Temperature Distributions

The flame temperature at the stagnation point was measured from H/d_p = 1 to 10 for the premixed flame with the conditions as shown in *Figure 6.1.1* and *Figure 6.1.2* correspondingly. *Figure 6.1.6 – Figure 6.1.9* show the stagnation point temperatures at the four fixed flow rates of air supply, respectively, with different Φs.

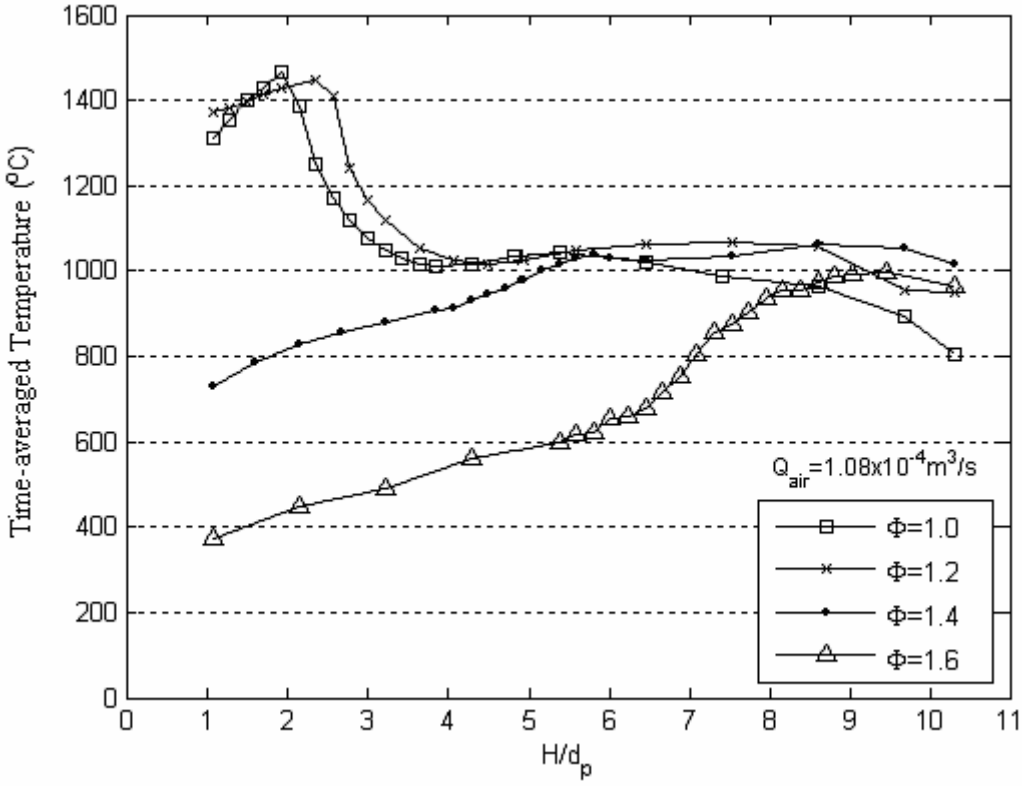

Figure 6.1.6. Stagnation point temperature profiles at different Φ with constant air flow rate Q_{air} = 1.08x10^{-4}m^3/s.

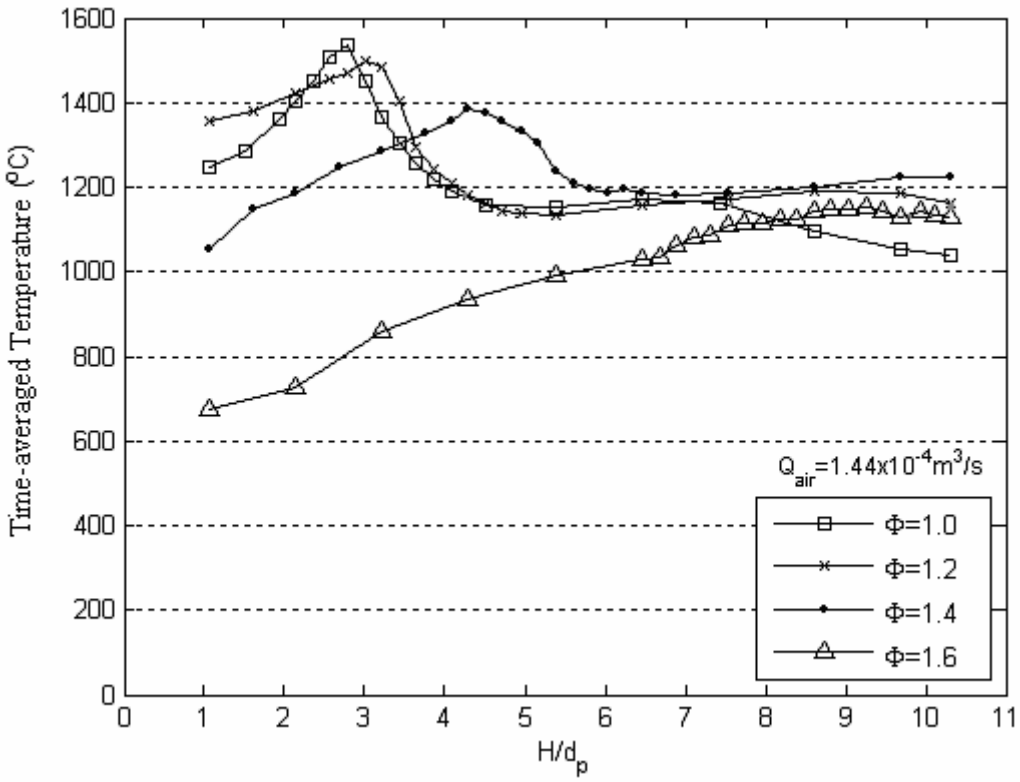

Figure 6.1.7. Stagnation point temperature profiles at different Φ with constant air flow rate Q_{air} = 1.44x10^{-4}m^3/s.

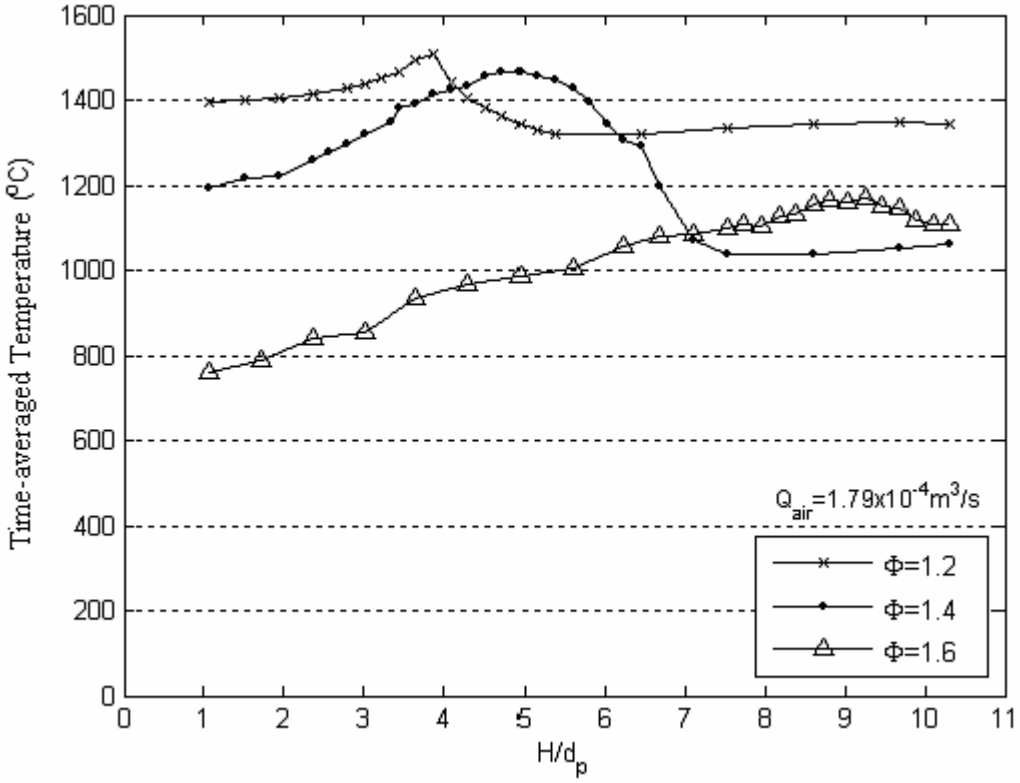

Figure 6.1.8. Stagnation point temperature profiles at different Φ with constant air flow rate Q_{air} = 1.79x10^{-4}m^3/s.

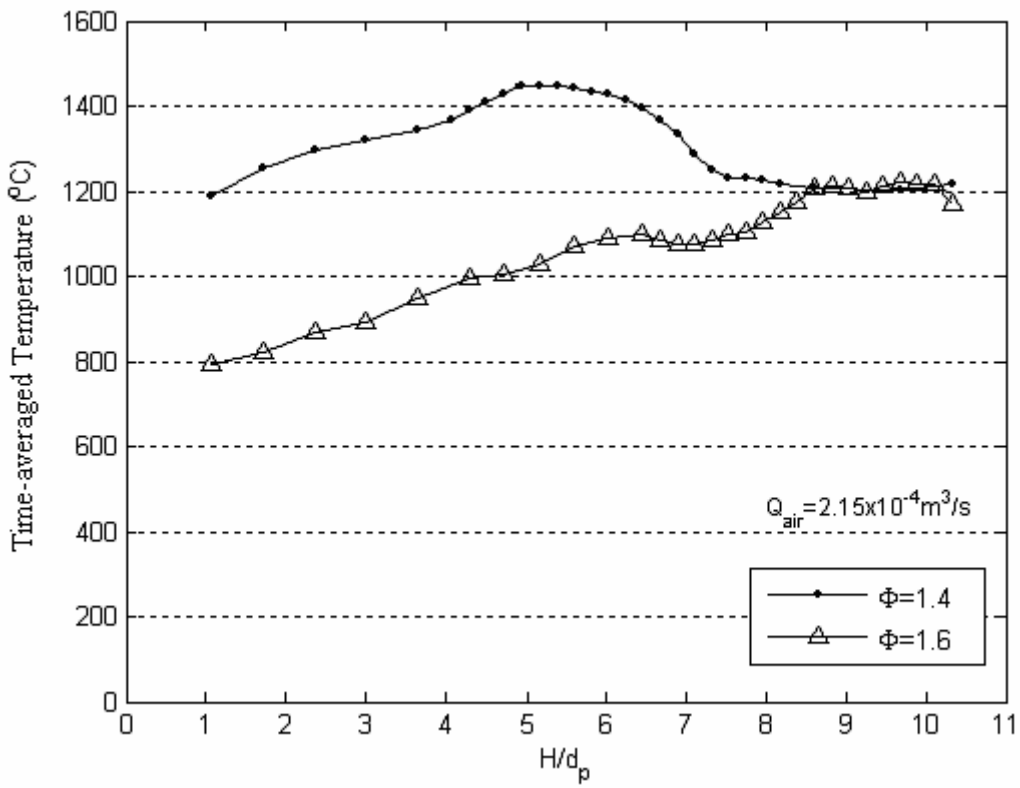

Figure 6.1.9. Stagnation point temperature profiles at different Φ with constant air flow rate Q_{air} = 2.15x10^{-4}m^3/s.

In these Figures, from H/d_p = 1 to 10, at Φ =1.0 and 1.2, the stagnation point flame temperature increases to a maximum value and decreases sharply and remains quite constant thereafter. However, at Φ = 1.0, the stagnation point flame temperature drops instead of keeping constant at higher values of H/d_p. When Φ is increased to 1.4, the stagnation point flame temperature also increases to a maximum value, but is only found at larger values of H/d_p. It then decreases gradually and remains quite constant with increasing H/d_p. When Φ is further increased to 1.6, the stagnation point temperature increases with the increasing nozzle-to-plate distance until H/d_p is around 8 – 9 and then decreases slightly thereafter. It is observed that, at constant Q_{air} and with higher

level of Φ, value of the maximum stagnation point flame temperature decreases at larger values of H/d_p.

Refer to the flame shapes as shown in *Figure 6.1.1* and *Figure 6.1.2*, the trends of the stagnation point temperature distribution can be explained. First, the sharp peak of the stagnation point temperature distribution occurs at the height slightly lower than the tip of the reaction zone for Φ = 1.0 and 1.2. Second, for the flame at Φ = 1.4 and 1.6, the tip of the reaction zone is opened due to the increasing fueling rate, hence the Re_p is increased. Therefore, the flame temperature is lower at the stagnation point. Third, a much larger nozzle-to-plate distance is needed to entrain more air from the surroundings so that sufficient air can be obtained to achieve a more complete combustion for the fuel-rich mixture, Φ = 1.2 – 1.6. As a result, value of the maximum stagnation point flame temperature decreases at larger values of H/d_p.

(b) Radial Temperature Distributions

In order to study the effects of the nozzle-to-plate distance on the flame temperature distribution on the impingement plate by the premixed flame, the radial temperatures were measured from r = 0mm – 50mm at H/d_p = 1.5 – 4 for the two conditions of Φ = 1.0 and Φ = 1.2 with the constant air flow rate Q_{air} = $1.44 \times 10^{-4} m^3/s$. The results are shown in *Figure 6.1.10* and *Figure 6.1.11*, respectively.

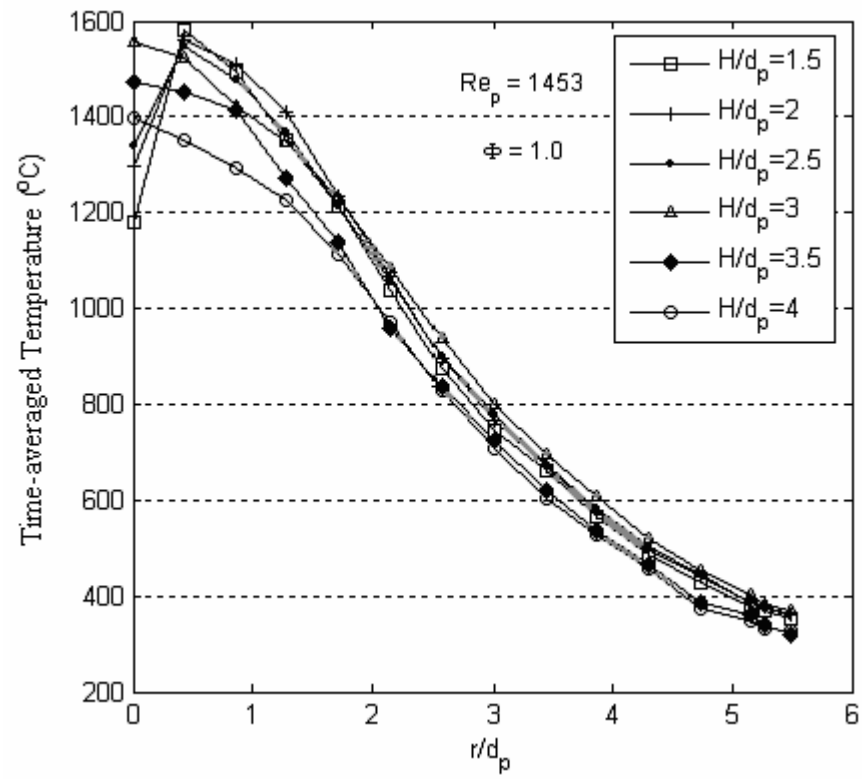

Figure 6.1.10. Radial temperature profiles at different H/d_p for $\Phi = 1.0$ and $Re_p = 1453$ with constant air flow rate $Q_{air} = 1.44x10^{-4}m^3/s$.

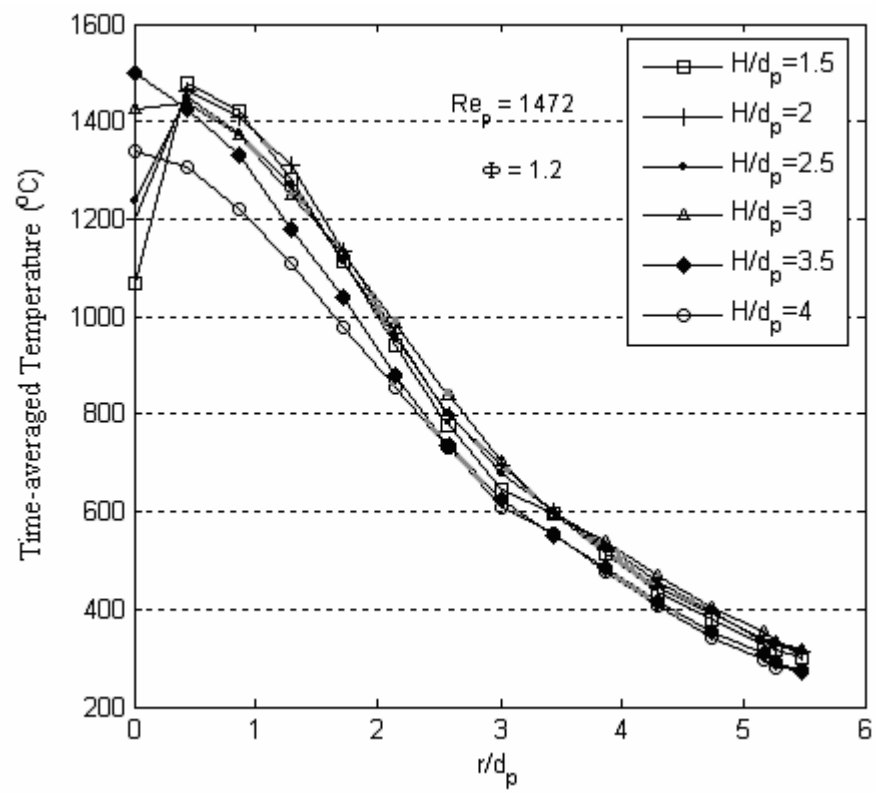

Figure 6.1.11. Radial temperature profiles at different H/d_p for $\Phi = 1.2$ and $Re_p = 1472$ with constant air flow rate $Q_{air} = 1.44x10^{-4}m^3/s$.

As observed from these *Figures*, at low values of H/d_p = 1.5, 2 and 2.5, the flame temperature near the stagnation point is low and the maximum temperature is at found r/d_p = 0.43. Then, temperature decreases gradually along the impingement plate. When H/d_p = 3 and 3.5, a bell-shaped temperature profile is obtained and the maximum temperature is found at the stagnation point. When H/d_p is further increased to 4, the temperature near the centerline drops significantly.

Refer to the impinging flame shapes as shown in *Figure 6.1.4* and *Figure 6.1.5*, it is clearly shown that the maximum temperature at each profile occurs at the region where the reaction zone strikes at the impingement plate. At H/d_p = 4, the impingement plate was impinged directly by the combustion gases only and not the reaction zone of the flame, therefore, low temperature was measured near the stagnation point of the plate.

6.1.3 Heat Fluxes

(a) Stagnation Point Heat Flux Distributions

The heat flux at the stagnation point was measured under the same conditions corresponding to the stagnation point temperature measurement as reported in the previous section. The results are presented from *Figure 6.1.12* to *Figure 6.1.15* for different Φs with the four fixed flow rates of air supply, respectively.

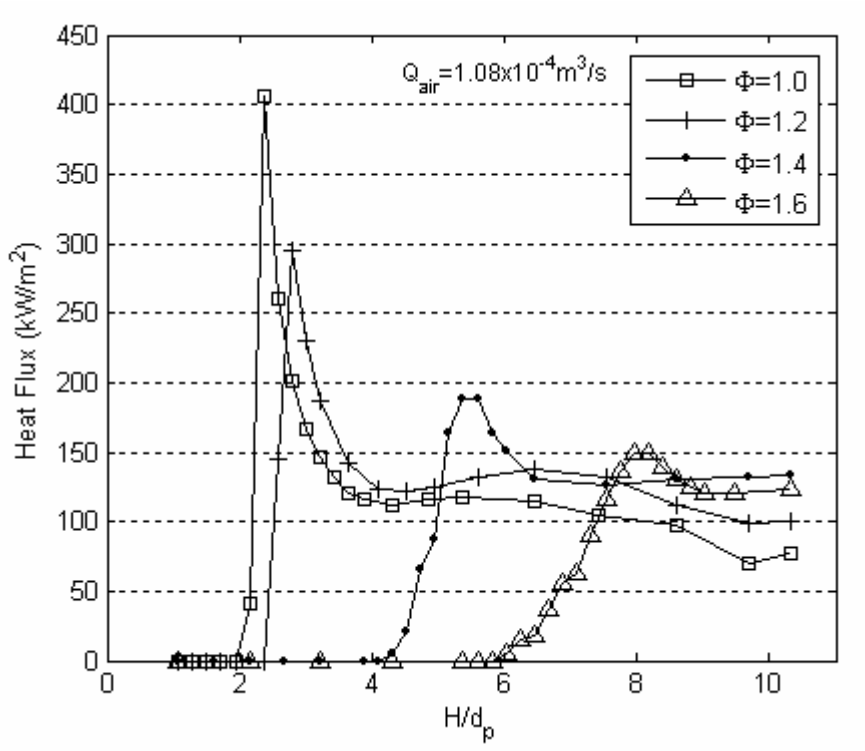

Figure 6.1.12. Stagnation point heat flux profiles at different Φ with constant air flow rate Q_{air} = 1.08x10^{-4}m^3/s.

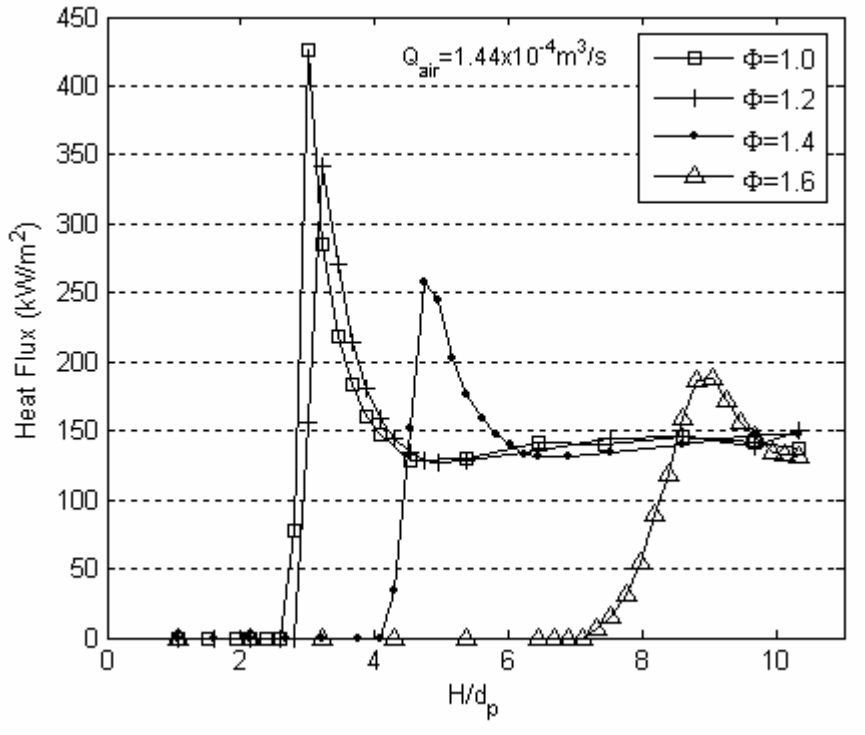

Figure 6.1.13. Stagnation point heat flux profiles at different Φ with constant air flow rate Q_{air} = 1.44x10^{-4}m^3/s.

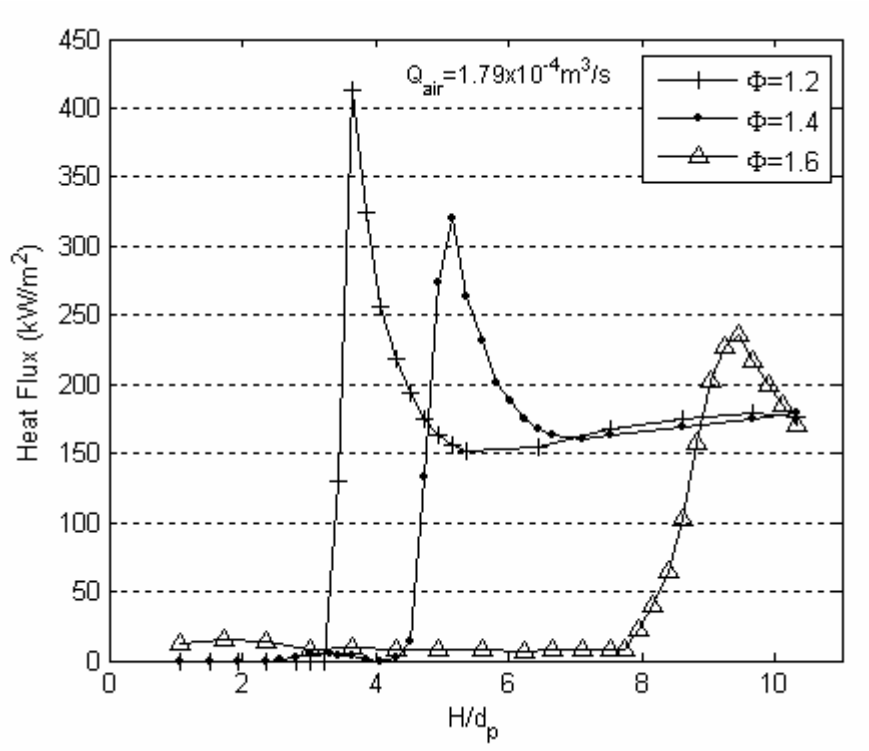

Figure 6.1.14. Stagnation point heat flux profiles at different Φ with constant air flow rate Q_{air} = 1.79x10^{-4}m^3/s.

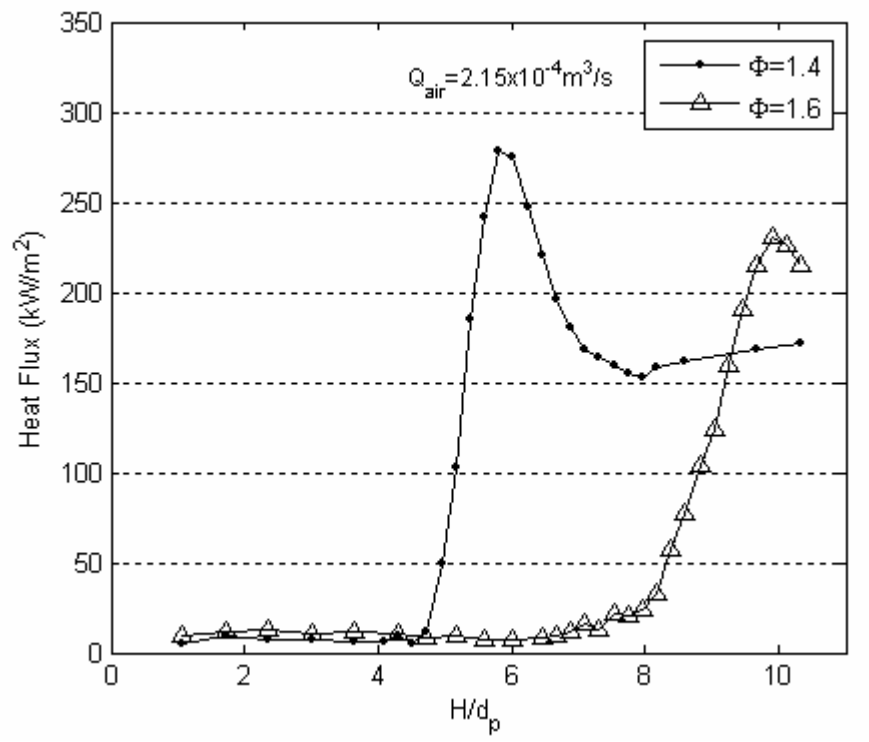

Figure 6.1.15. Stagnation point heat flux profiles at different Φ with constant air flow rate Q_{air} = 2.15x10^{-4}m^3/s.

It is observed from these figures that the stagnation point heat flux remains rather low at low values of H/dp, and then increases to a peak value as H/dp is increased for the range of Φ under consideration. For the profiles obtained at Φ = 1.0 – 1.4, the stagnation point heat flux reduces to a steady value instead of continues to increase as the H/dp is further increased. For the profiles at Φ = 1.6, the stagnation point heat flux remains very low across a large distance between the nozzle and the impingement plate and increases to a peak value at $H/d_p = 8$ for the four fixed air flow rates. Therefore, within the range of H/d_p being investigated, at Φ = 1.6, the stagnation point heat fluxes have not been observed to drop to the steady value. It is also observed that, at a fixed air flow rate and among the Φ being investigated, the peak stagnation point heat flux occurs at the lowest H/dp and the lowest Φ. In general, the peak heat flux drops at Φs and H/dps.

Refer to the flame shapes as shown in *Figure 6.1.4 and Figure 6.1.5*, at higher equivalence ratios the reaction zone of the premixed flame is lengthened due to the higher gas flow rate and hence a higher gas velocity. Thus, the peak of the reaction zone impinges directly upon the impingement plate at higher values of H/dp. In addition, a lower stagnation point temperature is obtained as the equivalence ratio increases beyond the stoichiometric value.

(b) Radial Heat Flux Distributions

The radial heat flux distribution on the plate impinged by a premixed flame jet is shown in Figure *6.1.16* and *Figure 6.1.17* at Φ = 1.0 and Φ = 1.2, respectively, under the same air flow rate, $Q_{air} = 1.44 \times 10^{-4} m^3/s$.

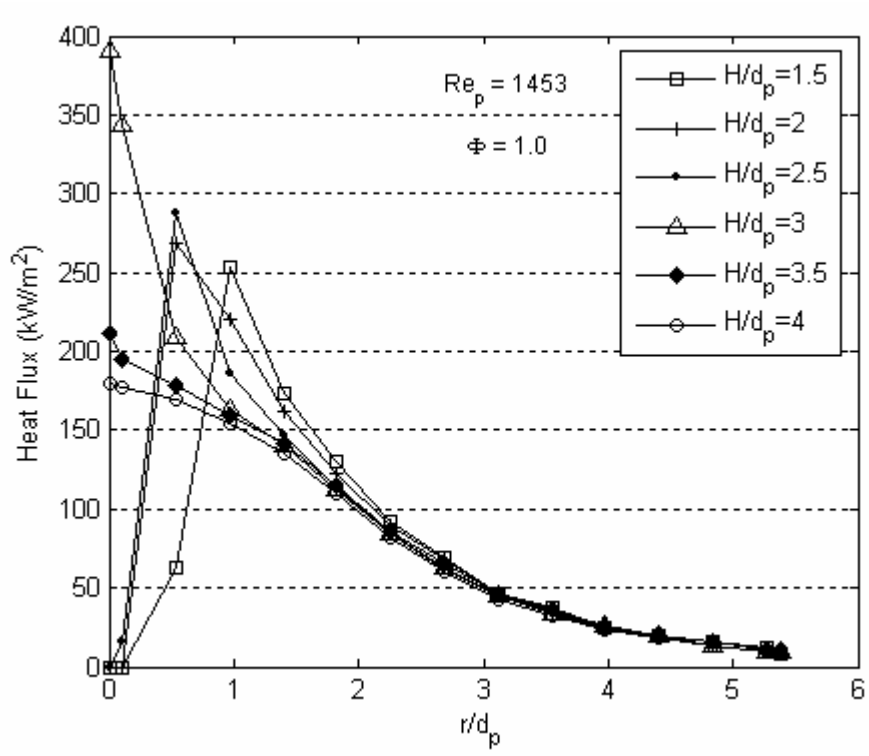

Figure 6.1.16. Radial heat flux profiles at different H/d_p for $\Phi = 1.0$ and $Re_p = 1453$ with constant air flow rate $Q_{air} = 1.44x10^{-4}m^3/s$.

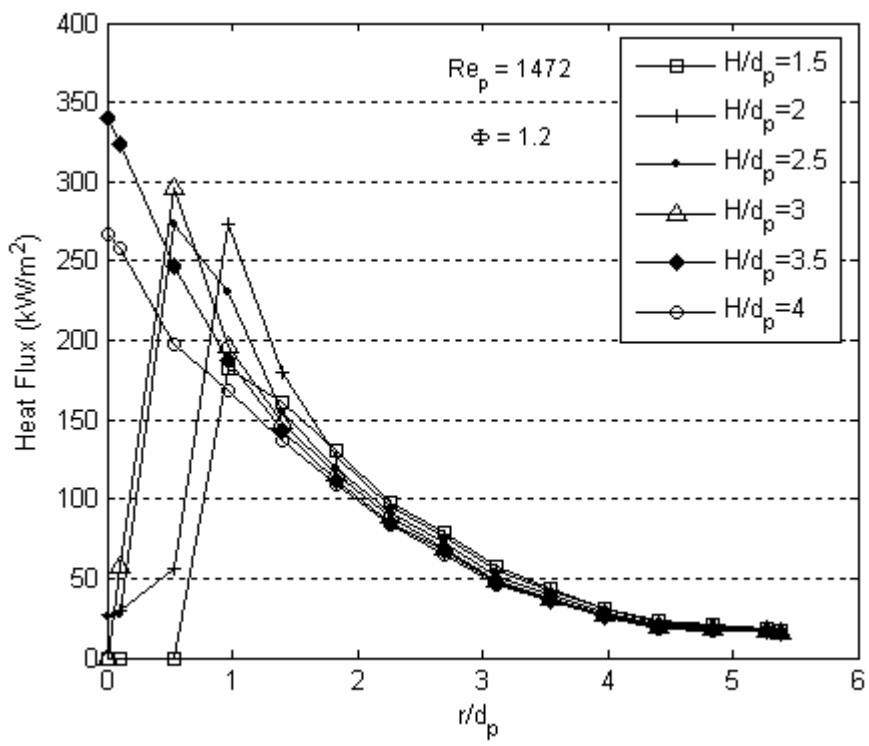

Figure 6.1.17. Radial temperature profiles at different H/d_p for $\Phi = 1.2$ and $Re_p = 1473$ with constant air flow rate $Q_{air} = 1.44x10^{-4}m^3/s$.

In *Figure 6.1.16*, the profiles show that the stagnation point is impinged upon by the cooler unburned gases at H/dp = 1.5, 2 and 2.5, by the peak of the reaction zone at H/dp = 3, and by the combustion gases at H/dp = 3.5 and 4. In Figure 6.1.17, the stagnation point is impinged by the tip of the reaction zone at H/d_p=3.5. Comparing the profiles, they are rather different at the stagnation point region but quite similar around the wall jet region.

6.1.4 Combustion Species Concentrations

The concentrations of the combustion species, including O_2, CO_2, CO, NO and HC were also measured for the premixed flame, using the test rig as shown in *Figure 3.1.3*. With the same method as used in measuring the combustion species concentrations of the IDF, the combustion gases were sampled through a tap with 1.5mm diameter at the center of the impingement plate. The flue-gas analyzer (Anapol EU-5000) was used for measuring the species concentrations. The O_2, CO_2, and CO concentrations were measured in percentage (%) and the NO and HC concentration were recorded in part per million (ppm).

Radial distributions of the combustion species concentrations were recorded at Φ = 1.0 and 1.2. In each case, flow rate of the air supplied to the premixed flame was the same, Q_{air} = $1.44 \times 10^{-4} m^3/s$, and the nozzle to plate distance were chosen at 1.5, 2 and 4.

Figure 6.1.18 and *Figure 6.1.19* show the radial concentration profiles of O_2 and CO_2 at Φ = 1.0 and 1.2, respectively. Under the two conditions of Φ, when H/d_p is increased, at the stagnation region and the early wall jet region the O_2 concentration shifts downwards while the CO_2 concentration shifts upwards. Since the contact area between the premixed flame and the impingement plate is small as observed from *Figure 6.1.4* and *Figure 6.1.5*, the O_2 or CO_2 concentrations are the same at $r/d_p = 3$ with different H/d_ps. Besides, when H/d_p is increased, more O_2 will be consumed in the intensive combustion leading to an increase in the CO_2 concentration.

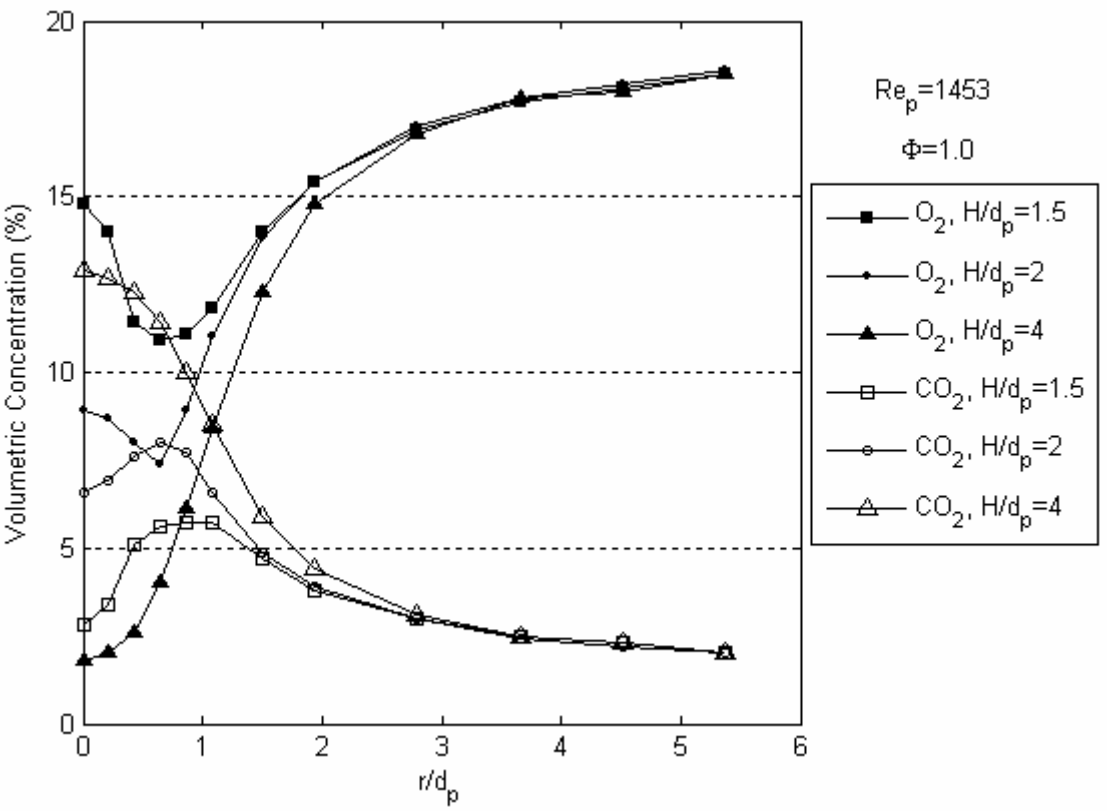

Figure 6.1.18. Distributions of the concentrations of O_2 and CO_2 under different H/d_p at Φ = 1.0 and R_p = 1453 with constant air flow rate Q_{air}= 1.44x10^{-4}m^3/s.

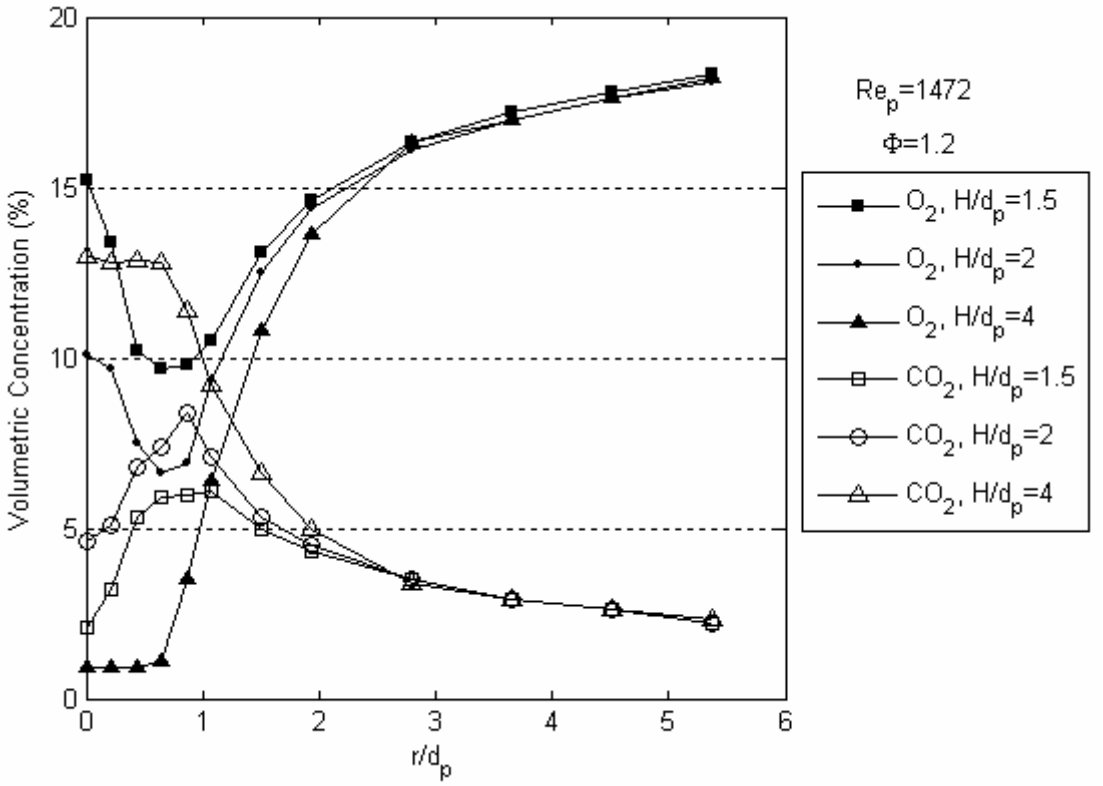

Figure 6.1.19. Distributions of the concentrations of O_2 and CO_2 under different H/d_p at $\Phi = 1.2$ and $R_p = 1472$ with constant air flow rate $Q_{air} = 1.44x10^{-4} m^3/s$.

When compare to the radial heat flux distributions as shown in Figure 6.1.16 and Figure 6.1.17, the trends of such profiles are similar to the CO_2 concentration profiles at the corresponding H/d_p. They increase from the centerline of the impingement plate to the peak values, which occur at $r/d_p = 0$, 0.6 and 1 with H/d_p = 1.5, 2 and 4, respectively, and then decrease exponentially. However, the intensive combustion indicated by the O_2 concentration occurs at $r/d_p = 0$, 0.6 and 0.7 for the values of $H/d_p = 1.5$, 2 and 4, respectively. Therefore, at low value of H/d_p = 1.5, the maximum heat flux occurs at the downstream of the intensive combustion region, which may be due to the cooling effect of the impingement of the unburned mixture upon the plate at the upstream.

With Φ increases from 1.0 to 1.2, the minimum value of O_2 concentration decreases while the maximum value of the CO_2 concentration increases at constant H/d_p. The increase in Φ means more fuel is supplied to the flame, thus, more O_2 will be consumed, leading to the increase in the CO_2 concentration.

Figure 6.1.20 and *Figure 6.1.21* show the CO concentrations with different H/d_ps at Φ = 1.0 and 1.2, respectively. In *Figure 6.1.20*, at Φ = 1.0 and H/d_p = 1.5 and 2, the plate is impinged by the mixture of air and fuel, leading to a higher level of CO production due to the combustion of a fuel-rich mixture. At a higher level of H/d_p = 4, there is more room for mixing of the air and fuel, leading to a lower level of CO due to leaner combustion conditions. In all cases, around the wall jet region, the CO formed during fuel-rich combustion is converted into CO_2. There is practically no CO beyond r/d_p of 3.

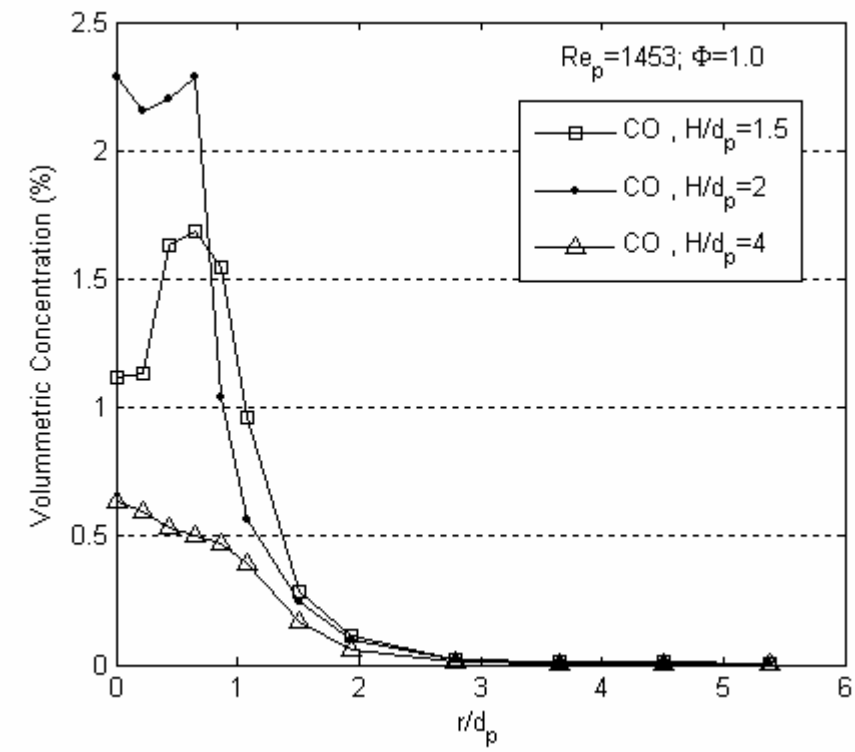

Figure 6.1.20. Distribution of the concentration of CO under different H/d_p at Φ = 1.0 and Re_p = 1453 with constant air flow rate Q_{air}= 1.44x10^{-4}m^3/s.

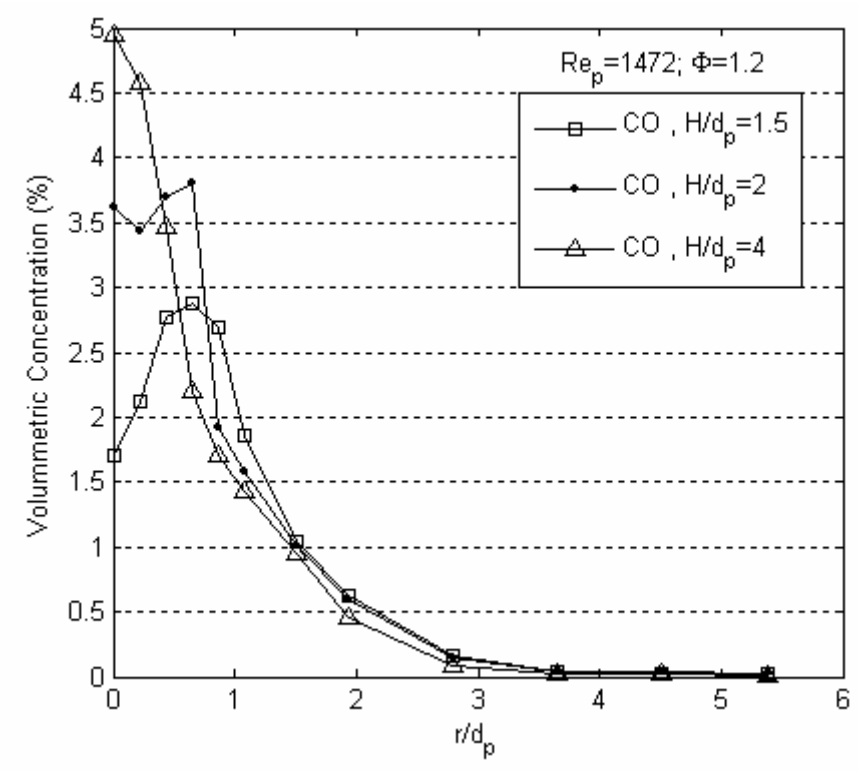

Figure 6.1.21. Distribution of the concentration of CO under different H/d_p at Φ = 1.2 and Re_p = 1472 with constant air flow rate Q_{air} = 1.44x10^{-4}m^3/s.

Compare *Figure 6.1.20* and *Figure 6.1.21*, the CO concentration increases obviously when Φ is increased. It is because at a fuel rich combustion, Φ=1.2, there is insufficient air supplied to support the complete combustion. Also, the CO concentrations at the stagnation region are still high when H/d_p = 4, which indicates that there is also insufficient O_2 for the CO to convert into CO_2.

The radial HC concentration distributions are shown in *Figure 6.1.22* and *Figure 6.1.23* for Φ = 1.0 and Φ = 1.2 respectively. It is observed that, at H/d_p = 1.5 and 2, very high HC concentration occurs at the stagnation point and a sudden and rapid decrease occurs thereafter. The measured HC concentrations at the stagnation point are 23400ppm, 12100ppm and 55ppm for Φ=1.0 and

28000ppm, 19200ppm and 39ppm for Φ = 1.2 at H/d_p = 1.5, 2 and 4, respectively. At r/d_p = 1, the HC concentrations drop to 276ppm, 119ppm and 52ppm for Φ = 1.0 and 240ppm, 152ppm and 48ppm for Φ = 1.2 at the corresponding H/d_p.

It is explained that, at H/d_p = 1.5 and 2, high HC concentrations are caused by the unburned air and fuel mixture impinging on the plate due to lack of space for flame development. When H/d_P is increased to 4, there is enough room for mixing of the air and fuel and subsequent combustion, hence the HC concentration is very low.

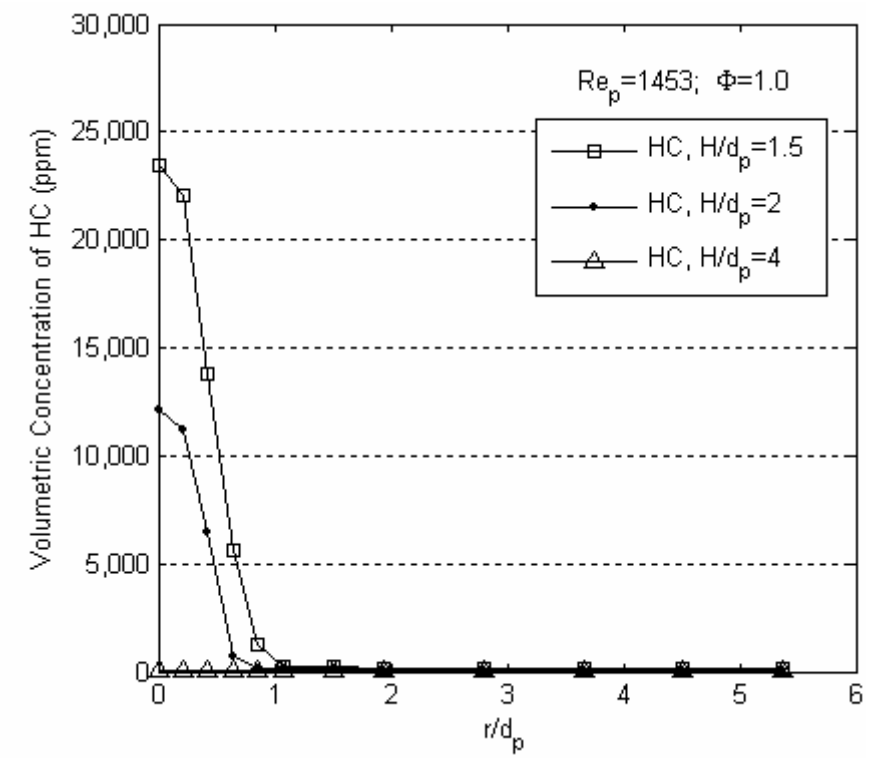

Figure 6.1.22. Distribution of the concentration of HC under different H/d_p at Φ = 1.0 and Re_p = 1453 with constant air flow rate Q_{air} = 1.44x10^{-4}m^3/s.

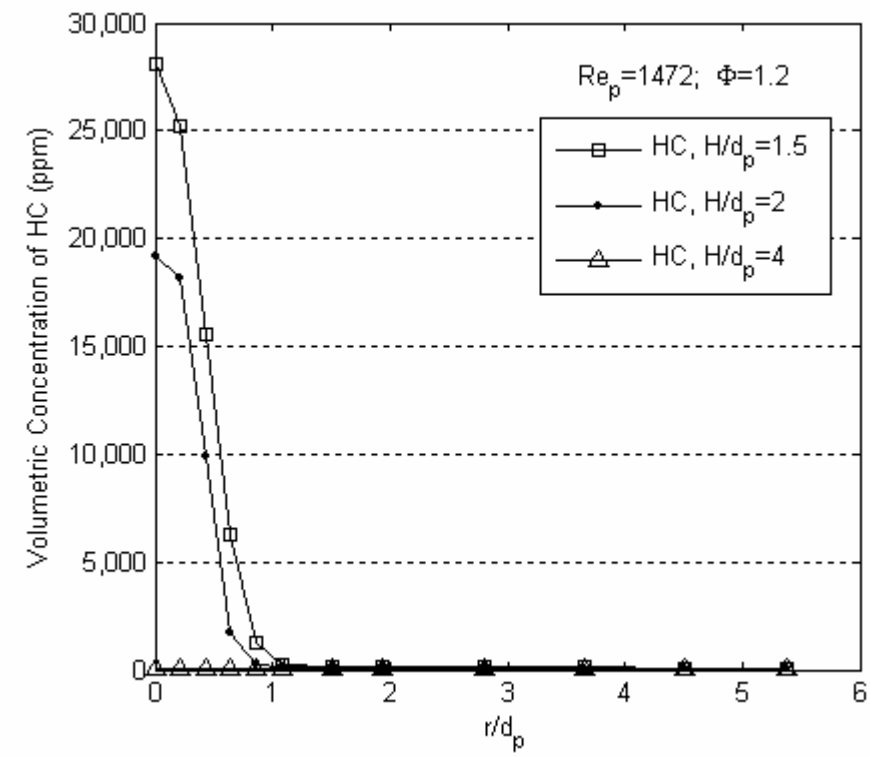

Figure 6.1.23. Distribution of the concentration of HC under different H/d_p at $\Phi = 1.2$ and $Re_p = 1472$ with constant air flow rate $Q_{air} = 1.44x10^{-4}m^3/s$.

When Φ is increased from 1.0 to 1.2, the HC concentrations increase at H/d_p = 1.5 and 2, because of the higher fueling rate at Φ = 1.2 causing more fuel to impinge on the plate while it is lacking of space for flame development. However, the HC concentrations are low and similar at Φ = 1.0 and 1.2 when H/d_p = 4, due to the availability of sufficient room for a more complete combustion to occur at these two values of Φ.

Figure 6.1.24 and Figure 6.1.25 show the NO concentration distributions of the impinging premixed flame at Φ = 1.0 and 1.2, respectively.

At H/d_p = 1.5 and 2, the NO concentrations are very low at the values of Φ = 1.0 and 1.2. There is less than 5ppm of NO at r/d_p < 3 and there is less than 1ppm of NO at r/d_p = 3 as observed in the Figures. This is due to the whole flame is relatively cool as it spreads along the plate with a significant proportion of unburned mixture of air and fuel at low values of H/d_p, and dilution effect occurs around the wall jet region. At H/d_p = 4, NO concentration is very high and there are 15ppm and 5ppm detected at r/d_p = 3 for Φ = 1.0 and Φ = 1.2, respectively. It is because the flame temperatures at this H/d_p are high, and at the same time, the stagnation point flame temperature distributions show that the temperatures are very high at 2.5 < H/d_p < 4, hence increase the residence time.

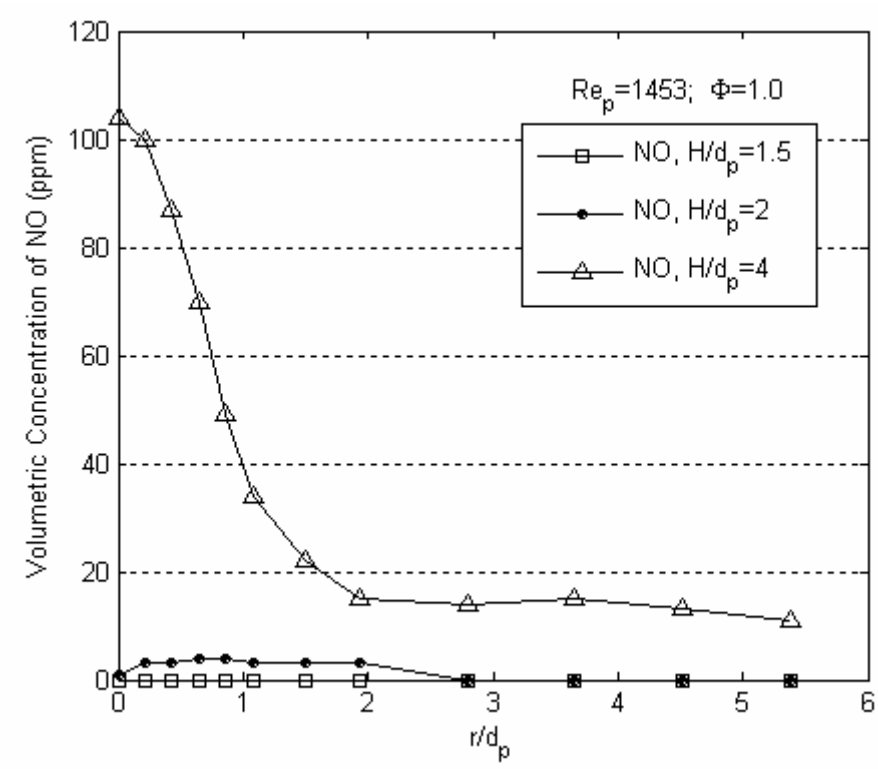

Figure 6.1.24. Distribution of the concentration of NO under different H/d_p at Φ = 1.0 and Re_p = 1453 with constant air flow rate Q_{air} = 1.44x10^{-4}m^3/s.

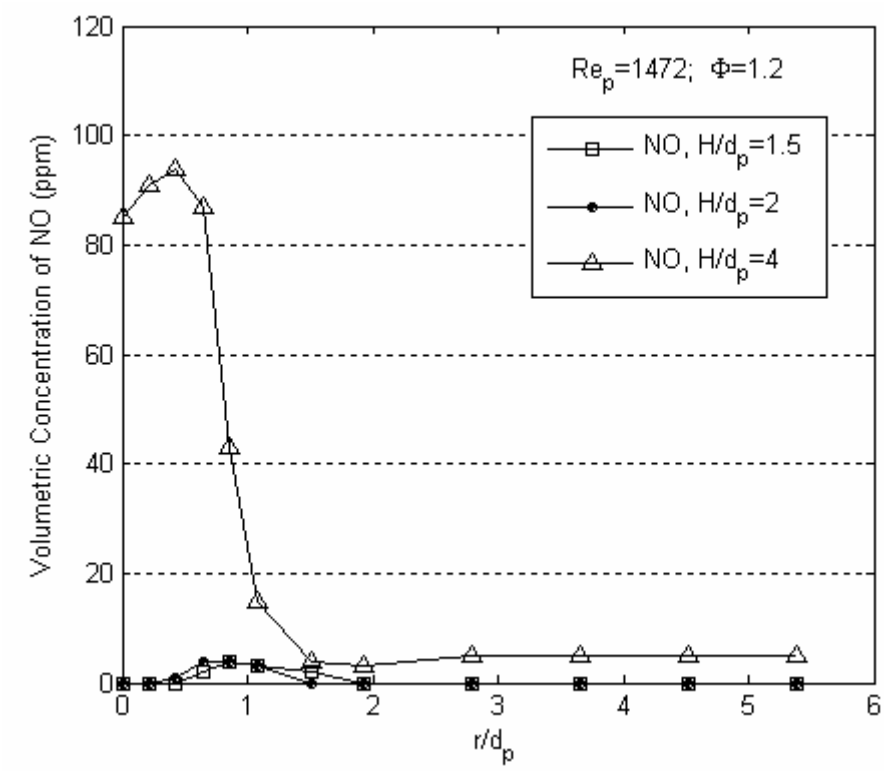

Figure 6.1.25. Distribution of the concentration of NO under different H/d_p at $\Phi = 1.2$ and $Re_p = 1472$ with constant air flow rate $Q_{air} = 1.44x10^{-4}m^3/s$.

It is observed that, the NO concentration decreases with Φ. From the radial flame temperature profiles, the flame temperature decreases with Φ, hence, lower NO concentration. The Figures also show that the peak NO concentration occurs at the region of the most intensive combustion as indicated by the corresponding O_2 concentration.

When referring to the heat flux distribution, it is found that high heat fluxes are found in the reaction zone coincided with high concentrations of CO, NO and CO_2 and very low concentrations of O_2. The result is well agreed with the finding of Dong et. al [52], who investigated a premixed slot butane/air flame impinging jet.

6.2 Comparison of thermal and emission performances between IDF and premixed flame

6.2.1 Flame Shape Observations

Comparing the photos of the premixed flame jet obtained using the low speed shuttle (refer to *Figure 6.1.2* to *Figure 6.1.5)* and the free IDF jet (refer to *Figure 4.1.7*), the flame shapes are different and the flame structure of the premixed flame is simpler. At the same flow rates of air and fuel supplies, the premixed flame is observed to be longer. The reaction zone is elongated more significantly for the premixed flame when Φ is increased and the flow rate of air supply is maintained constant. The reaction zone of a premixed flame has a rather thin outer layer when it is compared to that of the free IDF jet. In addition, a less brilliant orange flame is observed for the premixed flame jet.

When compared to the free IDF jet as shown in *Figure 4.1.7*, the premixed flames are more stable than the IDF as shown by the photos recorded at the high-speed shutter.

For both the impinging IDF and premixed flame jets, it is observed that the flame impinges at the wall jet region is not as large as expected. This is due to the quenching effect when the hot flame is impinging upon the cool impingement plate surface.

6.2.2 Flame Temperatures

The profiles of the flame temperature at the stagnation point of the plate impinged upon by a premixed impinging flame jet (refer to *Figure 6.1.6* to *Figure 6.1.9*) are significantly different from those of the impinging IDF jet (refer to *Figure 5.2.2* to *Figure 5.2.5*). For the four fixed air flow rates, the premixed flames have higher peak stagnation point temperatures at Φ = 1.0 and 1.2 than the IDFs operating with the same flow rates of air and fuel supplies, but a reverse senior occurs when Φ is increased to 1.4 and 1.6. It is also observed that the H/dp, at which the peak stagnation point temperature is obtained, increases when Φ is increased for the premixed flame jet. While the peak stagnation point temperatures occur at rather similar H/d_{IDF} when Φ is increased from 1.0 to 1.6 for the IDF jet.

The radial temperature profiles on the impingement plate impinged upon by either the premixed flame jet (refer to *Figure 6.1.10* and *Figure 6.1.11*) or the IDF jet (refer to *Figure 5.2.10* to *Figure 5.2.13*) are similar. It is observed that: when the same air and fuel flow rates are supplied, the premixed flames have higher peak radial temperature than the IDFs at Φ = 1.0 for the range of nozzle-to-plate distances under consideration. However, lower peak radial temperature is obtained at Φ = 1.2 for the premixed flame.

6.2.3 Heat Fluxes

Profiles of the stagnation point heat flux of the premixed impinging flame (refer to *Figure 6.1.12* to *Figure 6.1.1*5) are also different significantly from those of the impinging IDF (refer to *Figure 5.2.21* to *Figure 5.2.24*). Comparing the values of the peak stagnation point heat flux of the premixed flames with those of the IDFs, they are always higher at Φ = 1.0 and 1.2, but rather similar at Φ = 1.4 and even lower at Φ = 1.6, for the four fixed air flow rates.

Again, the H/dp, at which the peak stagnation point heat flux occurs, increases rather significantly when Φ is increased. While the peak stagnation point heat fluxes for the IDFs occur at rather similar H/d_{IDF} when Φ is increased from 1.0 to 1.6.

At the same flow rates of air and fuel supplies, the premixed flame (refer to *Figure 6.1.16* and *Figure 6.1.1*7) and the IDF (refer to *Figure 5.2.27* and *Figure 5.2.28*) have quite different radial heat flux profiles. At low values of nozzle-to-plate distance, the radial heat flux of the premixed flame increase sharply to the maximum value when r/d_p is increased, while the radial heat flux of the IDF increases gradually to the maximum value when r/d_{IDF} is increased. At high values of nozzle-to-plate distance, the radial heat flux of the premixed flame decreases steeply from the centerline of the impingement plate. While it decreases only gently for the IDF. Besides, the premixed flames have lower radial heat fluxes at the wall jet region as observed in the corresponding Figures. Thus, the energy is spread more uniformly along the plate and is transferred to the wall jet region for the IDF.

6.2.4 Combustion Species Concentrations

Comparing the radial combustion species concentration distributions of the premixed flame jet with those of the IDF jet, in general, the premixed flames have a more intensive combustion near the stagnation point as indicated by the O_2 concentrations (refer to *Figure 5.2.35* to *Figure 5.2.37* for IDF and *Figure 6.1.18* and *Figure 6.1.19* for premixed flame).

Among the different nozzle-to-plate distances, premixed flames have higher CO concentrations as observed from the corresponding Figures (refer to IDF *Figure 5.2.38* to *Figure 5.2.40* for IDF and *Figure 6.1.20* and *Figure 6.1.21* for premixed flame), which indicates that combustion in the premixed flame is less complete than that in the IDF. Such incomplete combustion senior is also indicated by the HC concentrations for the premixed flame (refer to *Figure 5.2.38* to *Figure 5.2.40* for IDF and *Figure 6.1.22* and *Figure 6.1.23* for premixed flame), there is more than 40 ppm found in the radial distance at $H/d_p = 4$ for the premixed flame, while less than 20 ppm found at $H/d_{IDF} = 10$ for the IDF, at both $\Phi = 1.0$ and 1.2. It can be explained that the chemical reactions with the secondary air by the unburned fuel along the impingement plate is more significant in the IDF. On the one hand, the CO formed is gradually converted into CO_2 in the wall jet region; and on the other hand, the unburned fuel reacts with the secondary air, hence lower HC concentration is also obtained along the wall jet region.

The NO concentration for the premixed flame at $H/d_p = 4$ is very high when compared with that for the IDF at $H/d_{IDF} = 10$ (refer to *Figure 5.2.41* to *Figure 5.2.43* for IDF and *Figure 6.1.24* and *Figure 6.1.25* for the premixed flame). It is because the peak temperatures at the stagnation point and also the radial distance for the premixed flame at $\Phi = 1.0$ and 1.2 are both higher than those for the IDF. The very high NO concentration detected in the premixed flame is resulted from both the high local flame temperature and the long residence time from the very high flame temperature at $2.5 < H/d_p < 4$.

It can be observed that, the cool core zone inside the IDF has a greater effect on the heat being transferred to the plate when compare to the unburned gas inside the premixed flame. For the IDF, the maximum heat flux occurs at the downstream of the intense combustion region indicated by the O_2 and CO_2 concentration profiles when the nozzle-to-plate distance is small. However, for the premixed flame, high heat fluxes are always found in the reaction zone coinciding with high concentrations of CO, NO and CO_2 and very low concentrations of O_2.

6.2.5 Area-averaged Heat Flux and Heat Transfer Efficiency

The effects of nozzle-to-plate distance on the area-averaged heat flux and the heat transfer efficiency of the premixed flame are provided in Figure 6.2.1 and Figure 6.2.2, respectively. Since the premixed flame can release more heat at a smaller nozzle-to-plate distance than the IDF, the area-averaged heat flux and the heat transfer efficiency are compared at different ranges of nozzle-to-plate distance. Each of them is corresponding to the range at which respective intensive combustion is obtained for the flame under consideration. The heights chosen for the premixed flame are H = 14 – 37.2 mm (corresponding to H/dp = 1.5 – 4), and that for the IDF are H = 24 – 60 mm (corresponding to H/d_{IDF} = 4 – 10). Figure 6.2.1 and Figure 6.2.2 show the area-averaged heat flux and the heat transfer efficiency of the two flames operating at Φ = 1.0 and Φ = 1.2 under the same air flow rate of $Q_{air} = 1.435 \times 10^{-4}$ m^3/s, which is corresponding to Re_{air} = 2000 for the IDF.

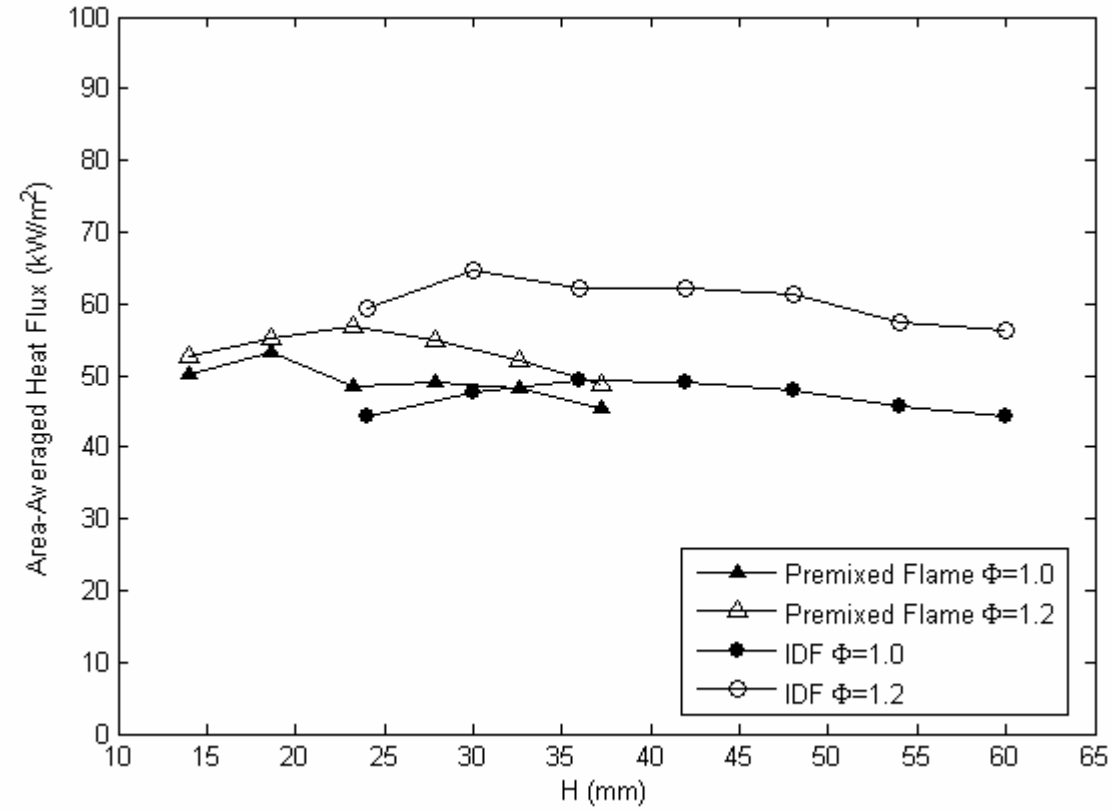

Figure 6.2.1. Comparison of area-averaged heat flux for the premixed flame and the IDF under identical volume flow rates of air and fuel.

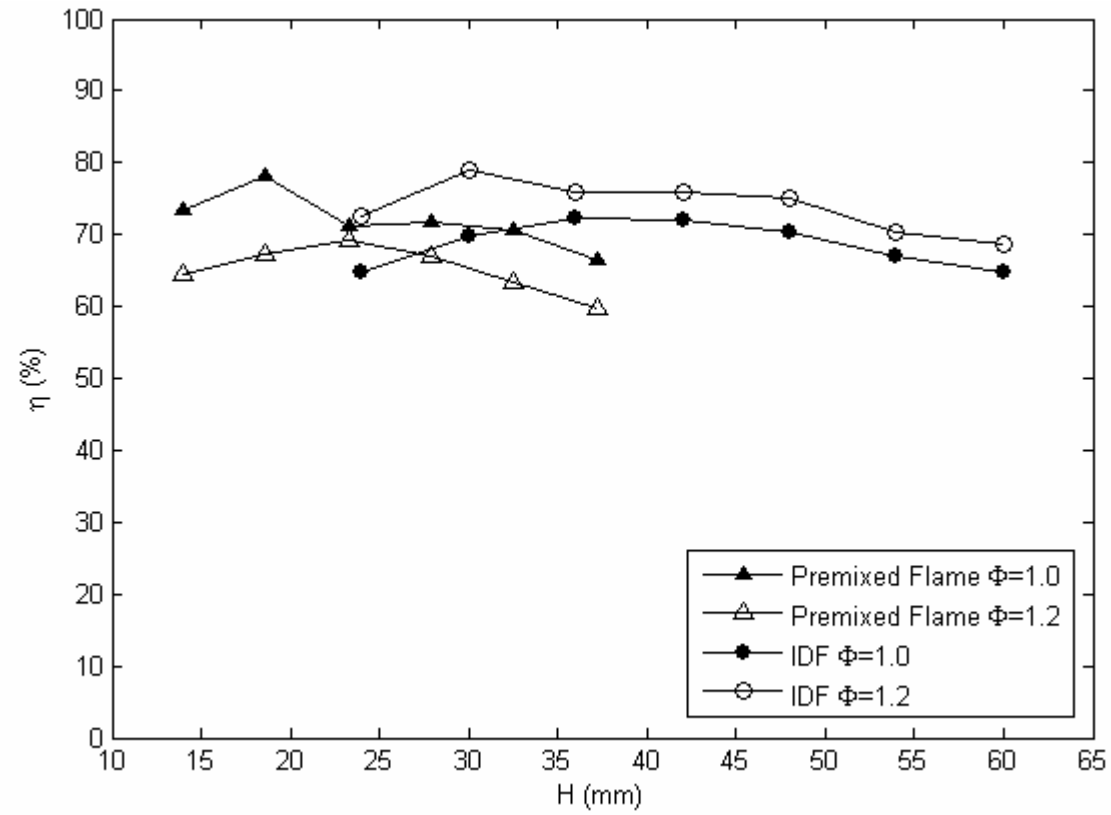

Figure 6.2.2. Comparison of heat transfer efficiency for the premixed flame and the IDF under identical volume flow rates of air and fuel.

From the above figures, it is observed that for each flame type there are certain variations in the area-averaged heat flux and the heat transfer efficiency with different nozzle-to-plate distances within the range under consideration. At Φ = 1.0, the premixed flame has higher area-averaged heat flux and heat transfer efficiency than the IDF. For the premixed flame, the highest heat transfer efficiency of 78.1% is obtained at H = 8.6mm (corresponding to H/dp = 2), at which the impingement surface is slightly lower than the tip of the reaction zone. The results agrees with the finding of Hou and Ko [42]. The lowest heat transfer efficiency of the premixed flame is 66.3%. Thus, there is a difference of 11.8% over a nozzle-to-plate distance of 23.2 mm. For the IDF, the maximum heat transfer efficiency is only 72.1% at H/d_{IDF} = 6 while the lowest heat transfer efficiency is 64.7%. Thus, there is a difference of 7.4% over a nozzle-to-plate distance of 36 mm.

When Φ is increased to 1.2, the area-averaged heat fluxes of both flames increase. For the same increase in the fuelling rate, the area-averaged heat flux has been increased by an average of 13.7 kW/m^2 for the IDF, but for the premixed flame, the average increase is only 4.3 kW/m^2. This results in an increase in the heat transfer efficiency of the IDF and a reduction in the premixed flame, compared with their corresponding values at Φ = 1.0. The maximum heat transfer efficiency of the IDF is 79.0% at H/d_{IDF} = 5 while for the premixed flame, the maximum heat transfer efficiency drops to 69.2% at H/d_p = 2.5.

An observation of the flames shows that the IDF at Φ = 1.0 is in fact fuel lean while at Φ = 1.2, the flame appears closer to a stoichiometric condition. However, for the premixed flame it is at the stoichiometric condition at Φ = 1.0 but becomes fuel rich at Φ = 1.2. Therefore, there is an increase in the heat transfer efficiency of the IDF but a decrease for the premixed flame when Φ of the flame is increased from 1.0 to 1.2. Figure 6.2.2 shows that the heat transfer efficiency of the IDF at Φ = 1.2 is even higher than that of the premixed flame at Φ = 1.0 over the range of nozzle-to-plate distance under investigated.

Thus, the heat transfer efficiency of a premixed flame is more sensitive to the nozzle-to-plate distance than the IDF. The IDF appears to have the advantage of having higher heat transfer efficiency than its counterpart over a large range of nozzle-to-plate distance.

6.3 Summary

The premixed flame consists of a thin layer of reaction zone which appears to be a sharp boundary between the inner unburned gases and the outer burned gases. The premixed flame is observed to be more stable than the IDF from photos of the flame obtained by using high speed shutter.

Comparing the results obtained from the IDF with those of the premixed flame indicates rather different stagnation point flame temperatures, stagnation point heat fluxes and radial heat flux profiles existed between them. While the radial flame temperature profiles are rather similar between these two flame types. The sharp increases of the flame temperature and heat flux at the stagnation point of the impingement plate impinged upon by a premixed flame show its ability to achieve intensive combustion within a shorter nozzle-to-plate distance. While the gradual increases of these parameters at the stagnation point of the IDF shows the intensive combustion is obtained over a longer nozzle-to-plate distance.

Considering the radial profiles, the premixed flame has a rather high peak value of flame temperature and a sharp peak value of heat flux near the stagnation point of the impingement plate, whereas the IDF has relatively high values for these two parameters around the wall jet region. Thus, the fuel energy is spread more uniformly along the plate and a significant proportion is transferred to the wall jet region for the IDF.

Comparing the concentrations of the combustion species of the IDF with those of the premixed flame, the O_2 concentration shows that the premixed flame has a more intensive combustion near the centerline, but more incomplete and poorer combustion is also indicated at the same time by the high values of CO and HC concentrations. Also, the NO concentration of the premixed flame is higher at the post-combustion flame zone.

By considering the heat flux and the corresponding combustion species measurements, the cool core zone inside the IDF cools the heat generated in the partially premixed flame zone. It has a greater effect on the heat being transferred to the plate when compare to the unburned gas inside the premixed flame. Therefore, the maximum heat flux occurs at the downstream of the intense combustion region at low value of H/d_{IDF}; and for the premixed flame, high heat fluxes are always found in the reaction zone coinciding with high concentrations of CO, NO and CO_2 and very low concentrations of O_2.

When Φ increases from 1.0 to 1.2, the premixed flame has a slightly increase in the area-averaged heat flux, while the IDF has a more significant increase. However, the heat transfer efficiency of the premixed flame has a peak value of 78.1% at Φ = 1.0 and H/dp = 2. It decreases at higher Φ and higher or lower H/dp. The IDF has a peak value of 79% at Φ = 1.2 at H/d_{IDF} = 5, which indicates that the flame appears to behave as a stoichiometric flame.

As a result, the premixed flame has a better thermal performance at the particular nozzle-to-plate distance when Φ=1. However, it has a more narrow range of flammability, within which the flame will be blown out at high Reynolds numbers and low equivalence ratios. The IDF has wider range of flammability, which can be ignited within the experimental conditions under consideration. Relatively high heat transfer rates can also be maintained over a large range of nozzle-to-plate distances. Results obtained from the species concentration measurement show that the IDF has lower emissions including CO_2, CO, HC and NO.

Chapter 7 Conclusions

In this study, the main objective was to investigate the thermal and emission characteristics of an inverse diffusion LPG flame in the form of a free jet and when impinging on a flat plate experimentally. Effects of the Re_{air}, Φ and H/d_{IDF} were examined. In the studies of thermal performance of the impinging IDF, the area-averaged heat flux and the heat transfer efficiency were also examined. The results of the impinging IDF were compared with the impinging premixed flame jet (round) on the thermal and emission characteristics and also the thermal performance.

Five tasks as specified as the main objective of this study were successfully achieved. In the experiments, the profiles at both axial and radial distribution of heat flux evident the IDF's wide range of flammability. The relatively high heat transfer can be maintained over large range of H/d_{IDF}. Also, the pollutant emissions of the IDF are low and it can achieve relatively high heat transfer efficiency at the optimum operating conditions.

When compare to a premixed impinging flame, the IDF seems to have the advantage of having higher heat transfer efficiency than the premixed flame over a rather large range of nozzle-to-plate distance with lower pollutant species emissions. As a result, the impinging IDF is a cleaner flame with wider range of flammability. It is suggested as a better flame for surface heating and the IDF may be very useful in the applications in both industrial and domestic.

The results in this study are concluded at the following sections.

7.1 IDF – Free Jet Experiments

The flame structure of the CAP IDF as a free jet is divided into a base zone and an elongated main flame zone separated by a neck region formed by the low pressure created by the central high momentum air jet. At the elongated main flame zone, a reaction zone with premixed combustion is found enclosing a cool core zone and enclosed by a post-combustion flame zone at the same time, in which, the zones characteristics can be identified by the axial and radial mean and rms fluctuation temperature distributions.

The flame length and the heights of the base zone, cool core zone and the diffusion zone increase when Φ increases. The direct image of the flames show that more brilliant orange flames are observed in the post-combustion flame zone and the neck region at higher level of Φ with lower Re_{air}. These are due to more fuel supplied at fixed air flow rate and poorer fuel inducement effect with decreasing $Re_{air.}$

When high-speed shutter of 1/1000 second exposure time is used to record the flame images, complex flows are found at the elongated main flame zone. The intense mixing at the neck region leads to the instabilities in the downstream of the flame, where increasing scale of vortexes are covected. By observing the flame images, it is believed that the flow in the base zone is laminar, while the flow in the elongated main flame zone is turbulent.

At higher values of $H/d_{IDF,}$ the flame temperature increases in both axial and radial directions as Re_{air} increases, while this effect is more significant in the axial direction. It is also found that the emissions of free jet IDFs are low. The CO concentration is zero, except of the case Re_{air}=3000. Among the investigated Re_{air} and Φ=1, the NO concentration is about 20ppm in the exhaust gas.

7.2 IDF – Impinging Jet Experiments

When the IDF is under impinging, the part of the flame below the horizontal flat plate is not much affected. The structure of the flame impinged on the plate can be divided into 2 parts: a stagnation region, where the flame just reaches the plate before distortion; and a wall jet region, where the part of the flame above the plate is highly distorted and spread horizontally along the plate.

Basically, both of the flame temperature and the heat flux of the impinging IDF increases with either Re_{air} or Φ ($0.8 \leq \Phi \leq 1.6$) is increased, because the increase in these two parameters means the fueling rate is increased. For the stagnation point distributions, the maximum stagnation point heat flux at any Φ occurs with the maximum stagnation point temperature correspondingly at the similar H/d_{IDF}. However, the stagnation point flame temperature decreases gradually after reaching the peak value, while the stagnation point heat flux drops obviously once after reaching the peak value. In other words, after the peak value, the heat transferred to the plate is limited even there is still a high flame temperature. The heat flux is affected by the gas

temperature as well as other parameters, for example, the convective heat transfer coefficient. In such case, the drop in heat flux is due to the weakened convective heat transfer coefficient rather than the gas temperature.

For the radial distributions, both of the flame temperature and the heat flux are low near the centerline when either Φ or H/d_{IDF} is low, which indicate the effect of the central cool core zone. When H/d_{IDF} increases, at fixed value of Φ, the flame temperature and the heat flux near the centerline increase and the radial profile becomes bell-shaped. The temperature and the heat flux distributions are affected by the nozzle-to-plate distance near the centerline, but only slightly affected in the wall jet region.

Besides that, in the combustion species analysis in the impinging IDF, when either Re_{air} or Φ is increased, the O_2 concentration decreases while the CO_2, CO and NO concentrations increases. That means, when there is more fuel supplied ($0.8 \leq \Phi \leq 1.2$), more O_2 is consumed and more intense combustion occurs leading to produce high flame temperature, hence high level of NO. However, the combustion becomes more incomplete when Φ=1.8 as there is insufficient O_2. Therefore, CO concentration increases due to the dissociation of CO_2 increases under high flame temperature. In any radial profiles, the intense combustion is indicated by the lowest value of O_2 level, where the highest values of NO, CO_2 and CO levels were found. Such findings are agreed with Sze [2].

The concentration of HC evident that the fuel is forced to impinge and spread along the plate by the air jet for the flame at Φ=0.8 and more fuel is accumulated along the plate at lower Re_{air} (Re_{air}=2000). When the fuel is too rich (Φ=1.8), the unburned fuel is also forced to spread along it. The HC concentration shows that the flame at Φ=0.8 is processing a very incomplete combustion, while the most complete combustion is occurred at Φ=1.2.

Both Φ and H/d_{IDF} influence the heat transfer mainly at the stagnation region. At low value of H/d_{IDF}, the maximum heat flux occurs at the downstream of the intense combustion region indicated by the O_2 and CO_2 concentration profiles. This may due to the effect of the cool core. When H/d_{IDF} increases, the effect of the cool core decreases. Therefore, the intense combustion region and the maximum heat flux occur at the same location.

In general, the calculated area-averaged heat flux increases with Re_{air} and Φ since both imply an increase in the fueling rate. However, there is little variation of the area-average heat flux with H/d_{IDF} for the range of H/d_{IDF} from 5 to 8. The value at Re_{air}=1500 and Φ=0.8 is at a high level in an unexpected way. According to the HC concentration measurement, the fuel is forced to impinge and spread along the impingement plate by the air jet, thus, more fuel is burnt near the plate.

For the range of Φ investigated and at Re_{air}=2000 to 3000, the heat transfer efficiency has a peak value at Re_{air}=2000 and Φ=1.2. At higher Re_{air} and at higher Φ, the heat transfer efficiency decreases. One of the main reasons of the drop in heat transfer efficiency is due to the heat escaped beyond the integration area used for the evaluation of the heat transfer efficiency.

As a result, for the investigated operating conditions of the impinging IDF, the flame at Re_{air}=2000 and Φ=1.2 burnt in a most complete combustion with the least pollutant emissions and also has the best heat transfer efficiency.

7.3 Comparison of Thermal and Emission Performances Between IDF and Premixed Flames

The premixed flame consists of a thin layer of reaction zone which appears to be a sharp boundary between the inner unburned gases and the outer burned gases. The premixed flame is observed to be more stable than the IDF from photos of the flame obtained by using high speed shutter.

Comparing the results obtained from the IDF with those of the premixed flame indicates rather different stagnation point flame temperatures, stagnation point heat fluxes and radial heat flux profiles existed between them. While the radial flame temperature profiles are rather similar between these two flame types. The sharp increases of the flame temperature and heat flux at the

stagnation point of the impingement plate impinged upon by a premixed flame show its ability to achieve intensive combustion within a shorter nozzle-to-plate distance. While the gradual increases of these parameters at the stagnation point of the IDF shows the intensive combustion is obtained over a longer nozzle-to-plate distance.

Considering the radial profiles, the premixed flame has a rather high peak value of flame temperature and a sharp peak value of heat flux near the stagnation point of the impingement plate, whereas the IDF has relatively high values for these two parameters around the wall jet region. Thus, the fuel energy is spread more uniformly along the plate and a significant proportion is transferred to the wall jet region for the IDF.

Comparing the concentrations of the combustion species of the IDF with those of the premixed flame, the O_2 concentration shows that the premixed flame has a more intensive combustion near the centerline, but more incomplete and poorer combustion is also indicated at the same time by the high values of CO and HC concentrations. Also, the NO concentration of the premixed flame is higher at the post-combustion flame zone.

By considering the heat flux and the corresponding combustion species measurements, the cool core zone inside the IDF cools the heat generated in the partially premixed flame zone. It has a greater effect on the heat being transferred to the plate when compare to the unburned gas inside the premixed flame. Therefore, the maximum heat flux occurs at the downstream of the intense combustion region at low value of H/d_{IDF}; and for the premixed flame, high heat fluxes are always found in the reaction zone coinciding with high concentrations of CO, NO and CO_2 and very low concentrations of O_2.

When Φ increases from 1.0 to 1.2, the premixed flame has a slightly increase in the area-averaged heat flux, while the IDF has a more significant increase. However, the heat transfer efficiency of the premixed flame has a peak value of 78.1% at Φ = 1.0 and H/dp = 2. It decreases at higher Φ and higher or lower H/dp. The IDF has a peak value of 79% at Φ = 1.2 at H/d_{IDF} = 5, which indicates that the flame appears to behave as a stoichiometric flame.

As a result, the IDF seems to have the advantage of having higher heat transfer efficiency than the premixed flame over a rather large range of nozzle-to-plate distance with lower pollutant species emissions.

REFERENCES

[1] U.S. Department of Energy, Energy Information Administration, 2005, “International Energy Outlook 2005”, Report DOE/EIA-0484 Washington, D.C.

[2] L.K. Sze, C.S. Cheung, C.W. Leung, 2004, “Temperature Distribution and Heat Transfer Characteristics of an Inverse Diffusion Flame with Circumferentially”, International Journal of Heat and Mass Transfer, vol. 47, pp. 3119-3129.

[3] L.K. Sze, C.S. Cheung, C.W. Leung, 2006, “Appearance, Temperature, and NO_X Emission of Two Inverse Diffusion Flames with Different Port Design”, Combustion and Flame, vol.144, pp.237-248.

[4] G.K. Hargrave, M. Fairweather and J.K. Kilham, 1987, “Forced Convective Heat Transfer From Premixed Flame-Part 1: Flame Structure”, International Journal of Heat and Fluid Flow, vol.8, pp.55-63.

[5] S. P. Burke, and T.E. Schumann, 1928, “Diffusion Flames”, Industrial and Engineering Chemistry, vol.20, pp.988-1004.

[6] J. Barr, 1953, “Flame of fuel jets: diffusion flame”, Fourth Symposium (International) on Combustion, pp.765-771.

[7] R.E. Mitchell, A.F. Sarofim and L.A. Clomburg, 1980, “Experimental and Numberical Investigation of Confined Laminar Diffusion Flames”, Combustion and Flame, vol.37, pp.227-244.

[8] A. Cavaliere, R. Ragucci, 2001, “Gaseous Diffusion Flames: Simple Structures and their Interaction”, Progress in Energy and Combustion Science, vol.27, pp.547-585.

[9] J.N. Friend, 1922, “The Chemistry of Combustion”, London: Gurney & Jackson, pp.34.

[10] K.T. Wu, 1984, “The Comparative Structure of Normal and Inverse Diffusion Flames”, PhD Dissertation, The Ohio State University.

[11] K.T. Wu and R.H. Essenhigh, 1984, “Mapping and Structure of IDF of Methane”, Twentieth Symposium (International) on Combustion, pp.1925-1932.

[12] Y. Bindar and A. Irawan, 2002, “Size and Structure of LPG and Hydrogen Inverse Diffusion Flames at High Level of Fuel Excess”, 6th Asia-Pacific International Symposium on Combustion and Energy Utilization, pp.124-130.

[13] A. Sinha, R. Ganguly and I.K. Puri, 2005, “Control of Confined Nonpremixed Flames Using a Microjet”, International Journal of Heat and Fluid Flow, vol.26, pp.431-439.

[14] A. Sobiesiak, J.C. Wentzell, 2005, “Characteristics and Structure of Inverse Flames of Natural Gas”, Proceedings of the Combustion Institute, vol.30, pp.743-749.

[15] R. Ganguly, Ishwar K. Puri, 2004, “Nonpremixed Flame Control with Microjets”, Experiments in Fluids, vol.36, pp.635-641.

[16] Y.C. Ko, S.S. Hou, T. H. Lin, 2005, “Laminar Diffusion Flames in a Multiport Burner”, Combustion Science and Technology, vol.177, pp.1463-1484

[17] T.W. Lee, M. Fenton and R. Shankland, 1997, “Effects of Variable Partial Premixing on Turbulent Jet Flame Structure”, Combustion and Flame, vol.109, pp.536-548.

[18] R.F. Huang and C.L. Lin, 1994, “Characteristic Modes and Thermal Structure of Nonpremixed Circular-Disc Stabilized Flames”, Combustion Science and Technology, vol.100, pp.123-139.

[19] R.F. Huang, J.T. Yang and P.C. Lee, 1997, “Flame and Flow Characteristics of Double Concentric Jets”, Combustion and Flame, vol.108, pp.9-23.

[20] T. Takagi, Z. Xu and M. Komiyama, 1996, “Preferential Diffusion Effects on the Temperature in Usual and Inverse Diffusion Flames”, Combustion and Flame, vol.106, pp.252-260.

[21] C.R. Shaddix, T.C. Williams, L.G. Blevins and R.W. Schefer, 2005, “Flame Structure of Steady and Pulsed Sooting Inverse Jet Diffusion Flames”, Proceedings of the Combustion Institute, vol.30, pp.1501-1508.

[22] R. Viskanta, 1996, “Convective and Radiative Flame Jet Impingement Heat Transfer”, The Ninth International Symposium on Transport Phenomena in Thermal-Fluids Engineering, pp.46-60.

[23] Y. Zhang and K.N.C. Bray, “Characterization of Impinging Jet Flames”, Combustion and Flame, Vol. 116, pp.671-674, 1999

[24] T. Foat, K.P. Yap and Y. Zhang, 2001, “The Visualization and Mapping of Turbulent Premixed Impinging Flames”, Combustion and Flame, vol.125, pp.839-851.

[25] A. Milson and N.A. Chigier, 1973, “Studies of Methane and Methane-Air Flames Impinging on a Cold Plate”, Combustion and Flame, vol.21, pp.295-305.

[26] J.R. Rigby and B.W. Webb, 1995, “An Experimental Investigation of Diffusion Flame Jet Impingement Heat Transfer”, 4th ASME/JSME Thermal Engineering Joint Conference, Eds. L.S. Fletcher and T. Aihara, vol.3, pp. 117-126.

[27] J. Wu, J. Seyed-Yagoobi and R.H. Page, 2001, “Heat Transfer and Combustion Characteristics of an Array of Radial Jet Reattachment Flames”, Combustion and Flame, vol.125, pp.955-964.

[28] R.H. Page, L.L. Hadden and C. Ostowari, 1989, “Theory for Radial Jet Reattachment Flow”, AIAA Journal, vol.27, pp.1500-1505.

[29] D.K. Habetz, R.H. Page and J. Seyed-Yagoobi, 1994, “Impingement Heat Transfer from a Radial Jet Reattachment Flame”, 10th International Heat Transfer Conference, Brighton, U.K., vol.6, pp.31-36.

[30] J.W. Mohr, J. Seyed-Yagoobi and R.H. Page, 1996, “Combustion Measurements from an Impinging Radial Jet Reattachment Flame”, Combustion and Flame, vol.106, pp.69-80.

[31] J.W. Mohr, J. Sayed Yagoobi and R.H. Page, 1997, “Heat Transfer from Pair of Radial Jet Reattachment Flames”, Journal of Heat Transfer, vol.199, pp. 633 – 635.

[32] C.E. Baukal, L.K. Farmer, B. Gebhart, and I. Chan, 1996, “Heat Transfer Mechanisms in Flame Impingement Heating”, in 1995 International Gas Research Conference, vol.II, D.A. Dolenc, Ed., Govt. Institutes, Rockville, MD, pp.2277-2287.

[33] S. Chander, A. Ray, 2005, “Flame Impingement Heat Transfer: A Review”, Energy Conversion and Management, vol. 46, pp.2803-2837

[34] L.L. Dong, C.S. Cheung and C.W. Leung, 2001, “Heat Transfer Characteristics of an Impinging Butane/Air Flame Jet of Low Reynolds number”, Experimental Heat Transfer, vol.14, pp.265-82.

[35] L.L. Dong, C.S. Cheung and C.W. Leung, 2002, “Heat Transfer Characteristics of Premixed Butane/Air Flame Jet Impinging on an Inclined Flat Surface”, Heat and Mass Transfer, vol.39, pp.19-26.

[36] C. Subhash and R. Anjan, 2005, “Flame Impingement Heat Transfer: A Review”, Energy Conversion and Management, vol.46, pp.2803-2837.

[37] A. Milson and N.A. Chigier, 1973, “Studies of Methane Air Flames Impinging on Cold Plate”, Combust and Flame, vol.21, pp. 295 – 305.

[38] C.E. Baukal and B. Gebhart, 1998, “Heat Transfer from Oxygen-Enhanced/Natural Gas Flames Impinging Normal to Plane Surface”, Experimental Thermal Fluid Science, vol.16, pp.247 – 59.

[39] L.L. Dong, C.S. Cheung and C.W. Leung, 2002, “Heat Transfer from an Impinging Pre-mixed Butane/Air Slot Flame Jet”, International Journal of Heat and Mass Transfer, vol.45, pp.979 – 992.

[40] K. Mizuno, R. Mittal and R. Viskanta, 1996, “An Experimental Study of Pre-mixed Flame Impingement Heat Transfer”, In: Papper DW, et al., editors, Proceedings of ASME heat transfer division, vol.4, HTD-vol.335, New York: ASME, pp.245 – 252.

[41] E.M. Schutle, 1972, “Impingement Heat Transfer Rates from Torch Flames”, Journal of Heat Transfer, vol.94, pp.231- 233.

[42] S.S. Hou, Y.C. Ko, 2004, “Effects of Heating Height on Flame Appearance, Temperature Field and Efficiency of an Impinging Laminar Jet Flame”, Energy Conversion and Management, vol.45, pp.1583-1595.

[43] S. Jugjai, S. Tia and W. Trewetasksorn, 2001, “Thermal Efficiency improvement of an LPG Gas Cooker by a Swirling Central Flame”, International Journal of Energy Research, vol.25, pp.657-674.

[44] S. Jugjai, N. Rungsimuntuchart, 2002, “High Efficiency Heat-Recirculating Domestic Gas Burners”, Experimental Thermal and Fluid Science, vol.26, pp.581-592.

[45] C.R. Kaplan and K. Kailasanath, 2001, “Flow-Field Effects on Soot Formation in Normal and Inverse Methane-Air Diffusion Flmaes”, Combustion and Flame, vol.124, pp.275-294.

[46] G.W. Sideotham and I. Glassman, 1992, “Flame Temperature, Fuel Structure, and Fuel Concentration Effects on Soot Formation in Inverse Diffusion Flames”, Combustion and Flame, vol.90, pp.269-283.

[47] E.J. Lee, K.C. Oh and H.D. Shin, 2005, “Soot Formation in Inverse Diffusion Flames of Diluted Ethene”, Fuel, vol.84, pp.543-550.

[48] Viskanta, 1993, “Heat Transfer to Impinging Isothermal Gas and Flame Jets”, Experimental Thermal and Fluid Science, vol. 6, pp. 111-134.

[49] J.W. Mohr, 1996, “Studies of Single and Multiple Impinging Radial Jet Reattachment Flames”, Ph.D. Thesis, Texas A&M University.

[50] L.L. Dong, C.S. Cheung and C.W. Leung, 2003, “Combustion Optimization of Slot Flame Jet Impinging System”, Journal of the Institute of Energy, vol.76, pp.80-88.

[51] D.P. Mishra, 2004, “Emission Studies of Impinging Premixed Flames”, Fuel, vol.83, pp.1743-1748.

[52] J. Chedaille and Y. Braud, 1972, “Industrial Flames Vol.1: Measurements in Flames”, Edward Arnold Publishers Limited, pp.3.

[53] T.W. Kerlin, 1999, “Practical Thermocouple Thermometry”, Instrument Society America, pp.12, 67.

[54] L.C. Kwok, 2003, “Studies of the Pre-mixed Butane/Air Impinging Flame Jets”, Mphil Thesis, The Hong Kong Polytechnic University, Hong Kong.

[55] A. Sato, K. Hashiba, M. Masatani, S. Sugiyama and J. Kimura, 1975, “A Correctional Calculation Method for Thermocouple Measurement of Temperature in Flames”, Combustion and Flames, vol.24, pp.35-41.

[56] G.L. Borman and K.W. Ragland, 1998, “Combustion Engineering”, McGraw-Hill, Boston, pp.64-66, Appendix D.

[57] M. Mahmood, 1980, “Heat transfer from swirling impinging jets”, Ph.D. Thesis, Cranfield Institute of Technology.

[58] S.G. Tuttle, B.W. Webb, M.Q. McQuay, 2005, “Convective Heat Transfer from a Partially Premixed Impinging Flame Jet. Part I: Time-average results”, International Journal of Heat and Mass Transfer, vol.48, pp.1236-1251.

[59] Spiegel and R. Murray, 1992, “Probability and Statistics”, Schaum’s Outline Series, McGraw-Hill, New York, pp.34-40.

[60] S.J. Kline and F.A. McClintock, 1953, “Describing Uncertainties in Single-Sample Experiments”, Mechanical Engineering, vol.75, pp.3-8.